Technische Universität Dresden

Optimization of performance and reliability of HZO-based capacitors for ferroelectric memory applications

M. Sc.

Monica Materano

der Fakultät Elektrotechnik und Informationstechnik der Technischen Universität Dresden

zur Erlangung des akademischen Grades

Doktoringenieurin

(Dr.-Ing.)

genehmigte Dissertation

Vorsitzender: Prof. Dr.-Ing. habil. Christian Georg Mayr
Gutachter: Prof. Dr.-Ing. Thomas Mikolajick
Gutachter: Prof. Dr Catherine Dubourdieu

Tag der Einreichung: 14.09.2021
Tag der Verteidigung: 31.01.2022

A Nonna Rosa
Per la tenacia e la tenerezza

Abstract

In an era in which the amount of produced and stored data continues to exponentially grow, standard memory concepts start showing size, power consumption and costs limitation which make the search for alternative device concepts essential. Within a context where new technologies such as DRAM, magnetic RAM, resistive RAM, phase change memories and eFlash are explored and optimized, ferroelectric memory devices like FeRAM seem to showcase a whole range of properties which could satisfy market needs, offering the possibility of creating a non-volatile RAM.

In fact, hafnia and zirconia-based ferroelectric materials opened up a new scenario in the memory technology scene, overcoming the dimension scaling limitations and the integration difficulties presented by their predecessors perovskite ferroelectrics. In particular, $Hf_xZr_{1-x}O_2$ stands out because of high processing flexibility and ease of integration in the standard semiconductor industry process flows for CMOS fabrication. Nonetheless, further understanding is necessary in order to correlate device performance and reliability to the establishment of ferroelectricity itself.

The aim of this work is to investigate how the composition of the ferroelectric oxide, together with the one of the electrode materials influence the behavior of a ferroelectric RAM. With this goal, different process parameters and reliability properties are considered and an analysis of the polarization reversal is performed. Starting from undoped hafnia and zirconia and subsequently examining their intermixed system, it is shown how surface/volume energy contributions, mechanical stress and oxygen-related defects all concur in the formation of the ferroelectric phase.

Based on the process optimization of an $Hf_xZr_{1-x}O_2$-based capacitor performed within these pages, a 64 kbit 1T1C FeRAM array is demonstrated by Sony Semiconductor Solutions Corporation which shows write voltage and latency as low as 2.0 V and 16 ns, respectively. Outstanding retention and endurance performances are also predicted, which make the addressed device an extremely strong competitor in the semiconductor scene.

Contents

List of Figures

List of Tables

1 Motivation

In the era of digitalization, data storage has become of extreme importance in our daily lives. Starting from personal computers, moving to mobile phones, cameras, smart housewares and looking forward to the Internet of things, everyone of us is surrounded by or even carrying billions of incredibly tiny capacitors and transistors which allow us to store information in the form of a bit, of a "1" or a "0".

The miniaturization of data memories brings several challenges along. Device requirements do not only include high storage density but also cost-effectiveness, low power consumption and high speed operation.

Table 1.1: Comparison of the main features of SRAM, DRAM, and ferroelectric memory technologies. Adapted from [1]–[5].

Property	**SRAM**	**DRAM**	**perovskite-based FeRAM**	**HfO_2-based FeRAM**	**HfO_2-based FeFET**
Operation voltage	> 0.5 V	> 1 V	> 1 V	> 2.5 V	> 3 V
Program time	< 10 ns	< 20 ns	< 20 ns	< 14 ns	250 ns
Endurance	$> 10^{15}$	$> 10^{15}$	$> 10^{15}$	$> 10^{15}$	$> 10^{5}$
Read time	< 10 ns	< 20 ns	-	-	-
Non-volatile	no	no	yes	yes	yes
Memory cell	6T	1T1C	1T1C	1T1C	1T
Min. feature size	$> 100F^2$	$6F^2$	$\sim 30F^2$	$6F^2$	$6\text{-}10F^2$
Technology node	28 nm	18 nm	$\sim$ 90 nm	$\sim$ 20 nm	22 nm

Traditional memory concepts struggle to follow market evolution for different reasons. In fact, technologies such as static random access memories (SRAM) present size limitations with its six transistors [6]. Solutions such as dynamic random access memories (DRAM) show power consumption issues related to volatility and consequent continuous request of a supplied voltage. In this landscape, new memory concepts emerged such as magnetic RAM, resistive RAM, and last but not least ferroelectric RAM, which could fill the gap in the traditional memories hierarchy and present a solution both in terms of high density i.e. high scalability, low power consumption because of non-volatility and low program voltage and latency and promised high endurance. Table 1.1 reports a comparison in terms of operation speed and performance of the more traditional memory concepts (SRAM, DRAM) and the newer ferroelectric technologies.

100 years ago ferroelectricity was first reported [7] and after that many materials have been found showing a remanent polarization at zero applied fields. Perovskite-based materials such as lead zirconate titanate (PZT) and strontium barium titanate (SBT) seemed to be promising until a final stop was reached in terms of scalability, leaving device concepts based on these materials at the 90-nm technology node and only usable for niche applications [8].

The first publication showing a ferroelectric hysteresis in hafnia doped with Si by Böscke in 2011 [9] paved the way towards better device integration in the state-of-the-art technology nodes. In the last couple of years, a 28-nm technology node integrated ferroelectric Si-doped hafnia field-effect transistor (FeFET) and the first fully working FeRAM arrays based on a combination of hafnium and zirconium oxides were successfully demonstrated by industry [4], [10].

Besides classic data storage, hafnia-based ferroelectric devices show great potential in the field of neuromorphic computing. Technologies such as FeFET can well emulate the biological behavior of a brain network, serving both as neurons and as synapses [11], [12]. This particular skill is related to the inherent presence of a transistor and a non-volatile element in the FeFET structure. A tunable conductance behavior was also demonstrated in HfO_2-containing ferroelectric tunnel junctions, which are therefore also good candidates for neurosynaptic computing [13], [14]. Not of lower importance is also the observation of negative capacitance effects in structures combining a ferroelectric and a dielectric layer [15], [16].

The feasibility of such devices was only possible thanks to major steps in material and technology research which have been achieved in the last ten years. Nonetheless, challenges are still present and the success of this memory concept on the market still strongly depends on device optimization on a material level.

That given, this work pursues the optimization of ferroelectric capacitors whose active layer is a solid solution of hafnium and zirconium oxide. The intention behind this research stems from the interest of Sony Semiconductor Solutions Corporation in a high endurance, fast operation and long-lasting memory device. For this purpose, FeRAM was chosen as targeted architecture, given its outstanding performance as already elucidated in table 1.1. The study and improvement of ferroelectric capacitors are therefore targeted not only in remanent polarization values but also in terms of device reliability with time and temperature and of lifetime meaning program and erase cycling performances.

First, an overview is given elucidating ferroelectric fundamental physics through the Landau-Ginzburg formalism. This is followed by a short overview of the existing ferroelectric memory device concepts and different material classes, with a particular focus on hafnia-based thin films.

The main figures of merit for ferroelectric devices are presented together with the challenges in terms of the reliability of this technology. After that, the techniques used within this study to fabricate and characterize the capacitors are listed and concisely explained in chapter 3.

The core of this work is represented by chapters 4, 5, 6 and 7, where the optimization of the fabricated ferroelectric capacitors is addressed first by studying the hafnium-zirconium oxide layer (chapter 4) and later by observing the influence of the used electrode materials (chapter 5). In chapter 6, the polarization switching mechanism in hafnia-based ferroelectric thin films is investigated in relation to material properties. Different models are surveyed and an interpretation of the polarization reversal mechanism is suggested. Finally, chapter 7 aims to elucidate the interplay of the different factors playing a role in the establishment of ferroelectric properties in HfO_2/ZrO_2-based capacitors, eventually showing how oxygen content, mechanical stress and surface/volume energy effect all concur in the stabilization of the polar phase in such films.

Last but not least, the results obtained by Sony Semiconductor Solutions Corporation when integrating the optimized ferroelectric layer in a 64 kbit 1 transistor - 1 capacitor (1T1C) array are shortly exposed in chapter 8, demonstrating a successful optimization of the FeCap building blocks allowing device operation at high speed and low voltages.

2 Fundamentals

2.1 Basics of ferroelectricity

Ferroelectric materials are a subgroup of polar dielectric materials which present a non-linear response with respect to the electric field. A ferroelectric material is characterized by two opposite spontaneous polarization states P_s which are retained even in the absence of an external electric field. Switching between these two opposite polarization states i.e. polarization reversal can be obtained by applying an electric field in the opposite direction [17].

Despite containing the word "ferro", ferroelectricity does not deal with the chemical element Fe (iron). The etymology of the word finds its roots in the similarity with ferromagnetism. In ferromagnetic materials, the magnetic flux density B shows a hysteretical dependence on the applied external magnetic field H. Similar behavior is proper of ferroelectric materials, where the magnetic flux B is replaced by the electric displacement D and the magnetic field H by the electric field E [18].

In a linear dielectric, the displacement field D is correlated to the electric field E through the following relation:

$$D = \varepsilon E = \varepsilon_0 \varepsilon_r E \tag{2.1}$$

where ε is the electrical permittivity, which can be expressed as the product of the vacuum permittivity ε_0 and the permittivity of the medium in question ε_r. In a ferroelectric material, this relation is not linear and the displacement field D can be also expressed as a function of the electrical polarization P as follows:

$$D = \varepsilon_0 E + P \tag{2.2}$$

where P can be also expanded as a function of the spontaneous polarization P_s and of the linear dielectric response:

$$P = \varepsilon_0 \chi E + P_s \tag{2.3}$$

$$D = \varepsilon_0 E + \varepsilon_0 \chi E + P_s \tag{2.4}$$

where χ is the electrical susceptibility of the medium.

The presence of the spontaneous polarization P_s gives rise to the typical hysteresis curve observed when plotting the polarization P vs. the applied electric field E i.e. the P-E characteristics. The two intercepts with the positive and negative y-axis represent the positive and negative remanent polarization $P_{r,+}$ and $P_{r,-}$, respectively.

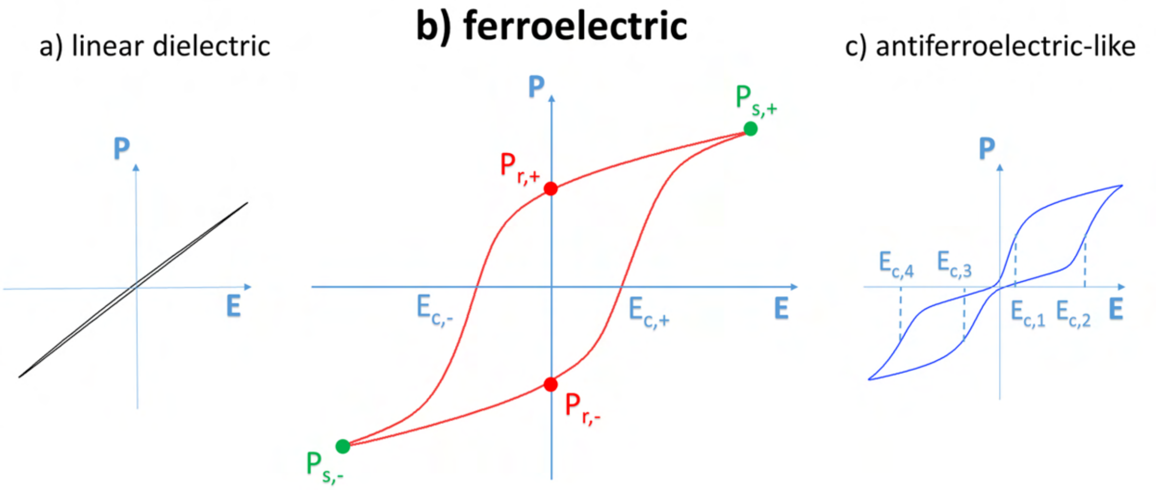

Figure 2.1: Polarization P vs. electric field E for materials showing a) linear dielectric behavior b) ferroelectric behavior c) antiferroelectric-like behavior. Remanent polarization, spontaneous polarization and coercive fields are indicated in red, green and blue, respectively.

A single domain ferroelectric would show polarization switching at one single field, called coercive field E_c and representing the intercept of a perfect squared ferroelectric hysteresis curve with the x-axis. This ideal case is unlikely and a ferroelectric film rather presents many domains, switching each at a different electric field. This gives rise to a certain distribution of coercive fields and a slightly tilted ferroelectric hysteresis. This deviation from ideality also causes the back-switching of some of the domains after field reversal before the opposite coercive field is reached.

In figure 2.1, the typical P-E characteristics for a a) linear dielectric, b) ferroelectric (FE) and c) antiferroelectric-like (AFE-like) behavior are schematized. In a linear dielectric material, the displacement field equals zero when no electric field is applied. Conversely, a ferroelectric behavior is characterized by two equilibrium states in which a certain polarization P_r is retained even in the absence of an electric field. These two equilibrium states macroscopically correspond to two minima in the free energy landscape of the material, each one associated with one position of one or more ion(s) in the unit cell. Therefore, the energetic landscape of a ferroelectric material presents a double-well potential, with each well corresponding to one equilibrium position for the displacing atom(s). An external electric field is needed to overcome the energy barrier between the two minima, displace the interested ions and therefore reverse material polarity. Differently from ferroelectric materials, antiferroelectric ones present two sub-lattices with antiparallel spontaneous polarization, which therefore induce a zero remanent polarization as a sum of the two equal and opposite contributions when no external field is applied. The application of the latter generates a dipole alignment and/or a phase transition in the polar phase, which is reversible upon field removal. This causes the formation of the positive and negative hysteresis subloops, as shown in Fig. 2.1 c).

2.1.1 Depolarization fields

Another non-ideality factor is represented by the so-called depolarization fields. In an ideal ferroelectric capacitor with two perfect interfaces between the ferroelectric material and the metal electrodes, the polarization charge would be exactly balanced out by the free charges in the metal contacts. Real metals present nonetheless a finite screening length [19] and a certain parasitic interface can be formed between the electrodes and the ferroelectric, for example in the form of a thin oxide interlayer or non-switching phase portions [20], [21]. These two factors contribute to the establishment of a depolarization field E_{dep} which leads to the reduction of the remanent polarization [22], to the creation of multiple domains for energy minimization [23] and to back-switching phenomena. The depolarization field related to the presence of a dead layer can be calculated as follows:

$$E_{dep} = -\frac{P_r}{\varepsilon_{FE}\varepsilon_0}\left(1+\frac{C_d}{C_{FE}}\right)^{-1} = -\frac{P_r}{\varepsilon_{FE}\varepsilon_0}\left(1+\frac{\varepsilon_d d_{FE}}{\varepsilon_{FE} d_d}\right)^{-1} \tag{2.5}$$

where ε_{FE}, C_{FE} and d_{FE} represent the relative permittivity, the capacitance and the thickness of the ferroelectric layer whereas ε_d, C_d and d_d stand for the relative permittivity, the capacitance and the thickness of the dead dielectric layer. To weaken the effect of the E_{dep}, it is necessary to maximize the ratio between the thickness of the ferroelectric and the one of the dielectric. A high electrical permittivity of the dielectric also contributes to decreasing the depolarization fields [24].

Depolarization fields strongly influence device reliability, as will be shown in chapter 5. In fact, the set polarization state can be gradually lost because of back-switching. Charge injection and trapping can also occur to counterbalance the bound polarization.

2.1.2 The Landau-Ginzburg formalism

One of the most accepted theories describing (anti-)ferroelectricity is the Landau-Ginzburg formalism [25], [26]. According to this model, the free energy of a ferroelectric material can be described in the following manner:

$$G = \frac{1}{2}\alpha P^2 + \frac{1}{4}\beta P^4 + \frac{1}{6}\gamma P^6 - EP \tag{2.6}$$

where α, β and γ are the Landau coefficients. Contrarily to β and γ, α shows a temperature dependency. The first and second derivatives of the free energy G with respect to the polarization P gives insights on system stability, whose conditions change with respect to the sign of the Landau coefficients. Minima are obtained for the free energy when the following conditions are satisfied:

$$\frac{\delta G}{\delta P} = 0 \rightarrow E = \alpha P + \beta P^3 + \gamma P^5 \tag{2.7}$$

$$\frac{\delta^2 G}{\delta^2 P} > 0 \rightarrow \alpha + 3\beta P^2 + 5\gamma P^4 > 0 \tag{2.8}$$

The first trivial solution is found for P = 0 and corresponds to the paraelectric state. Otherwise, system stability will strongly depend on the coefficients.

The term γ at the highest power needs to be positive. A negative γ would translate in infinite negative free energy at high polarization values, implying system decomposition. The coefficient α represents the inverse of the electrical susceptibility and therefore presents a temperature dependence in the form

$$\alpha = \frac{1}{\chi} = \alpha_0(T - T_0) \tag{2.9}$$

where T_0 is a critical temperature called Curie-Weiss temperature which is normally equal or lower than the phase transition temperature T_c. At temperatures above T_0, α is positive and only one minimum is observed in the free energy with respect to polarization, meaning the system has a paraelectric behavior. For $T < T_0$ i.e. for negative α two minima are observed corresponding to the two ferroelectric polar states.

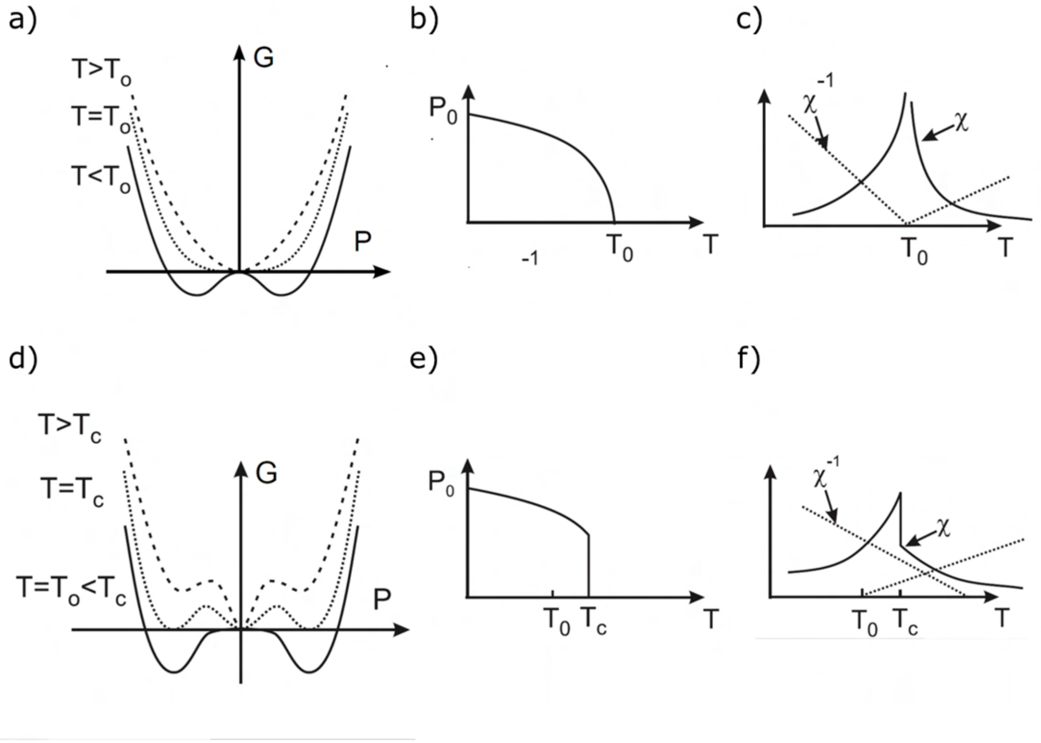

Figure 2.2: Qualitative trends of a) Gibbs free energy as a function of polarization, b) spontaneous polarization and c) electrical susceptibility as a function of temperature for a second order phase transition and of d) Gibbs free energy as a function of polarization, e) spontaneous polarization and electrical susceptibility as a function of temperature for a first order phase transition. Pictures taken from [27].

The sign of the term β determines whether a first or a second order phase transition takes place between the two polar states. If β is positive, a second order phase transition is observed. On the contrary, a phase transition of the first order takes place when $\beta < 0$.

For $\beta > 0$ i.e. in the case of a second order phase transition, neglecting γ, together with the trivial solution with $P = 0$ the following expression is obtained:

$$P_s^2 = -\frac{T - T_0}{\beta C_{Curie}} \tag{2.10}$$

where C_{Curie} is the Curie constant. This means that, for temperatures lower than the Curie temperature, a spontaneous polarization exists. In this case, T_0 coincides with the phase transition temperature T_c. Figure 2.2 (a), (b) and (c) show the trends of the free energy with respect to the polarization and of the polarization and the electrical susceptibility with respect to the temperature in the case of a second order phase transition. For $T > T_0$, only one minimum of G is observed corresponding to $P = 0$ i.e. to the paraelectric solution. When lowering the temperature below T_0, a continuous transition into the two minima corresponding to the two polarization states is observed.

For $\beta < 0$ i.e. in the case of a first order phase transition, assuming $\gamma > 0$, together with the trivial solution with $P = 0$ the following expression is obtained:

$$P_s^2 = (|\beta| + \sqrt{\beta^2 - 4C_{Curie}^{-1}(T - T_0)\gamma})\, 2\gamma \tag{2.11}$$

Figures 2.2 (d), (e) and (f) display the trends of the free energy with respect to the polarization and of the polarization and the electrical susceptibility with respect to the temperature in the case of a first order phase transition. Once again, above the phase transition temperature T_c, the free energy G has one minimum corresponding to $P = 0$. By cooling down the system, two minima are formed which are higher in energy compared to the global minimum at $P = 0$ until the Curie temperature T_0 is reached, meaning that the ferroelectric and the paraelectric phase co-exist with the ferroelectric phase being meta-stable. For $T < T_0$, the two minima corresponding to two finite polarization values are lower in energy compared to the minimum at $P = 0$ i.e. the two ferroelectric states are stable. The transition takes place in a discontinuous way, that is a jump in polarization from 0 to a finite value is observed.

2.2 Ferroelectricity for memory applications

The double configuration possessed by ferroelectric materials in terms of positive and negative polarization naturally allows them to be used as binary memory devices. In this section, the three basic memory concepts based on ferroelectricity will be explained. The working mechanisms behind ferroelectric random access memories (FeRAM), field-effect transistors (FeFET) and tunnel junctions (FTJ) will be exposed, with particular attention reserved to FeRAM. A review of the history and the functioning of the different ferroelectric memory concepts can be found elsewhere [5], [28].

2.2.1 Ferroelectric random access memory

The first ferroelectric memory was proposed by Dudley Allan Buck and dates back to 1952 [29]. His concept was based on a matrix of capacitors and presented therefore instability issues related to signal disturb and capacitor discharge when spatially consecutive devices in the array were addressed. To overcome this issue, a 1T1C was proposed where a transistor is combined with a ferroelectric capacitor. The 1T1C memory cell strongly resembles the DRAM architecture and is nowadays used in commercial ferroelectric devices [2], [30].

A standard 1T1C FeRAM structure is schematized in Fig. 2.3 a). The ferroelectric capacitor is addressed by pulses of a defined amplitude and polarity which may or may not induce a switching

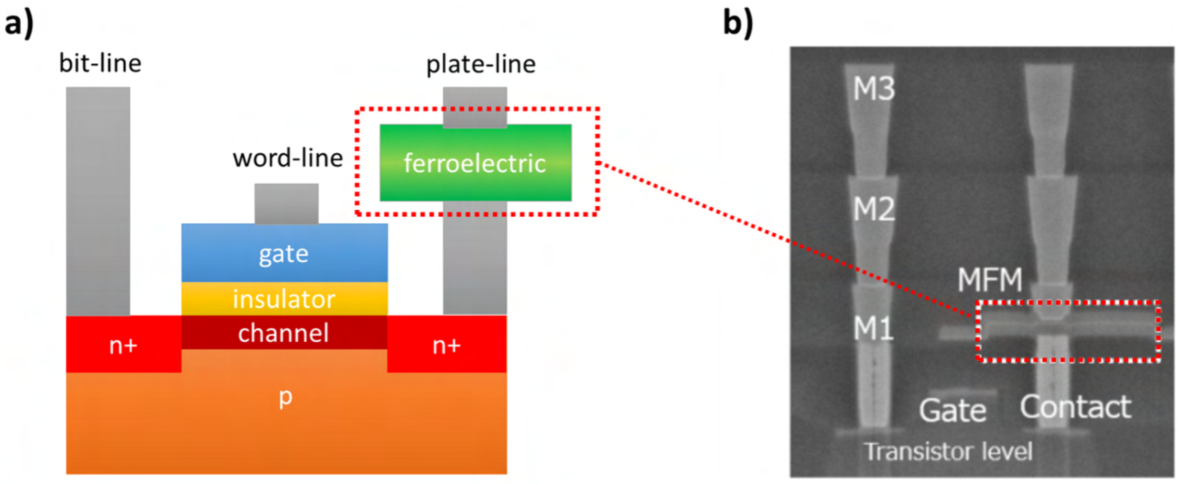

Figure 2.3: a) Schematics and b) SEM cross section of a 1T1C FeRAM memory. M1, M2 and M3 represent the metals used to create the bit-line contact during BEOL integration; MFM represent the metal-ferroelectric-metal (1C) structure of the 1T1C memory cell. Picture b) was taken with permission from [2].

event, depending on the capacitor polarization state at the moment the pulse is applied. After activating the transistor through the word line, its current is read as a voltage change at the bit line: a switching event in the ferroelectric capacitor will provide a positive difference between the read bit line voltage (V_{BL}) and a reference voltage, corresponding to an enhancement due to the switched polarization charge $2P_r \cdot A$, where A is the capacitor area. On the contrary, when no switching takes place, the read V_{BL} will equal the reference voltage. By differentiating these two cases, a "1" or a "0" bit can be read. The reading operation is destructive and the information has to be refreshed after read-out. Nonetheless, the ability to store a certain polarization state even in the absence of an electric field makes FeRAM non-volatile, in contrast to DRAM [31].

2.2.2 Ferroelectric field effect transistor

Another ferroelectric memory concept is the ferroelectric field-effect transistor (FeFET). It only consists of a 1T memory cell. In this case, the ferroelectric layer is placed between the gate and the channel and a shift in the transistor threshold voltage is observed depending on the polarization state of the ferroelectric [32]. The writing operation consists in applying a voltage between the word-line and the "bulk" (ground) of the transistor. During the reading operation, a fixed gate voltage is applied at the gate (word line) and a different drain current (on/off) is read at the bit line depending on the polarization state of the ferroelectric i.e. on the caused threshold voltage. This gives either a "1" or a "0" in the read-out. Conversely to the 1T1C concept, the reading operation of a 1T cell is non-destructive. The FeFET concept, unfortunately, suffers from strong retention issues mainly caused by charge trapping [33] and depolarization fields phenomena [34] originating from the dielectric interface generated between the ferroelectric and the semiconductor channel of the transistor. Furthermore, a relatively high coercive field is needed to be able to scale down the device and use lower ferroelectric layer thicknesses. The discovery of ferroelectricity in HfO_2 thin layers has eased the way towards integration of FeFET devices in standard CMOS lines [10], [35], [36]. Nonetheless, the aforementioned reliability issues still postpone the integration of the 1T cell into commercial concepts.

Despite its low retention and endurance, other factors contribute to making FeFET such an interesting technology. Cumulative switching was demonstrated, allowing multiple-level storage and opening the path towards neuromorphic [12], [37] and logic in memory [38] applications. Negative capacitance effects [15], [39] were also demonstrated.

2.2.3 Ferroelectric tunnel junction

Ferroelectric thin films can also be used on their own or in combination with a thin tunneling dielectric layer within ferroelectric tunnel junctions (FTJ), which mainly consist of capacitors whose polarization state is directly read by measuring the current flowing through the capacitor [40]. This device concept has only recently started to be investigated as compared to FeRAM and FeFET devices. In a single layer FTJ device, a very thin ferroelectric layer is placed between two different metal electrodes and the tunneling current level will depend on the ferroelectric polarization state [41].

Despite the concept itself being rather straightforward, its implementation presents several practical obstacles. As an example, it is difficult to obtain crystalline ferroelectric layers of the wished thickness (i.e. 2-3 nm). Furthermore, parasitic currents could easily be in the same range of the signal to be detected and make readout unreliable. To overcome such limitations, a new device concept has been elaborated in which a thin dielectric layer (e.g. Al_2O_3 [42] or SiO_2 [43]) is stacked with the ferroelectric layer into the capacitor structure. Nevertheless, this alternative concept also carries reliability issues that become similar to those observed in FeFETs, where the interplay between the thin ferroelectric layer and the creation of an additional oxide interface can result in strong depolarization fields and charge trapping. For this reason, the respective thicknesses of the ferroelectric and the thin dielectric have to be optimized to allow a high enough tunneling current and concurrently a decent retention performance [44].

2.3 Materials showing ferroelectricity

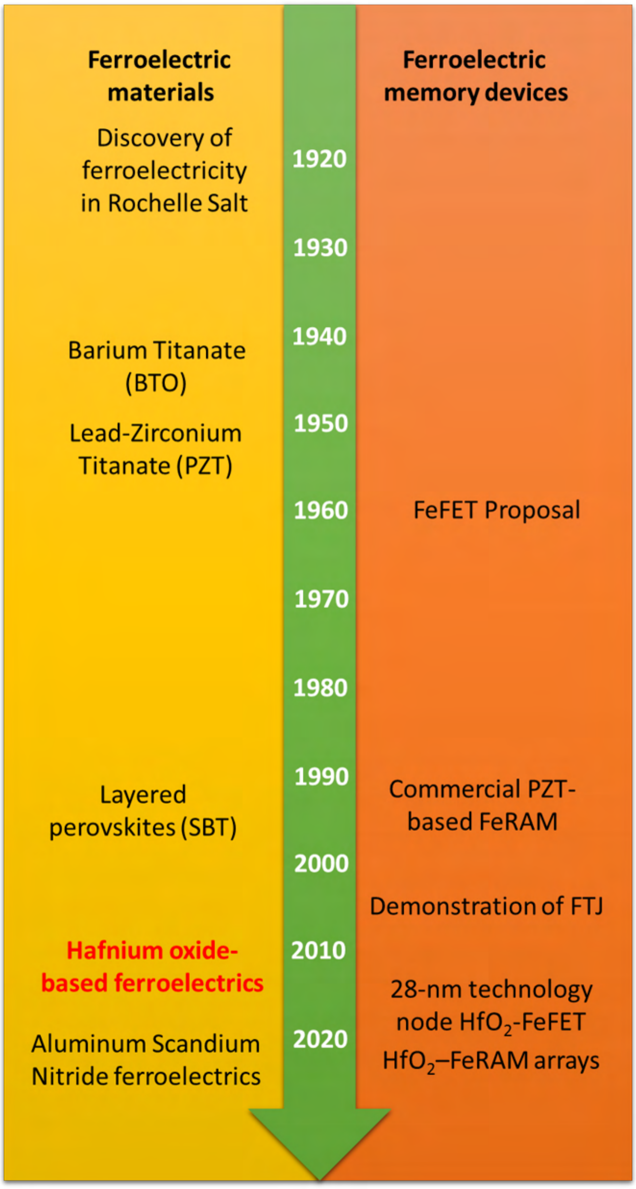

Figure 2.4: Timeline of meaningful discoveries and advancements in semiconductor ferroelectric science and industry from the first report [45] until today. Picture adapted from [28].

Figure 2.4 chronologically reports the advancements and the milestones reached both in the field of ferroelectric material research and from a memory device point of view. Ferroelectricity was first reported in 1921 when a ferroelectric hysteresis analogous to the well-known magnetic hysteresis was measured in Rochelle Salt [7]. Nevertheless, the interest in this material class only started growing when this property was first detected in perovskite structures such as barium titanate ($BaTiO_3$) [46] and later in lead zirconate titanate ($Pb(Zr_{1-x}Ti_x)O_3$ or PZT) [47], [48] or in layered perovskite structure such as strontium bismuth tantalite ($Sr_{1-x}Bi_{2+x}Ta_2O_9$ or SBT)

[49]. Ferroelectricity was also reported in organic systems such as polyvinylidene fluoride, co-polymerized with tri-fluoroethylene [P(VDF-TrFE)] [50], [51]. The discovery of ferroelectricity in hafnia-based material allowed the scaling down of memory devices accordingly to the state-of-the-art technology nodes. This allowed the integration of FeFET in the 28 nm technology node [36] and led to the demonstration of the first HfO_2-based FeRAM arrays [2], [30]. Concurrently, outstanding properties were also reported in AlScN-based films, opening promising parallel integration routes [52].

Table 2.1: Remanent polarization, coercive field and k-value in some of the most common ferroelectric systems. Values were extracted from [8], [52]–[54].

Property	**PZT**	**SBT**	**PVDF:TRFE**	**HfO_2**	**$Al_xSc_{1-x}N$**
Remanent polarization $[\mu C/cm^2]$	40-90	10-20	8-10	30-60	80-110
Coercive field [MV/cm]	0.05	0.035-0.055	0.6	0.8-2	2-5
k-value	1300	150-250	~ 16	~ 30	~ 25

Table 2.1 summarizes the main features belonging to the classes of ferroelectrics mentioned in this section. In the next sections, the properties of the different materials systems will be elucidated in detail. After that, ferroelectricity in hafnium oxide-based thin films will be addressed both for undoped and doped HfO_2, as well as for HfO_2-ZrO_2 solid solutions.

2.3.1 Perovskite-based ferroelectrics

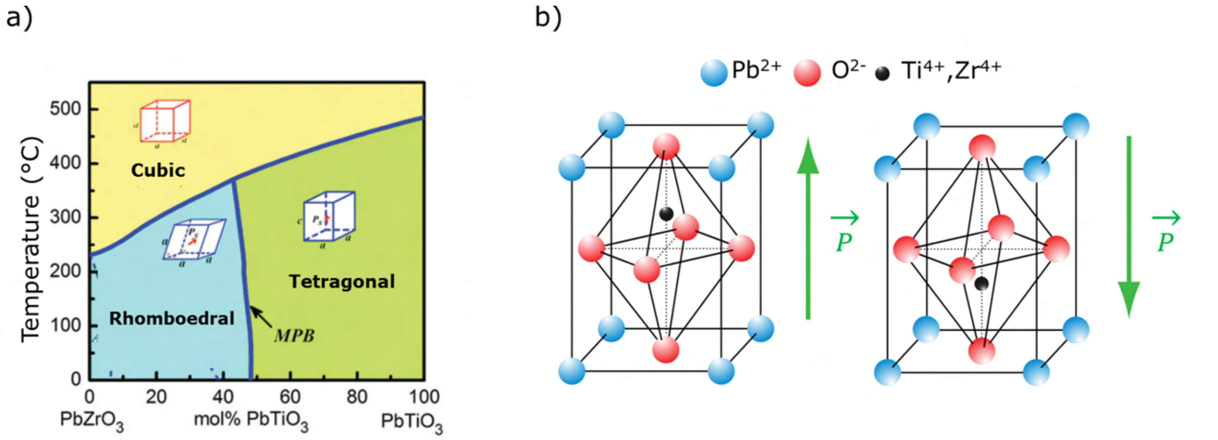

Figure 2.5: a) Phase diagram of $Pb(Zr_{1-x}Ti_x)O_3$ showing the three polymorphs stabilized as a function of temperature and material composition. The morphotropic phase boundary (MPB) between the rhomboedral and the tetragonal phase is indicated with an arrow; b) PZT unit cell in the tetragonal, ferroelectric phase in the two different polarization states depending on the position of the Ti, Zr ions. Adapted from [55] and https://en.m.wikipedia.org/wiki/File:Perovskite.svg

PZT is probably the most frequently found material system within the literature for perovskite ferroelectrics. $Pb(Zr_{1-x}Ti_x)O_3$ is a solid solution of $PbZrO_3$ and $PbTiO_3$. It presents two ferroelectric polymorphs, i.e. the rhombohedral (high Zr content) and the tetragonal phase (high Ti content), whereas a non-ferroelectric, cubic phase is stabilized for temperatures larger than the Curie temperature. Figure 2.5 a) shows the temperature-composition phase diagram of the PZT system [55]. For x values of about 0.47, a morphotropic phase boundary is encountered, where the maximum values of the dielectric permittivity and the piezoelectric coefficients were measured [55]–[57]. However, to induce ferroelectricity in FeRAM concepts, x values of 0.6 or 0.7 can be preferred [58]. Figure 2.5 b) reports as an example how the two polarization states can be stabilized in the tetragonal phase depending on the displacement of the Ti/Zr ions. Unfortunately, the high dielectric constant of this material, together with its low observed coercive field and the difficult integration within the CMOS process flow make the scaling of this material below a thickness of 90 nm rather problematic [59]–[61]. Ferroelectric memories were therefore put aside from that technology node onwards and research was re-oriented towards emerging concepts such as resistive switching, magnetoresistance and phase change memories until ferroelectricity was first discovered in hafnia-based materials [62].

2.3.2 Polymer-based ferroelectrics

To suppress fabrication costs, polymers including polar chains were suggested as candidates for deployment in FeRAM. Differently from the FeRAM as described above, polymeric ferroelectric RAM is fabricated in the form of a dense matrix of capacitors i.e. polymer sandwiched between two metal electrodes, which are addressed through word and bit lines. This means, no transistors are included in a memory cell and single capacitors can be stacked on top of each other in the form of a 3D memory. This makes polymer FeRAM interesting for the field of high-density data storage [63]. Furthermore, flexible structures overcoming temperature instabilities were also demonstrated [64]. Nonetheless, given the long access times, this concept is rather used to compete with NAND Flash memories than with perovskite and hafnia-based FeRAMs. Recent developments in NAND Flash eventually made the concept obsolete.

2.3.3 Aluminum scandium nitride

Only in 2019, ferroelectricity was reported in AlScN films [52]. AlN was already known to present piezoelectric and pyroelectric properties [65]. The addition of ScN to the well-known system not only increased the piezoelectric response [66] but also provided additional ferroelectric switching to the layer. This was pursued through stress effects which lowered the otherwise very high coercive fields for ferroelectric switching below the breakdown field of the material. Outstanding remanent polarization values were already reported in early works, setting hopes for a great optimization potential for this technology [67]. Given the mature deposition techniques already implemented for its deployment in modern actuators, integration of AlScN into the ferroelectric semiconductor industry is rather seamless, making this material exceptionally promising. The remaining challenges are strongly related to the further lowering of the high coercive fields.

2.4 Hafnium oxide thin films

Already for decades, HfO_2 is intensively studied in the semiconductor industry within different device concepts. This material possesses indeed outstanding properties in terms of temperature stability, reasonably high dielectric constant, relatively high bandgap and compatibility with Si [68], [69] which make it very attractive for numerous applications such as high-k gate stacks in CMOS [70] and active layer DRAM [71] or RRAM [72]. In 2011, Böschke et al. reported for the first time the observation of ferroelectricity in HfO_2 thin films doped with Si [9]. The interest in this material as an enabler of scaling down and power lowering of ferroelectric devices has not stopped growing ever since. In particular, being it already utilized in the CMOS process flow, its high scalability and integration possibilities make it a great replacement of traditional perovskites such as PZT, which conversely come with thickness constraints and processing-related difficulties.

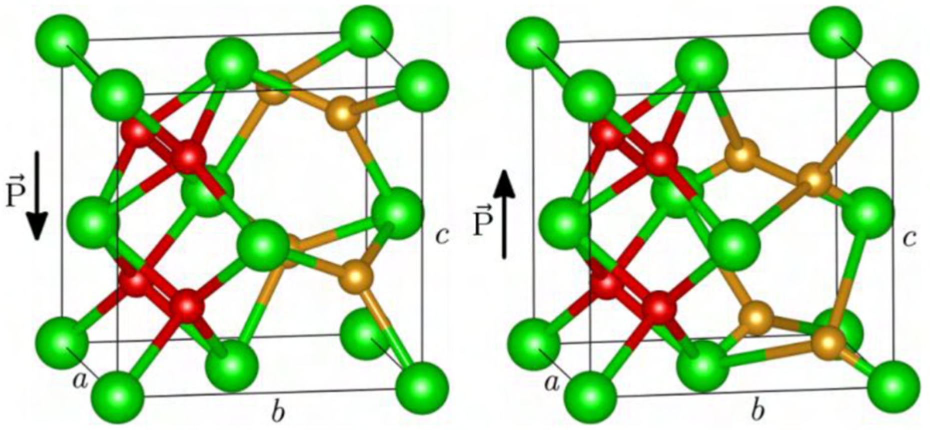

Figure 2.6: Schematics of the unit cell of the $Pca2_1$ group corresponding to the polar orthorhombic phase in the two opposite polarization directions. Hf atoms are represented in green, oxygen atoms in red and oxygen atoms whose position defines the polarization state in golden. Picture taken from [73].

In the past 10 years ferroelectricity has been reported in HfO_2 thin films doped with many different elements [74], but also in solid solutions of HfO_2 with its sister oxide ZrO_2 [75], [76] or even in undoped HfO_2 layers [77]. Furthermore, despite atomic layer deposition (ALD) being the most widely used technique, ferroelectricity has been demonstrated also in layers deposited with alternative techniques such as physical vapor deposition (PVD) [78], [79], pulsed layer deposition (PLD) [80], chemical vapor deposition (CVD) [81] and chemical solution deposition (CSD) [82]. What all these systems have in common is the appearance of the polar orthorhombic $Pca2_1$ phase group, which is otherwise absent in the classical phase diagram of HfO_2 [83]. In this particular lattice configuration, the oxygen atoms present two possible equilibrium positions, each corresponding to a polarization direction. The application of an external electric field can trigger the displacement of the oxygen atoms from one equilibrium position to the other, enabling polarization switching. The two oxygen positions in the lattice represent the two minima in the free energy landscape of HfO_2.

Among the factors considered as contributors to the stabilization of the otherwise metastable polar orthorhombic phase surface/volume effects [84], the inclusion of dopant atoms [74], the presence of oxygen vacancies [85], [86], rapid quenching [87] and mechanical stress [88]–[90] have been widely studied. Their effects are nevertheless still difficult to discriminate.

In the last years, different groups approached ferroelectricity in undoped HfO_2, trying to discern the effect of the oxygen-related defects from the one of dopant inclusion. A similar approach will be followed in this section, where a brief result collection will be displayed first for undoped HfO_2, then for doped HfO_2 and eventually for HfO_2-ZrO_2 mixed systems.

2.4.1 Undoped hafnium oxide

The phase diagram of bulk HfO_2 shows no stabilization regions for the orthorhombic phase at atmospheric pressure conditions. This material is normally found in the m-phase, whereas the tetragonal and the cubic phase are only stabilized for extremely high temperature or pressure values [73], [91]. Nevertheless, particular non-equilibrium conditions such as very low thickness or high oxygen-related defectivity seem to ease the stabilization of the polar phase [73].

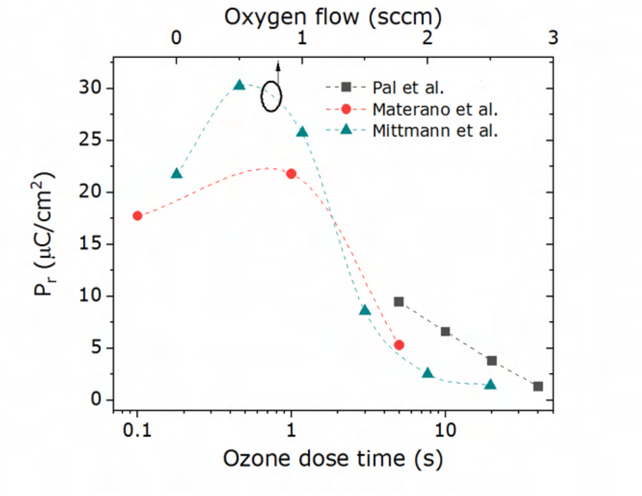

Figure 2.7: Remanent polarization of undoped HfO_2 layers as a function of oxygen supplied during deposition i.e. oxygen flow in sccm (upper x-axis) for PVD and ozone dose time (lower x-axis) for ALD. Picture adapted from [92].

In the last years, many groups engaged themselves in the achievement of ferroelectricity through tuning of the oxygen supply during deposition of undoped HfO_2 thin films to study the effect of oxygen vacancies. As shown in figure 2.7, non-zero remanent polarization values were measured in layers deposited both with sputtering [85] and ALD [77], [86]. In all three cases displayed in the figure, additional GIXRD measurements demonstrated the increase in oxygen content corresponded to a stabilization of the m-phase whereas high remanent polarization values could be correlated to the presence of the polar o-phase.

Results indicate that in sub-stoichiometric conditions, that is when little oxygen is supplied during deposition and likely oxygen vacancies are generated, the o-phase and ultimately the t-phase can be stabilized, as also suggested by ab initio calculations [86], [93].

Experimental data concerning undoped HfO_2 deposited both via sputtering and ALD will be displayed in the upcoming section 4.3 and 4.6. Concurrently, a model for phase stabilization from ab initio calculations will be suggested in chapter 7.

2.4.2 Doped hafnium oxide

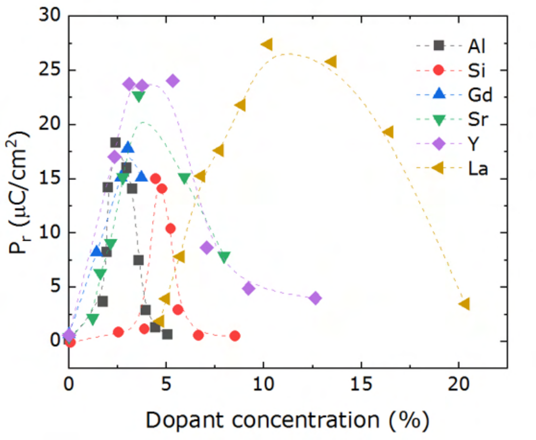

Figure 2.8: Remanent polarization of doped HfO_2 layers deposited via ALD as a function of dopant concentration (%). The dashed lines are meant as a guide for the reader. Data taken from [94].

Ferroelectricity was successfully demonstrated in HfO_2 thin films doped with various elements. Among those Si [62], [95], Al [96], La [97], [98], Gd [99], Sr [100], Y [80], Ge [101] and Sc [101] came with experimental evidences. Figure 2.8 summarizes some of the experimentally measured values for doped HfO_2 layers deposited via ALD as a function of dopant content. Nonetheless, simulation works included further elements such as Ce, Sn, Ti, etc [102]. Recently, a non-zero remanent polarization was shown even in bulk Y:HfO_2 with 50 mm size and 2 g mass crystallized via floating zone method [103].

In general, the gradual inclusion of atoms of the aforementioned dopant elements seems to first cause the disappearance of the monoclinic phase, followed by a stabilization of the o-phase and

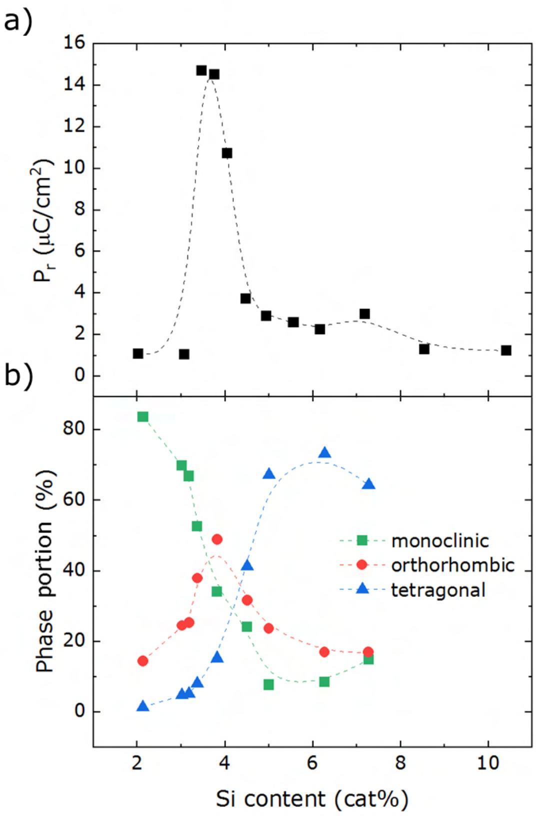

Figure 2.9: a) Remanent polarization and b) orthorhombic, monoclinic and tetragonal phase fractions as calculated from GIXRD measurements for Si-doped HfO_2 layers as a function of Si content. The highest remanent polarization values correspond to the highest detected polar orthorhombic phase. The dashed lines are meant as a guide for the reader. Data taken from [104].

later of the tetragonal or the cubic phase. As the dopant content increases, a decrease in the unit cell aspect ratio is encountered independently of the radius of the dopant atom. Conversely, the unit cell volume decreases when the t-phase is stabilized (see the case of Si), whereas it increases in the presence of the cubic phase (as seen for La) [104]–[106]. The phase evolution from the m- through the ferroelectric o-phase to the t- or c-phase is accompanied by a change in the measured polarization-voltage characteristic. Figure 2.9 shows the trend in remanent polarization and phase fractions of Si-doped HfO_2 as a function of Si content. At first, a paraelectric behavior with no ferroelectric switching is observed. For increasing dopant concentration i.e. as the o-phase is stabilized a ferroelectric hysteresis is measured. The maximum measured remanent polarization corresponds to the highest detected orthorhombic phase portion. The stabilization of the t-phase comes from an anti-ferroelectric-like pinching of the hysteresis until a paraelectric behavior is again detected. For the c-phase, the AFE-like stage is skipped and a direct transition to a paraelectric characteristic is observed [94].

Not all elements can grant ferroelectricity in the same content interval. The process window in terms of dopant concentration differs highly between the different employed species. In particular, a five-time larger window was demonstrated for La with respect to Si [104], [106]. The high capability of lanthanoids to stabilize ferroelectricity was also a result of simulation works [107] and was recently attributed to higher promoted texture in the films [88].

The introduction of a dopant species acts as impurity and therefore increases crystallization temperature. For this reason, high annealing temperatures are normally employed which can cause undesired oxidation of the interface to the electrodes. A parasitic titanium oxide layer was for example demonstrated through hard X-rays photoelectron spectroscopy (HAXPES) and time-of-flight secondary ions mass spectroscopy (ToF-SIMS) measurements in samples that had TiN as electrode material, which caused an internal bias field and therefore reliability issues such as additional hysteresis pinching and imprint [108]–[110]. This will be more extensively discussed in the following section 2.4.4 and chapter 5.

2.4.3 Hafnium-Zirconium mixed oxide

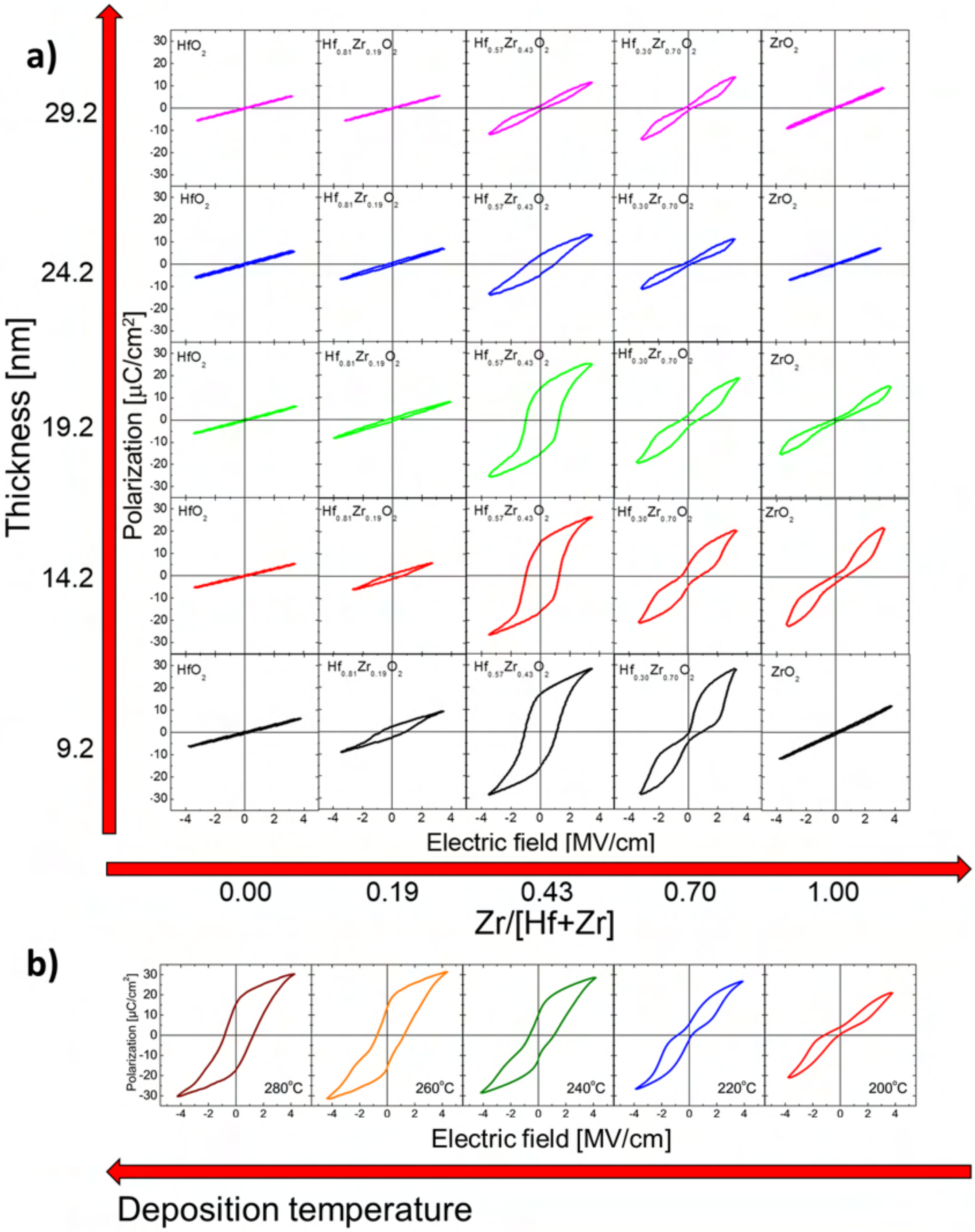

Figure 2.10: Polarization-field curves for a) $Hf_xZr_{1-x}O_2$ layers with different Hf:Zr ratios and different thicknesses; b) 10 nm thick $Hf_{0.5}Zr_{0.5}O_2$ layers deposited at different temperatures via ALD. Adapted from [111].

Differently from other dopant species, Zr replaces Hf atoms in a considerably larger amount. Therefore, in this case, speaking of a solid solution rather than doping is more adequate. Zr and Hf are in the literature often referred to as "sister materials", given they both being IV-valent elements and having an almost identical atomic radius. Nevertheless, the effect of gradual Zr addition in HfO_2 layers resembles the one obtained with the previously discussed dopant atoms: increasing Zr content seems to cause the layers to transition from the m-phase to the polar o-phase and later to the t-phase. Concurrently, a distribution of remanent polarization values is obtained as a function of Zr concentration which peaks at a Hf:Zr ratio of around 1:1, corresponding to the largest amount of detected orthorhombic phase. This result could be reproduced in various literature reports [76], [109], [111].

One of the main advantages of using ZrO_2-HfO_2 solid solutions consists in the extremely wide concentration window available for the achievement of ferroelectric properties, which makes processing very flexible [84]. Ferroelectric $Hf_xZr_{1-x}O_2$ layers were deposited with various thicknesses [84], at different deposition temperatures [112] and were exposed to different annealing treatments [113]. Figure 2.10 summarizes the works from Park et al. [84] (Fig 2.10 a)) and Lu et al. [114] (Fig. 2.10 b)) where $Hf_xZr_{1-x}O_2$ layers with thicknesses between 9.2 and 29.2 nm, Hf:Zr ratios from 1:0 to 0:1 and deposition temperatures from 200°C to 280°C were investigated. Ferroelectric switching is observable in most of the aforementioned conditions in the form of a more or less opened ferroelectric hysteresis. Different deposition techniques such as ALD [86], PVD [79], epitaxial growth via PLD [115] and even nanolaminates deposition [114], [116], [117] yielded films showing non-zero remanent polarization.

The great number of process possibilities [118], together with the mature CMOS integration knowledge resulting from the field of DRAM [119] and the lower required thermal budgets make HfO_2-ZrO_2 solid solutions of particular interest for the semiconductor industry. Therefore, $Hf_xZr_{1-x}O_2$ layers are nowadays extensively studied in the field of ferroelectric device applications.

This work focuses on the characterization of $Hf_xZr_{1-x}O_2$ layers films. The effect of zirconium and oxygen content will be analyzed in-depth in chapter 4, with the support of ab initio calculations and a comparison between ALD and PVD layers. The interaction of such films with different electrodes will be afterward exposed in chapter 5.

2.4.4 Reliability in hafnium oxide based thin films

In this section, reliability aspects connected to hafnium oxide-based devices will be addressed, with a particular focus on ferroelectric capacitors. First, factors related to the material stack itself will be exposed. Subsequently, unideal behaviors emerging from program/erase field cycling will be introduced. Later, retention and imprint will be explained, where the longevity of one polarization state is evaluated. Afterward, a brief overview of the reliability issues playing a role in other devices based on hafnium oxide will be presented. A review covering the mentioned topics for the main ferroelectric device concepts can be found elsewhere [120], [121].

Ferroelectric capacitors material stack

Oxygen-related defects are the most present kind of defects in HfO_2 thin films. Considerations based on Fermi level and charge neutrality have led to the result that neutral oxygen vacancies are the most likely to form, followed by oxygen interstitials and later by charged oxygen vacancies, hafnium vacancies and hafnium interstitials. [122]. The energy for defect formation has been shown to be strongly dependent on the crystalline phase of the material [123]–[126]. For example, oxygen vacancies have been calculated to more likely be present in the t- and in the po-phase as compared to the m-phase [127]. In thin films and at the interface with the electrodes, charge neutrality conditions can be violated, leading to a stronger presence of charged oxygen vacancies [124].

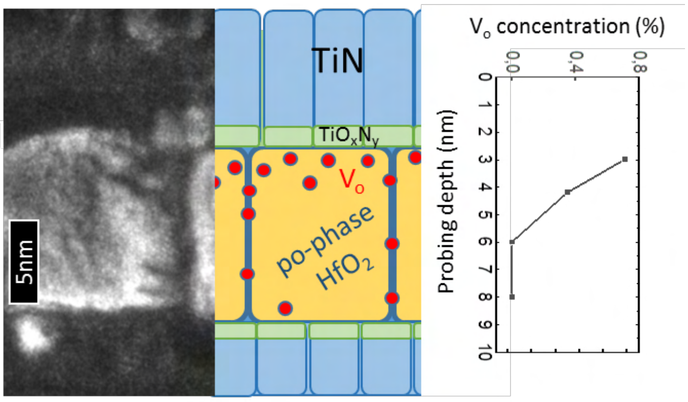

Figure 2.11: Schematic of an HfO_2 layer sandwiched between two TiN electrodes with corresponding transmission electrode microscopy (TEM) picture. A parasitic TiO_xN_y interface is visible at the interface with the top electrode, where the most oxygen vacancies are formed. An oxygen vacancy concentration profile is shown, with data taken from ref. [110].

Oxygen vacancies and in general oxygen-related defects can affect and are concurrently be affected by the electrode material and the eventual interface between hafnium oxide and electrode. Different electrodes such as oxide-based materials (e.g. RuO_2, IrO_2) [128], elemental electrodes (like W and Pt) [129] and nitrogen-based compounds (very commonly TiN and TaN) [99] have been used within FeCap stacks and their chemistry has been shown to have an effect on device performance. For example, Hoffmann et al. [99] reported that the stronger oxidation of the TaN electrode caused by the HfO_2 ALD deposition and later by oxygen scavenging during the annealing treatment caused a higher amount of oxygen vacancies in HfO_2 thin films deposited on TaN as compared to TiN. Electrode oxidation was detected also through HAXPES measurements. In particular, a different oxidation state was reported for the bottom and the top electrodes, which also caused an oxygen vacancy concentration profile within the HfO_2 films [110], [130], [131]. Figure 2.11 shows a transmission electron microscopy picture of an HfO_2 thin film sandwiched between two TiN electrodes, where single ferroelectric grains are visible. A schematic is used to represent the growth of the parasitic TiO_xN_y interface, which is different between the top and the bottom electrodes. This difference results in an inhomogeneous distribution of the oxygen vacancies within the oxide layer, as measured via HAXPES.

As previously explained, the presence of an oxidized parasitic interface between the electrode and ferroelectric oxide is considered responsible for provoking a depolarization field [21] which can cause an undesired pinching in the ferroelectric hysteresis. Furthermore, a large voltage drop in the film region close to the interface could cause an increase in charge injection and leakage current, also affecting device reliability.

Field cycling behavior

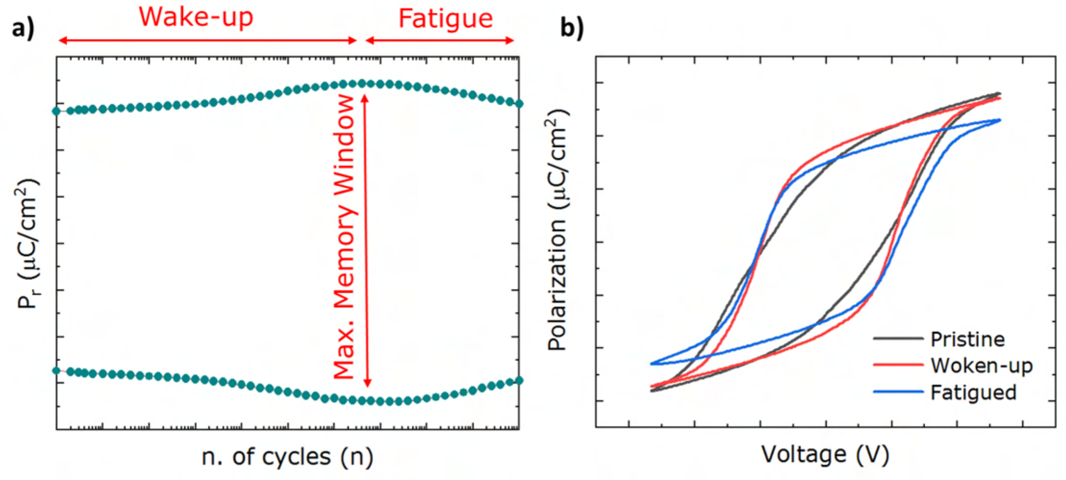

Figure 2.12: a) Example of positive and negative remanent polarization as a function of applied field cycles. The stages preceding and following the maximum memory window opening are defined as wake-up and fatigue phase, respectively. b) Example of P-V curves for a capacitor in the pristine, the woken-up and the fatigued state.

During its lifetime, each memory device undergoes a series of write and re-write cycles, aimed to set a certain memory state i.e. a bit. In the case of ferroelectric capacitors, a "1" or a "0" bit is stored depending on the polarization state of the ferroelectric layer. To set the capacitor in a certain polarization state (e.g. write "0"), an electric field that is higher than the coercive field has to be applied. Polarization reversal is subsequently performed by applying a field in the opposite direction which is in absolute value larger than the opposite coercive field (e.g. write "1"). This double process is simulated through a sequence of positive/negative square pulses, as described in section 3.3.1. Stability with respect to field cycling represents one of the most crucial requirements and yet challenges for ferroelectric random access memory devices.

Hafnium oxide-based ferroelectric capacitors present a non-ideal behavior with respect to field cycling. During the lifetime of the device, different stages are observed depending on the number of applied program/erase cycles. The memory window, defined as the difference between the positive and the negative remanent polarization, first increases due to an opening of the ferroelectric hysteresis and later decreases in the last cycles of the lifetime of the device. Both the increase and the decrease of the memory window are undesired, as they make the response to external field inconsistent during device lifetime and represent therefore a challenge for device reliability. Figure 2.12 shows the trend of the memory window with respect to the number of applied writing cycles.

The different phases which are observed as a function of the number of applied writing cycles can be summarized as follows:

- **Pristine state:** When the capacitor is in its initial configuration, the ferroelectric hysteresis often presents some irregularities such as pinching, a shift in one voltage direction or lower remanent polarization. The transient current can present two or more switching peaks which afterward merge during wake-up cycling (see below) [132]. This can be related to internal bias fields, also called depolarization fields. The origin of such parasitic contributions is widely discussed in the literature, both for traditional perovskite and hafnia-based ferroelectrics [19], [21]. An unequal charge distribution within the layer or at the two electrodes, the presence of a dead interfacial layer originating from the oxidation of the electrode materials, non-polar layer portions can all be responsible for the observed constricted pristine hysteresis. Furthermore, charges in the layer could pin some of the domains and inhibit their switching, therefore reducing the switchable polarization [24].

- **Wake-up:** During the wake-up phase, the memory window opens up to its maximum value. The increase in P_r accounts for a higher number of domains participating in the switching process. The continuous application of a bipolar external electric field actuates the suppression of internal bias fields through charge redistribution or field-induced crystalline phase transition, most likely from the t-phase to the polar o-phase [21], [129], [133], [134]. Furthermore, a short can be created within the parasitic oxidized interface to the electrode, which cancels out the voltage drop observed in the first cycles [135], [136]. Additionally, external fields could cause ferroelastic switching and thus 90° domain reorientation from an in-plane axis to the out-of-plane polar axis of the polar o-phase, as recently reported, causing more domains to participate in the switching [137], [138]. Oxygen vacancies redistribution favored by field cycling could play a major role in all the aforementioned processes, as demonstrated by calculated activation energies for the wake-up process, which in some cases match those measured for V_o migration within HfO_2 [92].

- **Woken-up state:** The ferroelectric hysteresis opens up and the maximum remanent polarization values are achieved. The measured I-V curves present normally one single switching peak for each voltage polarity.

- **Fatigue (or aging) phase:** A drop in remanent polarization is observed with further field cycling. The fatigue phase is often associated with the creation of new charged defects which pin the switching domains reducing once again the observed polarization. Pesic et al. measured an increase in leakage current which was attributed to the creation of new defects during the aging stage of the device [139]. Similar reports showed up to a 10-fold increase in trap density during the fatigue stage, which leads to a decrease in the trap distance and subsequently to a hard breakdown of the device (see below) [126], [140]. The creation of charged defects could also trigger charge trapping and field inhomogeneities, resulting in a lower effective field perceived from the ferroelectric materials. Some domains could therefore not be switched by their effective field, causing a reduction in P_r [24].

- **Hard breakdown:** A short between the top and the bottom electrodes is created as a consequence of layer degradation, often because of charge accumulation and the creation of leakage paths.

The topic of field cycling behavior was already deeply addressed in the field of traditional perovskite ferroelectrics [141], [142]. A combination of domain pinning and depinning [143], seed inhibition [144] and formation/disappearance of a dead parasitic layer [145] were all suggested as causes for the observation of wake-up and fatigue. Improvements were induced through different electrode materials. Both metal and oxide electrodes were deployed and endurance values larger than 10^{12} cycles were measured [49], [146]. Performance was considerably enhanced also by tuning the material composition of the ferroelectric layer itself [147], [148].

Similar studies have been conducted for hafnia based ferroelectrics, addressing the understanding [132], [149] and the improvement [86], [150] of the memory window evolution with respect to field cycling. Similar strategies focused on ferroelectric film composition [98] and electrode material choice [151] were employed for this class of material as well, allowing the achievement of high number of cycles before device hard breakdown [98], [152] and of wake-up free FeCaps [86]. Both the effect of film chemistry and structure of the electrode material will be extensively discussed in chapter 4 and 5, respectively.

Data retention and imprint

The remanent polarization stored in a ferroelectric capacitor can also degrade under the effect of time and temperature. The loss of the programmed polarization state can normally be distinguished in imprint i.e. a rigid shift of the ferroelectric hysteresis in one voltage direction and polarization reversal because of depolarization fields, which act similarly to what was described in the previous paragraphs [153].

The deployment of ferroelectric devices in commercial applications requires data storage performances i.e. data retention for over 10 years. To simulate such conditions, conditioning at higher temperatures of 85 °C or 125 °C is normally applied during device testing. A standard retention measurement was first proposed in [154] and will be explained in section 3.3.1.

Imprint manifests itself as a change in the coercive field, that is in a shift of the P-V hysteresis in one voltage direction. Due to this phenomenon, some domains acquire a coercive field that is higher than the readout voltage. As a consequence, as the read-out takes place fewer domains are successfully switched with the imposed signal, causing a reduced switched charge and eventually a readout failure.

Imprint is caused by the appearance of internal bias fields within the stack. These are likely originated by defects in the bulk which pin the ferroelectric domains [155], by the presence of a dead, non-polar layer [8] or of charged defects at the interface between the ferroelectric and the electrode [126], [139] which can screen or enhance the internal remanent polarization [156]. As a result, the written state is strengthened whereas switching to the opposite state requires higher fields [157].

Table 2.2: Calculated or simulated activation energy values for oxygen vacancies movement or reliability-related phenomena in ferroelectric hafnia-based layers. Reproduced from [92].

Ref.	Phenomenon	Activation energy (eV)
[140]	Wake-up	0.54
[140]	Imprint	1.01/1.03
[153]	Imprint	0.54
[158]	Singly charged V_O migration	1.2
[158]	Doubly charged V_O migration	0.7
[159]	V_O migration	1.2
[139]	V_O migration	1.1
[160]	V_O migration	1.5

The phenomena of retention loss and imprint were already broadly studied for pervoskite ferroelectrics. In most reports, this reliability issue was described as capacitor "aging" [145]. Many phenomena were considered as possible cause for device aging, among which dipole alignment [161], charged defects [143], [162] and charge injection at the interface with the electrodes [163]–[165]. Accordingly, improvements were tackled through film stoichiometry tuning [143], interface improvement through the use of different electrode materials [164] or annealing atmospheres [166].

Similar to traditional perovskite ferroelectrics, charge (de-)trapping, built-in bias fields and subsequent defect migration seem to play a strong role in the reliability performance of HfO_2-containing devices in terms of polarization retention [167].

Table 2.2 summarizes the calculated values for wake-up, imprint and oxygen vacancies related phenomena taking place within hafnia-based ferroelectric stacks. As previously discussed in sections 2.4.4, internal bias fields observed in HfO_2 films are often related to the presence of oxygen vacancies [139]. In fact, the oxygen content in the layer can influence the defectivity of the stack either through the creation of charged defects in the bulk or at the interface with the electrodes or through the formation of a more or less thick dead layer in the form of a parasitic oxidized interface or non-switching phase portions. Activation energy values were calculated for the motion of oxygen vacancies within ferroelectric HfO_2-based films. Such values oscillate between 0.7 and 1.2 eV and can therefore be associated with the activation energies calculated for the above-discussed reliability issues i.e. wake-up and imprint phenomena.

Different methods were used for the evaluation of data retention and imprint phenomena. In particular, Fengler et al. [140] used thermally stimulated depolarization current to extract the activation energy for the imprint. The calculated energies resulted similar to the ones which can be found in literature for to the movement of charged oxygen vacancies 2.2. Chouprik et al. [153] carefully studied the phenomena with the help of piezo-force microscopy (PFM) and transient capacitance measurements and showed that imprint can be associated with the diffusion of the oxygen vacancies due to a polarization gradient within the ferroelectric layer. Mittmann et al. [85] measured the rigid shift of the ferroelectric hysteresis after sequentially longer baking steps at temperatures of 85 and 125 °C. In both cases, it looked like samples with an optimized oxygen content and the highest polar phase portions behaved the most reliable by showing a lower shift of the P-V curve on the voltage axis. Similar results were shown by Bouaziz et al. [168], who used positive-up-negative down (PUND) and alternating positive-up-negative-down and negative-down-positive-up (PUND-NDPU) measurements to study the retention performance of hafnia-based FeRAM. By comparing a set of samples, they reported the best retention properties for the film which showed the least wake-up. Mohan et al. [169] studied polarization retention in $Hf_{0.5}Zr_{0.5}O_2$ metal-ferroelectric-insulator-semiconductor structures with various thicknesses of the ferroelectric layer. Polarization loss was considerably stronger when thinner films were employed (90 % vs. 5 % for 5 and 20 nm thick layers, respectively), demonstrating the increasing importance of the depolarization fields when the ratio in thickness between the ferroelectric and the insulator decreases.

In the work of Bouaziz et al. [168] two models were proposed to fit the data and study the imprint phenomenon with respect to time and temperature which had already been used to treat perovskite-based devices. A stretched exponential [170]–[172] and a simple power law model [164], [173], [174]. They could observe two different trends in the decrease of switching polarization with time. From this, they concluded that retention loss is dominated by imprint at short times and later by depolarization phenomena.

Similar observations can be found in the work from Mart et al. [175], who recognized a logarithmic trend in their polarization degradation with time. Namely, two regimes were detected for short and long poling times, that is for times below and above 100 s, respectively. This finding was explained by attributing the short-time degradation to electrons being de-trapped from oxygen vacancies leaving charged defects behind, which afterward diffuse within the layer because of depolarization fields with different behavior with respect to time.

Nonetheless, electron trapping was found to be independent of oxygen defectivity in HfO_2 in a recent publication from Izmailov et al. [176]. By combining experimental measurements and simulation work, the group showed that electron trapping was not different in Si- and Al-HfO_2 thin films, and rather associated with the presence of electron traps to the boundaries between crystalline and amorphous regions in the layer.

In this study, imprint and retention measurements were performed and related to layer stoichiometry (see chapter 4) and used electrodes (see chapter 5). The results are accordingly presented and discussed in the related chapters.

2.4.5 Theory of polarization switching

Polarization switching can be described as the formation and the subsequent growth of a domain in one polarity starting from a domain in a different (often opposite) polarization state. This process can be triggered by the application of an external voltage for a certain time. The applied voltage and the switching time are correlated to each other. This relation is normally expressed through the well know Merz's law [177]:

$$\tau = \tau_0 \cdot exp\left(\frac{E_a}{E}\right) \tag{2.12}$$

where τ_0 is an intrinsic switching time and E_a is the temperature-dependent activation field for the polarization reversal. This law indicates a correlation between switching time and activation field. Films with a higher E_a will need a longer time to switch their polarization state for a certain applied field E.

The limitation of Merz's law consists in the fact that no description of the mechanism is provided. Therefore, different models have been formulated first for traditional ferroelectrics and later for HfO_2-based materials which will be hereby discussed.

For single-crystal perovskite ferroelectrics such as PZT, the Kolmogorov-Avrami-Ishibashi (KAI) is the most used model. According to the KAI model, domain nucleation happens instantaneously. After nucleation, domain walls start moving in the horizontal direction triggering domain expansion, until another domain wall is encountered [178]–[180]. Therefore, domain expansion is the most time-consuming process within polarization switching. The amount of switched polarization ΔP within a certain time interval t is expressed through the following equation:

$$\Delta P(t) = 2P_s[1 - exp-(t/\tau)^n] \tag{2.13}$$

where P_s is the spontaneous polarization and n a dimensionality factor taking into account in which dimensions nuclei expansion takes place (1, 2 or 3 D).

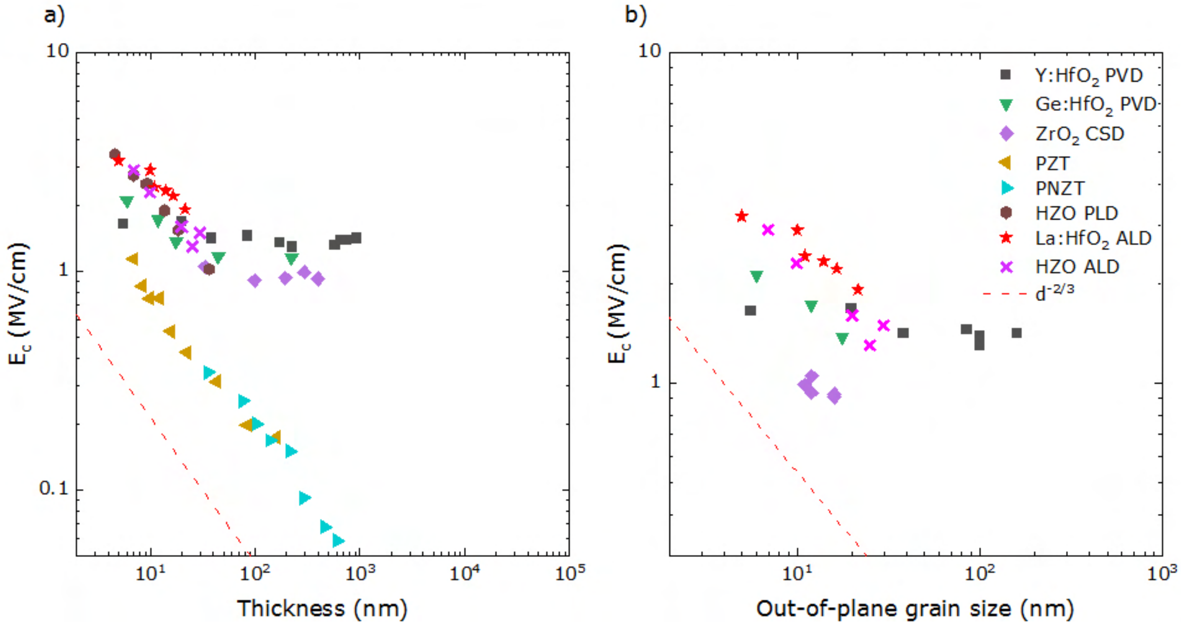

Figure 2.13: Coercive fields E_C vs. a) layer thickness and b) grain size in the field (out-of-plane) direction for different ferroelectric layers (perovskite and HfO_2 based ferroelectrics fabricated with various deposition methods). Taken from [181].

In the absence of defects, a single nucleus and its subsequent expansion could be responsible for the switching of the whole film. Hafnia-based ferroelectric films with a thickness of around 10 nm are unlikely to present a single crystal structure. More grains are found with an out-of-plane size which often coincides with layer thickness and an in-plane size of few tens of nm. In some cases, one grain can even host more than one ferroelectric domain. Due to the polycrystalline nature of the layers, domain propagation is rather limited and instead of one switching event with subsequent domain propagation, more nucleation events are observed with rather small nuclei sizes [182]. In fact, grain boundaries, interfaces with electrodes as well as impurities could serve as nucleation sites [183], [184]. Additionally, an almost zero or negative 180° domain wall energy was recently demonstrated in HfO_2-based thin films [185], [186]. To account for these observations, new models have been formulated. Among those, the nucleation limited switching (NLS) model is widely utilized in the literature to describe polarization reversal both in traditional perovskites and in thin HfO_2-based films [37], [183], [187]–[189]. According to this theory, many nucleation events are initiated at different sites i.e. at discontinuities in the film. The nuclei growth rate will depend on volume and surface energetic contributions. That is, once a certain critical nucleus radius is reached, the free energy for nuclei expansion becomes negative and growth is favored [37]. This implies a size dependency of the field necessary for polarization reversal. By assuming the switching field being positively proportional to the coercive field E_C, an empirical relation is found between the ferroelectric layer thickness d_{FE} and E_C in the form $E_C \sim d_{FE}^{-2/3}$ [190]. This relation was experimentally confirmed for perovskite-type ferroelectrics for a wide range of order of magnitudes of layer thickness. Contrarily, HfO_2 thin films seem to follow the trend at low thicknesses until a saturation plateau is reached, after which E_C stays constant and independent from layer thickness. By deepening this analysis and treating the coercive field not as a function of thickness but of grain size, it can be seen that the data points belonging to the plateau collapse in a cluster corresponding to the maximum observed grain size. This points out the fact that the critical size parameter is grain size rather than the film thickness. Given the greater amount of nuclei that are concurrently formed, domain wall displacement for nuclei expansion only lasts very shortly until a new domain is encountered. Therefore, the nucleation events dominate the polarization switching kinetics. Starting from the Du-Chen model for NLS [187], the following equation correlating the time τ and the voltage V necessary for polarization switching to occur was proposed in [37]:

$$\tau = \tau_0 \cdot exp\left(\frac{\delta}{k_b T} \cdot \frac{1}{(V - V_0)^2}\right) \tag{2.14}$$

where τ_0 represents the shortest time necessary for nucleation to take place, δ a fitting parameter including a thermodynamic contribution of domain wall energy and thickness effects, k_b the Boltzmann constant, T the temperature and V_0 a possible voltage offset [191].

The NLS model provides an insight into the microscopic mechanisms related to polarization switching kinetics, which is a description of the evolution of a single nucleus. On the contrary, a macroscopic perspective is gained when studying the phenomenon starting from the thermodynamics described by the Landau-Devonshire theory of ferroelectricity [192]. In this framework, considerations on the free energy of single crystal-like domains are utilized to explain polarization reversal and switching is defined as intrinsic and independent from the domain's surrounding [193], [194]. Namely, two energy minima occur in the free energy landscape of a ferroelectric switching unit, corresponding to the two opposite polarization states. An energy barrier is present between the two and the activation energy for the polarization reversal is associated with the field which has to be externally supplied to overcome this barrier. The duration of the applied field pulse, that is the frequency of the signal does not affect the coercive field of the material, which is therefore considered intrinsic. This contradicts experimental observations, which report a correlation between time and voltage needed for switching. With this knowledge, the multi-grain Landau-Khalatnikov approach was suggested for HfO_2-based ferroelectrics [15]. A time-dependence is therefore included taken into account a macroscopic distribution of fields averaged over several regions composing the ferroelectric films.

An alternative approach was proposed in 2010 by Zhukov et al. [195], called inhomogeneous field mechanism (IFM). In the IFM each domain is considered to switch at its own effective electric field dictated from the position of the domain within the film. Factors such as domain orientation, proximity to the electrode, dielectric constant, crystalline phase in the neighboring grains are all factors that can influence the unique local field experienced by each domain. The distribution of these fields is then calculated, whose standard deviations can be correlated to the homogeneity of polarization reversal in the considered layer [189], [195], [196].

Chapter 6 of this work focuses on the polarization reversal mechanisms in $Hf_{0.5}Zr_{0.5}O_2$ capacitors, trying to match the described switching mechanisms with experimental observations. A dedicated measurement sequence for polarization switching was elaborated, which will be exposed in detail in chapter 3.

3 Fabrication and characterization methods

In this chapter, the experimental methods used within this Ph.D. work are presented both in terms of fabrication processes and characterization techniques. The steps composing the capacitor process flow are illustrated, with a particular focus on atomic layer deposition (ALD). Subsequently, the structural characterization techniques are introduced and last but not least the different routines for electrical characterization of the samples are described, spanning from standard ferroelectric material characterization to more device-oriented measurements such as reliability assessment through retention and switching kinetics.

3.1 Capacitor process flow

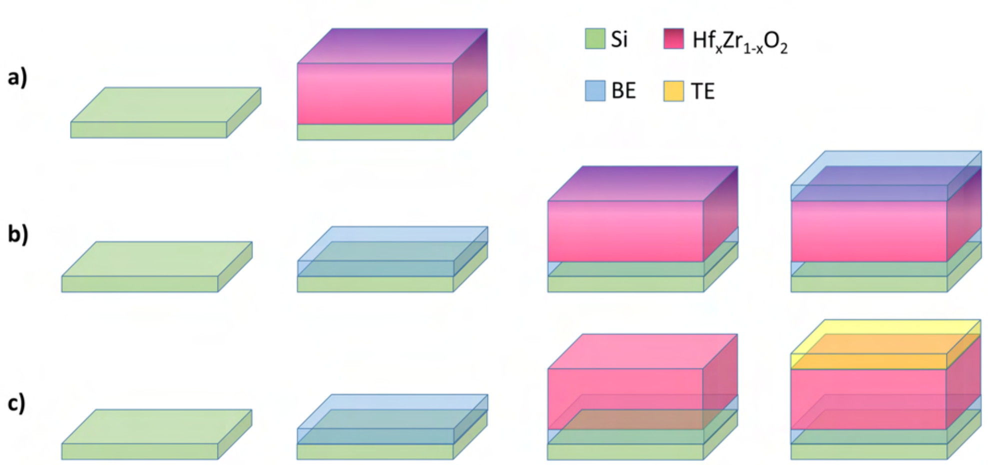

Figure 3.1: Schematics of sample fabrication depending on the different characterization purposes. a) $Hf_xZr_{1-x}O_2$ films deposited directly on Si for growth behavior analysis, b) Standard TiN/$Hf_xZr_{1-x}O_2$/TiN stack FeCap fabrication for structural and electrical characterization of different $Hf_xZr_{1-x}O_2$ layers, c) $Hf_{0.5}Zr_{0.5}O_2$-based FeCap with different TE and BE for structural and electrical characterization and assessment of the influence of the electrode material on capacitor performance.

In this section, the basic process flow used to fabricate the ferroelectric capacitor structures will be exposed. Medium or highly doped Si wafers (10^{16}-10^{18} cm^{-3} dopant concentration) were used as substrate. The first deposition step consisted in the sputtering (physical vapor deposition, PVD) of the bottom electrode (BE). This was followed by the deposition of the ferroelectric oxide via atomic layer deposition (ALD). Afterward, the top electrode (TE) was sputtered either through a shadow mask or as a full coverage blanket. The capacitor subsequently underwent a rapid thermal anneal (RTA) treatment to achieve crystallization in the ferroelectric phase. In the case of TE sputtered in the form of a complete capping blanket, capacitor size was then defined by e-beam evaporation of Ti and Pt contacts through a shadow mask. Finally, a wet etching step was performed to remove the exposed TiN. For the purposes of this work, mainly three kinds of structures were fabricated, depending on the targeted characterization, as schematized in figure 3.1:

a) $Hf_xZr_{1-x}O_2$ films directly deposited on Si: these structures were used to characterize the growth behavior depending on the different ALD parameters (precursor molecule, deposition temperature, oxygen dose time, etc.) which were tuned to optimize the ferroelectric properties of the studied FeCaps;

b) Standard TiN - $Hf_xZr_{1-x}O_2$ - TiN stacks: used for structural and electrical characterization, with the aim of comparing different $Hf_xZr_{1-x}O_2$ films;

c) $Hf_{0.5}Zr_{0.5}O_2$ layers sandwiched between different TE and BE: while the ferroelectric oxide was kept the same, the effect of the use of different materials as TE and BE was addressed through both structural and electrical analysis.

In this section, the main deposition techniques (ALD, PVD) used in this work will be shortly described, followed by a summary of the last fabrication steps for capacitor structuring (RTA, e-beam evaporation, wet etching).

3.1.1 Atomic layer deposition

As of today, ALD is the most used technique for the deposition of thin HfO_2-based ferroelectric layers. Being in general widely used in the semiconductor industry, this 4-step deposition method presents as the main advantage the possibility of controlling film growth on an atomic level, allowing precise thickness targeting and integration in complex 3D structures [197].

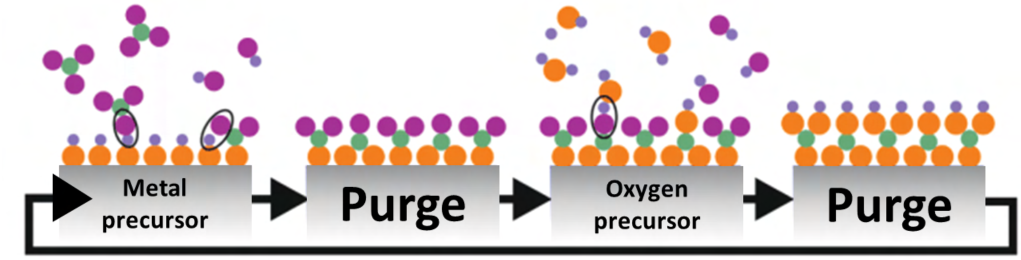

Figure 3.2: Schematics of an ALD cycle. First, the metal precursor is introduced into the reaction chamber and sticks to the substrate. A purging step is then applied to remove the precursor molecules which did not absorb. Afterward, the oxygen source is pulsed. The metal precursor is oxidized. A new purging step is applied in order to remove unreacted molecules and reaction by-products from the chamber.

An ALD cycle consists of two self-limiting processes: first, the metal precursor is pulsed into the reaction chamber where it absorbs on the available sites on the substrate until a monolayer is formed. Afterward, the oxidant is also released into the chamber and it reacts with the absorbed metal precursor molecules to form a (sub-)monolayer of metal oxide. Between the two pulsing steps, a purge is performed to remove the exceeding un-reacted molecules and the reaction by-products from the chamber. If the precursor reaction and/or the purging step are not performed correctly, residual reactants can impact layer quality and homogeneity, in terms of thickness, density and defectivity. If the two self-limiting sub-processes proceed sequentially, an accurate thickness control can be achieved. The thickness of one monolayer deposited through one ALD cycle is normally referred to as growth per cycle (GPC). Common GPC values for a well-performed ALD cycle are in the order of 1 Å.

Within this work, HfO_2, ZrO_2 and intermixed $Hf_xZr_{1-x}O_2$ layers were deposited in an OpAL Oxford ALD tool and a Roth and Rau ALD tool. In the case of $Hf_{0.5}Zr_{0.5}O_2$ mixed structures, the metal-precursor cycle ratio between Hf and Zr was adjusted to obtain the different compositions. A maximum number of three cycles of the same kind were performed after another to avoid the deposition of nanolaminates. The used hafnium precursors were TEMA-Hf ($Hf[N(CH_3)(C_2H_5)]_4$) and HyALD (Cp-$Hf[N(CH_3)_2]_3$). Analogously, TEMAZr ($Zr[N(CH_3)(C_2H_5)]_4$) and ZyALD (Cp-$Zr[N(CH_3)_2]_3$) were used as Zr sources. Deposition temperatures ranging from 250 to 300 °C were used. Water (H_2O), oxygen plasma or ozone (O_3) were employed as oxidants. Details on ALD process optimization will follow in the next chapter.

3.1.2 Physical vapour deposition

Physical vapor deposition (PVD) or sputtering was used to deposit electrodes of different materials. In a sputtering chamber, the target is hit by gas ions (typically Ar+) which are accelerated by an electric field. A plasma of the target material is formed which then reaches and deposits onto the substrate sample. Target and substrate are facing each other or confocally arranged in the chamber. Reactive sputtering is deployed to deposit compound materials. In this case, a second reactant will be introduced in the form of a gaseous atmosphere (e.g. nitrogen, oxygen,...) which will react with the target material. The final stoichiometry of the compound largely depends on the partial pressure of the atmosphere gas. The sputtering process is schematized in Figure 3.3.

For this study, either an Alliance Concept CT200 sputtering tool or a Bestec ultrahigh vacuum sputter cluster were used for the deposition of the electrodes. The used materials were TiN, Ti, W, Nb, NbN, MoOx, TiAlN and RuOx. All depositions were performed at room temperature. Details on the influence of the electrode material on the performance of ferroelectric capacitors will be exposed in detail in Chapter 5.

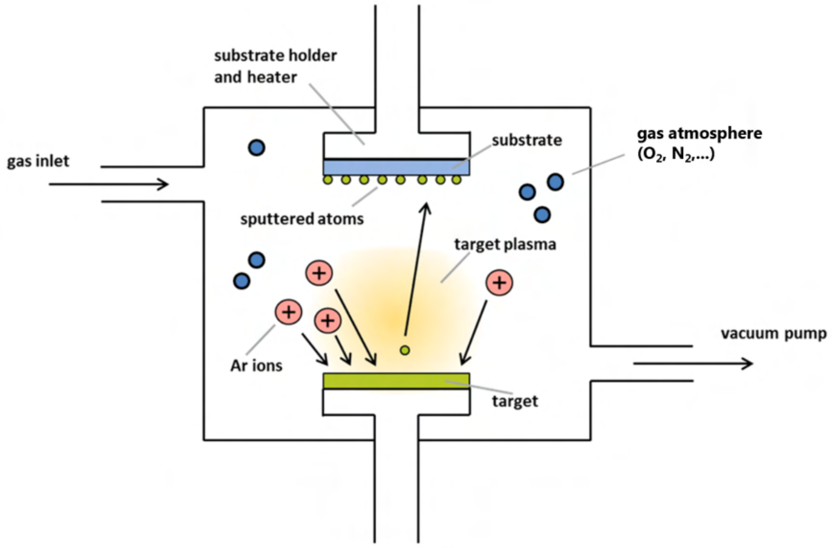

Figure 3.3: Schematics of a sputtering chamber. Target and substrate are facing each other and a plasma of the target material is generated when the latter is hit by ionized gas atoms. The material composing the plasma deposits onto the substrate in its pure form or within a compound, if an additional gas is supplied in the chamber atmosphere (reactive sputtering).

3.1.3 Capacitor finishing and structuring

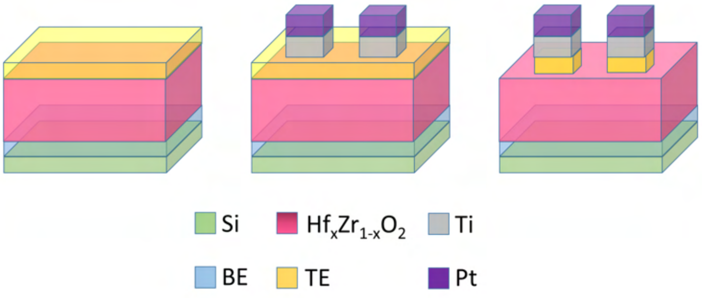

Figure 3.4: Schematics of capacitor patterning through e-beam evaporation of Ti/Pt dots through a shadow mask and subsequent etching of the exposed top electrode portions.

The process route after TE deposition follows afterward some standards steps which are intended to crystallize and pattern the capacitor structure (Figure 3.4).

Rapid thermal anneal

An annealing treatment is applied to trigger the crystallization of the $Hf_xZr_{1-x}O_2$ films, which are otherwise amorphous in the as-deposited state. In order to achieve good ferroelectric properties, crystallization in the polar orthorhombic phase of group $Pca2_1$ is targeted [83], [86]. The standard thermal treatment was performed in a N_2 atmosphere at 600 °C for 20 s. Layers annealed at lower temperatures showed either incomplete crystallization or high tetragonal phase portions. Layers annealed at higher temperatures or for longer times often transitioned to the monoclinic phase.

E-beam evaporation

To define the final capacitor structures, Ti/ Pt dots with a diameter ranging from 110 to 450 µm and a thickness of 10 and 25 nm for Ti and Pt, respectively, were deposited via e-beam evaporation through a shadow mask.

Wet etching

The exceeding top electrode surface was removed using a standard cleaning 1 (SC1) procedure. Water (H_2O), hydrogen peroxide (H_2O_2) and ammonia (NH_3) were mixed in a 50:2:1 solution. Samples were then etched for 5 min at 50 °C in the aforementioned solution.

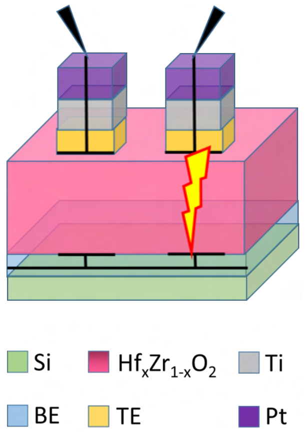

Figure 3.5: Schematics of contact to bottom electrode formation through the application of a high voltage and creation of a short.

Formation of electrical contact to the bottom electrode

In figure 3.5 the formation of the electrical contact to the BE is shown. Two capacitors are contacted and a high voltage is applied to achieve a breakdown event and create a short circuit between the two. For electrical characterization, one of the capacitors will then serve as a contact to the bottom electrode whereas a new structure will be measured.

3.2 Structural and chemical analysis

In this section, the characterization methods used for structural and chemical analysis will be briefly introduced, with a focus on grazing incidence angle x-ray diffraction (GIXRD), used for crystalline phase determination. Additionally, some of the measurements that will be shown in the next chapters (4, 5 and 7) were performed within project collaborations at the following institutions:

- Time-of-Flight Secondary Ion Mass Spectrometry (ToF-SIMS) [198]: Department of Material Science of North Carolina State University, USA, by Chuanzhen Zhou;

- Transmission Electron Microscopy (TEM) [199]: National Institute of Material Physics, Bucharest Magurele, Romania, by Lucian Pintilie;
- X-Ray Photoelectron Spectroscopy (XPS) [200]: CEA, Institut rayonnement matière de Saclay, Paris, France, by Wassim Hamouda;
- Raman Spectroscopy [201]: Fraunhofer Institute for Photonic Microsystems, Dresden, Germany, by Peter Reinig.

3.2.1 X-Ray Reflectivity

X-Ray Reflectivity (XRR) is used to collect information on thickness, roughness and density of thin films [202]. X-Rays with a fixed wavelength are sent to the sample while the incidence angle 2θ is varied. The signal is then reflected by the sample and finally reaches a detector. The response pattern is a modulated signal, whose intensity depends on constructive/destructive interference conditions given by the beams reflected at the top and the bottom of the measured layers. Therefore, information on sample thickness can be extracted.

In this work, to facilitate signal de-convolution, single layer films directly deposited on Si were analyzed (see Fig. 3.1 a).) A Bruker D8 Discover tool with Cu-K_α (λ= 0.154 nm) radiation was used to carry out the experiments.

3.2.2 Grazing incidence X-ray diffraction

Grazing incidence X-Ray Diffraction (GIXRD) is a powerful method used for the crystalline phase identification of thin layers [203]. Very low incidence angles are used (in this work 0.45 °) to penetrate only the first few nm of the measured samples. The detected intensity pattern as a function of 2θ will present a series of peaks corresponding to the conditions of constructive interference of the diffracted beams generated by the periodic arrangement of the atoms in the crystal lattice. Each peak corresponds therefore to a specific interference condition i.e. crystal symmetry and a combination of different peaks can be used to recognize a particular phase or a combination of phases in polycrystalline films. Reference patterns are used to de-convolute the measured spectra. Relative intensities of the detected peaks can give information on the amount of each crystalline phase present in the layer, whereas FHMW is used to calculate crystallite size. Other contributions such as mechanical stress and texture can also be analyzed. Unfortunately, some crystalline phases present very similar characteristic patterns which make their discernment rather complicated. This is for example the case of the orthorhombic $Pca2_1$ and the tetragonal $P4_2/nmc$ phase in HfO_2, which present their main diffraction peak at a very similar 2θ value of 30.5 and 30.8 °, respectively [204].

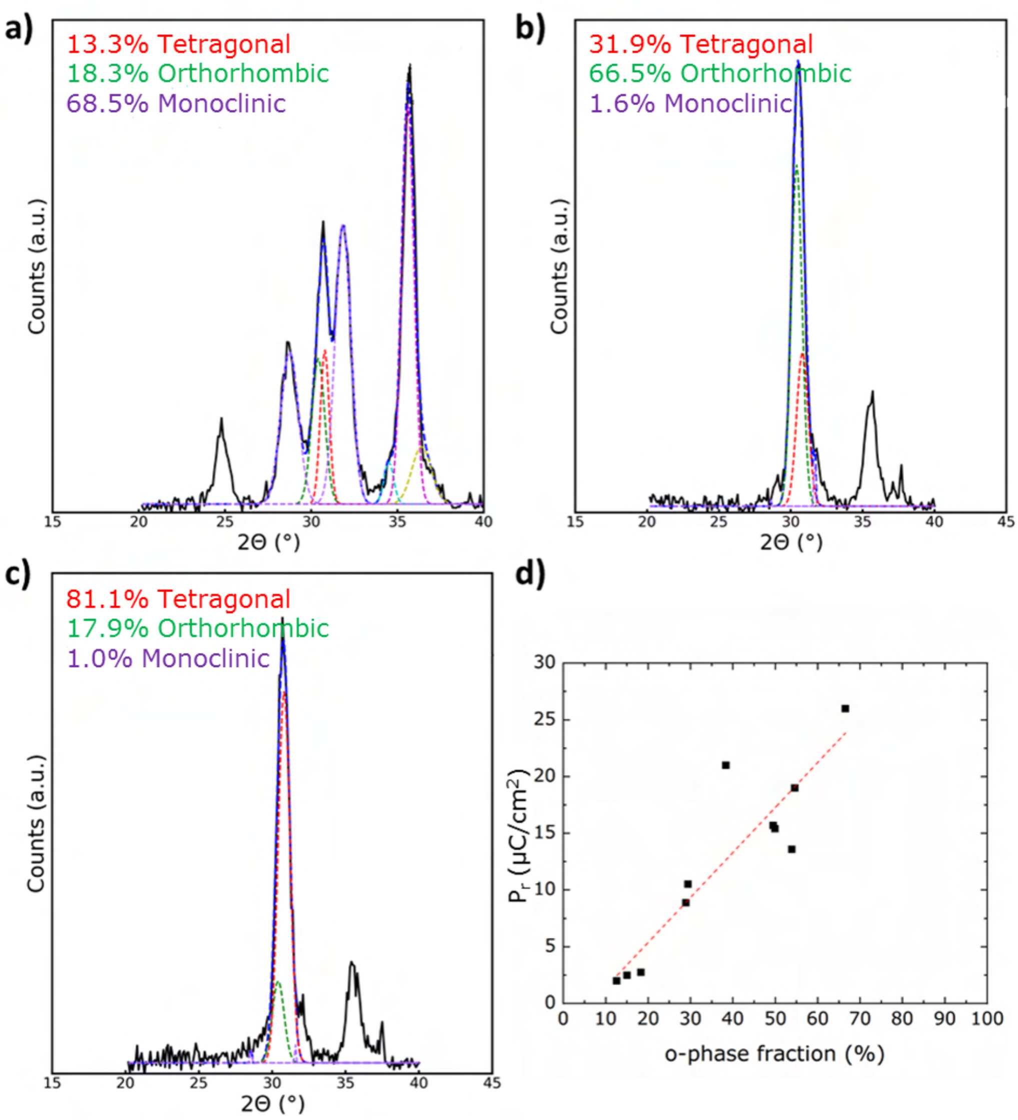

Figure 3.6: GIXRD patterns and peak deconvolution for 10 nm HfO_2 films deposited via ALD which present a large amount of a) monoclinic, b) orthorhombic and c) tetragonal phase, respectively. d) Remanent polarization vs. o-phase fraction for different $Hf_xZr_{1-x}O_2$ layers deposited via ALD.

GIXRD measurements performed within this work were carried out with a Bruker D8 Discover tool with Cu-K_α (λ= 0.154 nm) radiation. A 2θ range from 20 to 40 °C was used for pattern acquisition. A simple deconvolution of the measured patterns and a gaussian fit of the main peaks belonging to the monoclinic, the tetragonal and the orthorhombic phase was chosen for phase determination as shown in Fig. 3.6. The peak intensity was used for the calculation of the phase content, whereas the FWHM for the grain size for each detected phase (not reported here). The presence of all the three crystalline phases was assumed for the deconvolution and considerations on the accuracy of the fit were made based on the plausibility of the calculated grain size. A more detailed Rietveld analysis could be performed. However, it was previously demonstrated that this method is rather inconclusive in the case of $Hf_xZr_{1-x}O_2$ thin films. Effects of mechanical stress in the layers were not taken into account in the analysis and rather considered as an offset. By plotting remanent polarization values as a function of the o-phase fraction, a linear trend was obtained which indicates that stress may play a role but has no effect on the correlation between polar phase and observed ferroelectricity. In literature, stress values for doped HfO_2 films are reported to be in the range of 2 GPa [88].

More details on phase composition depending on process parameters will follow in chapter 4.

3.3 Electrical characterization

In this section, first, the standard methods for ferroelectric electrical characterization are introduced. Afterward, methods for assessing retention performance and switching behavior are addressed.

3.3.1 Basic ferroelectric characterization

Ferroelectricity is normally evaluated through some specific figures of merit: remanent polarization, number of field cycles before hard breakdown, often referred to as cycling endurance and amount of wake-up, that is the difference between the maximum remanent polarization obtained with field cycling (woken-up state) and the one measured at the very first measurement (pristine state). To access information on these values, two kinds of measurements are performed, which will be hereby shortly described.

Dynamic Hysteresis Measurement

The dynamic hysteresis measurement (DHM) is a sequence of triangular voltage waves which allow the direct measurement of a current and from it the indirect calculation of a polarization. The output values of the measurement are therefore a current-voltage (I-V) and a polarization-voltage (P-V) curve, that is a ferroelectric polarization hysteresis. Crucial values such as remanent polarization, saturation polarization, relaxed remanent polarization and positive (negative) coercive field can be extracted with this method. Details on circuitry behind this measurement can be found elsewhere [45].

During a DHM measurement, four pairs of up/down triangular pulses are applied with a certain frequency f (see Fig. 3.7). Within this work, f equaled 1 kHz. Each pair of triangular pulses is separated in time from a delay of 1 s. This allows the calculation of the relaxed remanent polarization, which gives information on the short-time retention. DHM measurements were performed in this context with a TF 3000 analyzer by aixacct system.

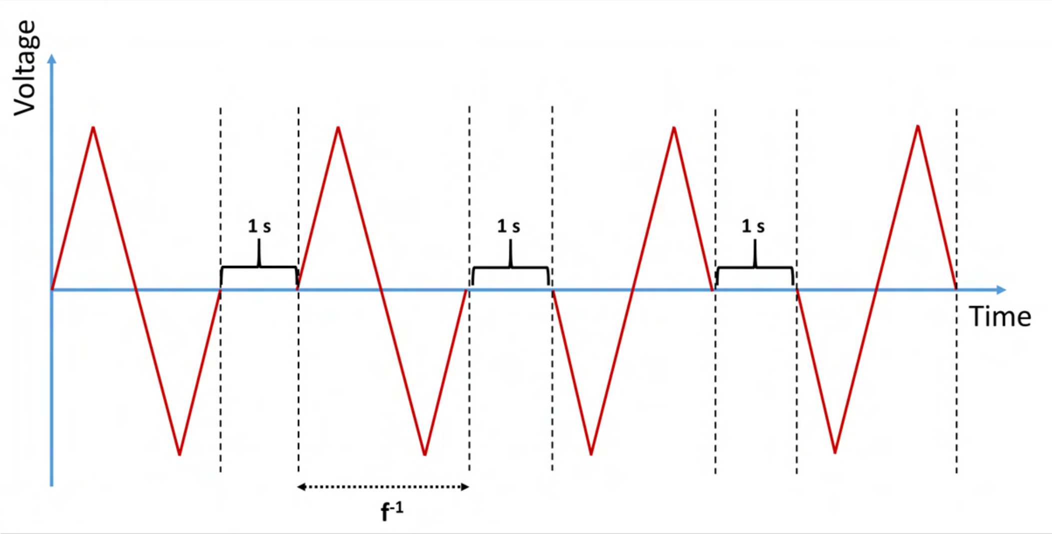

Figure 3.7: Voltage waveform applied to ferroelectric capacitors during a standard dynamic hysteresis measurement. f represents the measurement frequency. A delay of 1 s is applied between periods in order to register the relaxed polarization.

Field cycling measurement

The field cycling measurement, also often referred to as fatigue measurement or endurance measurement allows the characterization of the ferroelectric response as a function of the number of applied write cycles.

In an endurance measurement, single P-V measurements i.e. triangular waveforms with frequency f_1 are applied between increasing amounts of field cycles i.e. square waves with frequency f_2 to monitor the ferroelectric response with respect to device lifetime stage, as schematically shown in figure 3.8. In the very first measurement, the capacitor is in the so-called pristine state, often showing a pinched hysteresis loop caused by the presence of non-polar phase portions [129], [205], [206] depolarization fields [135], [136], inhomogeneously distributed charges and pinned ferroelectric domains [183]. By applying several up/down pulses (i.e. field cycles), the wake-up process is triggered which leads to an opening of the ferroelectric hysteresis because of either electric field-induced phase transition or disappearance of the depolarization fields. After wake-up, a new stage may be entered called fatigue, where the ferroelectric hysteresis closes again as a result of the creation of new charged defects, domain pinning or charge injection [126], [139], [140]. Finally, the capacitor reaches hard breakdown with the creation of a short. As explained in chapter 2, both wake-up and fatigue represent nonidealities in the device performance with respect to field cycling. Therefore, an important part of device optimization addresses their avoidance. Within this work, field cycling measurements were performed with a TF 3000 analyzer by aixacct system and with frequencies f_1 and f_2 of 1 and 100 kHz, respectively.

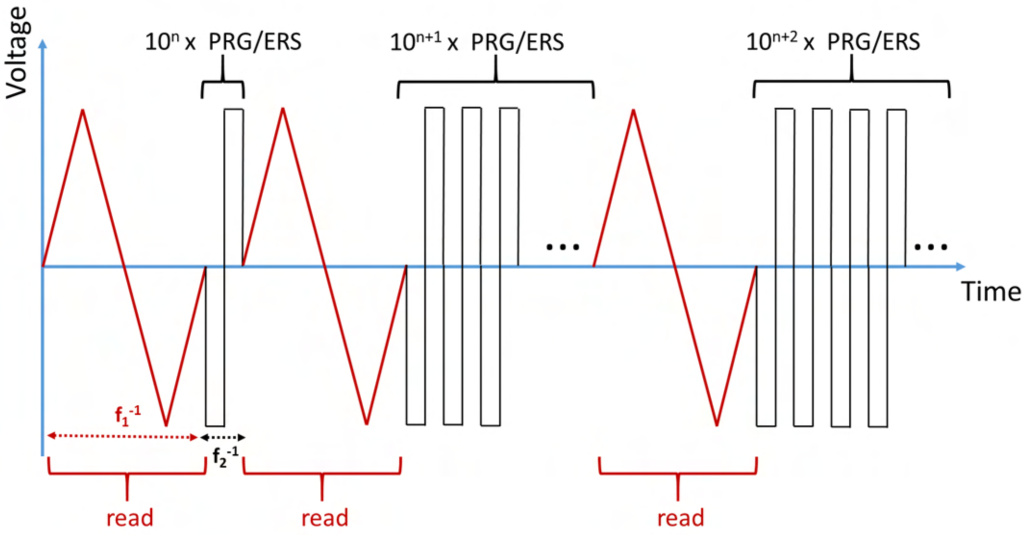

Figure 3.8: Voltage waveform applied to ferroelectric capacitors during a field cycling measurement. f_1 and f_2 represent the frequency of the triangular read pulses and of the square write pulses, respectively. The number of write cycles is increased by one order of magnitude after each read sequence.

3.3.2 Capacitance-voltage measurement

During a small signal capacitance-voltage (C-V) measurement, an alternate bias with an amplitude in the range of 50 mV and a frequency of 100 kHz is applied on top of a DC bias sweep. In the case of ferroelectric materials, ferroelectric switching is observed in the capacitance response which leads to a typical butterfly shape of the C-V curve. From the saturated capacitance (i.e. values extracted for fields larger than the switching fields, where switching events can be excluded) the k-value can be extracted, which gives an indication of the crystalline phase of the material.

C-V measurements were performed in this study either with a Keithley 4200 electrical characterization unit or with a TF3000 analyzer by aixacct systems.

3.3.3 Retention measurement

A retention test assesses the ability of a memory device to preserve the stored polarization state even after the removal of the supplied voltage. On a short time scale, relaxed polarization measured after 1 s can be utilized (see section **Dynamic hysteresis measurement**). To access a longer time scale, retention measurements are performed at high temperature and allow extrapolations to 10 years as described elsewhere [154].

A retention measurement uses 4 capacitors to which 4 different waveforms are applied. Between one application of the pulse sequence and the next one, a "baking" step of increasing length is performed, meaning the sample is stored in the oven for time intervals of increasing duration after each

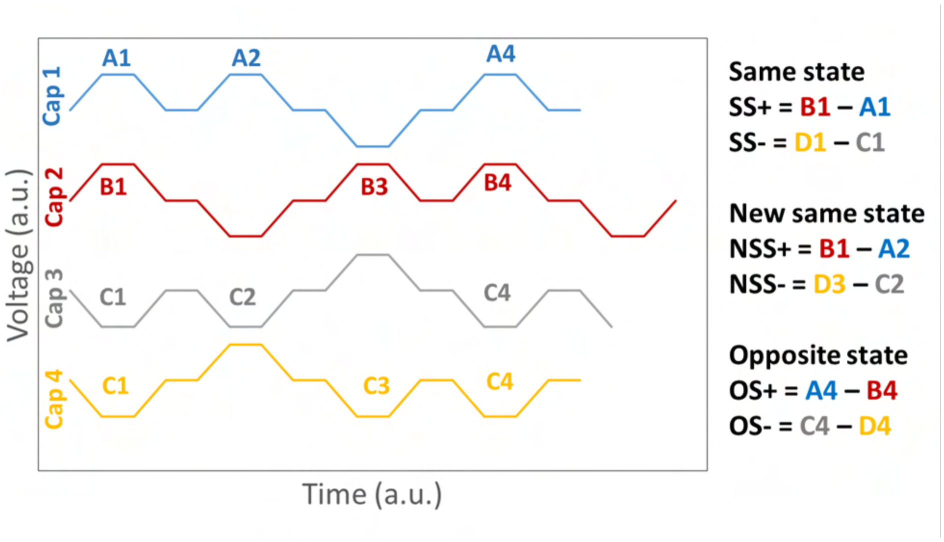

Figure 3.9: Voltage waveforms applied to four ferroelectric capacitors during a retention measurement. Different combination of pulses give information on the same state, new same state and opposite state retention, as described in Ref. [154].

waveform application. A combination of the measured signals allows the calculation of the same state, new same state and opposite state retention (SS, NSS and OS, respectively) as schematized in figure 3.9. Different models are available in literature [165], [168] for the extrapolation of the retention after 10 years of device operation. Normally the OS shows the strongest degradation.

By storing the sample in one polarization direction at high temperatures for a certain amount of time, other reliability issues can emerge. The prolonged presence of a dipole could for example cause higher charge injection from the electrodes. Additionally, it was demonstrated that a gradient in polarization could cause charged defects, especially oxygen vacancies, redistribution. Both phenomena can contribute to the imprint [167]. More details were already provided in section 2 and experimental observations will be documented in chapter 5.

Retention measurements were performed in this study with a Keithley 4200 electrical characterization unit and using a thermo-oven for the baking steps at the temperatures of 85 and 125 °C. All interested capacitors underwent a complete wake-up prior to the execution of the effective measurement. Among the calculated polarization states described above, the OS showed the strongest degradation and its extrapolation to a 10 years device working time was used as a benchmark for reliability performance. The extrapolation consisted in a fitting of the experimental data points using a simple power law model as described in [165]:

$$y = a - b \cdot ln(t + c), \tag{3.1}$$

where a refers to the initially stored polarization, b is an indication of the polarization decay rate and c is a time fitting parameter.

3.3.4 Switching kinetics

In order to acquire information on the switching mechanisms in thin HfO_2-based ferroelectric layers, switching kinetics measurements were performed in which the time and fields needed for polarization reversal were investigated and mutually correlated.

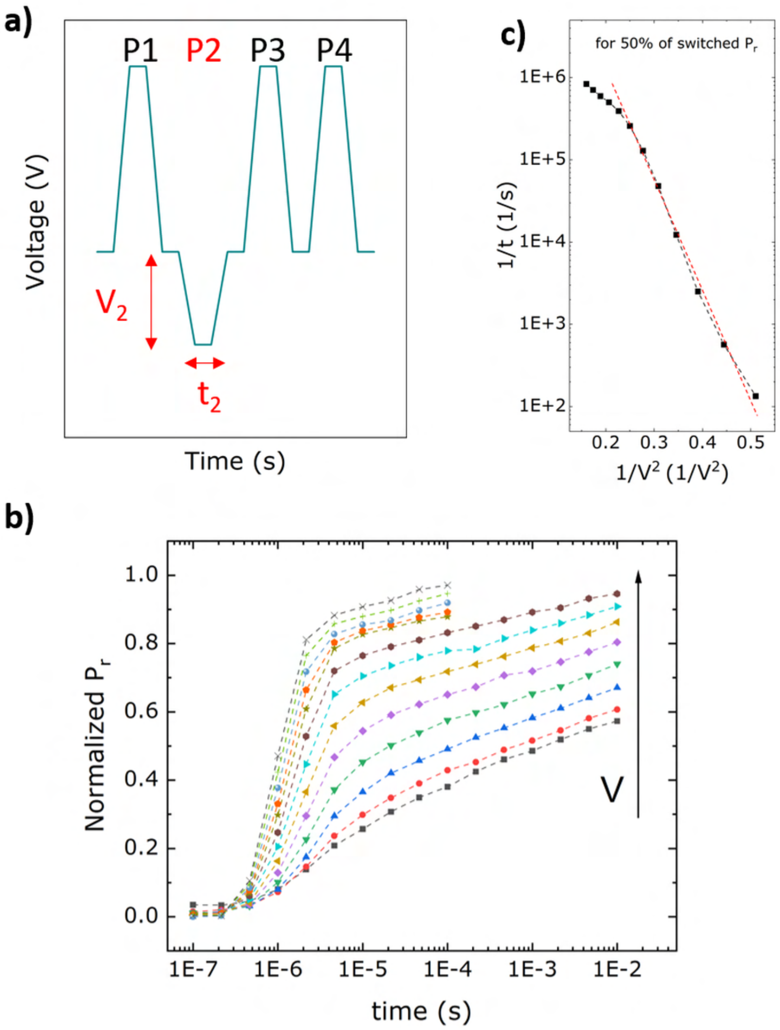

Figure 3.10: (a) Schematic of the waveform used for switching kinetics measurement, where P1 is used as the poling pulse, P2 as the setting pulse, and P3+P4 as the sensing pulses; each pulse Pn is characterized by a pulse width tn and a pulse amplitude Vn as described in the text. The example illustrates this for pulse P2; (b) $P_r/P_{r,max}$ as a function of amplitude V2 and width t2 of pulse P2; and (c) $1/t$ vs. $1/V^2$, where t and V are the time and the voltage necessary to switch 50% of the $P_{r,max}$, respectively. Taken with permission from [181].

A pulse sequence was exploited to experimentally acquire data for polarization reversal. As shown in figure 3.10, a waveform consisting of 4 different pulses is applied at the top electrode. P1 is used as a poling pulse, to set the capacitor in a certain polarization state. Afterward, a setting pulse P2 is applied in the opposite voltage direction, whose amplitude and width (V_2 and t_2, respectively) are varied. The pulses P3 and P4 are consequently used as sensing pulses in to detect how much of the polarization was successfully switched through P2. Precisely, when a switching event was effectively achieved by applying P2, a new switching event in the opposite direction will be registered by P3. In the opposite case, P3 will only detect the dielectric and leakage current response. P4 allows the subtraction of the dielectric current from the contribution registered from P3 to isolate the switching component of the signal, as in a PUND measurement. For the data displayed in figure 3.10, voltages V_2 ranging from 1.3 to 2.5 V and pulse times t_2 from 100 ns to 1 ms were employed. For each combination of V_2 and t_2 a certain percentage of P_r is successfully reversed, until for the higher voltages and longer times the whole film is switched.

Measurements results and their interpretation based on the chosen model will be fully displayed in chapter 6.

4 Effect of ALD deposition parameters on layer performance

As of today, atomic layer deposition represents the most used technique for the deposition of thin HfO_2 layers to be deployed in ferroelectric devices. ALD presents several advantages in terms of layer uniformity, deposition controllability and the possibility of accurately achieving 3D structures inside trenches or for pre-structured substrates. Despite the ALD process being well known and already described in the previous chapter, the main points will be hereby again discussed and further deepened.

A standard ALD process was previously described in chapter 3. Already from the cycle description, it is evident how many parameters can influence the outcome of the process. The most important parameters involved in the deposition of a $Hf_xZr_{1-x}O_2$ thin film are below listed and will be analyzed with the support of literature and experimental results within this chapter:

- Choice of the metal (hafnium and zirconium) precursors
- Choice of the oxygen precursor
- Effect of oxygen content
- Effect of zirconium content
- Effect of deposition temperature

While examining the different aspects playing a role in the deposition process, it is important to keep the nature of the targeted layer in mind. For this work, a thin amorphous $Hf_xZr_{1-x}O_2$ layer is desired. The deposition of the film in an amorphous state, together with an appropriate stoichiometry control, will allow the achievement of a certain crystalline phase after appropriate heat treatment [84]. A layer that is already crystalline after deposition may be hard to transform in another crystalline phase because of high energy barriers hindering phase transition. The desired phase can change depending on the final intended application of the film. An amorphous layer can be beneficial in the case of traditional MOSFET gate stacks because of lower defectivity originating from the formation of grain boundaries, which can serve as leakage paths for parasitic currents [207]. The t-phase shows high dielectric constant and is therefore optimal for DRAM applications [123], [208]. The polar o-phase is desired in the case of ferroelectric devices as extensively explained in the previous chapters [62], [96]. Deposition parameters control is also needed in order to deposit uniform and dense layers and limit reliability issues such as high leakage current or degraded interfaces with the electrodes [76].

4.1 Choice of the metal precursor

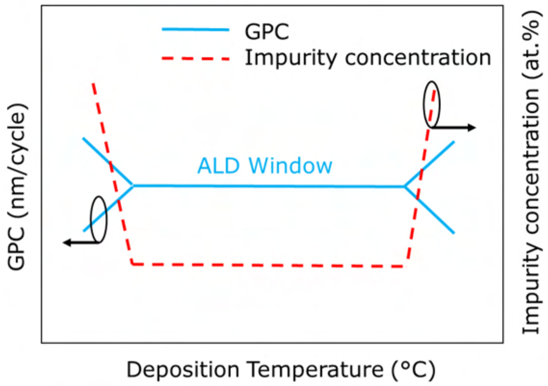

Figure 4.1: Schematic representation of the trend of growth per cycle and impurity concentration vs. deposition temperature in ALD growth.

As a starting point, various Hf and Zr precursors are examined by comparing literature data with experimental results obtained within this study. The chemical nature of precursor molecules present on the market is very diverse. As Hf source, together with halide-based compounds (e.g. $HfCl_4$, HfI_4) [209], [210] and organic compounds such as alkoxides and alkylamides (e.g. $Hf[O(CH_3)_2CH_2OCH_3]_4$, $Hf[N(CH_3)(C_2H_5)]_4$) [211], [212], more complex cyclopentadienyl precursors can be found (e.g. $Cp_2Hf(CH_3)_2$) [213], which were lately created in order to achieve a higher thermal stability of the molecules. Zr precursors were implemented in a similar fashion [214]–[217].

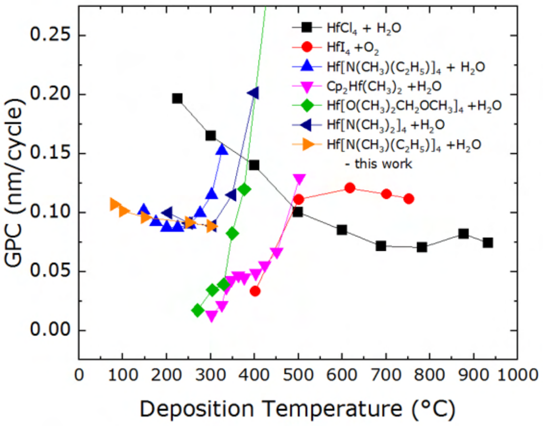

Figure 4.2: Growth per cycle for the most common HfO_2 metal precursors as a function of deposition temperature. Except for the $Hf[N(CH_3)(C_2H_5)]_4$ precursor used in this work, the data have been extracted from other sources. Taken with permission from [76].

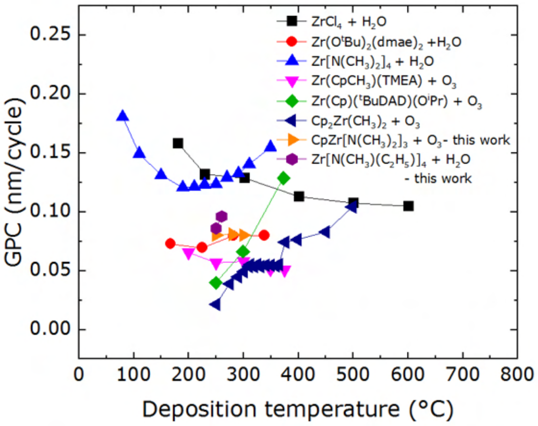

Figure 4.3: Growth per cycle for the most common ZrO_2 metal precursors as a function of deposition temperature. Except for the $Zr[N(CH_3)(C_2H_5)]_4$ and $Cp_2Hf(CH_3)_2$ precursors used in this work, the data have been extracted from other sources. Taken with permission from [76].

Each ALD precursor presents a stability interval with respect to deposition temperature in which the deposition rate (i.e. the growth per cycle, GPC) stays constant independently of pulse and purge times, given they are long enough to allow the reaction to take place. This temperature range is commonly referred to as ALD window [76] and is schematically shown in figure 4.1. The ALD window depends on the structure and the composition of the precursor molecule. At too low temperatures, the activation energy for molecule dissociation might not be reached. In this case, an incomplete reaction can give rise to phenomena such as condensation. The result will be films with low density and high impurity levels and therefore likely high leakage current levels [218]. At too high temperatures, the molecules could desorb or decompose. Precursor decomposition is often accompanied by high GPC due to incorrect molecule reaction and absorption [219]. By comparing Hf and Zr source molecules, the respective ALD windows show a similar extension as a function of temperature but result shifted with respect to each other, with Hf-containing molecules having a stability interval at slightly higher temperatures [220]. Wanting to deposit an amorphous $Hf_xZr_{1-x}O_2$ film, one has to take into account not only a temperature range in which both Zr and Hf precursors are stable but also the crystallization temperature of the material itself. This would further limit the range of employable temperatures. Indicatively, crystallization happens for temperatures higher than 300°C [210]. Nonetheless, lower crystallization temperatures were previously reported in the literature [221]. By having in mind the latest considerations and still aiming at a reasonable density and low leakage currents, a temperature range between 230 and 300 °C has been employed in this work for 10 nm thick $Hf_xZr_{1-x}O_2$ film deposition.

Figure 4.2 and 4.3 show the growth per cycle obtained while employing different Hf and Zr precursor molecules, respectively. As mentioned above, the stability of each precursor molecule depends on its chemistry. Alkoxide-based precursors show a sudden increase in GPC already at relatively low deposition temperatures, likely because of molecule decomposition [211], [216] On the contrary, halides-containing molecules are the ones exhibiting the widest stability range, where temperatures higher than 600°C can still be employed [209], [215], [222], [223]. Alkylamide-based precursors present a rather small ALD window. TDMA-Hf (Zr) ($Hf[N(CH_3)_2]_4$), $Zr[N(CH_3)_2]_4$)) show a steep increase in GPC at high temperatures if compared to TEMA-Hf (Zr) ($Hf[N(CH_3)(C_2H_5)]_4$, $Zr[N(CH_3)(C_2H_5)]_4$) [212], [217], [224], [225]. Cp-based precursors have instead a wider stability plateau at higher deposition temperatures [214], [226], [227].

The correlation between temperature stability and precursor molecules reflects itself in the kind and in the amount of impurities that can be found in the layer after deposition. Figure 4.4 schematically shows the correlation between deposition temperature and expected impurity concentration. In general, lower impurity levels are expected for higher temperatures because of better molecule dissociation. The impurity type is intuitively linked to the precursor chemistry. Figure 4.4 shows the a) hydrogen b) carbon and c) chlorine and nitrogen impurities detected in HfO_2 thin layers deposited via ALD with different metal and oxygen precursors combinations. If Cl impurities can be expected in halide-based precursors, C-containing groups are rather to be found in layers deposited starting from organic molecules. A new increase in impurity levels is also expected at the high-temperature edge of the ALD window, where molecule decomposition starts to take place.

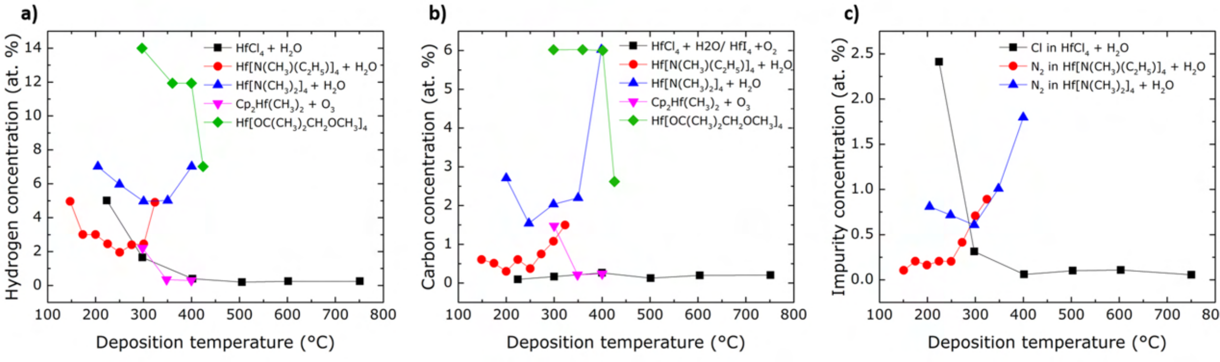

Figure 4.4: Impurity concentration levels as a function of deposition temperature for (a) carbon, (b) hydrogen, and (c) chlorine and nitrogen in atomic percent in layers deposited with different Hf-based precursors. Similar behavior is assumed for Zr-based precursors. Taken with permission from [76].

For the aim of this study, about 10 nm thick layers were deposited using TEMAHf + TEMAZr, TEMAHf + ZyALD ($Cp_2Zr(CH_3)_2$) and HyALD ($Cp_2Hf(CH_3)_2$) + ZyALD as precursor combinations. Capacitors were fabricated using TiN both as top and bottom electrode material. All the stacks were annealed at 600 °C in order to induce crystallization. The structural and electrical results obtained for those layers were then compared to those found in the literature for films stemming from TDMAHf + TDMAZr [117] and $HfCl_4$ + $ZrCl_4$ [228]. Different Hf to Zr ratios were explored.

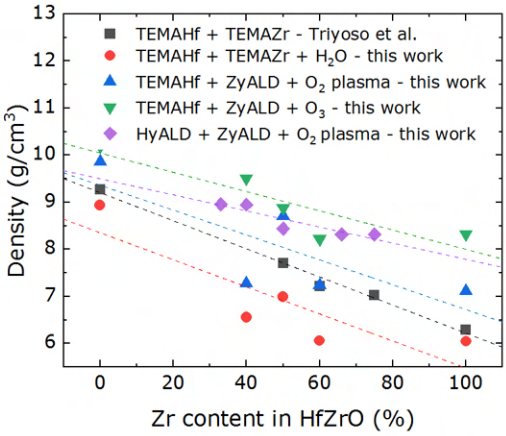

Figure 4.5: Density in as-deposited $Hf_xZr_{1-x}O_2$ as a function of the Zr content in the film for different Hf- and Zr-based precursor combinations. The data are partially produced within this work and partially taken from [229].

As a starting point, a structural characterization was performed. Through X-Ray Reflectivity layer thickness and density were measured for $Hf_xZr_{1-x}O_2$ films with different precursor combination and element ratios (i.e. different x). Film density represents an important parameter for layer reliability: in fact, low-density films often show high leakage current as a result of incorrect ALD deposition (see above). ZrO_2 presents a lower density as compared to its sister system HfO_2. As shown in figure 4.5, this trend was consistent for all the metal sources taken into consideration within this work. In general, Cp-containing molecules seem to yield the films with the highest density, probably resulting from higher precursor molecule stability.

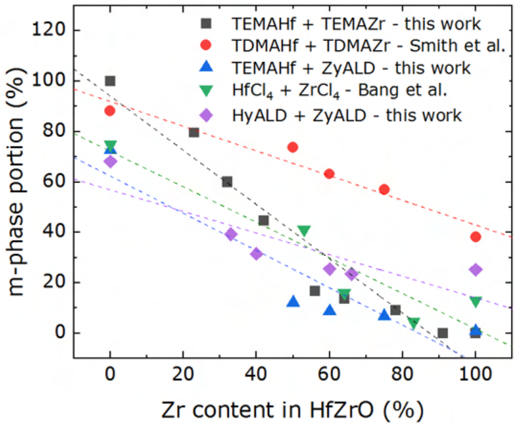

Figure 4.6: Monoclinic phase content in $Hf_xZr_{1-x}O_2$ as a function of the Zr content in the film for different Hf- and Zr-based precursor combinations. Films were annealed for crystallization or deposited as crystalline. The data are partially produced within this work and partially taken from [117] and [228].

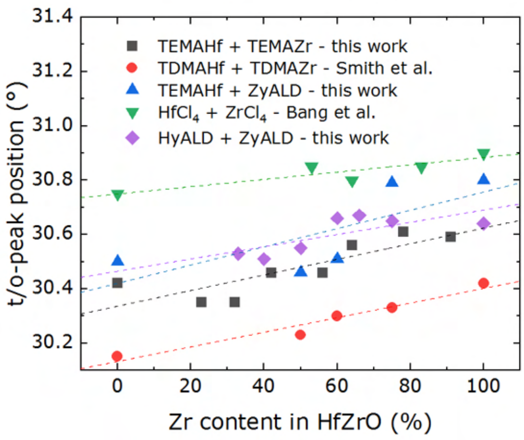

Figure 4.7: Tetragonal (101)/orthorhombic (111) peak position in GIXRD patterns of $Hf_xZr_{1-x}O_2$ as a function of Zr content in the film for different Hf- and Zr-based precursor combinations. Films were annealed for crystallization or deposited as crystalline. The data are partially produced within this work and partially taken from [117] and [228].

As mentioned in the previous chapters, a gradual transition from the monoclinic to the tetragonal phase has been by now many times demonstrated in the literature for increasing ZrO_2 content in $Hf_xZr_{1-x}O_2$ layers [73], [230]. For Hf:Zr ratios close to 1, a concentration interval is found where the metastable o-phase can be stabilized [73], [231]. The hereby deposited layers were measured via GIXRD and the m-phase portion was extracted for each composition starting from the peak intensity of the most prominent peaks through the following equation:

$$\text{m-phase portion} = 100 * \frac{\mathrm{I}_{m(111)} + \mathrm{I}_{m-(111)}}{\mathrm{I}_{m(111)} + \mathrm{I}_{m-(111)} + \mathrm{I}_{o(111)/t(101)}}, \tag{4.1}$$

where I represents the maximum peak intensity for the peaks as indicated by the indexes. The results are displayed in figures 4.6 and 4.7. For all precursor combinations, an increase in the m-phase portion with increasing Zr content was demonstrated. Concurrently, the peak representing the (111) reflection of the o-phase and the (101) reflection of the t-phase, which are difficult to be distinguished given their 2θ similarity (30.5 and 30.8 °, respectively [95]) showed a shift to higher 2θ values, indicating an increase in the t-phase portions for high Zr content [232]. It is worth to be mentioned that a shift in peak angles could also be observed as a result of stress in the layers [233].

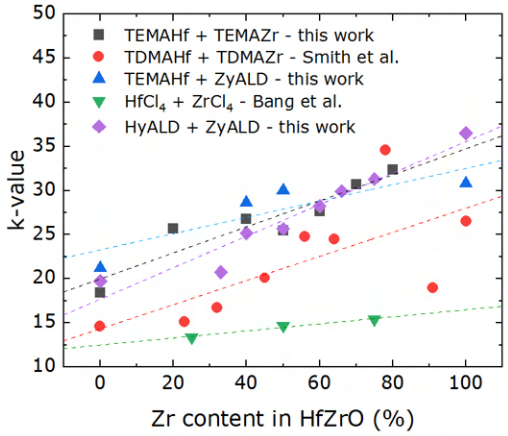

Figure 4.8: Dielectric constant of crystalline $Hf_xZr_{1-x}O_2$ as a function of the Zr content in the film for different Hf- and Zr-based precursor combinations. The displayed data are partially produced within this work and partially taken from [117] and [228].

An electrical characterization followed the structural analysis. It is well known that the tetragonal phase is the one with the highest dielectric constant. On the contrary, the m-phase shows lower k-values. In fact, theoretical values up to 70 are suggested in the literature for HfO_2 and ZrO_2 in the tetragonal phase [123], [208], though experimentally extracted values are found to be around 20, 28 and 40 for the monoclinic, the orthorhombic and the tetragonal phase, respectively [76]. In general, an increase of dielectric constant is expected for high Zr content as a result of lattice modifications [232]. Extraction of the k-values from current-voltage measurements allowed to confirm this trend, as displayed in figure 4.8. Dielectric constant values increased as the composition was tuned from undoped HfO_2 to undoped ZrO_2. This was similar for each of the analyzed precursor combinations. $Hf_xZr_{1-x}O_2$ layers deposited with halide precursors showed exceptionally low k-values, probably due to thickness determination inaccuracies [228].

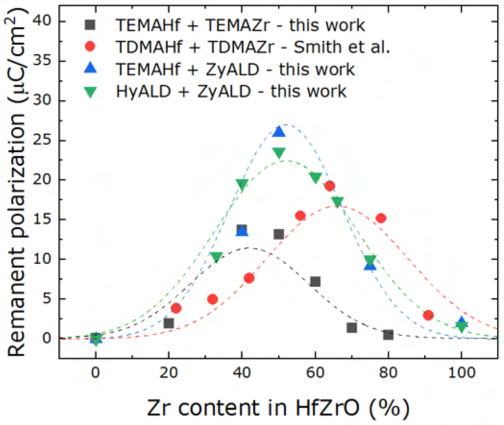

Figure 4.9: Remanent polarization of crystalline $Hf_xZr_{1-x}O_2$ as a function of the Zr content in the film for different Hf- and Zr-based precursor combinations. The dashed lines represent Gaussian fits of the experimental data points. The displayed data are partially produced within this work and partially taken from [117].

Heading to the ferroelectric properties, remanent polarization values were measured and plotted in figure 4.9 for the different precursor pairs addressed in this work. As described in the previous sections, both the monoclinic and the tetragonal phases are accompanied by zero remanent polarization values as a result of a non-polar crystalline structure. Being undoped HfO_2 and ZrO_2 preferentially stabilized in the m- and in the t-phase, respectively, no retained polarization at zero electric fields is expected for the two edge compositions. The ferroelectric phase is stabilized at an approximately 1:1 Hf:Zr ratio, where a peak in P_r values is observed for all considered systems [76].

To summarize, it was shown how different ALD metal precursor molecules yield different impurities depending on their chemistry and deposition temperature. Different Hf and Zr source combinations were explored both experimentally and through literature and all of them presented coherent trends both from a structural and from an electrical point of view. Cp-containing molecules showed good temperature stability and their use during deposition resulted in high-density layers with high k-values and remanent polarization values. A weighing of all observations led to the choice of the TEMAHf + ZyALD combination as a standard for future experiments within this work.

4.2 Influence of deposition temperature

As already explained in the previous section, deposition temperature plays a strong role in the ALD process. In fact, too low or too high temperatures give rise to undesired reaction mechanisms which cause the inclusion of un-reacted by-products or result in either too high or too low growth per cycle and low-density films with high defectivity. Deviations from the envisioned reaction behavior at high and low temperatures define the so-called ALD window. Nonetheless, even within this temperature interval, differences can be encountered depending on the chosen reactor chamber. Furthermore, an amorphous layer is required after deposition to be able to target the metastable polar orthorhombic phase through the annealing treatment and therefore achieve ferroelectricity [84]. The two considerations limit the temperature window to a small range which is normally found between 200 and 300 °C, for the case of an intermixed deposition of HfO_2 and ZrO_2. [76].

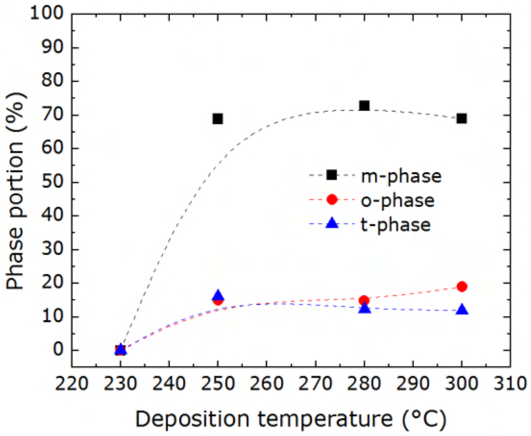

Figure 4.10: Phase portions obtained from GIXRD measurements of as deposited 10 nm thick HfO_2 layers deposited via ALD at different chamber temperatures. The dashed lines serve as a guide for the reader.

Experiments were performed in which both undoped HfO_2 and later $Hf_{0.5}Zr_{0.5}O_2$ layers were deposited at different chamber temperatures. GIXRD patterns were measured and compared. Figure 4.10 shows m-, t- and o-phase portions for undoped HfO_2 layers as a function of deposition temperature. From the displayed data it can be inferred that only layers deposited at 230°C showed no crystallinity in the as-deposited state. On the contrary, from 250 °C onward, a prevalent monoclinic phase was detected already prior to the annealing treatment.

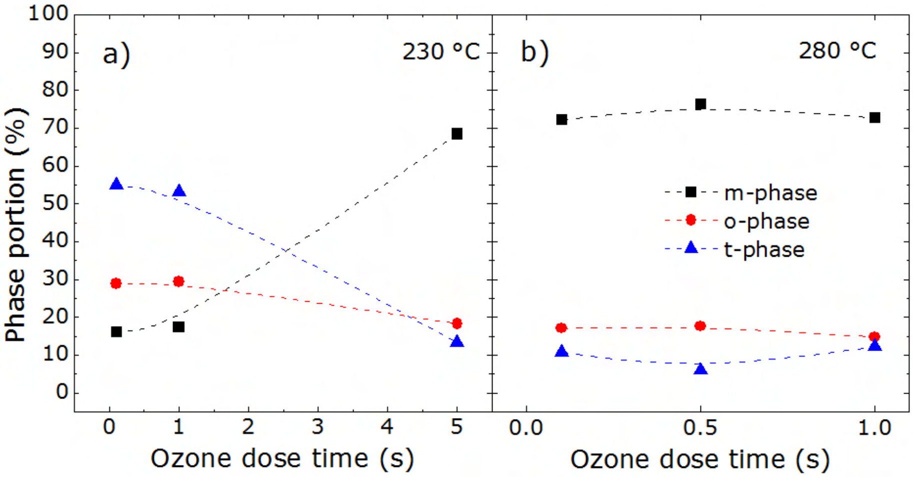

Figure 4.11: Phase portions obtained from GIXRD measurements of 10 nm thick HfO_2 layers deposited via ALD at 230 °C and 280 °C and annealed at 600°C for 20 s in N_2 atmosphere. The dashed lines serve as a guide for the reader.

By comparing the patterns obtained after a 20 s RTA at 600°C in N_2 atmosphere displayed in figure 4.11, it is evident how for the 230 °C case the tetragonal and the polar orthorhombic phases could be stabilized through the annealing treatment. The final phase was dependent on the oxygen amount supplied during deposition. On the contrary, the layers deposited at 280°C, which were already crystalline and in the m-phase in the as-deposited state, underwent no changes through RTA.

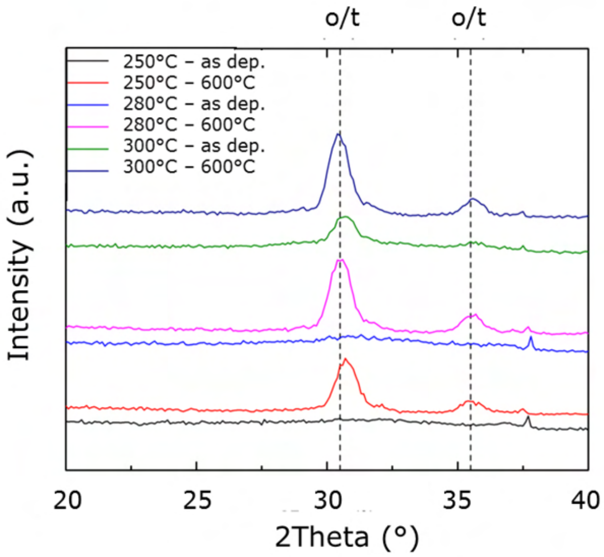

Figure 4.12: GIXRD patterns of 10 nm thick $Hf_{0.5}Zr_{0.5}O_2$ layers deposited via ALD at 250, 280 and 300 °C, both as deposited and annealed at 600°C for 20 s in N_2 atmosphere.

Analogously, $Hf_{0.5}Zr_{0.5}O_2$ films with a thickness of 10 nm were deposited with TEMAHf and

ZyALD as Hf and Zr precursors, respectively, at 250, 280 and 300°C. Figure 4.12 shows the GIXRD spectra obtained for the different layers both as-deposited and after RTA. Contrarily to films deposited at 250 and 280 °C, the one at 300 °C shows crystallization already in the as-deposited state. As a consequence, the amount of monoclinic phase detected in this sample after RTP is higher.

Park et al [84] and Alcala et al. [234] performed analogous experiments on $Hf_{0.5}Zr_{0.5}O_2$ layers deposited at temperatures ranging from 200 °C to 280 °C and from 250 °C to 350 °C, respectively. Comparable results were obtained. In particular, a pinched hysteresis was shown by Park et al. for low deposition temperatures. Among the suggested causes, they proposed the presence of unreacted C impurities supporting the stabilization of the t-phase because of surface energy contributions. A more detailed explanation can be found in Chapter 2.

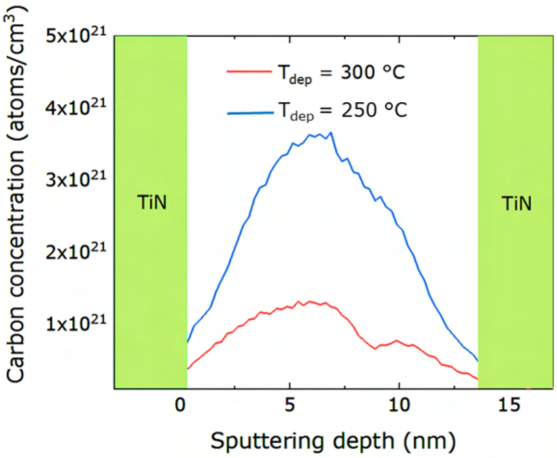

Figure 4.13: C impurities ToF-SIMS patterns for ZrO_2 layers deposited at 250 and 300 °C.

As a matter of fact, ToF-SIMS measurements performed on films deposited in the same fashion but at two different chamber temperatures showed almost one order of magnitude higher carbon content when the deposition temperature was decreased by 50 °C (Fig. 4.13). Analogous measurements were performed by Kim et al. [112] via Auger electron spectroscopy, which reported a tenfold decrease in C concentration with increasing deposition temperature from 180 to 260°C.

4.3 Influence of oxygen content

Once precursor types have been decided for both metals and oxygen sources, process optimization has to proceed through the amount of oxygen to be supplied to the layer during deposition.

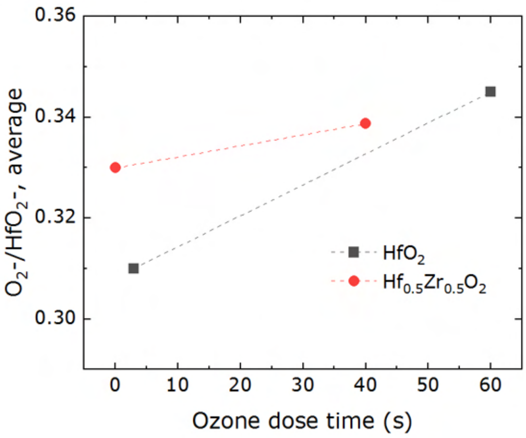

Figure 4.14: $O_2-/Hf_xZr_{1-x}O_2$ ratios comparison as a function of ozone dose time as obtained from ToF-SIMS measurements averaged across the whole layer thickness. A slight increase in oxygen content in the layers is detected for increasing ozone dose times.

$Hf_xZr_{1-x}O_2$ layers were deposited with different ozone dose times, spanning from 0.1 to 60 s. Time of flight mass spectroscopy measurements were performed for both undoped HfO_2 and $Hf_{0.5}Zr_{0.5}O_2$ films deposited with either very short or very long ozone pulse times. As shown in Fig. 4.14, the measurements confirmed the latter directly influences the oxygen content in the layers. Unfortunately, an estimation of the actual oxygen content in the layers is difficult to perform. Therefore, ratios have been reported, which were averaged on the whole film thickness.

As mentioned in the previous chapters, oxygen content i.e. the concentration of oxygen vacancies in the layer is, together with other factors such as stress [235], dopant inclusion [74] and surface energy [84] one of the aspects determining ferroelectricity in HfO_2 and ZrO_2 based layers [77], [86], [236]. A non-centro-symmetrical phase is necessary in order to promote ferroelectricity, whose polarity is influenced by the placement of oxygen atoms within the crystal lattice. Therefore, it is intuitive how oxygen content and ferroelectricity are directly related.

In general, both neutral and charged oxygen-related defects such as oxygen interstitials and vacancies are commonly found in HfO_2 [124]. The formation energy of such defects strongly depends on the crystalline phase of the material and varies for inequivalent bonds, that is for different sites in a crystal or sites in different crystal phases. A lower defect formation energy was found for the material being in the m-phase when compared to the t- and the polar o-phase, and in ZrO_2 compared to HfO_2 [126], [127]. On the other hand, the presence of defects influences lattice volume and therefore phase formation. Effects on bond lengths and cell volume also strongly come into play when a dopant atom is introduced. III-valent dopants such as La, Al or Y strongly reduce oxygen defects formation energies as compared to IV-valent dopants such as Si, Ta or Ti [93], [123], [125]. More details on doped HfO_2 were nonetheless already provided in chapter 2 and will be further discussed in chapter 7.

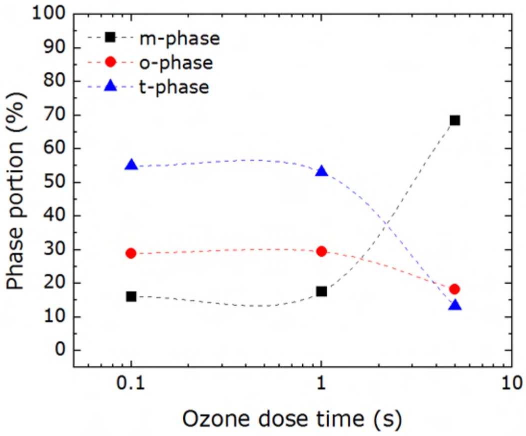

Figure 4.15: Phase fraction of HfO_2 layers as a function of the oxygen supplied during deposition via ALD. The ozone dose time was used to control the oxygen in the films. The phase portions were calculated by fitting of the experimentally measured GIXRD patterns. The dotted lines are only meant as a guide for the reader.

To discriminate the influence of the oxygen vacancy concentration from the other factors inducing ferroelectricity, especially from dopant inclusion, 10 nm thick undoped HfO_2 layers were first deposited with different ozone dose times. The crystalline phase was determined through GIXRD measurements. The measured patterns were de-convoluted and phase fractions were extracted by Gaussian fitting of the main plane reflections and subsequent calculations of the ratios between peak areas. No stress contributions were taken into account but trends should be consistent between similarly processed samples. A detailed explanation of measurement de-convolution can be found in 3.2. As shown in Fig. 4.15, the monoclinic phase gets stabilized for oxygen dose times longer than 1 s. At low ozone dose times, the tetragonal phase seems to take over.

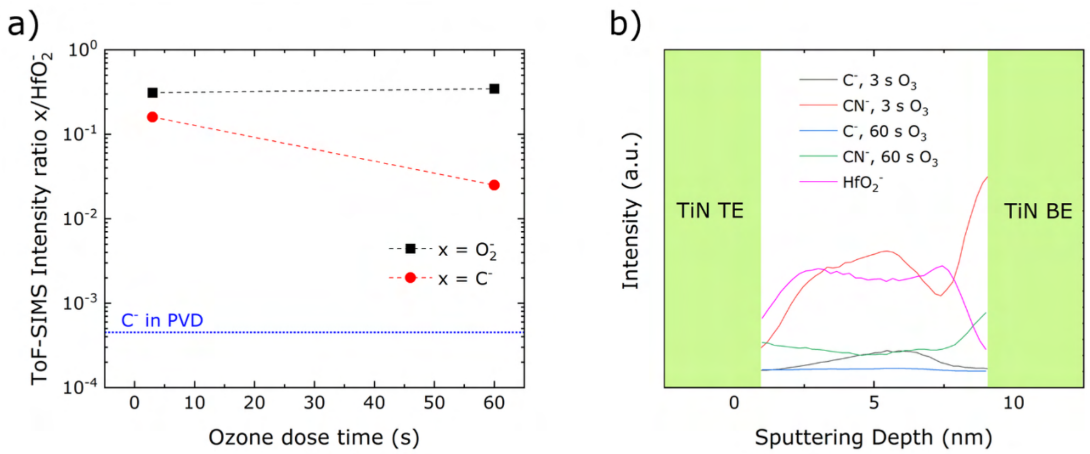

Figure 4.16: (a) C^- and O_2^- content measured via ToF-SIMS for ALD-deposited HfO_2 layers as a function of the ozone dose time during deposition. The value measured on a PVD sample is shown as a dotted blue line for comparison. (b) C- and CN- ToF-SIMS intensity profiles for HfO_2 films deposited with 3 and 60 s ozone dose times. Taken with permission from [86].

ToF-SIMS measurements also show an increase in C and CN residuals as the oxidant supply is reduced (see Fig. 4.16), very likely due to incomplete oxidation during the ALD process [76]. Unfortunately, it is complicated to discern the effect of oxygen vacancies from the effects of carbon contamination. The latter is known to affect the phase of the material and consequently its ferroelectricity because of either unintentional doping or effects on surface energy which limit grain growth [102], [237]–[239]. The comparison with layers deposited via PVD starting from high purity targets hints nonetheless to similar trends with respect to the oxygen supply, even in the absence of detected carbon [86]. More on the topic can be found in the following sections (see section: Comparison with PVD).

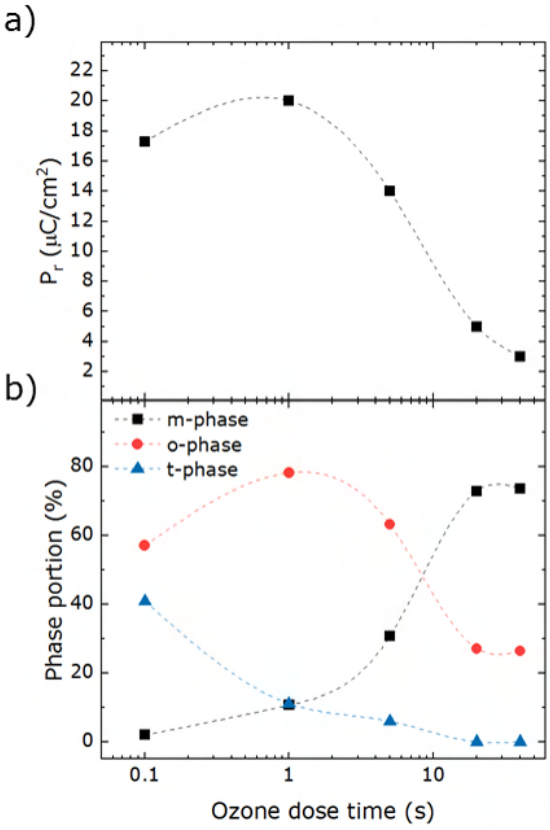

Figure 4.17: a) Remanent polarization and b) monoclinic, orthorhombic and tetragonal phase portion as a function of oxygen dose times in $Hf_{0.5}Zr_{0.5}O_2$ thin films annealed at 600 °C. The highest P_r values correspond to the highest detected polar orthorhombic phase. A lower remanent polarization is observed in films were high t- and m-phase portions are detected. Dashed lines are only meant as a guide for the eye.

Remanent polarization and crystalline phase portions were also measured for 10 nm thick $Hf_{0.5}Zr_{0.5}O_2$ films deposited with different ozone dose times. As reported in figure 4.17, opposite trends could be observed for the m- and the t-phases. The former is favored by high oxygen contents, whereas the formation of the latter is preferred in oxygen-poor atmospheres, similar to the findings related to undoped HfO_2. In between, the polar orthorhombic phase is stabilized and high remanent polarization values are obtained. Results were consistent for films deposited both at 280 and 300 °C and annealed both at 600 and 500 °C. Figure 4.17 only shows values for layers deposited at 300 °C and annealed at 600 °C.

4.4 Reliability as a function of oxygen content

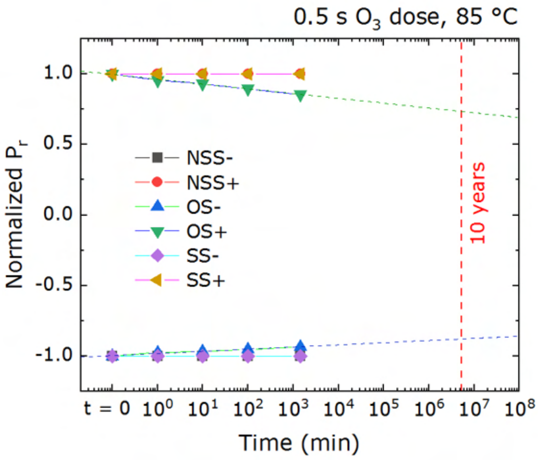

Figure 4.18: Positive and negative same state (SS+, SS-), new same state (NSS+, NSS-) and opposite state (OS+, OS-) retention measured at 85 °C for a ferroelectric capacitor based on a 10 nm $Hf_{0.5}Zr_{0.5}O_2$ film deposited with 0.5 s O_3 dose time as a function of baking time. The initial P_r values are of 19 $\mu C/cm^2$. The OS retention shows the strongest reduction and was therefore extrapolated for 10 years operation in order to benchmark device degradation.

Imprint and retention performances were also tested for $Hf_{0.5}Zr_{0.5}O_2$ films and trends were studied with respect to the amount of oxygen in the layers according to the measurement procedure described in chapter 3. In figure 4.18 the results are reported for a ferroelectric capacitor whose $Hf_{0.5}Zr_{0.5}O_2$ layer was deposited with 0.5 s O_3 dose time. The remanent polarization was normalized to its initial value to estimate its degradation with time and temperature. A detailed explanation of the standard procedure is described in [154] and in section 3.3.3. The trend of the normalized polarization was monitored with time considering positive and negative same state (SS+, SS-), new same state (NSS+, NSS-) and opposite state (OS+, OS-). P_r values are far above the detection limit, as demonstrated in figure 4.17. As mentioned above, the opposite state shows the strongest degradation and will therefore be considered in the following discussion as the main figure of merit for retention loss. In figure 4.18, an extrapolation to 10 years working time using a power law (see chapter 2, equation 3.1) shows the device retains more than 50 % of its initial polarization, meeting industry requirements.

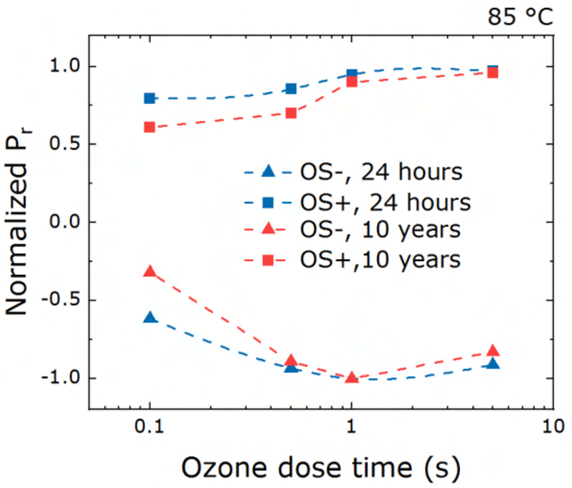

Figure 4.19: Normalized positive and negative opposite state polarization after 24 h baking at 85 °C and extrapolated to 10 years device operation as a function of ozone dose times. Dashed lines are only meant as a guide for the eye.

Figure 4.19 shows the opposite state retention after 24 hours baking and extrapolated to 10 years working time as a function of the ozone dose time with which the $Hf_{0.5}Zr_{0.5}O_2$ thin films have been deposited. It is straightforward how samples deposited with shorter O_3 dose times show stronger retention degradation. In particular, the sample with 1 s O_3 dose time presents the best behavior. This well correlates with the higher orthorhombic phase fraction and remanent polarization values which were detected in the previously displayed measurements.

In particular, samples with low oxygen content could present higher defectivity, lower crystallinity or higher tetragonal non-polar phase fractions. In all cases, oxygen vacancies could contribute to more diffuse electron trapping and together with non-polar portions generate depolarization fields which cause back-switching, imprint and in general retention loss.

Figure 4.20 shows the imprint calculated as the rigid hysteresis shift on the voltage axis ($(E_C, - + E_C, +)/2$) for both 85 °C and 125 °C baking steps of 24 hours. Also, in this case, it can be observed how the layers deposited with 1 s O_3 dose time show the best performances i.e. the lowest hysteresis shift with time and temperature, confirming what is stated above. In general, for $Hf_{0.5}Zr_{0.5}O_2$-based ferroelectric capacitors, 1 s O_3 dose time seems to result in the best values in terms of phase stabilization, remanent polarization and reliability.

In the next section, the ratio between HfO_2 and ZrO_2 will be varied and the most important ferroelectric figure of merits will be evaluated by varying concurrently Hf:Zr ratio and oxygen content i.e. ozone dose time.

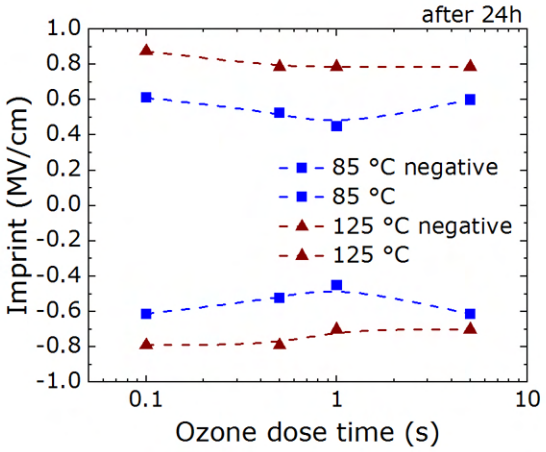

Figure 4.20: Negative and positive opposite state imprint calculated as a shift of the ferroelectric hysteresis along the voltage axis after 24 h baking at 85 and 125 °C as a function of ozone dose times. The initial, not normalized P_r values can be found in figure 4.17. Dashed lines are only meant as a guide for the eye.

4.5 Influence of zirconium content

A new degree of freedom was added by implementing a matrix of $Hf_xZr_{1-x}O_2$ layers where oxygen and zirconium content were tuned concurrently through ozone dose time and Hf:Zr cycle ratio, respectively.

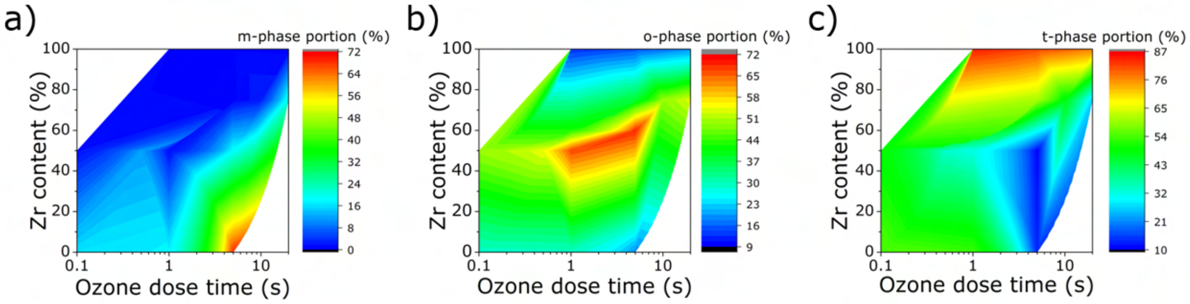

Figure 4.21: Phase fraction for (a) m-phase, (b) o-phase, and (c) t-phase in ALD-deposited $Hf_xZr_{1-x}O_2$ layers as a function of Zr content and O_3 dose time calculated by fitting the experimentally measured GIXRD patterns. Taken from [86].

In figure 4.21, contour plots report the amount of each crystalline phase (a) m-phase, b) polar o-phase and c) t-phase) as a function of the ozone dose time (x-axis) and Zr content in percentage (y-axis) calculated from the deconvolution of the measured GIXRD signals. 13 data points were used for each plot. Details on the procedure were previously explained in section 3.2. As shown in figure 4.21, similar to the case of undoped HfO_2, high oxygen content encourages the stabilization of the m-phase, as well as high Hf content. Conversely, the tetragonal phase was stabilized for low ozone dose times and high Zr content. The o-phase found a stabilization interval for intermediate values, that is for a Hf:Zr ratio of around 1:1 and ozone dose times in the range of 1 s.

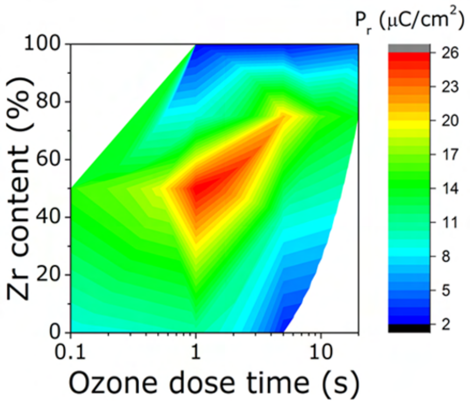

Figure 4.22: Remanent polarization as a function of Zr content and ozone dose time in good correlation to a high o-phase content in Figure 4.21 b). The maximum remanent polarization values are obtained for a linear relationship between Zr content and ozone dose time. Taken with permission from [86].

Remanent polarization values were also measured for films with different oxygen and zirconium content. By comparing Fig. 4.21 b) and Fig. 4.22, it is evident that they well correlate with the amount of polar orthorhombic phase detected in the thin films. Large P_r values could be obtained for the same conditions required for o-phase stabilization, by appropriate tuning Zr and oxygen content, which seem to have an opposite effect.

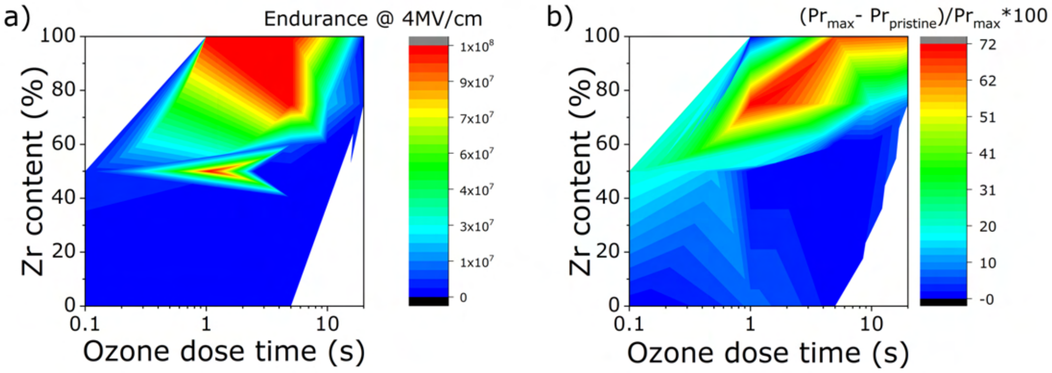

Figure 4.23: a) Endurance defined as the number of cycles before device hard breakdown and b) amount of observed wake-up defined as the difference between the woken-up P_r and the pristine P_r, normalized to the woken-up P_r for different $Hf_xZr_{1-x}O_2$ layers as a function of Zr content and O_3 dose time. Taken with permission from [86].

Endurance with respect to field cycling was plotted in Fig. 4.23 a) by applying write cycles with an amplitude of 4 MV/cm and noting the number of cycles the device could withstand before reaching hard breakdown. The experiments show that endurance is reduced for high amounts of Hf with respect to Zr and larger oxygen contents. This figure of merit can be well associated with the m-phase fraction detected in the $Hf_xZr_{1-x}O_2$ layers. In fact, a larger m-phase portion seems to limit device endurance. Similar observations were previously reported in the literature. Already in the context of DRAM stack optimization, a correlation between the non-polar m-phase and high defectivity was demonstrated, which harmed device reliability [240].

The wake-up behavior was also analyzed as a function of Zr and oxygen content by applying field cycles to each film and comparing the P_r values corresponding to the maximum opening of the memory window and the pristine case. The number of cycles necessary for complete wake-up varied from sample to sample. Wake-up seems to be particularly pronounced for films in which the t-phase results strongly stabilized, i.e. for short O_3 pulses and high Zr content, as evident by comparing Fig. 4.21 c) and Fig. 4.23 b). Those films show the largest increase in P_r values with wake-up cycling, which is the biggest difference between the woken-up remanent polarization and the pristine one. At least two phenomena seem to be good candidates as adequate interpretation of the experimental observations. On the one hand, a field-induced phase transition could take place, most likely from the t- to the o-phase, increasing the amount of switchable domain and consequently causing the opening of the ferroelectric hysteresis [129], [134], [135]. On the other hand, wake-up phenomena could originate from charge redistribution within the layer, most likely oxygen vacancies [139]. Such defects are more commonly found in films where less oxygen is provided and have been shown to have lower energy formation in ZrO_2 as compared to HfO_2.

To summarize, the introduction of Zr seemed to provoke an opposite effect as compared to increased oxygen content, favoring the stabilization of the t-phase and resulting in a more pronounced wake-up and an improvement in device lifetime with respect to the number of applied field cycles. An optimum in remanent polarization i.e. the largest polar o-phase portion was obtained for an Hf:Zr ratio of $\sim$ 1:1, as already found in previous literature reports [76], [118].

4.6 Comparison with films deposited via physical vapor deposition

In this section, films deposited via sputtering will be compared to the previously shown results on ALD. In order to control oxygen supply during deposition, the oxygen flow in the sputtering chamber (expressed in sccm) is tuned. PVD deposited undoped HfO_2 films were first studied and reported by Mittmann et al. in [236].

Fig. 4.24 shows the m-, t- and o-phase fractions in a) sputtered and b) ALD deposited undoped HfO_2 layers. All considered films were 10 nm thick and underwent a thermal treatment for crystallization. It is worth mentioning that sputtered films require a higher annealing temperature as compared to ALD deposited films to acquire optimal ferroelectric properties [236]. An annealing temperature of 800 and 700 °C was therefore chosen for the two cases. A coherent trend with respect to oxygen content can be detected in both layers subgroups. An elevated amount of supplied oxygen stabilizes the monoclinic phase in both cases. However, a difference in the most present phase can be found for low oxygen contents. In fact, if on one hand, the o-phase is the most stable one in the case of films sputtered with low oxygen flow, on the other hand, short ozone dose times seem to stabilize the t-phase for ALD layers. Such a difference could arise because of the presence of unreacted C impurities in the ALD layer, which are not found in layers sputtered in ultra-high vacuum conditions starting from high purity targets. ToF-SIMS measurements displaying the

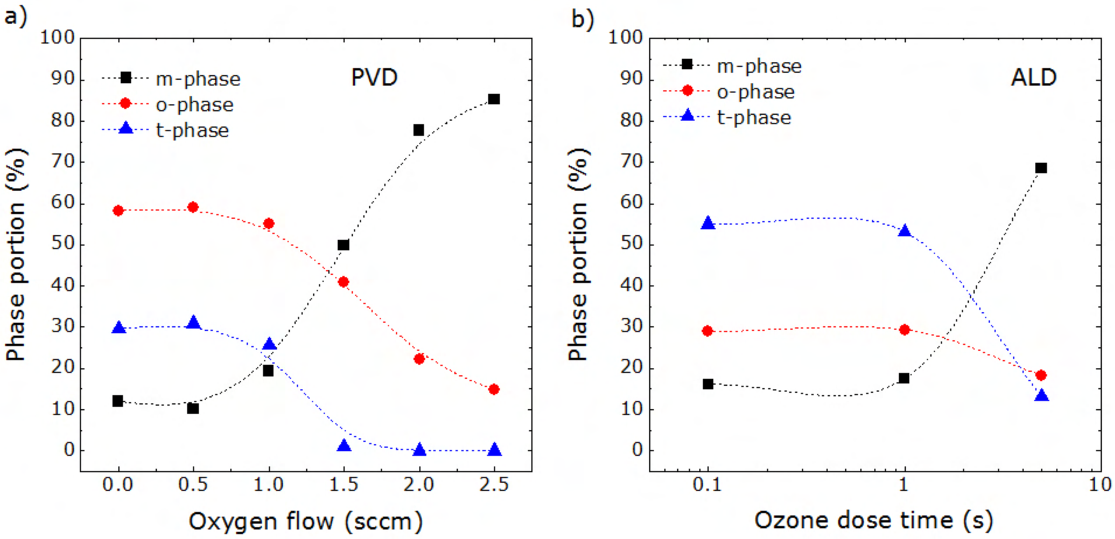

Figure 4.24: Crystalline phases (m-, o- and t-) fractions for undoped HfO_2 layers deposited via a) sputtering and b) ALD as a function of supplied oxygen calculated from GIXRD measurements. For PVD, the oxygen supply was controlled via oxygen flow (sccm) whereas in ALD through the duration of the ozone dose pulse. The dashed lines are only meant as a guide for the reader. Taken with permission from [86].

amount of detected C both in PVD and ALD layers were previously displayed in Fig. 4.16 a). As already reported both in this work and in the literature [239], C impurities can help the stabilization of the t-phase over the m- and the o-phase both by acting as a dopant and by limiting grain growth and therefore triggering surface/volume energy contributions.

Another difference in crystallization can be observed in as-deposited PVD and ALD films. As reported by Mittmann et al. in [236], PVD films were often already crystalline right after deposition, despite the latter taking place at room temperature, likely because of the elevated plasma power used during deposition. This was mostly the case for samples deposited in oxygen-rich atmospheres, which crystallized in fact in the m-phase. The subsequent RTA managed to transform the amorphous layers into mostly orthorhombic films, whereas the ones which were already highly monoclinic after deposition stayed in the m-phase also after the annealing treatment.

Figure 4.25 shows remanent polarization values for both ALD and PVD films as a function of supplied oxygen. For both deposition methods, the stabilization of the polar orthorhombic phase and the tetragonal phase results in non-zero remanent polarization values, with a maximum at around 0.5 sccm oxygen flow and 1 s ozone dose times for PVD and ALD, respectively. In both cases, P_r values of around 10-15 $\mu C/cm^2$ were measured.

Mittmann et al. also deposited a matrix of $Hf_xZr_{1-x}O_2$ layers by concurrently tuning oxygen and Zr content during deposition [79]. Once again, increased oxygen flows seemed to trigger the stabilization of the m-phase, independent from Hf:Zr ratio. Nonetheless, contrarily to what was observed in ALD, high ZrO_2 contents encouraged the stabilization of the m-phase, as well. This difference was attributed to the higher reactivity of the HfO_2 target with oxygen, compared to the

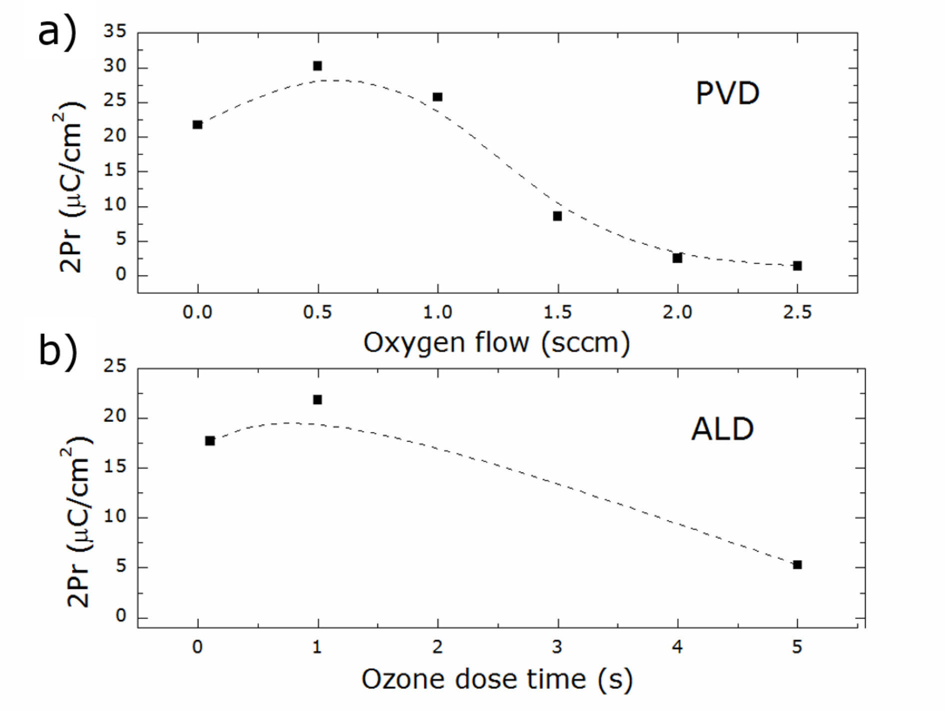

Figure 4.25: Remanent polarization values $2P_r$ for undoped HfO_2 layers deposited via a) sputtering and b) ALD as a function of supplied oxygen calculated from GIXRD measurements. For PVD, the oxygen supply was controlled via oxygen flow (sccm) whereas in ALD through the duration of the ozone dose pulse. The dashed lines are only meant as a guide for the reader. Taken with permission from [86].

ZrO_2 target. A lower reaction rate, similarly to low deposition rates, could mean that more oxygen interstitials are incorporated during deposition.

4.7 Summary

In this chapter, an overview of the main parameters playing a role during ALD deposition of $Hf_xZr_{1-x}O_2$ thin films was supplied. First, a comparison between different metal precursor molecules was shown. Structural and electrical properties of capacitors based on $Hf_xZr_{1-x}O_2$ thin films were characterized and compared for different precursor combinations and Hf:Zr ratios. After that, the effect of chamber temperature during deposition on the layer crystallization pathway was addressed. Zirconium and oxygen contents were afterward concurrently tuned through Hf:Zr cycle ratio and dose time, respectively. It was shown how both the main structural and ferroelectric properties and the reliability performances of FeCap devices strongly depend on these two parameters. An opposite trend was reported for the progressive increase in Zr and oxygen content in the deposited layers. In general, high remanent polarization values corresponded to strongly stabilized polar orthorhombic phase and were accompanied by enhanced reliability properties in terms of retention, endurance and wake-up. The results regarding ALD were finally compared to measurements on sputtered $Hf_xZr_{1-x}O_2$ thin films. Common trends were highlighted and the physics behind the two processes was used to explain the observed differences. Despite the overall results between the two techniques being similar, a higher thermal budget is needed for the crystallization of PVD-deposited films in the ferroelectric o-phase, making ALD the technique of choice for BEOL applications.

An optimized process can be extrapolated by combining the results of this chapter. A 1:1 Hf:Zr ratio was picked to be used within this work. For standard $Hf_{0.5}Zr_{0.5}O_2$ used in the next chapters, TEMAHf and ZyALD were used as the metal precursors and ozone was supplied through 1 s long dose steps. The deposition process took place at 280°C. A post metallization annealing treatment was performed at 600 °C.

5 Effect of electrodes on device performance

Hafnia-based ferroelectric capacitors are most commonly sandwiched between two TiN electrodes. Nonetheless, different electrode materials have been tested and performances have been compared with standard TiN, ranging from metal nitride electrodes like TaN, semiconductors such as Si and Ge, pure metals like W, Pt, Ru, Ir and their metal oxides such as IrO_2 and RuO_2.

In the work of Park et al. [241], a comparison between standard TiN and Pt bottom electrodes can be found. According to their study, TiN BEs seem to promote high tensile stress along the c-axis of the t-phase, which results in enhanced ferroelectricity. A similar finding is reported in the work of Cao et al. [242], who deployed Pt as the TE, along with Pd, Au, W, Al and Ta, and kept TiN as the bottom electrode. Different thermal expansion coefficient mismatches were measured between HfO_2 and the used electrode materials, which caused a different amount of stress in the ferroelectric layer. Among the used TE materials, W yielded the highest remanent polarization, followed by TiN and then by Pt ($2P_r$ = 32.7, 36.9 and 38.7 μC/cm^2 for Pt, TiN and W top electrode, respectively). W seemed to be advantageous not only because of stress-tuning but also because of the suppression of the formation of a parasitic dead layer between the BE and the ferroelectric layer. The latter is most likely formed during the HfO_2 deposition process or because of exposure of the BE to the atmosphere between the different processing steps. Lee et al [243] compared W to Ni, TiN and Mo. Capacitor stacks including a W BE showed limited oxidized layer formation and the best ferroelectric properties. Similar findings were reported by Karbasian et al. [244], where W demonstrated superior properties as compared to TiN.

The formation of an oxidized interface also emerges in the case of semiconductor-based electrodes. Lomenzo et al. [245] compared the performances of two capacitor stacks based on Si:HfO_2 deposited either on p+ Ge or p+ Si and reported a lower dead layer thickness in the case of Ge. Therefore, they proposed p+ Ge as a good candidate to replace Si as the substrate material in FeFETs.

From the knowledge acquired from traditional PZT, oxide materials seemed to bring the advantage of suppressing oxygen vacancies formation when used as electrode materials. This resulted in lower defectivity and consequently in strong improvements in device reliability [246], [247]. For this reason, Ir, Ru and their respective oxides IrO_2 and RuO_2 were also scanned as electrode materials for FeCaps based on fluorite ferroelectrics. Unfortunately, the findings were not reproducible for this class of materials. In the work of Park et al. [248], a IrO_x parasitic interface was formed when Ir was used as bottom electrode material, probably due to exposure to the atmosphere between the electrode and the ferroelectric oxide deposition. According to their hypothesis, this led to the stabilization of the m-phase and the consequent deterioration of the ferroelectric properties because of the formation of bigger grains. The polar orthorhombic phase was only successfully stabilized for low $Hf_{0.5}Zr_{0.5}O_2$ film thicknesses. Mittmann et al. [151] deposited symmetrical FeCaps, where IrO_2 served both as TE and BE. Again the oxide electrode rather harmed capacitor performances, conversely from what was observed in PZT. The additional oxygen provided from the oxide electrode seemed to de-stabilize the polar o-phase in favor of the non-polar m-phase. An analogous degradation was observed by Park et al. [109] when deploying RuO_2 as electrode material for $Hf_{0.5}Zr_{0.5}O_2$–based FeCaps. This material seems to be instead promising when looking at the recent work by Goh et al. [150], [249]: the use of RuO_2 instead of TiN as electrode material yielded a decrease in the thickness of the non-polar interface between ferroelectric and electrode. This proved particularly advantageous when RuO_2 was deployed as the top electrode. The results were supported by XPS measurements, which detected a reduced amount of oxygen vacancies in the oxide electrode-based capacitors, supplying an explanation for the improved device reliability. Also Ru in its elemental state showed low reactivity with $Hf_{0.5}Zr_{0.5}O_2$ in the work of Cao et al. [250], resulting in better device performance of Ru/$Hf_{0.5}Zr_{0.5}O_2$/Ru capacitors as compared to TiN/$Hf_{0.5}Zr_{0.5}O_2$/TiN ones, with great reliability advantages especially in terms of reduced leakage current and increased number of field cycles before device hard breakdown.

In general, the choice of the electrode material affects the stacks both from a chemical and an electrical point of view. Depending on the chosen material, a more or less pronounced formation of a parasitic interface with the HfO_2-based layer is observed, which often results in different stress/strain and surface energy contributions induced by temperature-dependent expansion coefficient and lattice mismatches between the ferroelectric oxide and the electrode [138], [251]. Both factors can influence the defectivity of the oxide, the amount of oxygen i.e. of oxygen vacancies in the electrode proximity, the size of the grains and ultimately the crystalline phase of the ferroelectric layer. Furthermore, depending on the work function (WF) value of the two electrodes and/or of the created interfacial layer, an internal bias field can arise which manifests itself in the shift of the ferroelectric hysteresis in one or the other voltage direction. Last but not least, depending on the band alignment between the ferroelectric and the electrode materials, charge injection can take place. Injected charge from the electrode into the ferroelectric can also be trapped at defect sites at the interface. All the aforementioned phenomena still represent big reliability challenges for device applications.

In this chapter, first, the effect of electrode materials with different work functions will be elucidated. A nitride, an oxide and a metal electrode will be chosen and compared to the most common TiN electrodes. Afterward, a more global comparison will be carried out. The influence of the material choice on device reliability will be addressed. Finally, device applications will be suggested which could exploit the above-mentioned hysteresis shift.

5.1 Work function of electrode materials

Knowing the work function ϕ_m of the electrode material is of fundamental importance since, together with the electron affinity of the ferroelectric oxide χ_e, it determines the conduction band offset CBO between the two materials and therefore influences the conduction mechanisms (see Fig. 5.1). Nonetheless, dipoles, defects and trap states with energy levels within the insulator band-gap could influence the barrier through pinning of the Fermi level of the metal to the charge-neutral level of the insulator. Such features could depend on both the ferroelectric layer and the electrode defectivity and their interaction. Charge injection is also affected by the CBO between the ferroelectric and the electrode, with the phenomena being encouraged for lower CBOs i.e. in materials with a lower work function. Everything considered it is evident how an appropriate understanding and fine-tuning of the processing is necessary to achieve the wished band alignment and control device behavior.

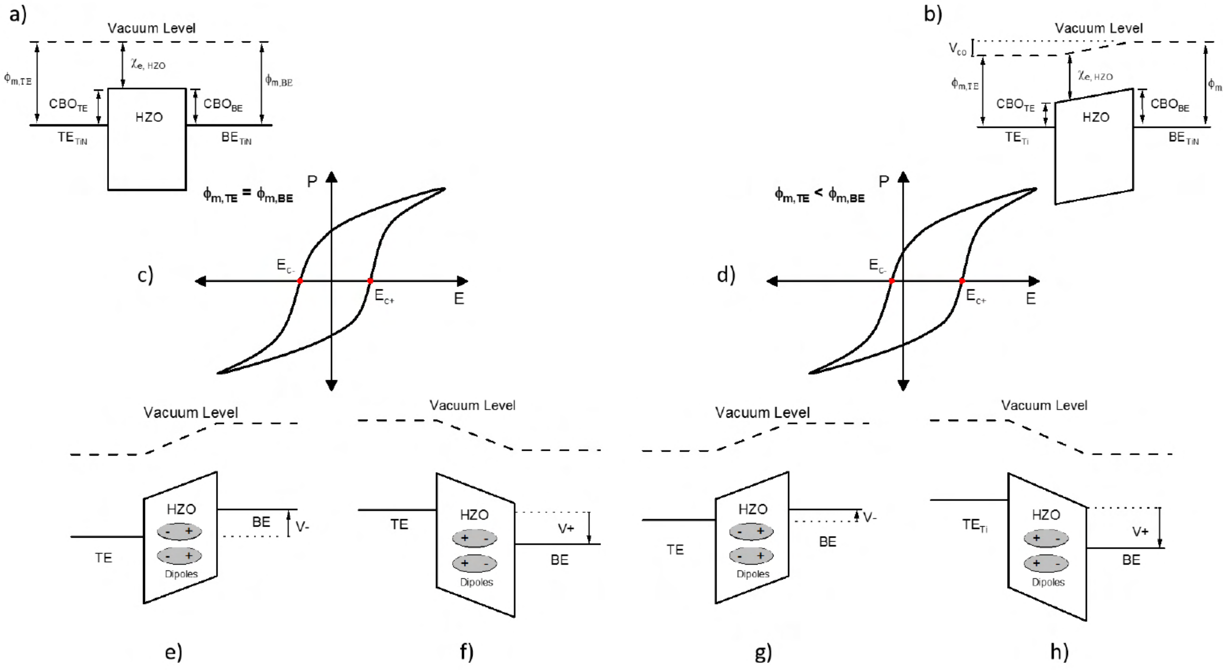

Figure 5.1: Energy band diagrams for a) a capacitor stack with symmetrical electrodes showing the same WF and b) one with asymmetrical electrodes showing different WF. c) and d) show the measured ferroelectric hysteresis for the cases displayed in a) and b). A shift in the FE-loop along the voltage axis is observed when a WF difference is present. e), f), g) and h) schematize the band diagrams for cases a) and b) when a negative (e), g)) or a positive (f) and h)) internal bias is included. Picture taken from [252].

An asymmetrical stack with two different materials employed as top and bottom electrodes, respectively, will show a ferroelectric hysteresis that is not centered with respect to the polarization axis. As shown in figure 5.1, the work function difference between the two electrode materials generates an internal bias field within the stack which provokes a rigid shift of the hysteresis along the voltage axis. This means the ferroelectric will require a different absolute field to be switched in the two opposite polarity directions.

Depending on the two WF of the two electrodes, a shift either in the positive or in the negative direction will be observed. As an example, if the external voltage is supplied at the top electrode and if TiN is used as the bottom electrode, a rigid shift in the positive voltage direction will be expected for all materials presenting a higher WF than TiN. Conversely, a shift in the negative voltage direction is presumed if the TE material has a lower work function compared to TiN or if the TE and the BE are swapped.

This effect is also detected in symmetrical stacks where the same electrode material is differently oxidized depending on its processing history. Interestingly, it was exploited by Pešić et al. [253], which demonstrated the concept of antiferroelectric RAM by intentionally shifting the antiferroelectric-like double looped hysteresis until a finite remanent polarization was obtained through the centering of one of the two sub-loops. This application will be discussed more in detail in the last section of this paragraph.

Table 5.1: Work function of various electrode materials (on HfO_2/ZrO_2). Values were calculated within this work by assuming a WF of 4.7 for TiN at BE. A different stoichiometry can be observed for the same material depending on its positioning within the capacitor stack (i.e. TE or BE), resulting in different WF values.

Material	Work function at BE (eV)	Work function at TE (eV)
TiN	4.7	4.5
TiAlN	4.5 (± 0.2)	4.5 (± 0.2)
Nb	4.1	4.1
MoO_x	4.7	5
RuOx	5.5	5.5
W	4.7	4.7
NbN	5.3	4.7

The work function of different materials on HfO_2 (i.e. on ZrO_2) can be calculated by using different methods, such as X-ray photoelectron spectroscopy, hard X-ray photoelectron spectroscopy and internal photoemission spectroscopy. Table 5.1 summarizes some of the values extracted within this work by calculating the ferroelectric hysteresis shift of asymmetric $TiN/Hf_{0.5}Zr_{0.5}O_2/x$ or $x/Hf_{0.5}Zr_{0.5}O_2/TiN$ stacks, where x is an alternative electrode material and a work function of 4.5 or 4.7 eV is assumed for TiN as a top and a bottom electrode, respectively. The electrodes were approximately 10 nm thick and all capacitor stacks were annealed at a temperature of 600 °C in nitrogen after top electrode deposition. The difference in work function shown by TiN when employed as TE or BE is originating from the different oxidation states of the layer depending on annealing and deposition conditions, as already discussed above and in the literature [131], [140]. The work function values for other electrode materials can be found elsewhere [254].

5.2 Nitride electrodes: the case of TiAlN

As previously mentioned, a shift in the ferroelectric hysteresis can be detected even in stacks where the same material is used both as top and bottom electrodes. This is related to the fact that the electrode material can be differently oxidized depending on the processing it underwent [255]. For example, it was shown that TiN presents different oxidation at the top and at the bottom of a capacitor based on hafnia [110], [140]. Different processing steps are responsible for this result:

- first of all, the TiN bottom electrode is often exposed to the atmosphere before the HfO_2 layer is deposited. This can lead to a more or less pronounced surface oxidation;
- subsequently, the TiN BE layer is exposed to an oxygen-containing atmosphere during the deposition of the HfO_2 layer itself. This can provoke further surface oxidation;
- Finally, the complete structure including TE, ferroelectric layer and BE is often thermally treated to induce crystallization of the hafnia-based layer. During annealing, oxygen is scavenged from the oxide layer towards the TiN. The result of this last processing step is the formation of a parasitic TiON layer between HfO_2 and TiN. If a surface oxide layer is already present (as in the case of TiN BE), the driving force for oxygen scavenging will be lower, leading to a thinner parasitic TiON layer and to a lower amount of oxygen vacancies in the vicinity of the BE as compared to the TE.

The result of the different oxidation state of the two electrodes i.e. the presence of a parasitic oxidized layer at one of the two interfaces is a different band alignment and consequently an internal bias field that rigidly shifts the ferroelectric loop in one voltage direction.

To accurately study this effect, Al was gradually added to the TiN top electrode by introducing and increasing the Al power during sputtering. Al has a lower work function compared to TiN. An increased Al power during deposition should therefore lower the total work function of the TiAlN electrodes. Al powers of 100, 150 and 200 W were used. In the next paragraphs, the effects of the gradual Al inclusion into the top TiN electrodes will be presented through structural and electrical characterization. A comparison of the effect of thermal treatment on stacks including TiN and TiAlN was also carried out utilizing standard ferroelectric measurements and results will hereby follow.

5.2.1 Structural analysis and crystalline phase deconvolution

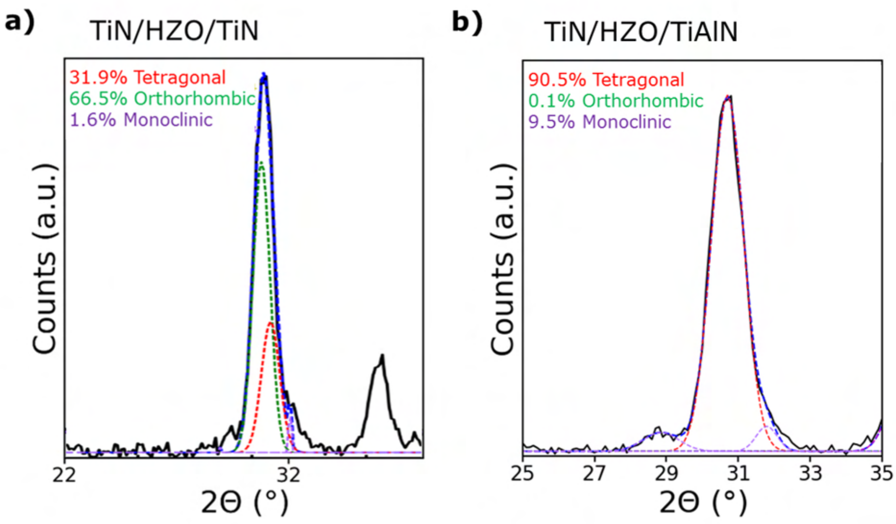

Figure 5.2: Phase deconvolution of the GIXRD spectra of a a) TiN/HZO/TiN and b) a TiN/HZO/TiAlN capacitor stack according to the procedure explained in chapter 3.

GIXRD patterns were measured for two $Hf_{0.5}Zr_{0.5}O_2$-based ferroelectric capacitors having TiN as bottom electrode and TiN or TiAlN deposited with 150 W Al power as top electrode. The measured spectra are displayed in figure 5.2 a) and b), respectively, together with a gaussian fitting of the data (see chapter 2 for details on the fitting procedure). According to the structural measurements, a negligible difference in phase composition is observed for the two analyzed capacitor stacks, which both only show the main o-/t- peak and almost no crystallization in the m-phase.

According to these results, the introduction of Al into the standard TiN electrode does not seem to affect the crystallization path of the ferroelectric oxide. In the next sections, electrical results will nonetheless show clear differences between the two stacks. The formation of a parasitic interface between electrode and oxide will be suggested as an explanation for the observed trends.

5.2.2 Hysteresis shift and field cycling behavior

Figure 5.3 shows the P-V (a),c)) and I-V (b), d)) curves of woken-up capacitors for TiAlN electrodes deposited prior to the thermal treatment (a), b)) and for capacitors where the annealing was performed first with a standard TiN TE which was subsequently etched via SC1 and replaced by a TiAlN TE (c), d)).

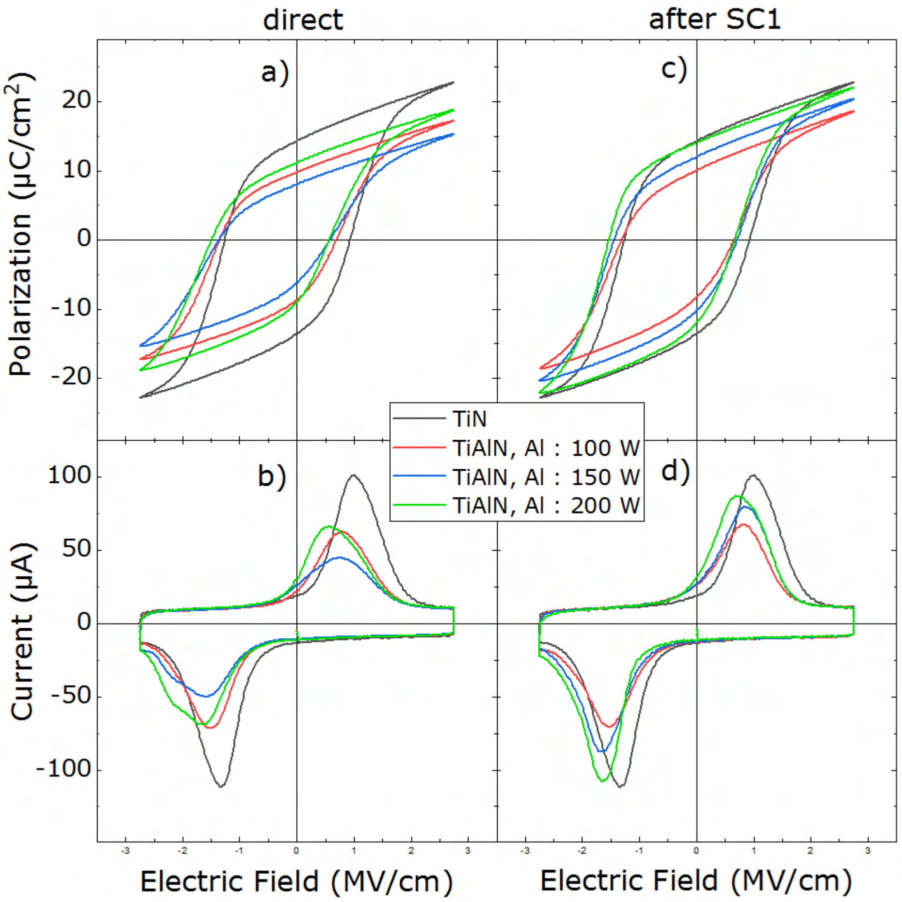

Figure 5.3: P-V (a),c)) and I-V (b), d)) curves of woken-up capacitors for TiAlN electrodes deposited prior to the thermal treatment (a), b)) and for capacitors where the annealing was performed first with a standard TiN TE which was subsequently replaced by a TiAlN TE (c), d)). A shift of the P-V and I-V curves in the negative voltage direction can be observed as the Al sputtering power is increased from 0 (TiN) to 200 W.

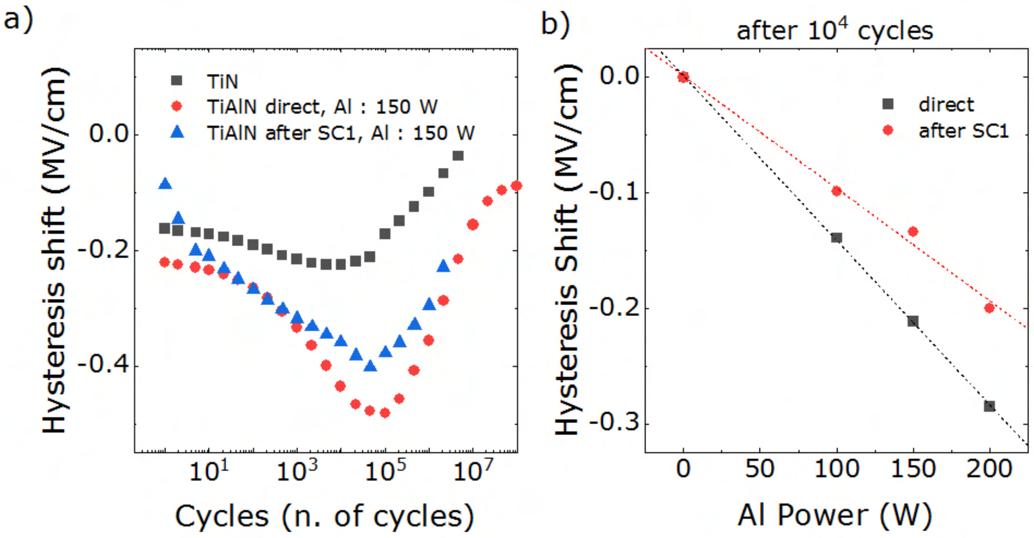

Figure 5.4: a) Hysteresis shift as a function of the number of applied field cycles for HZO-based FeCaps with TiN as BE and TiN or TiAlN as TE; b) Hysteresis shift after 10^4 cycles as a function of Al power used for TiAlN sputtering for woken-up TiN/HZO/TiAlN stacks.

As shown in the figure, the ferroelectric hysteresis presents a shift towards the negative voltage direction as Al is introduced into the top electrode, coherently with the lowering of its work function. For woken-up devices, a direct correlation between Al power and coercive field change is detected, as shown in figure 5.4 b). Unfortunately, figure 5.4 a) shows this is not valid along the complete device lifetime. In fact, almost no shift is observed in the pristine state. The hysteresis displacement becomes more and more relevant as the number of cycles increases. In the case of direct deposition of the TiAlN electrode prior to annealing, the hysteresis shift is accompanied by a reduction in remanent polarization and by a broadening of the switching peaks (figures 5.3 a), b)). This can be attributed to the formation of an interface layer between the TE and the ferroelectric layer during the thermal treatment, which screens the applied external field or supplies a stronger depolarization field. In order to prevent this, another set of samples was deposited which was first annealed with a standard TiN TE. The latter was subsequently removed via SC1 and replaced with the desired TiAlN. For this second structure type, only a minor reduction in remanent polarization was detected along with the coercive field change.

10 nm thick $Hf_{0.5}Zr_{0.5}O_2$ ferroelectric capacitors with TiN BE and TiAlN TE were cycled with a field of ± 3 MV/cm. Figure 5.5 a) and c) show the behavior of the positive and negative P_r with respect to the number of field cycles the device was subjected to for different used Al powers. A sensible reduction in P_r is encountered with respect to symmetrical $TiN/Hf_{0.5}Zr_{0.5}O_2/TiN$ devices for all used Al powers in the case of direct TiAlN deposition. Furthermore, strong fatigue is encountered after 10^4 cycles. No clear trend with Al power can be detected. All samples show an improvement in the number of cycles before hard breakdown i.e. a higher endurance. This can be caused both by the lower remanent polarization and by sub-cycling if part of the applied external field is screened at the oxidized parasitic interface.

By first depositing TiN, annealing the structure and subsequently replacing TiN with TiAlN, most of the remanent polarization is recovered and the fatigue behavior is also improved. Nonetheless, the advantages in endurance are lost (see figure 5.5 c)).

To support the hypothesis attributing the lowering in P_r to the creation of an interface generating a depolarization field, the relaxed remanent polarization was investigated, i.e. the amount of remanent polarization retained one second after application of the switching field. As shown in figure 5.5 b) and d), a strong degradation in the relaxed remanent polarization is observed for the negative voltage direction. The effect is particularly strong for the cycling stage corresponding to the onset of fatigue, corroborating the hypothesis according to which fatigue and retention degradation could both be triggered by depolarization fields. The effect seems attenuated when the TiAlN electrode is deposited after SC1 removal of the TiN TE, confirming the formation of a thicker parasitic interface in capacitors annealed with TiAlN TE.

X-Ray photoelectron spectroscopy measurements were performed by collaborators before and after the removal via SC1 of the TiN top electrode. The capacitor had been annealed before SC1. Figure 5.6 shows the results for the Hf 4f (a), d)), the Ti 2p (b), e)) and the N 1s (c)), f)) peaks before

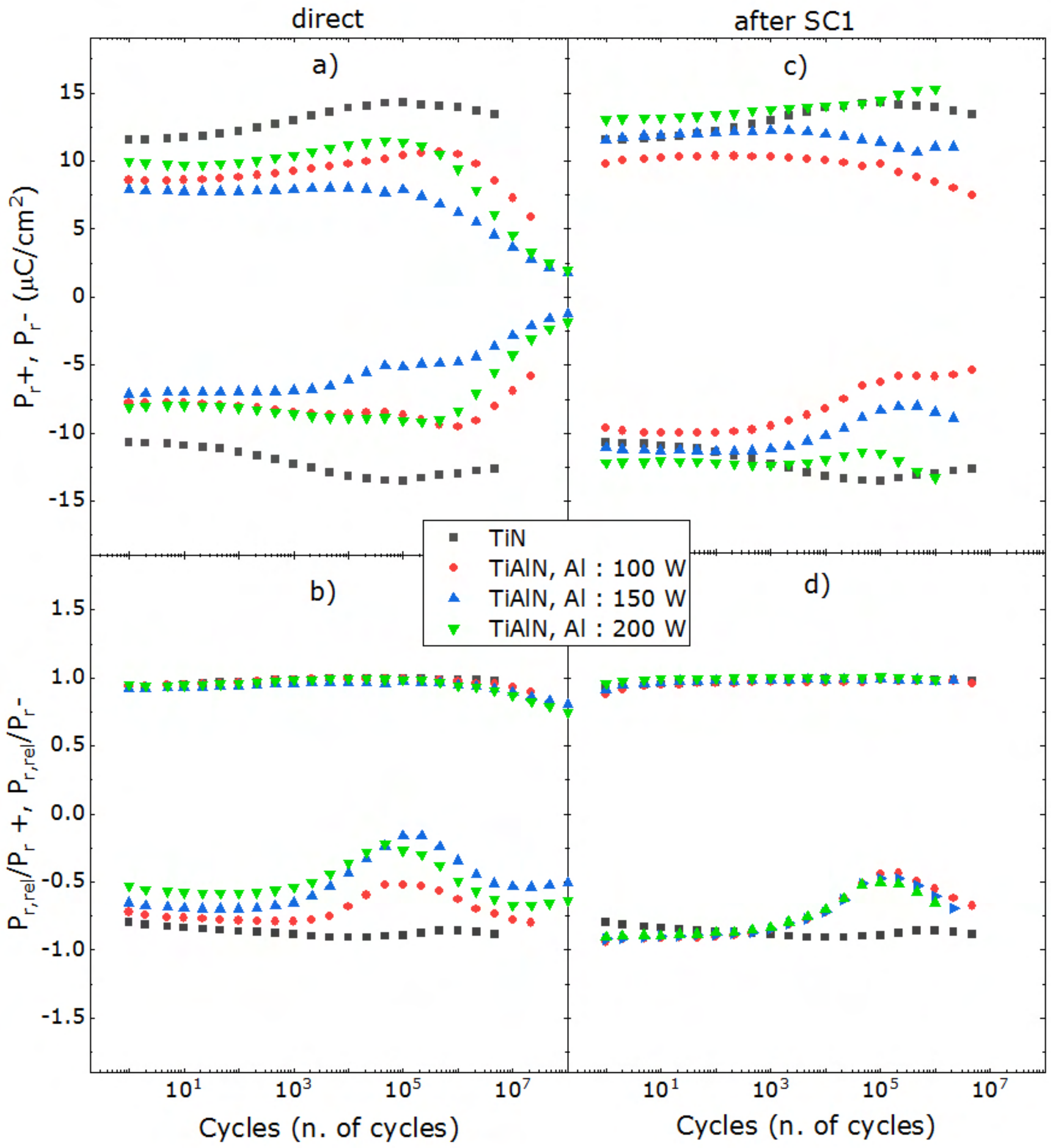

Figure 5.5: Positive and negative P_r (a),c)) and $P_{r,rel}/P_r$ (b), d)) with respect to field cycling for ferroelectric capacitors with TiN BE and TiAlN TEs deposited prior to the thermal treatment (a), b)) and for capacitors where the annealing was performed first with a standard TiN TE which was subsequently replaced by a TiAlN TE (c), d)). A stronger fatigue and a degradation in relaxed remanent polarization $P_{r,rel}$ is observed for capacitors with TiAlN TE with respect to those with TiN TE. The effect is improved when TiAlN is deposited after thermal treatment.

(a), b), c)) and after (d), e), f)) SC1 wet etching. By comparing the top and the bottom row of the figure i.e. the results before and after SC1, the following conclusions can be drawn: the Hf 4f peak remains unchanged, meaning the HfO_2 layer is not affected by the wet etching; the N 1s peak completely disappears, proving the effective removal of the TiN layer; the peaks at the binding energies associated to TiON and TiN also disappear; the TiO_2 peak decreases in intensity and shifts to higher binding energies, confirming the presence of a parasitic oxidized interface between the TE and the HfO_2 layer which is partially but not completely removed through the SC1 procedure.

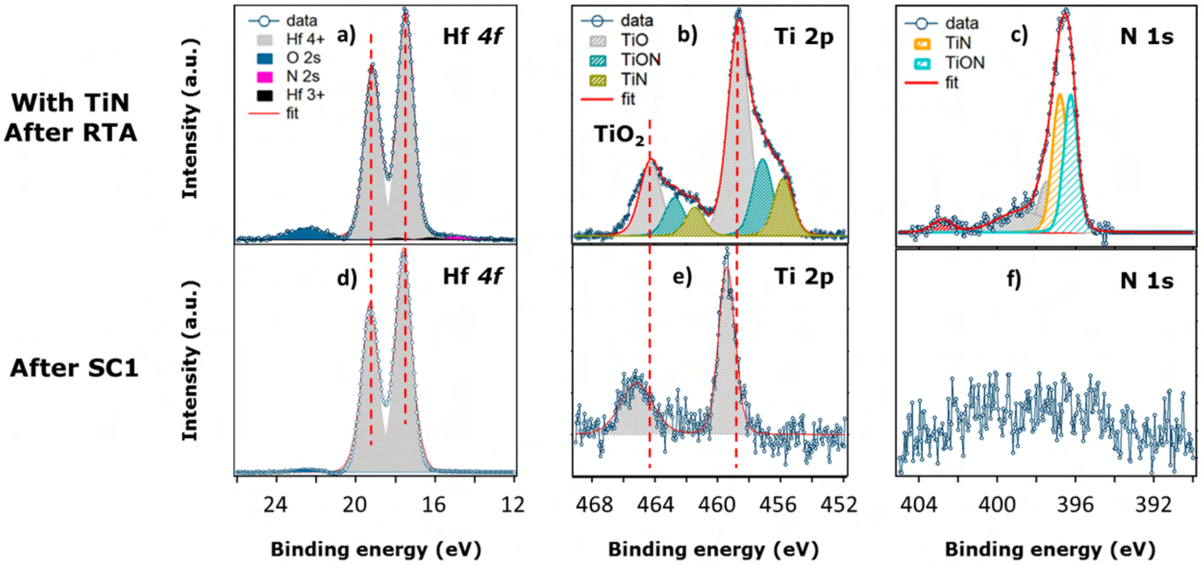

Figure 5.6: XPS measurements of a TiN/$Hf_{0.5}Zr_{0.5}O_2$/TiN capacitor annealed at 600°C for 20 s in N_2. The Hf 4f (a), d)), the Ti 2p (b), e)) and the N 1s (c)), f)) peaks before (a), b), c)) and after (d), e), f)) SC1 wet etching are shown.

5.2.3 Retention and imprint

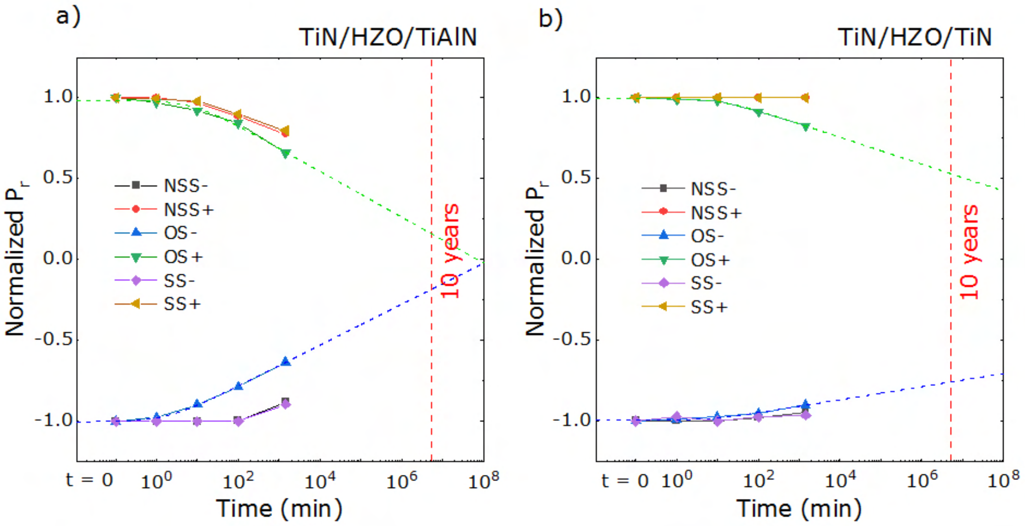

Figure 5.7: Positive an negative same state (SS+, SS-), new same state (NSS+, NSS-) and opposite state (OS+, OS-) retention measured at 85 °C for ferroelectric capacitors based on a 10 nm $Hf_{0.5}Zr_{0.5}O_2$ film sandwiched between a) TiN BE and TiAlN TE and b) TiN BE and TiN TE. The OS retention shows the strongest reduction and was therefore extrapolated for 10 years operation in order to benchmark device degradation.

Retention measurements were performed on capacitor stacks and results were compared for asymmetrical TiN/$Hf_{0.5}Zr_{0.5}O_2$/TiAlN (direct deposition) and symmetrical TiN/$Hf_{0.5}Zr_{0.5}O_2$/TiN capacitors (figures 5.7a) and b), respectively). The retained remanent polarization for the opposite state was fitted using a power law as described in chapter 3. For capacitors with TiAlN as the top electrode, half of the OS+ and OS- remanent polarization is lost after only 10^4 min baking time. Eventually, the positive and negative state coincide and become almost indistinguishable at the 10 years limit. Better behavior is reported for the symmetrical stacks, where more than 50% of the remanent polarization is retained up to 10 years. Additionally, the TiN/TiAlN stack shows degradation also for the SS and the NSS states, whose polarization is instead very good retained in symmetrical, TiN-based FeCaps.

These observations can be correlated to a shift of the ferroelectric hysteresis loop in the negative voltage direction observed by replacing the TiN TE with a TiAlN TE. In fact, for this reason, some of the domains which show a coercive field that is higher than the supply voltage could be excluded from the switching process. This phenomenon gets worse during baking, as a consequence of the imprint caused by leaving the capacitor in a certain polarization state for a long time and at a high temperature, summing up to the already present shift caused by the work function difference.

In summary, the use of TiAlN electrodes instead of TiN seems not to be advantageous for device performance. The growth of a thick interface between the ferroelectric oxide and the electrode material is hypothesized as the main cause for ferroelectric properties and reliability degradation, as confirmed from the XPS results and the differences between TiAlN deposition prior or post thermal treatment. GIXRD measurements showed negligible differences for HZO layers sandwiched between two TiN electrodes and a TiN and a TiAlN one, hinting at a similar amount of oxygen vacancies in the ferroelectric layers. This was coherent with the similar behavior with respect to field cycling demonstrated by the capacitors where the TiAlN electrode was deposit post thermal treatment i.e. including a thinner additional parasitic interface. Depolarization fields caused by the latter are considered responsible for the strong polarization relaxation and retention loss in the case of annealing of FeCap with TiAlN TE.

5.3 Oxide electrodes: the case of MoO_x

In this section, structural and electrical characterization of devices where MoO_x was deployed either as bottom or as top electrode will be presented and compared to the traditional symmetrical TiN/HZO/TiN capacitors. MoO_x has a higher work function as compared to TiN, as already discussed with the help of table 5.1.

5.3.1 Structural analysis and crystalline phase deconvolution

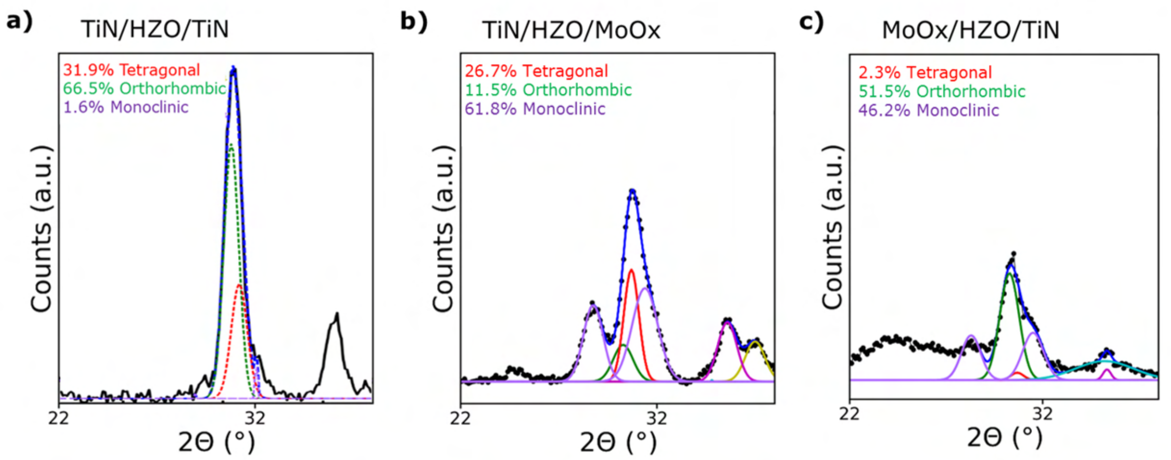

Figure 5.8: Phase deconvolution of the GIXRD spectra of a a) TiN/HZO/TiN, b) a TiN/HZO/MoO$_x$ and c) a MoO$_x$/HZO/TiN capacitor stack according to the procedure explained in chapter 3.

Figure 5.8 shows the GIXRD patterns measured for $Hf_{0.5}Zr_{0.5}O_2$ films sandwiched between a) two symmetrical TiN electrodes, b) a TiN BE and a MoO$_x$ TE and c) a MoO$_x$ BE and a TiN TE. By comparing the patterns, it is evident how the presence of an oxide electrode as MoO$_x$ tends to promote the formation of the monoclinic phase. This is valid for MoO$_x$ used both as BE and TE. An explanation foe this is the reduced driving force for oxygen scavenging from the ferroelectric layer into the oxide electrode, given the already oxidized surface of the latter [248]. This translates into a lower amount of oxygen vacancies and hinders the stabilization of the o-phase, along with what was observed in chapter 4. The presence of MoO$_x$ nanocrystallites is witnessed by the appearance of a peak at $2\theta \sim 25$ ° [256].

5.3.2 Hysteresis shift and field cycling behavior

The deposited capacitor stacks including MoO$_x$ either as bottom or as top electrode were cycled with a field of ± 3 MV/cm as explained in chapter 3. Remanent polarization values together with rigid hysteresis shift were monitored along device lifetime and results are reported in figure 5.9 a) and b) for the two parameters, respectively. 2P$_r$ values look rather similar as compared to the symmetrical TiN/HZO/TiN stack, except for the FeCap with W as BE and MoO$_x$ as TE. This fluctuation could also be related to the use of W rather than to MoO$_x$. A slight reduction in the number of cycles before device breakdown was detected for stacks with MoO$_x$ as the top electrode. In general, an improvement in the wake-up behavior, with a reduced difference between pristine and woken-up remanent polarization can be observed as compared to the standard TiN/TiN stack. The increased oxygen content provided by the usage of an oxide electrode could suppress oxygen

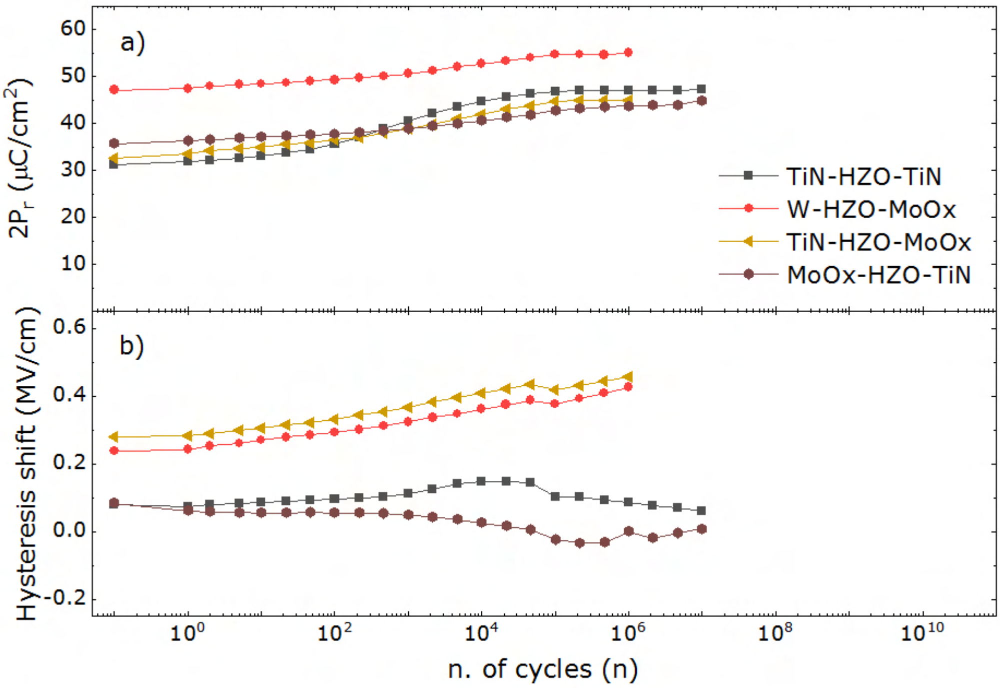

Figure 5.9: a) 2P$_r$ and b) hysteresis shift as a function of the number of applied field cycles for $Hf_{0.5}Zr_{0.5}O_2$ (HZO)-based capacitor stacks with different top and bottom electrode combinations including MoO_x and a reference TiN/HZO/TiN FeCap.

scavenging and oxygen vacancy formation, limiting wake-up either through t-phase suppression or because of reduced oxygen defects redistribution.

By looking at the rigid hysteresis displacement along the voltage axis, a shift of 0.3 MV/cm in the positive direction is observed for the FeCaps deploying MoO_x as TE. By assuming a WF of around 4.7 eV for the TiN and the W bottom electrode, a WF of around 5 eV is estimated for MoO_x as TE. Values were already reported in table 5.1. Conversely, almost no difference in hysteresis position was detected for the two-layer stacks with TiN as the top electrode. A reduction in the WF values of MoO_x after exposure to air was already reported in the literature [257] and could be responsible for the very similar hysteresis shift observed for the MoO_x/HZO/TiN and the symmetrical TiN/HZO/TiN stacks.

5.3.3 Retention and imprint

The retention behavior at 85 °C for a TiN/$Hf_{0.5}Zr_{0.5}O_2$/MoO_x ferroelectric capacitor was measured and compared to the one of a standard, TiN-based FeCap. Figure 5.10 shows the experimental results, together with an extrapolation to 10 years device working time. Coherently with the comparable behavior observed with respect to field cycling, only a slight degradation is observed when the TiN top electrode is replaced with a MoO_x one. The behavior can be explained as follows:

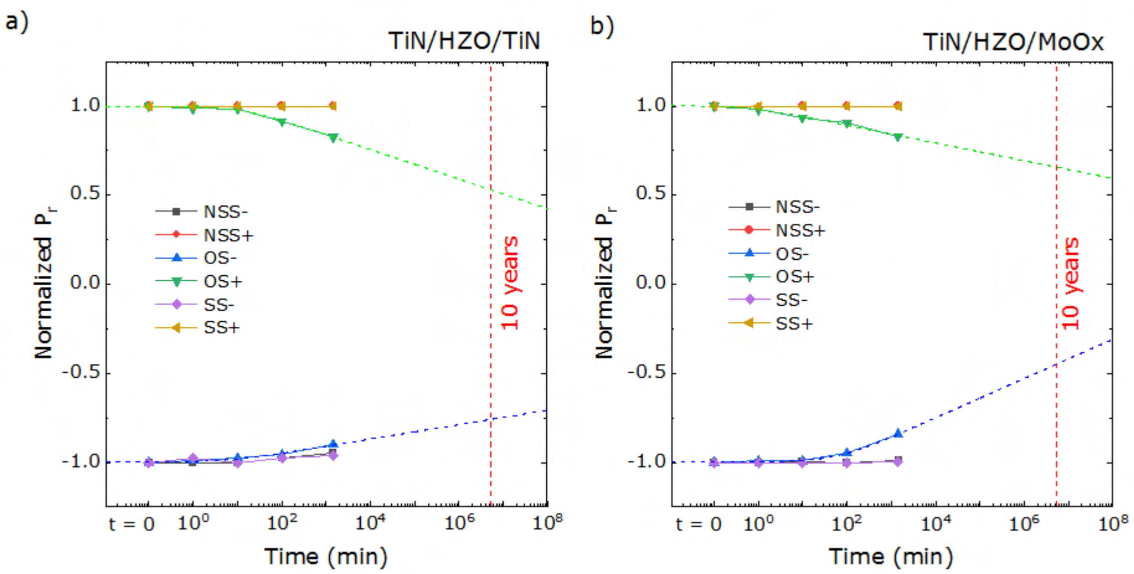

Figure 5.10: Positive and negative same state (SS+, SS-), new same state (NSS+, NSS-) and opposite state (OS+, OS-) retention measured at 85 °C for ferroelectric capacitors based on a 10 nm $Hf_{0.5}Zr_{0.5}O_2$ film sandwiched between a) TiN BE and TiN TE and b) TiN BE and MoO_x TE. The OS retention shows the strongest reduction and was therefore extrapolated for 10 years operation in order to benchmark device degradation.

first of all, the additional oxygen supplied by the oxide electrode suppresses the formation of oxygen vacancies. Furthermore, no hysteresis shift was observed between the two capacitor stacks, as shown in figure 5.9, meaning the two electrode materials present a similar work function and conduction band offset when in contact with the ferroelectric oxide. Therefore, the two mechanisms which are considered responsible for imprint and retention degradation i.e. oxygen vacancy redistribution and charge injection through the electrode can be considered to act similarly for the two presented cases.

In general, the deployment of a MoO_x electrode does not seem to be advantageous for HfO_2-based ferroelectric capacitors. The additional oxygen provided by the oxide electrode suppresses the formation of oxygen vacancies and induces the stabilization of the monoclinic phase. On the other hand, being the electrode material already oxidized, no parasitic interface formation is expected. The work function of MoO_x seems to depend on the position of the material in the capacitor stack, resulting in a strong hysteresis displacement of ~ 0.3 MV/cm only in the cases where MoO_x was used as TE material. The reduced wake-up observed as compared to TiN can be correlated to the lower amount of V_O. A slight degradation in the endurance and the retention behavior for MoO_x containing FeCaps, likely induced by the higher m-phase content, make TiN a more advantageous option.

5.4 Metal electrodes: the case of W

As a final example, W will be considered as a pure metal electrode in comparison with standard TiN. As reported in table 5.1, a zero hysteresis shift for asymmetrical stacks containing W and TiN as electrode materials was observed, implying a zero work function difference between the two materials. Below, first structural and then electrical measurements on such stacks will be presented and the differences between the two materials will be elucidated.

5.4.1 Structural analysis and crystalline phase deconvolution

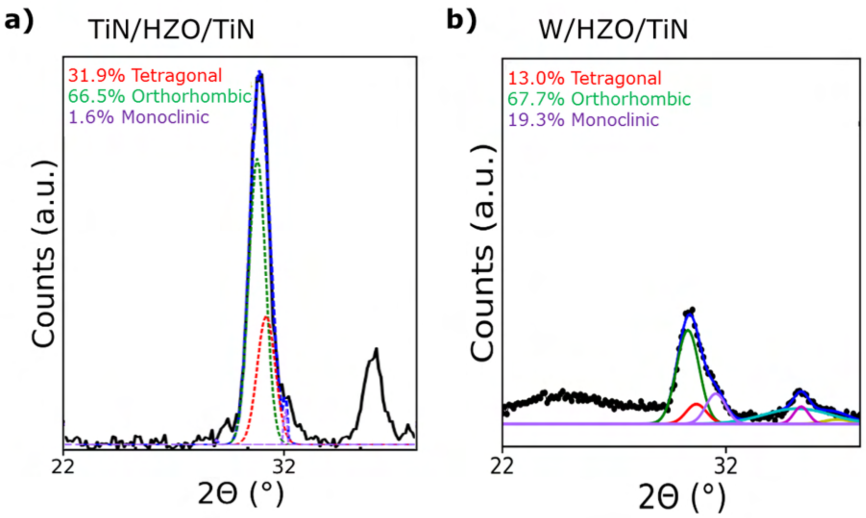

Figure 5.11: Phase deconvolution of the GIXRD spectra of a a) TiN/HZO/TiN, b) a TiN/HZO/MoO_x and c) a MoO_x/HZO/TiN capacitor stack according to the procedure explained in chapter 3.

Figure 5.11 reports the structural measurements performed via GIXRD for an a) TiN/$Hf_{0.5}Zr_{0.5}O_2$/TiN and a W/$Hf_{0.5}Zr_{0.5}O_2$/TiN capacitor stacks. For the case of the W bottom electrode, phase deconvolution suggests a stronger stabilization of the orthorhombic polar phase, together with some tetragonal and monoclinic phase portions. This result could hint at a higher oxygen content i.e. suppressed V_o formation when a W bottom electrode is deployed. The formation of a WO_{3-x} interface between W and HZO either during exposure to the atmosphere or in the first steps of the ALD process could suppress oxygen scavenging during the annealing treatment. The presence of a broad peak at $2\theta \sim 25$ °C indicates the formation of WO_{3-x} nanocrystallites [258].

XPS measurements were performed by collaborators on two symmetrical $Hf_{0.5}Zr_{0.5}O_2$-based capacitor stacks having either W or TiN as both top and bottom electrodes. The measured data were fitted and the Hf and N peaks were deconvoluted to estimate the amount of oxygen vacancies present at the interfaces between the electrodes and the ferroelectric oxide. As shown in figure 5.12,

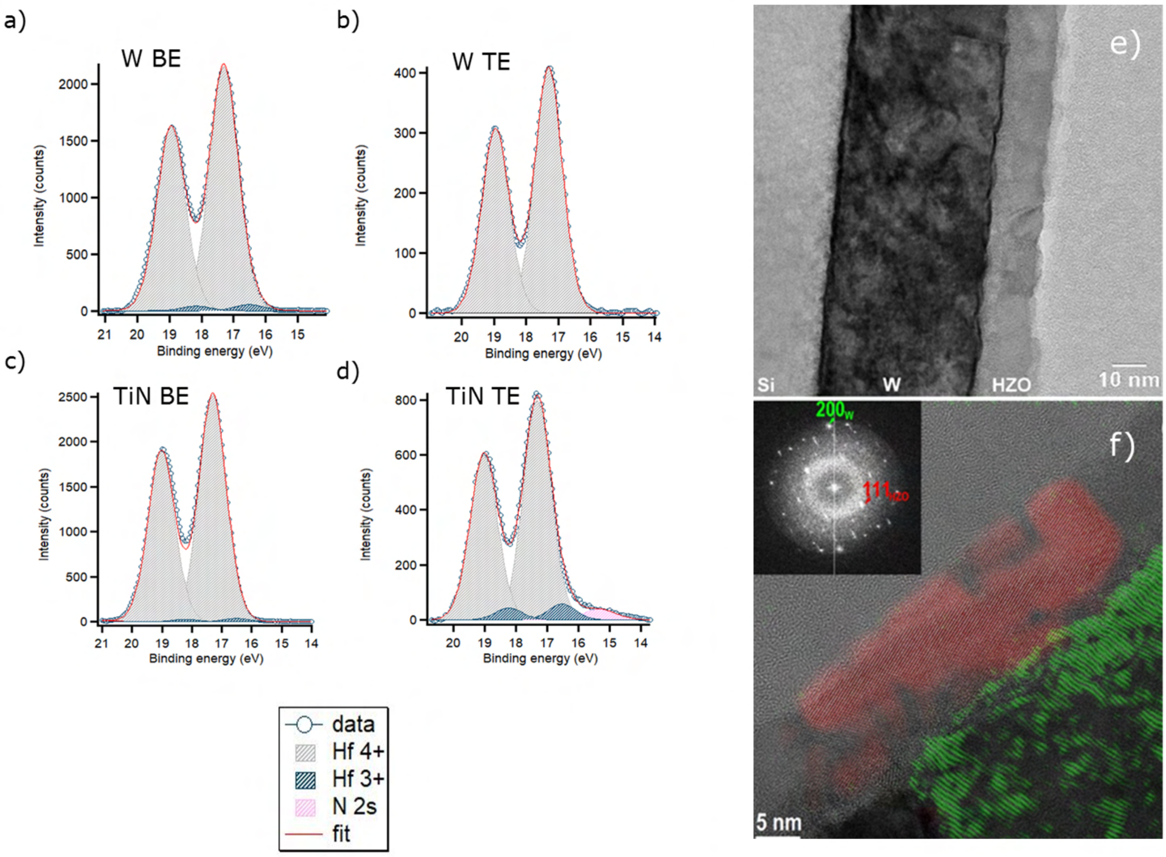

Figure 5.12: XPS measurements of $Hf_{0.5}Zr_{0.5}O_2$-based capacitor stacks at the a) bottom and b) top interface with W and c) bottom and d) top interface with TiN. The Hf 4+, Hf 3+ and N 2s peaks are deconvoluted and used to calculate the amount of V_O in the layer. In panel e) and f) TEM pictures of a Si/W (in green)/HZO (in red) stack, where an interface between W and HZO is shown.

the top interface with TiN shows the highest amount of V_O, followed by the bottom interface with W. The numerical values were extracted by collaborators using the following formula:

$$V_O(\%) \sim \frac{1}{8} \cdot \left(\frac{I_{Hf^{3+}}}{I_{tot}} \right). \tag{5.1}$$

The measured content of V_O was of ∼ 0.3 (W BE), 0 (W TE), 0.15 (TiN BE) and 0.75 (TiN TE) %. As mentioned above, the formation of a tungsten oxide interface already after exposure to the atmosphere or during the ALD process could be responsible for the lower scavenging during thermal treatment from the ferroelectric oxide towards the electrode, resulting in a lower amount of oxygen vacancies in the case of W as compared to TiN. The presence of this interface was confirmed by TEM, as displayed in figure 5.12 e) and f), where a thin layer is observable between the W (green in figure 5.12 f)) and the HZO (red in figure 5.12 f)).

5.4.2 Hysteresis shift and field cycling behavior

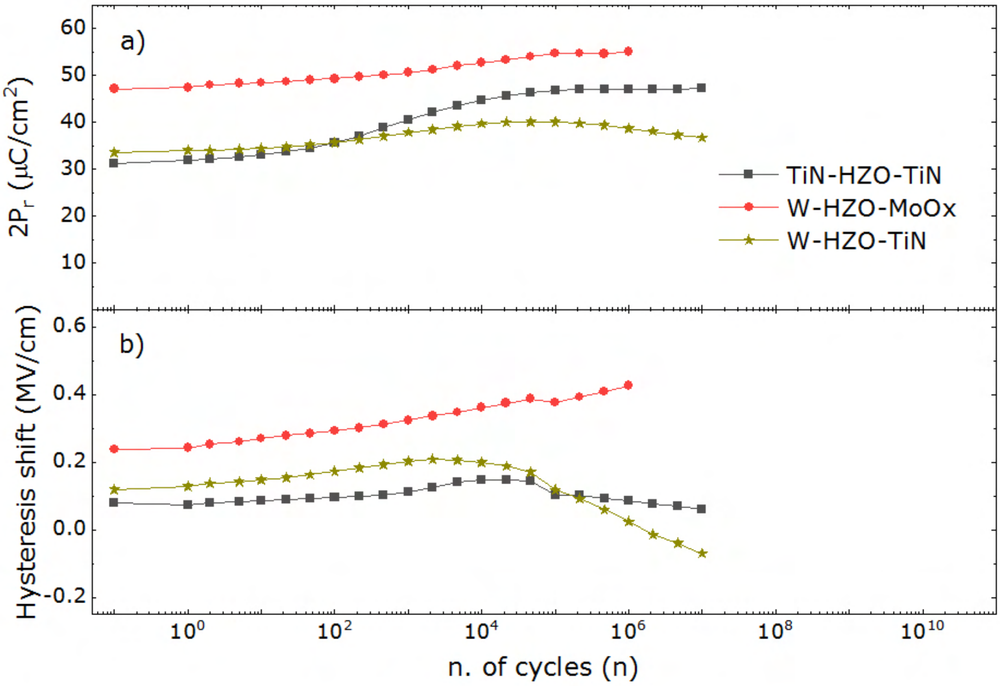

Figure 5.13: a) $2P_r$ and b) hysteresis shift as a function of the number of applied field cycles for $Hf_{0.5}Zr_{0.5}O_2$ (HZO)-based capacitor stacks with different top and bottom electrode combinations including W and a reference TiN/HZO/TiN FeCap.

FeCaps with W as the bottom electrode were subjected to cycling and the ferroelectric device properties were monitored as a function of the number of applied field cycles. Results for remanent polarization and hysteresis displacement on the voltage axis are reported in figure 5.13 a) and b), respectively. An increase in $2P_r$ is observed for the $W/Hf_{0.5}Zr_{0.5}O_2/MoO_x$ stack, whereas the $W/Hf_{0.5}Zr_{0.5}O_2/TiN$ capacitor shows comparable values with respect to a standard symmetrical TiN-based stack. The advantages in $2P_r$ presented by the $W/Hf_{0.5}Zr_{0.5}O_2/MoO_x$ structure are nonetheless accompanied by a degraded endurance with respect to field cycling and a strong hysteresis shift for the first and the second case, respectively. The reduction in the number of cycles before device hard breakdown observed in the case of the $W/HZO/MoO_x$ capacitor can be linked to the higher m-phase content related to the use of an oxide electrode (see the previous section).

5.4.3 Retention and imprint

Reliability with respect to time and temperature was also analyzed through a retention measurement for a $W/Hf_{0.5}Zr_{0.5}O_2/TiN$ stack and compared to the results obtained for the standard TiN/TiN FeCap. The measurement outcomes are displayed in figure 5.14. A fitting of the measured data utilizing a power law shows that both stacks behave similarly, as already confirmed from the

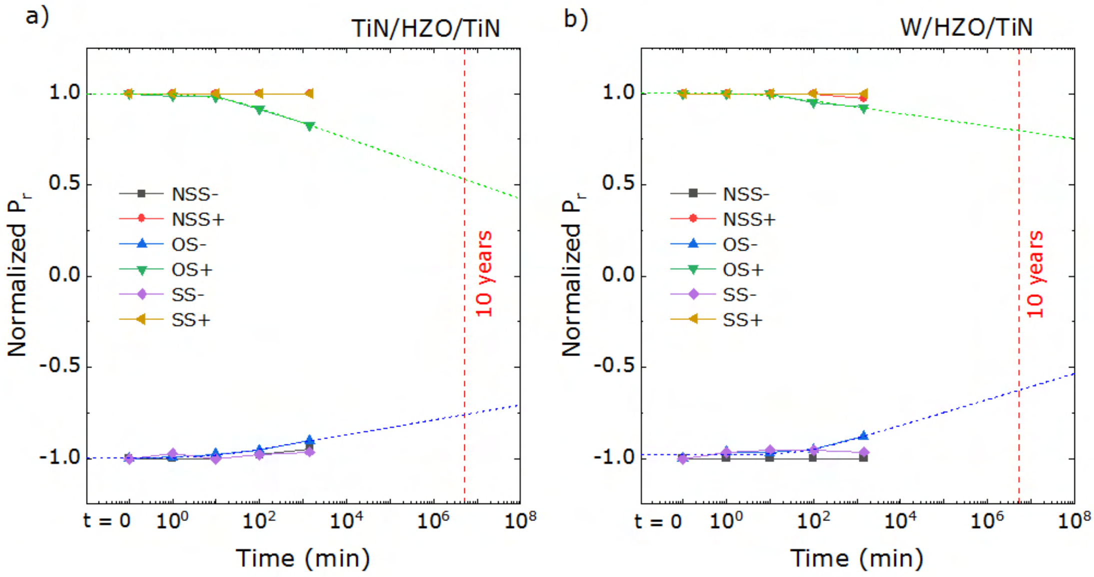

Figure 5.14: Positive an negative same state (SS+, SS-), new same state (NSS+, NSS-) and opposite state (OS+, OS-) retention measured at 85 °C for ferroelectric capacitors based on a 10 nm $Hf_{0.5}Zr_{0.5}O_2$ film sandwiched between a) TiN BE and TiN TE and b) W BE and TiN TE. The OS retention shows the strongest reduction and was therefore extrapolated for 10 years operation in order to benchmark device degradation.

fatigue measurements displayed in figure 5.13, retaining 50 % of the opposite state polarization even at the 10 years limit. Nonetheless, a slight improvement can be seen for the positive OS retention in the W/HZO/TiN stack, probably related to the reduced amount of oxygen vacancies generated at the bottom W interface as compared to TiN, as described above.

To summarize, a structural analysis of W and TiN electrodes demonstrated a lower amount of oxygen vacancies in the presence of W as compared to TiN. This was linked to the growth of a tungsten oxide interface either because of exposure to the atmosphere between the different processing steps or during the first cycles of the ALD deposition. This resulted in a higher detected m-phase portion in the $Hf_{0.5}Zr_{0.5}O_2$ film, as shown in the GIXRD measurements. Electrical measurements showed a comparable behavior for the W/HZO/TiN and the TiN/HZO/TiN FeCaps, whereas W in combination with MoO_x demonstrated a lower endurance and a pronounced hysteresis shift. Furthermore, W and TiN seem to be rather interchangeable in terms of retention performances.

5.5 General remarks on reliability aspects

By comparing capacitor stacks with different electrode materials, various phenomena emerged depending on the used electrode combination. It was shown how the crystalline phase, the symmetry of the ferroelectric hysteresis, the behavior with respect to field cycling and device reliability as a function of time and temperature were all depending on the material choice and the formation of a parasitic interface between the electrode material and the ferroelectric oxide. As mentioned above, interface properties are of fundamental importance because they govern the oxygen exchange between the hafnia-layer and the electrode itself, influencing layer defectivity i.e. the amount of oxygen vacancies in the ferroelectric layer. A variation in the V_O content was shown to affect both crystallization behavior and wake-up/fatigue properties because of defect redistribution. Not less important, depending on the band alignment between the ferroelectric, the electrode material and, if present, of the parasitic interface, charge injection can play a fundamental role, with defect sites also being available for trapping of the injected charges.

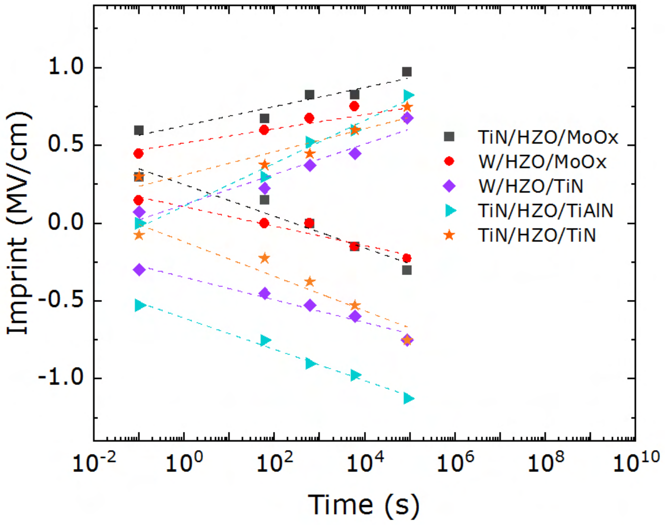

Figure 5.15: Shift of the ferroelectric hysteresis extracted from the measurement of the opposite state polarization as a function of baking time at 85°C. The dashed lines represent a fit and the slope is taken as an expression of the magnitude of the imprint i.e. how fast degradation through progressive imprint occurs. The starting point at t = 0 depends on the original hysteresis shift, caused by the work function difference between the two employed electrode materials.

Table 5.2: Positive and negative imprint slope calculated from the shift of the hysteresis with time at 85°C for different electrode combinations.

Stack	Positive imprint slope	Negative imprint slope
TiN/$Hf_{0.5}Zr_{0.5}O_2$/TiN	0.03	-0.05
TiN/$Hf_{0.5}Zr_{0.5}O_2$/TiAlN	0.06	-0.04
TiN/$Hf_{0.5}Zr_{0.5}O_2$/MoO_x	0.03	-0.04
W/$Hf_{0.5}Zr_{0.5}O_2$/TiN	0.04	-0.03
W/$Hf_{0.5}Zr_{0.5}O_2$/MoO_x	0.02	-0.03

The shift of the ferroelectric hysteresis with time during the opposite state retention measurement was assessed and analyzed for different capacitor stacks. Figure 5.15 shows how both shifts in the positive and in the negative voltage direction, depending on the polarity during baking, progressively increase with time. The initial non-zero imprint is coherent with the internal bias field generated from the work function difference between the electrode materials. The rate with which the hysteresis shifts, i.e. the slope of the imprint vs. baking time characteristic is taken as the parameter describing the magnitude of the imprint effect. The obtained values are summarized in table 5.2.

By combining what is shown in figure 5.15 and the values displayed in table 5.2, it can be assessed that the fastest degradation seems to take place in capacitor stacks where TiAlN is employed as TE. On the contrary, the best values are obtained for the W/HZO/MoO_x capacitor. Nonetheless, the latter shows a strong starting imprint originating from the WF difference of the two electrode materials.

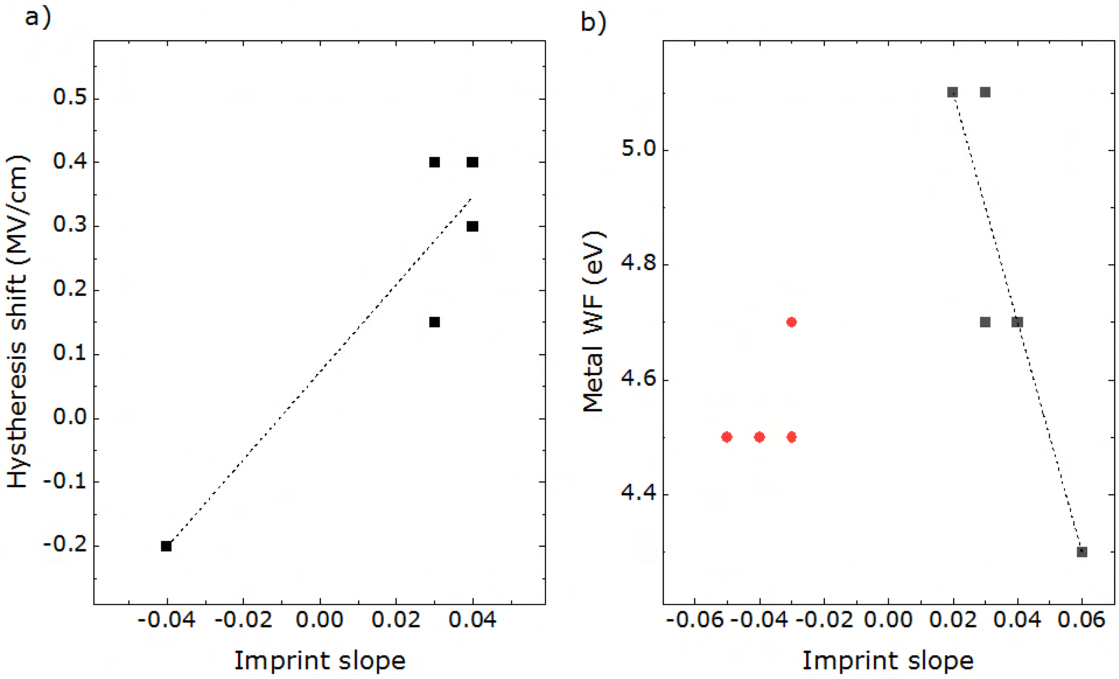

Figure 5.16: a) Hysteresis shift for FeCaps with different electrode combinations and b) work function of the electrode materials as a function of the measured imprint slope.

Figure 5.16 shows the hysteresis shift as a function of the imprint slope. The two values seem to be directly proportional, meaning a faster degradation is observed in ferroelectric capacitors where a stronger internal bias field is present. The internal bias field imposed by the different electrode combinations, caused either by parasitic interface formation or by the WF difference between the two electrode materials, could add up to the imposed polarization state during retention baking and increase charge (i.e. oxygen vacancy) migration, therefore worsening the degradation via imprint. In figure 5.16 b), the electrode work functions were plotted as a function of the imprint slope reported in table 5.2. The degradation seems to be stronger as the WF lowers. A charge injection mechanism from the electrode into the ferroelectric layer is hypothesized as one of the main causes for the observed imprint. A lower WF can result in a lower conduction band offset between the electrode and the ferroelectric, reducing the barrier for charge displacement. In other words, both charge migration because of internal bias fields and charge injection through the electrode seem to play a role in determining the amount of generated imprint during baking. The respective impact of the two mechanisms is rather difficult to be distinguished. Conversely, no relation between the behavior with respect to the number of applied field cycles and the electrode work function could be detected. The latter resulted in fact rather influenced by the formation of parasitic interfaces and by the dominant crystalline phase, as observed both in this chapter and in chapter 4.

To summarize what was observed for the different capacitor stacks and try to give an interpretation of the results, the main retention and imprint-related properties of each stack were plotted as a function of their remanent polarization.

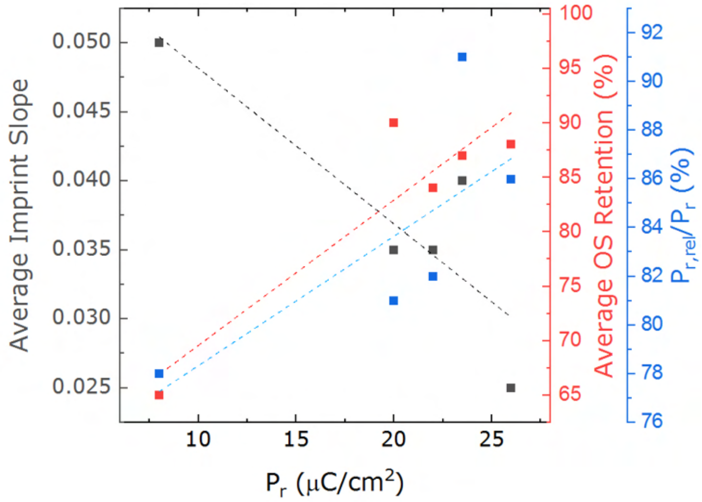

Figure 5.17: Average imprint slope (left y-axis), average opposite state retention (right y-axis, red) and normalized relaxed polarization (right y-axis, blue) as a function of remanent polarization for different FeCap stacks examined in the previous sections.

In figure 5.17, the average imprint slope, the absolute value of the average opposite state retention and the relaxed remanent polarization are plotted as a function of P_r. In general, an improvement in all three values is demonstrated as the remanent polarization increases. It was shown in chapter 4 that a higher remanent polarization corresponds to a greater amount of layer crystallized in the ferroelectric orthorhombic phase. Improved ferroelectric properties seem to come along with better retention. A lower portion of remanent polarization is lost both with time (relaxed P_r) and with temperature (average OS retention). The hysteresis loop is more stable and is less subject to modifications and shift with time (average imprint slope). A higher amount of ferroelectric polar phase translates logically in a lower amount of non-polar non-ferroelectric portions, which are often responsible for the observed depolarization fields. By improving layer and interface quality, such irregularities are discouraged and not only a higher P_r but also improved retention and imprint performances are obtained.

5.6 Summary

Table 5.3: Comparison of the detected crystalline phase, the assumed oxygen vacancy content, the measured hysteresis shifts the retention, and the endurance results for the capacitor stacks studied within this chapter.

Stack	Crystalline phase	V_o (assumed)	Measured hysteresis shift (MV/cm)	Retention	Endurance (n. of cycles)
TiN/HZO/TiN	t-/o-	medium	0.15	good	10^7
TiN/HZO/TiAlN	t-/o-	medium	-0.2	bad	10^8
TiN/HZO/MoO_x	o-/m-	low	0.4	medium	10^6
W/HZO/TiN	t-/o-/m-	medium	0.3	good	10^7
W/HZO/MoO_x	o-/m-	low	0.4	good	10^6
MoO_x/HZO/TiN	o-/m-	low	0	medium	10^7

In this chapter, asymmetrical capacitor stacks were fabricated, keeping $Hf_{0.5}Zr_{0.5}O_2$ as the standard ferroelectric layer and changing bottom and/or top electrode. The effect of the different electrode work functions, as well as of the interfaces between the electrodes and the ferroelectric oxide were evaluated through structural and electrical characterization. Reliability properties were also strongly affected by the formation of parasitic interfaces, especially in the case of TiAlN electrodes.

A mixture of different effects was induced depending on the material choice. Depolarization fields and charge injection phenomena were shown to be responsible for reliability issues such as polarization relaxation and imprint. The electrode material was also demonstrated to affect the crystallization within the ferroelectric layer.

A comprehensive comparison of all the fabricated stacks showed that an optimization of the ferroelectric properties in terms of remanent polarization i.e. stabilization of the polar orthorhombic phase concurrently yields advantages for device retention. This is different for the cycling endurance, which only results increased for TiAlN electrodes. In this case, a subcycling regime is likely to be reached because of a field drop at the parasitic interface formed between the electrode and the ferroelectric oxide.

Table 5.3 shows a comparison between some of the capacitor stacks fabricated and analyzed within this work. As previously shown, TiAlN-based electrodes harm the reliability properties because of the pronounced formation of an interface between the ferroelectric and the electrode material. This interface is responsible for depolarization fields which cause unwanted polarization reversal and worsen the wake-up behavior. Furthermore, the lower WF shown by TiAlN could facilitate charge injection and speed up the degradation via imprint. Oxide-based electrodes seem to promote the stabilization of the monoclinic phase, causing a slight decrease of the remanent polarization and the endurance to field cycling. The reduced amount of oxygen vacancies, together with the higher WF presented by MoO_x with respect to TiN seemed to be beneficial for the retention behavior of the devices, which resulted as stable as in the case of standard TiN. Last but not least, W seemed to behave comparably to TiN, with almost no hysteresis shift and very similar properties with respect to field cycling and baking. The formation of an oxide interface at the bottom W electrode prior to HfO_2 deposition was considered responsible for the slightly higher detected m-phase portion. All considered, TiN still seems to be one of the most advantageous choices for the fabrication of ferroelectric capacitors. Further improvements in device behavior with respect to field cycling could be pursued by targeting the stabilized crystalline phase and avoiding the formation of parasitic interfaces. On the other hand, materials with a higher work function could be considered to limit charge injection phenomena from the electrode into the ferroelectric oxide.

6 Switching mechanism in hafnium oxide thin films

The need for fast and low-power devices, as well as the growing interest in the deployment of fluorite ferroelectrics in neuromorphic applications [259], has made the understanding of the polarization switching phenomenon in thin HfO_2 films crucial.

In chapter 2 the different existing models describing polarization reversal in ferroelectric HfO_2-based films were discussed. In the following sections, experimental data were compared to the theoretical descriptions to provide an interpretation of the switching phenomena occurring in the fabricated $Hf_{0.5}Zr_{0.5}O_2$-based capacitors. In particular, the KAI model was excluded given the high defectivity and the low thickness of ALD deposited HfO_2-based films. The focus will therefore be on the NLS and the IFM models.

6.1 Switching kinetics in hafnia-based thin films: nucleation limited switching

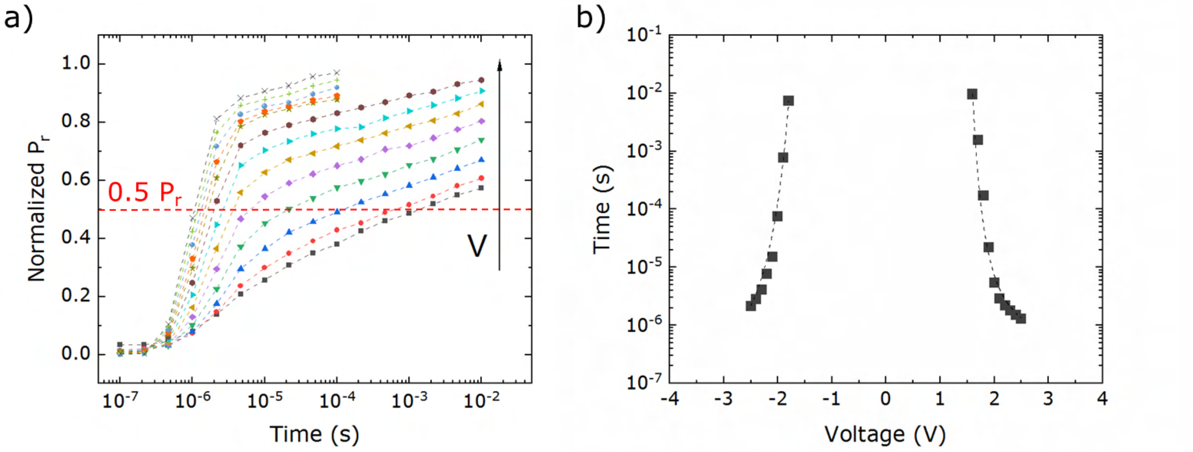

Figure 6.1: a) Switched remanent polarization as a function of switching pulse width for different pulse amplitudes; b) time vs. voltage needed to switch 50% of the P_r, max extracted as shown in a) for a TiN/HZO/TiN stack. The dashed lines represent data fitting with the NLS model through Eq. 2.14.

As explained in chapter 2, according to the Du-Chen NLS model, the relation between switching field and time can be expressed through equation 2.14 [187], [191]. By plotting the inverse of the time vs. the square of the inverse of the voltage needed to switch 50% of the remanent polarization, the data points can be accurately fitted (see Fig. 3.10 c).). Another way to visualize the data is to plot the switching time vs. the switching voltage (Fig. 6.1). Also in this form the data are well fitted and an activation energy value can be extracted.

Within this work, for a symmetrical TiN/$Hf_{0.5}Zr_{0.5}O_2$/TiN stack, activation energies of -0.95 and 1.15 V could be calculated for the negative and the positive polarity, respectively. These values well match the coercive fields which are normally observed for thin HfO_2-based films. The slight difference between positive and negative values could arise from the different interface with the top and bottom electrodes as a consequence of the asymmetrical oxidation during deposition and annealing [131], [139].

Both the phenomenology behind the NLS model and the accurate data fitting possible through the equation proposed by Du and Chen confirm the applicability of this theory to the description of polarization reversal events in HfO_2-based thin films [37], [181], [196].

6.2 Switching speed and homogeneity

As mentioned in the previous sections, HfO_2-based thin films present high defectivity due to their low thickness and polycrystalline nature. Defects can be found in form of external impurities, grain boundaries, non-polar phase portions, non-homogeneous dielectric constant distribution and discontinuous interface with electrodes. As a consequence, when an external voltage is applied, each ferroelectric domain will experience a unique effective field depending on its surrounding. The field necessary for polarization reversal is therefore described not with a single value but through a distribution of fields, whose width is proportional to layer inhomogeneity [195].

Figure 6.2 shows that for a TiN/$Hf_{0.5}Zr_{0.5}O_2$/TiN ferroelectric capacitor stack a fitting of the experimentally measured data collected as explained in figure 3.10 is also possible through the IFM model. In this case, the amount of switched polarization as a function of the applied pulse amplitude V_2 is plotted for each pulse width t_2. The first derivative of the resulting curves gives a distribution of fields for each t_2. As the pulse width decreases i.e. for shorter switching times t_2, the maximum of the distribution shifts towards higher switching voltages V_2. The normalization of the curves to the maximum P_r and the corresponding field yields an overlap of the different curves onto each other. Now the distributions can be fitted with the equation [189]:

$$\frac{\delta P(V_2, t_2)/\delta V}{\delta P(V_2, t_2)/\delta V|_{max}} = \frac{1}{\xi^2} \cdot exp\left[1 - \frac{1}{\xi^2} - \phi \frac{(1-\xi)^2}{\xi^2}\right] \tag{6.1}$$

where $\xi = V_2/V_{2,max}$ and $\phi = 2/(\sqrt{1+8\sigma^2} - 1)$. The value σ relates to the width of the distribution: the narrower the distribution, the lower the σ and the higher the switching homogeinity [189].

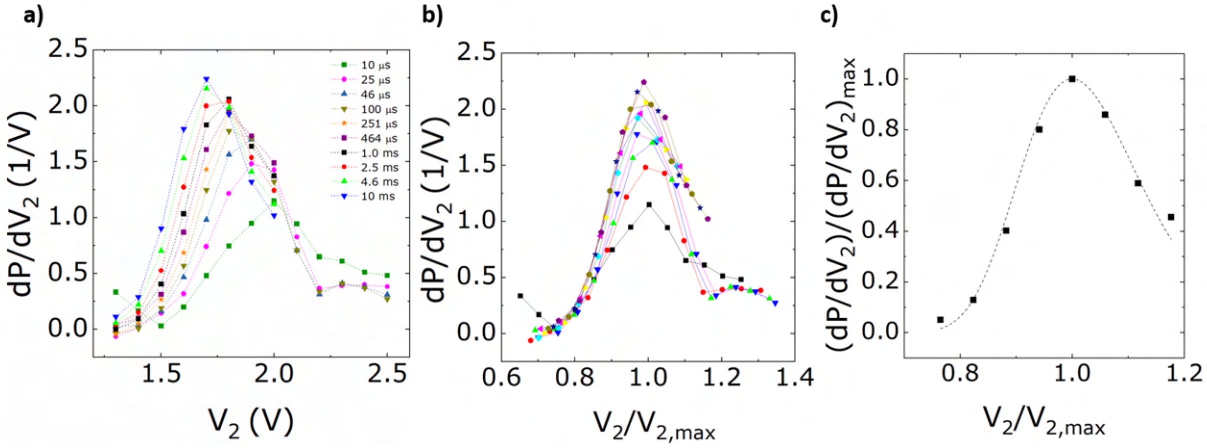

Figure 6.2: Calculation procedure and fitting of σ through the IFM model as presented in Ref. [189]. (a) The derivative of the normalized P_r (see Fig. 3.10) is plotted as a function of the switching pulse amplitude V_2 for the different pulse widths t_2. (b) When the voltage is normalized to the value corresponding to the maximum of dP/dV_2, the curves overlap and (c) a fitting according to Eq. 6.1 can be performed. In the figure, the curve at 100 μs pulse width is used for fitting. Taken with permission from [181].

Within this work, different sample sets could be measured and analyzed both with the NLS and with the IFM model. For the determination of the switching homogeneity through the factor σ, a standard $Hf_{0.5}Zr_{0.5}O_2$ layer was chosen. Different thicknesses, annealing temperatures, measurement temperatures and electrode combinations were considered. A pulse width of 100 μs was chosen. The results are discussed in the next sections, together with findings extrapolated from the literature.

6.3 Influence of processing and measurement parameters

As mentioned above, the parameter σ is an indicator of ferroelectric switching homogeneity. With that in mind, it should be possible to identify certain trends when changing the film's deposition parameters. The same should be valid in the case of field cycling: it can be assumed that switching phenomena become more or less homogeneous depending on the lifetime stage of the capacitor. A ferroelectric film in the pristine state, with a rather unequal defect distribution and pinned domains, could reasonably switch less homogeneously as compared to a woken-up one, after domain de-pinning and defect redistribution has been induced through wake-up cycling.

Several reports are present in the literature, where one degree of freedom is tuned and switching kinetics homogeneity was analyzed as a consequence of that variation. To mention some, Pandey et al. [196] monitored the evolution of σ with annealing temperature. Despite no dramatic change was observed, a slight increase in σ was measured, meaning the switching phenomenon became less homogeneous for films annealed at higher temperatures. Hyun et al. [189] tried to relate switching homogeneity to the device stage with respect to field cycling. In their case, polarization reversal seemed to happen more coherently as the sample was further cycled.

Within this work, film thickness, annealing temperature and measurement temperature were chosen as parameters to be tuned and the respective evolution of σ was monitored by applying the switching kinetics measurement procedure and extracting the homogeneity-related parameter according to equation 6.1. In the next sections, processing parameters and measurement conditions were tuned and switching kinetics was analyzed consequently. The results were finally compared to remanent polarization of the ferroelectric layer stack and the data previously shown in the literature.

6.3.1 Effect of film thickness

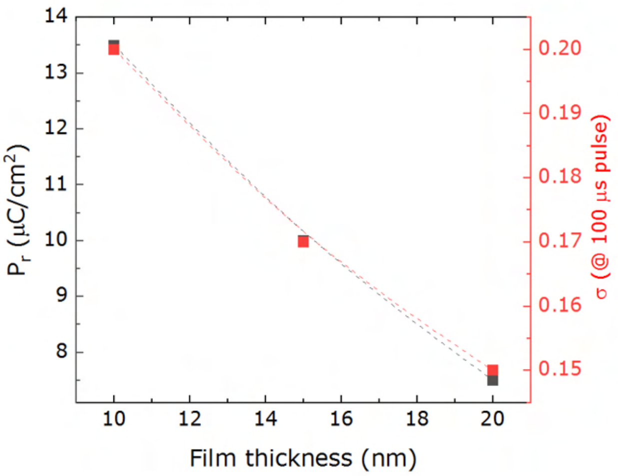

Figure 6.3: Remanent polarization (black symbols) and σ as calculated from Eq. 6.1 (red symbols) vs. $Hf_{0.5}Zr_{0.5}O_2$ film thickness. The dashed lines only serve as a guide for the reader.

Film thickness was chosen as the first degree of freedom. As discussed in chapter 4, different thicknesses of the ferroelectric film can yield a different crystalline phase and therefore modify the ferroelectric properties. To check how this affects the homogeneity of polarization reversal, $TiN/Hf_{0.5}Zr_{0.5}O_2/TiN$ capacitor stacks were fabricated with thicknesses of 10, 15 and 20 nm. Figure 6.3 reports the evolution of both P_r and σ with respect to film thickness. The observed decrease in remanent polarization can be expected as a consequence of the increased amount of monoclinic phase which becomes stabilized over the polar orthorhombic phase as the films become thicker. This result is accompanied by a decrease in the parameter σ from 0.20 down to 0.15, which translates into an increased switching homogeneity.

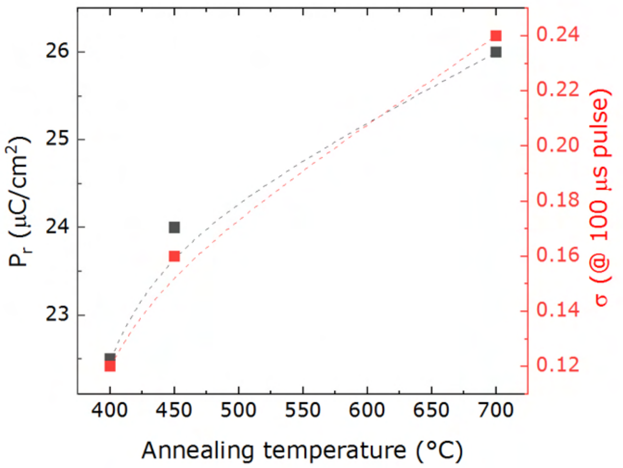

Figure 6.4: Remanent polarization (black symbols) and σ as calculated from Eq. 6.1 (red symbols) vs. post metallization annealing temperature. The dashed lines only serve as a guide for the reader.

6.3.2 Effect of annealing temperature

10 nm thick TiN/$Hf_{0.5}Zr_{0.5}O_2$/TiN capacitor stacks were annealed after top electrode deposition at the temperatures of 400, 450 and 700 °C. As shown in figure 6.4, both remanent polarization and σ increased from 0.12 up to 0.24 with the temperature of the thermal treatment. In other words, as more domains took part in the switching, as witnessed from the higher P_r, polarization reversal became less homogeneous.

In both the considered cases, σ seems to follow the same trends shown by the remanent polarization. A possible interpretation is that as more domains take part in the switching process, the latter becomes less homogeneous. It can be hypothesized that polarization reversal events taking place in confining grains interact with each other and that a larger amount of switching grains statistically results in a broader effective field distribution for the considered ferroelectric layer.

6.3.3 Effect of measurement temperature

As a next step, the TiN/$Hf_{0.5}Zr_{0.5}O_2$/TiN structures annealed at 700 °C were measured with the kinetics measurement sequence at different temperatures, ranging from room temperature up to 125 °C, in steps of 25 °C. Figure 6.5 shows the result of the inhomogeneous field mechanism analysis, together with the detected remanent polarization. This time, σ and P_r evolve rather differently with the tuned degree of freedom. In fact, the latter shows no abrupt variation with respect to measurement temperature, whereas switching becomes less homogeneous, with sigma evolving from 0.24 to 0.29.

Different from what was observed for the case of processing parameters, no additional switching

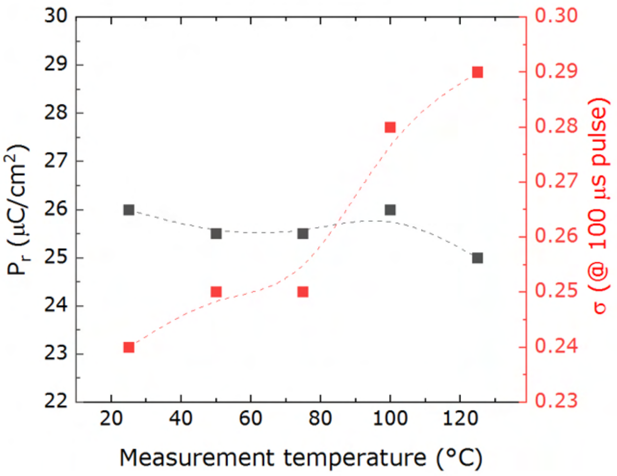

Figure 6.5: Remanent polarization (black symbols) and σ as calculated from Eq. 6.1 (red symbols) vs. measurement temperature. The dashed lines only serve as a guide for the reader.

grains are generated when increasing the temperature from 25 to 125 °C, this meaning the total number of switching events happening within the ferroelectric layer does not drastically change when the measurement temperature is changed. This is reflected in the unchanged remanent polarization with respect to measurement thermal conditions. Nonetheless, a higher temperature could induce local disorders and influence charge displacement, macroscopically resulting in a less homogeneous polarization reversal.

6.3.4 Trends comparison and general remarks

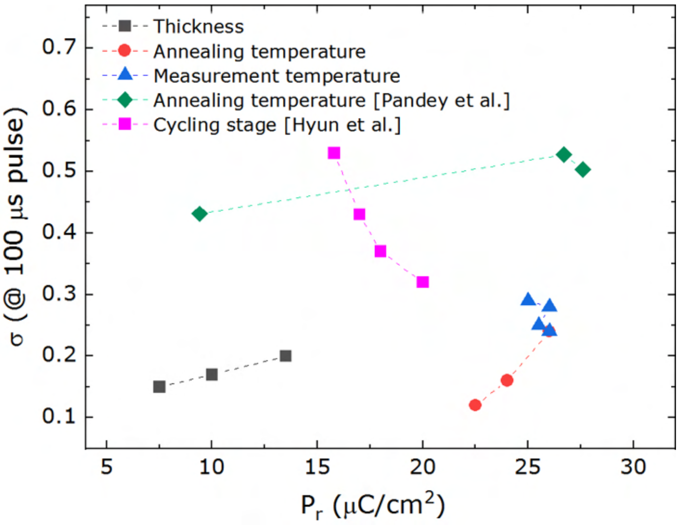

Figure 6.6: σ as calculated from Eq. 6.1 vs. remanent polarization for sample sets where one measurement (deposition) parameter at the time was changed. Both data obtained within this work and data collected from the literature are compared. The dashed lines only serve as guides for the reader. Adapted from [181].

By looking at the above-presented results, a trend in σ could be also identified with each tuned parameter. This was valid for both processing and measurement parameters and both within this work and in the literature. Nonetheless, it is difficult to give a global interpretation of the observed trends, which unifies the observations under a single interpretation.

To be able to compare the presented data and obtain a broader picture, remanent polarization was chosen as the figure of merit identifying the different measurement points and the parameter σ was plotted as a function of P_r. Unfortunately, no unequivocal relation can be found between the two values. If in some cases it seems like σ increases with increasing remanent polarization, in other cases the opposite is true. In the case of measurement temperature, a cluster of points is detected. As a result, it cannot be stated that a higher switching portion in the film corresponds to either a higher or a lower homogeneity in the polarization reversal phenomenon.

6.4 Switching kinetics and hysteresis shift

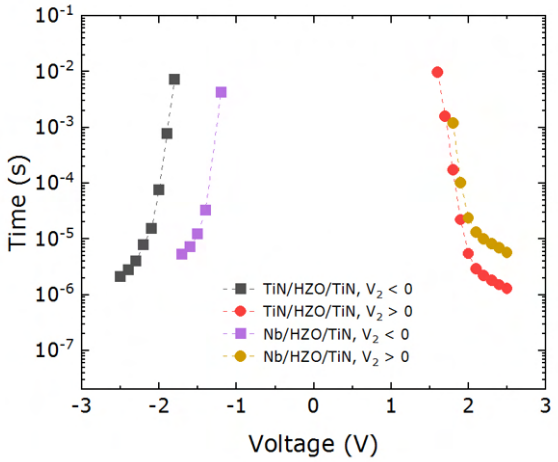

Figure 6.7: Time vs. voltage needed to switch 50 % of the $P_{r,max}$ for a TiN/$Hf_{0.5}Zr_{0.5}O_2$/TiN stack and a Nb/$Hf_{0.5}Zr_{0.5}O_2$/TiN stack. The dashed line represent data fitting with the NLS model using Eq. 2.14.

In chapter 5, the effect of the usage of an asymmetrical layer stack where the ferroelectric layer is sandwiched between two different electrode materials with a different work function was elucidated. The WF difference between the two electrode materials led to a shift of the ferroelectric hysteretic loop in one voltage direction, depending on the respective positioning of the two electrodes (BE or TE) and on their WF.

The shift of the P-V curve in one voltage direction can be detected also within switching kinetics measurement. As an example, figure 6.7 shows the time vs. the voltage needed to switch half of the maximum remanent polarization in two different stacks: a symmetrical one and one where a shift is expected. In fact, the WF of Nb was measured to be lower compared to that of TiN, that is 4.1 eV vs. 4.7 eV (see table 5.1). When using Nb as BE and TiN as TE, a shift in the positive voltage direction is expected. The shift is observable in the results of the kinetics measurement, too. This will mean, a lower absolute value of V_2 will be needed to switch the capacitor in the negative polarity, whereas a higher absolute value of V_2 will be needed to induce switching in the positive polarization direction. The rigid shift of the time vs. voltage curves of the asymmetrical stack compared to the symmetrical case in figure 6.7 is comparable to the WF difference between Nb and TiN i.e. to the hysteresis shift between the PV curves of the two capacitors.

6.5 Summary

Besides the KAI model, whose starting hypothesis of a defect-poor single layer where the horizontal movement of domain walls can take place cannot be meaningfully foreseen in HfO_2-based thin films, the other existing models describing polarization reversal seem not to be applicable and not mutually contradictory.

The multi-grain Landau-Khalatnikov model states for example that each ferroelectric domain switches at its intrinsic field and independently from the surrounding domains. A certain affinity is encountered when comparing this statement to the principle behind the inhomogeneous field model. As a matter of fact, also in the IFM, a statistical distribution of field is calculated starting from the hypothesis that each ferroelectric domain experiences its own effective field, which depends on the domain surroundings but is unique for the considered domain. With that in mind, the Landau-Khalatinkov and the IFM model seem to use the same basic hypothesis to analyze the phenomenon from two different perspectives: a physical and a statistical one, respectively. Both treatments yield a macroscopic picture of polarization reversal, without actually describing how the switching event occurs at a single domain level.

This job is undertaken from the nucleation limited model. In this case, a clear picture of polarization reversal is given, with nuclei forming at impurities and propagating until an energetically stable size is reached and a new domain is encountered. In this scenario, crystal grains can enclose one or more ferroelectric domains. The field which has to be supplied to reach the critical size for opposite polarity domain formation could still be unique for each domain and be dictated from the surrounding conditions, as in the multi-grain Landau-Khalatnikov and the IFM model. For this reason, the three models are not considered exclusive and could together be useful to give a more complete picture of the addressed phenomenon.

7 Impact of competing mechanisms on the establishment of ferroelectricity

In chapters 2, 4 and 5, the different causes yielding ferroelectricity in fluorite HfO_2-based films have been discussed. Experimental results have been presented demonstrating how the choice and processing of both the HfO_2-based film and the electrode layers can affect the emergence of this phenomenon. It was shown how both the crystalline structure of the layers and ultimately the reliability of ferroelectric capacitors could be tweaked by tuning processing parameters. As knowledge seems to deepen through literature study and experimental insights, it concurrently emerges how the different phenomena triggering the observation of the ferroelectric hysteresis are strongly intertwined.

As an example, the choice of the electrode material could concurrently affect the oxygen content, the compressive/tensile stress and the grain size in the ferroelectric layer [242]. The interface between the electrode material and the oxide layer could induce oxygen scavaging from the HfO_2 layer towards the electrode itself [243]. This provokes local stoichiometry changes in the ferroelectric layer, with a certain oxygen vacancy profile within the stack [110]. The magnitude of this effect might strongly depend on the chemistry of the electrode material [99], [248]. At the same time, lattice mismatches between the electrode and the ferroelectric oxide can induce tensile/compressive stress and local variation in grain sizes. As a result, oxygen vacancies, stress and surface/volume energy contributions can all easily play a role in inducing (anti-)ferroelectricity [260].

Similar effects could be obtained in the case of two stacks including the same electrode materials but a differently doped HfO_2 layer. Also in this case, the presence of dopant atoms could modify the stress/strain profile in the layer. The effect will strongly depend on the size difference between the impurity and the Hf atoms [261]. Furthermore, the electronic structure of the dopant element could support or discourage the formation of oxygen defects and therefore influence layer stoichiometry [92]. Last but not least, each dopant atom could represent a defect site that consequently affects the thermodynamics of crystallization and induces the formation of grains with different sizes [260]. It is therefore difficult to discriminate the effect of oxygen vacancies and surface/volume energy contributions in the establishment of ferroelectricity.

The thickness of the HfO_2-based layer was also taken into account as a degree of freedom influencing layer crystallization and eventually the ferroelectric properties of the stack. Besides this direct effect, other indirect consequences could be encountered depending on the thickness of the ferroelectric layer. If oxygen scavenging and stress effects are originating from the interface with the electrodes, a thicker layer will be intuitively less affected by the phenomena.

Also very relevant is the observation of a pinched, double-looped, antiferroelectric-like hysteresis in ZrO_2 and in some doped HfO_2 systems, which has been explained through a field-induced reversible phase transition between the non-polar tetragonal phase, with space group $P4_{2/nmc}$ and the polar orthorhombic phase, with space group $Pca2_1$ [205]. The hypothesis is that in such films the non-polar phase is stabilized over the polar one. Nonetheless, the energy difference between the two phases is low enough to allow an applied field to induce a transition from the former into the latter and therefore the observation of the two subloops. Once the field is removed, the layer turns back in its non-polar state and yields a zero remanent polarization. Once again dopant inclusion, high oxygen vacancy content, lower grain size and mechanical stress at the electrode/oxide interface are all to be found in the literature as possible triggers for the AFE-like hysteresis observation [262].

In this chapter, first, a model is proposed based on density functional theory (DFT) calculations with the help of Alfred Kersch and Max Falkowski of the Hochschüle München, Germany. In the presented model, the free energies for the different crystalline phases are calculated for undoped HfO_2 layers with tuned oxygen content. Later, the effect of the interplay between dopants and the oxygen environment is analyzed. Dopant elements are also scanned in terms of atomic size and their effect on stress and strain in the HfO_2 films is considered.

Afterward, observations on ZrO_2 films, traditionally considered to act in antiferroelectric-like fashion are drawn, by analyzing the effect of different thicknesses and of an Al_2O_3 interlayer, inducing either a double-looped or a single-looped hysteresis i.e. an antiferroelectric-like or a ferroelectric behavior in the films.

Last but not least, observations are summarized and oxygen vacancy content together with stress in the layer and surface energy contributions are shown as main factors ultimately governing the (A-)FE response of HfO_2 and ZrO_2-based films.

7.1 A model for phase stabilization: the role of oxygen defects

According to its phase diagram, bulk hafnium oxide in standard pressure and temperature conditions is normally found in the monoclinic phase. However, experimental results in chapter 4 showed how by supplying non-equilibrium conditions i.e. in thin films where low oxygen amount is supplied during deposition it is possible to stabilize the polar orthorhombic and the tetragonal phase in such films.

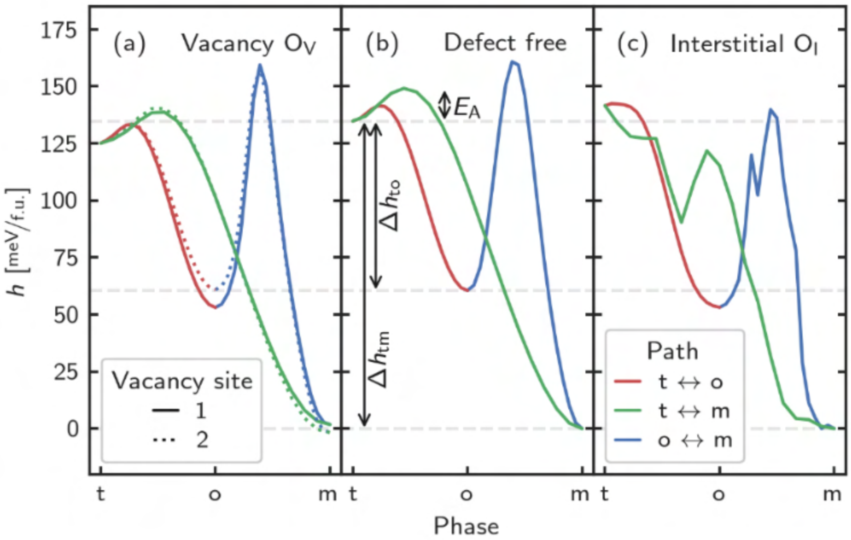

Figure 7.1: Energy of the minimum energy paths (MEPs) along the reaction coordinate between crystal phases at T = 0 K for HfO_2, relative to the m-phase, (a) including a vacancy (3.125 f.u. %), (b) defect-free HfO_2, and (c) including an interstitial (3.125 f.u. %) within a 96-atom HfO_2 supercell. The transition rate assuming a nucleation-limited transformation depends on the values of Δh that are illustrated in (b) for the transitions between the t- and the o- (index to) and the t- and the m- (index tm) phases, respectively. Taken with permission from [86].

DFT calculations were performed by collaborators in order to corroborate the results obtained experimentally [86]. The effect of oxygen defects on the crystallization and the transition paths between the different crystalline phases in undoped HfO_2 were evaluated. A starting hypothesis was set according to Ostwald's rule, which foresees nucleation crystallization initially occurring in the t-phase [263]. The energy of the stable crystal phases in 96(±1)- atomic supercells and the minimum energy paths (MEPs) were calculated depending on film stoichiometry and plotted in figure 7.1. The dependence of the formation energy h on the crystalline phase itself leads to energy differences Δh between crystal phases as a function of defect concentration. After a nucleus is formed in the t-phase, the possible transition into the polar o-phase (red line) competes with the transition into the m-phase (green line). The m-phase corresponds to the lowest energy phase. The polar o-phase is also metastable but the further transition into the m-phase is inhibited by a kinetic energy barrier (blue line). The phase transition rate R to a phase with lower energy can be calculated as follows:

$$R \sim exp(\frac{-G^*}{k_b T}) \tag{7.1}$$

where G* is a thermodynamic barrier expressed by:

$$G^* = \frac{32\psi^3}{|\Delta h|^2} \tag{7.2}$$

which becomes therefore dependent on defect concentration (as well as doping concentration) through the energy difference Δh between the higher energy phase and the lower energy phase. In this model, only the metastable equilibrium structures are relevant. As shown in figure 7.1, oxygen vacancies lower the phase energy Δh of all phases relative to the lowest energetic m-phase. In particular, a stabilization valley for the t-phase is created at very low oxygen contents, which disappears in the case of oxygen surplus, where the transition to the m-phase becomes energetically inevitable. This system will rapidly decay into the m-phase, disrupting ferroelectricity.

The reported model shows that even in the absence of dopant atoms and in analogous thickness and stress conditions, ferroelectricity can be affected by the presence of oxygen defects, in the form of both vacancies and interstitials. In the next section, the effect of the introduction of a dopant will be addressed with the help of experimental results and simulation work.

7.2 Introduction of a dopant atom

As discussed in chapter 2, ferroelectricity has been demonstrated and calculated in HfO_2 layers which were doped with several different dopant atoms. These elements can be very diverse both in atomic size and coordination number, depending on the electronic structure of the dopant atom.

Table 7.1: List of dopant ions which have been shown to induce (anti-)ferroelectric properties when hosted into the HfO_2 lattice. The elements are listed in an ascending atomic radius order and the properties of the Hf ion are included as a reference. Expected phase transition paths are also listed.

Dopant species	**Crystal ionic radius [pm]**	**Stabilized phase (for increasing dopant concentration)**
Si^{+4}	54	m → po → t
Al^{+4}	67.5	m → po → t
Hf^{+4}	**85**	-
Zr^{+4}	86	m → po → t
Y^{+3}	104	m → po → c
Gd^{+3}	108	m → po → c
Ca^{+2}	114	m → po → c
La^{+3}	117	m → po → c
Sr^{+2}	132	m → po → c

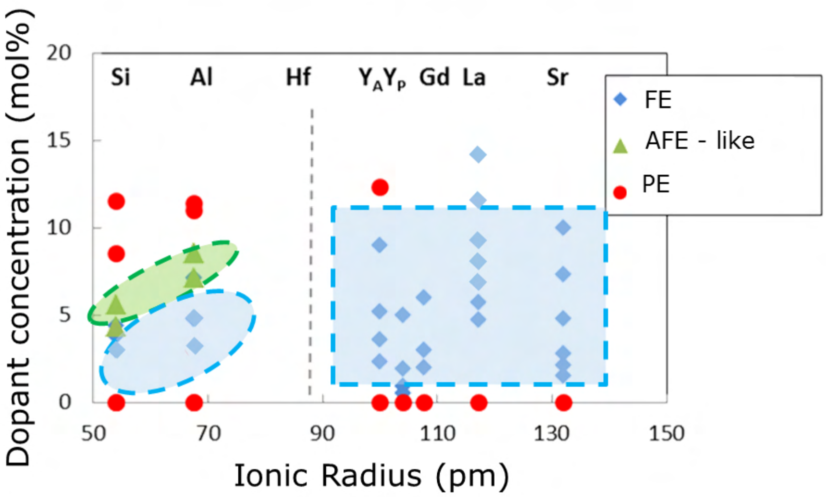

Figure 7.2: Summary of the ferroelectric properties (blue, green and red symbols indicate ferroelectric, antiferroelectric-like and paraelectric response, respectively) observed in doped HfO_2 layers depending on dopant radius (x-axis) and dopant concentration (y-axis). Adapted from [74].

Table 7.1 includes a list of the elements which are known to alter the phase diagram of HfO_2 and to trigger the stabilization either of the polar o-phase or of the cubic or tetragonal phase, depending on the element and on the dopant concentration which is supplied to the film. Figure 7.2 shows the polarization response of doped HfO_2 layers depending on the dopant species i.e. on their ionic radius and on the chosen doping concentration [74]. When the doping concentration equals zero, that is for undoped HfO_2 layers, a paraelectric behavior is detected with a linear polarization response with respect to the applied external field (red symbols). This observation corresponds to the stabilization of the monoclinic phase. As the dopant concentration increases, similar to what was shown for the case of the HfO_2-ZrO_2 intermixed systems, the remanent polarization tends to disappear again, as a result of the stabilization of non-polar phases, that is the cubic and the tetragonal phase (red symbols). In between, a doping concentration interval can be found where the polar orthorhombic phase is stabilized (blue symbols). If the latter and the tetragonal phase are concurrently stabilized, a reversible field-effect transition can be observed which results in a pinched hysteresis and an AFE-like behavior (green symbols).

By combining the information in table 7.1 and in figure 7.2, it can be asserted that the evolution towards the cubic phase is expected in systems where the dopant has a higher ionic radius as compared to Hf, whereas systems including a dopant with a smaller radius rather evolve towards the t-phase for increasing dopant concentration.

Recently, Lomenzo et al. [261] associated this effect to the appearance of a compressive or of tensile stress due to lattice contraction or elongation for dopant ions showing a smaller and a higher radius as compared to Hf, respectively. By adding a mechanical stress term and one considering the electronic configuration of the dopants to the Landau-Ginzburg formulism of the free energy (see chapter 2, equation 2.6), they were able to accurately simulate the phase transition and the consequent emergence of a (pinched) hysteresis in doped HfO_2 thin films.

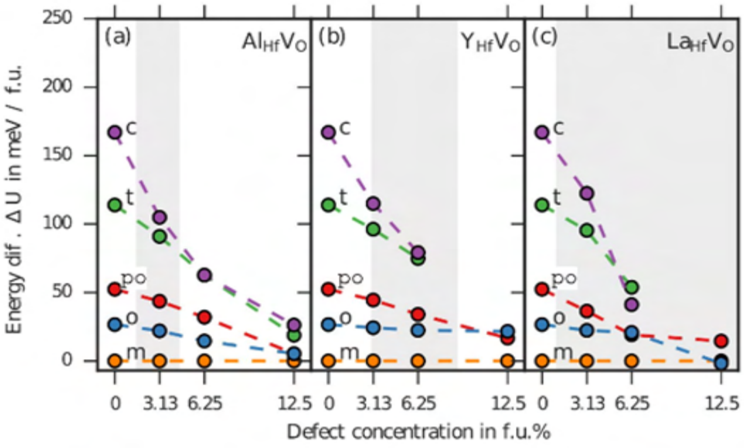

Figure 7.3: Effect of mixed compensated defects $M_{Hf}V_o$ on the total energy differences between the different HfO_2 polymorphs (cubic, tetragonal, polar-orthorhombic, nonpolar orthorhombic) and the monoclinic phase. Subplot (a) displays the results for Al, (b) for Y, and (c) for La dopants. The experimentally observed range of dopant concentrations for ferroelectricity is highlighted by the grey area. Reproduced from Ref. [92] with permission from the Royal Society of Chemistry.

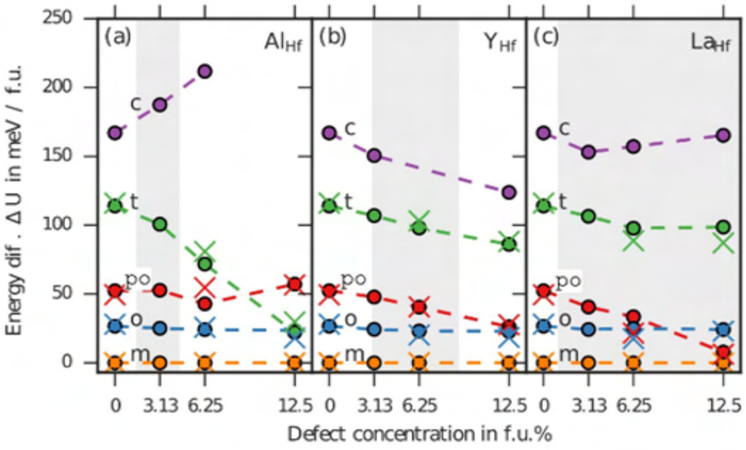

Figure 7.4: Effect of electronically compensated substitutional defects M_{Hf} on the total energy differences between the different HfO_2 polymorphs (cubic, tetragonal, polar-orthorhombic, nonpolar orthorhombic) and the monoclinic phase. Subplot (a) displays the results for Al, (b) for Y, and (c) for La dopants. The experimentally observed range of dopant concentrations for ferroelectricity is highlighted by the grey area. The cross-marks show the results of Fritz Haber Institute ab initio molecular simulations (FHI-aims) calculations. Reproduced from Ref. [92] with permission from the Royal Society of Chemistry.

Nonetheless, dopant ions radius and valence seem to be not the only two factors influencing phase formation. In a report from Kuenneth et al. [102], the behavior of HfO_2 layers doped with the same element seemed to vary depending on the supplied oxygen conditions i.e. on the amount and type of oxygen defects in the layer.

Figure 7.3 and 7.4 show the energy differences between the different phases encountered in doped HfO_2 thin films with respect to the most stable monoclinic phase for III-valent dopants (M = dopant species) forming mixed $M_{Hf}V_o$ or electronically compensated M_{Hf} defects, respectively, depending on the oxygen partial pressure. Precisely, mixed compensated defects form at low oxygen partial pressure conditions as a complex of the dopant atom element M_{Hf}, substituting Hf in the HfO_2 crystal lattice, and an oxygen vacancy V_o. III-valent dopants such as La, Y and Al were shown to effectively lower the formation energy of the higher symmetry phases (such as cubic, tetragonal and polar orthorhombic phase) with respect to the lower symmetry monoclinic phase [125]. Despite having the same valence, the three dopants behave differently and the simulated results agree with what is shown above. While larger concentrations of La and Y tend to stabilize the c-phase over the po-phase, Al favors the formation of the t-phase, coherently with the previous considerations on dopant ionic radius and induced compressive/tensile stress.

In the work from Kuenneth et al. [125], the interaction of dopant atoms with oxygen-related defects also seemed to impact the stabilization of the different phases. By comparing the energy difference values in figures 7.3 and 7.4 it is clear that the oxygen conditions supplied to the layer i.e. the type of oxygen-related defect which is the most stable in the layer affects phase stabilization patterns even for the same kind of dopant. For example, the effect of the introduction of Al in HfO_2 layers strongly affects phase stabilization for both the favored defect configurations. In the case of La and Y doping instead, the energy differences relative to the c- and the t-phase are only slightly affected by the increasing introduction of the dopant in the case of the electronically compensated defects. As more oxygen vacancies are formed, both the c- and the t-phase result instead strongly favored.

The results of the simulations of Lomenzo et al., together with what was shown by Kuenneth et al. hints at a strong interplay between the stress caused by the introduction of a dopant atom and the amount of oxygen i.e. of oxygen defects present in the layer. This seems to be true in particular for the case of dopant elements having a larger ionic radius as compared to Hf (see Y, La) and to only moderately affect phase stabilization in films with a dopant atom smaller than Hf (see Al).

7.3 Introduction of an interlayer

Recently, the effect of surface-induced stress on phase stabilization and ferroelectric properties of hafnia-zirconia-based thin films has been also investigated in detail by various groups. Recently, a very direct proof of the correlation between remanent polarization and stress/strain in the hafnia layer was supplied by Kruv et al. [264], who electrically measured the current-voltage dynamic characteristics of Si-doped HfO_2 films while applying mechanical tensile and compressive solicitation to the wafers, detecting an improvement and degradation of the P_r for the two cases, respectively.

In the literature, mainly two different process-based approaches can be found, aimed to monitor and/or induce mechanical stress in HfO_2-based layers: in some cases, the impact of different interfaces i.e. of different electrodes is evaluated; alternatively, reports are present where an interlayer is inserted within the ferroelectric layer itself.

Lombardo et al. [251] demonstrated that by switching the substrate for ZrO_2 deposition from the standard TiN to Si/SiO_2, a ferroelectric hysteresis could be obtained rather than the commonly observed antiferroelectric-like, pinched one. Using scanning transmission electron microscopy measurements, they were able to extract the lattice parameters and conduct a phase analysis for the ZrO_2 films deposited either on thermally grown SiO_2 or TiN. The results obtained for the SiO_2 substrate showed the co-existence of the tetragonal and the polar orthorhombic phase and revealed only a small stress amount. Differently, a periodically distorted lattice was detected in the case of ZrO_2 deposited on TiN, resulting in a higher strain in the layer and, electrically, in the appearance of a double-looped hysteresis. Through DFT calculations, they extracted the stress value needed to support the stabilization of the tetragonal phase over the orthorhombic phase and obtained a value of $\sim$ 4%, which well agreed with the experimentally measured stress in ZrO_2-on-TiN antiferroelectric-like structures. Cai et al. [265] evaluated the stress imposed by a W top electrode by changing its growth conditions and the annealing treatment of their capacitor stacks. Improvements in reliability were obtained for higher stress values, which they attributed to lower defectivity in the HZO layer.

Kim et al [262] placed an HfO_xN_y interlayer between the TiN bottom electrode and the HfO_2-based layer of their capacitors, demonstrating an optimized ferroelectric performance and reliability. According to their work, the interlayer had both the advantage of suppressing grain expansion and consequently m-phase formation and concurrently participated in reliability improvement by avoiding oxygen exchange from the HfO_2-based layer towards the TiN electrode.

Joh et al. [266] compared the performance of a capacitor stack based on a 22 nm thick $Hf_{0.5}Zr_{0.5}O_2$ layer where a 2 nm thick TiO_2 or SiO_2 interlayer was deposited between two identical 10 nm thick $Hf_{0.5}Zr_{0.5}O_2$ layers. As discussed above, increasing oxide thickness facilitates the stabilization of the m-phase over the t- and the po-phase in hafnia- and zirconia-based systems. The presence of an interlayer seemed to provoke additional in-plane stress and to reduce m-phase formation, in favor of t- and po-phase stabilization.

A set of three ZrO_2-based capacitors was fabricated to further investigate the mutual effect of oxygen content, induced stress and surface energy contributions i.e. grain size. Each capacitor was deposited at 350°C in order to induce crystallization during deposition and avoid diffusion of the interlayer elements during the annealing treatment.

For the sake of simplicity, the capacitors will be referred to as Stack 1, 2 and 3 and can be described as follows:

- **Stack 1:** 15 nm ZrO_2;
- **Stack 2:** 30 nm ZrO_2;
- **Stack 3:** 15 nm ZrO_2 + 5 ALD cycles Al_2O_3 interlayer + 15 nm ZrO_2.

The absence of an annealing treatment ensures the separation of the two 15 nm thick ZrO_2 layers within Stack 3. This way, grains within a single ZrO_2 layer from Stack 3 should grow analogously to those in Stack 1, with vertical growth limited by the 15 nm layer thickness.

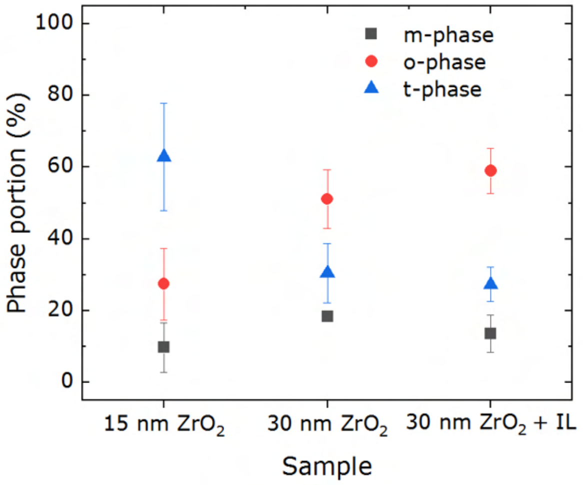

Figure 7.5: Phase portions detected via GIXRD Measurements and Gaussian fit as described in chapter 3 for a 15 nm, a 30 nm and a 30 nm + Al_2O_3 interlayer ZrO_2-based capacitor stacks.

GIXRD measurements were performed on the three stacks and phase portions were extracted according to the method presented in chapter 3. Results are displayed in figure 7.5. The capacitor including 15 nm ZrO_2 crystallized mostly in the t-phase, showing almost no monoclinic phase and a relatively low polar o-phase amount. Conversely, the stacks with 30 nm ZrO_2 showed a comparably high po- and t-phase portion, with the values being slightly lower in the case of the sample without Al_2O_3 interlayer, where 20 % of the layer crystallized in the m-phase.

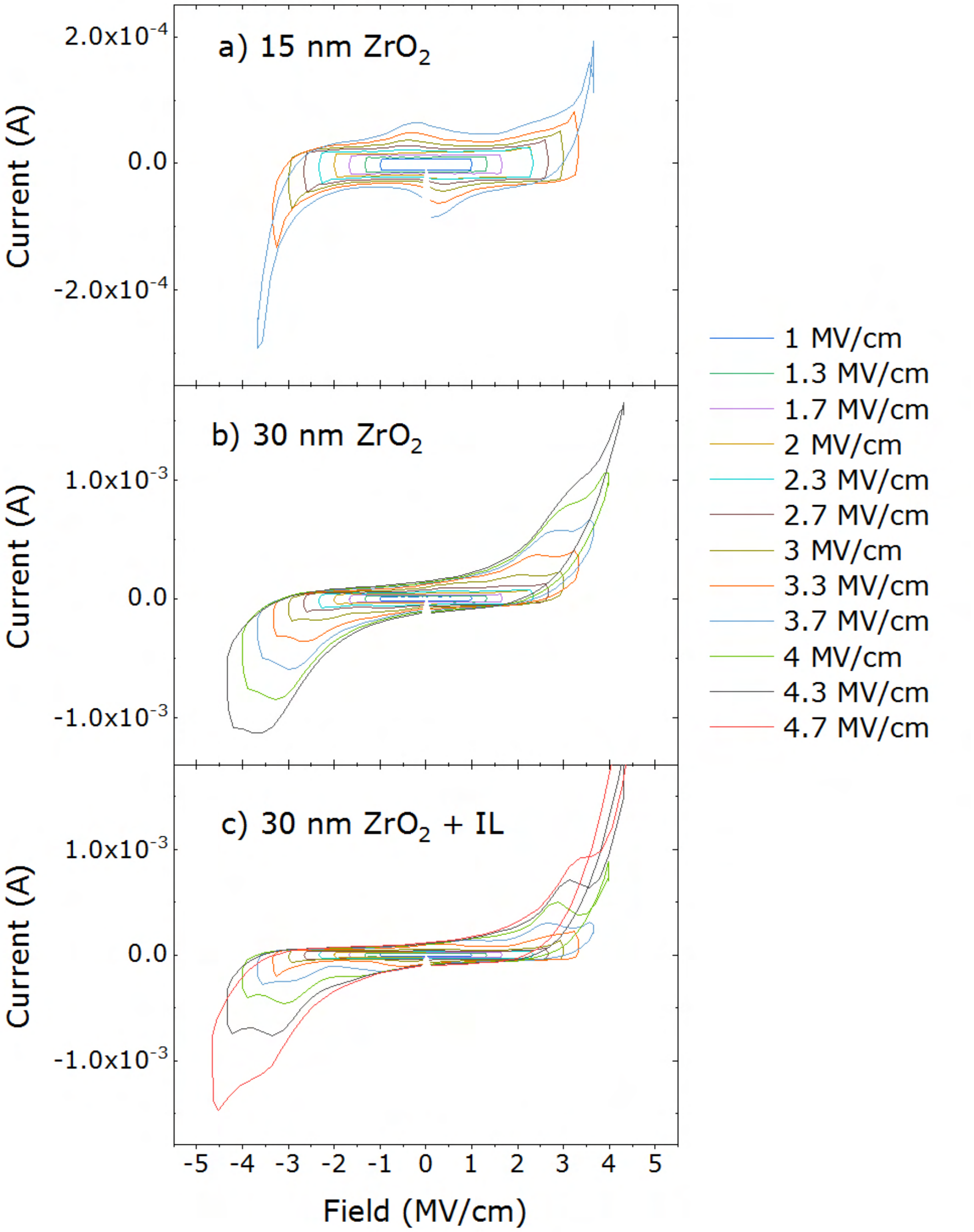

Figure 7.6: I-V curves as from dynamic hysteresis measurements for a) Stack 1, b) Stack 2 and c) Stack 3, measured with progressively increasing triangular pulse amplitude.

DHM measurements were subsequently performed with progressively increasing field amplitude for the three capacitor stacks. The following remarks can be drawn for the three samples:

- **Stack 1:** starting from a field of 2 MV/cm, back-switching peaks start to appear; at 3 MV/cm, the main switching peaks also become visible. The peak position stays constant and the sample behaves in an antiferroelectric-like fashion, where a reversible field-induced phase transition takes place upon the application of an external electric field resulting in the observation of the two sub-loops.
- **Stack 2:** starting from a field of ∼ 2 MV/cm, switching peaks start to appear. By increasing the field, a new couple of peaks appears which finally merges with a rather fast wake-up process with the previously detected switching peaks;
- **Stack 3:** Starting from a field of ∼ 2.5 MV/cm, switching peaks start to appear. At 3 MV/cm, a second switching peak starts to appear. Both peaks shift towards high absolute values fields until they merge in a single peak. The starting peaks show a greater separation as compared to those detected in Stack 2, resulting in a more pronounced wake-up process.

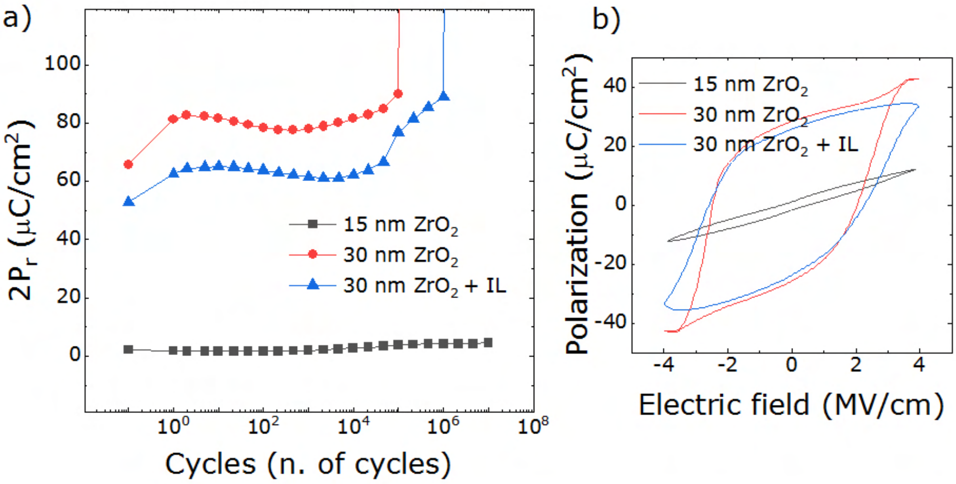

Figure 7.7: a) $2P_r$ with respect to the number of applied field cycles and b) dynamic leakage compensated polarization vs. electric field curves after 10^2 field cycles for a 15 nm, a 30 nm and a 30 nm + Al_2O_3 interlayer ZrO_2-based capacitor stacks.

The behavior with respect to field cycling was also investigated. Figure 7.7 a) shows the evolution of the remanent polarization for the three layer stacks with respect to the amount of imposed write cycles with a field of 4 MV/cm. The AFE-like behavior of Stack 1 is confirmed along the whole device lifetime, with rather constant, close to 0 remanent polarization values. The high amount of detected t-phase allows the device to survive 10^7 field cycles before hard break-down. The behavior of Stacks 2 and 3 is instead different, with high remanent polarization values of $2P_r$ of ∼ 60 and 80 $\mu C/cm^2$, respectively, although an overestimation of ∼ 20% in the P_r values is expected due to the prominent leakage current contributions, as observable in figure 7.6 at high fields values. Figure 7.7 b) shows the dynamic leakage compensated P-E meausurements for the three capacitors extracted after 100 field cycles with the procedure described in [267], which confirm lower P_r values for Stack

3. The slightly larger amount of monoclinic phase detected in Stack 2 could be responsible for the early break-down of the device. Stack 3 seems to show the strongest wake-up, reaching similar remanent polarization values as the ones shown by Stack 2 only in the last two cycle decades of its lifetime.

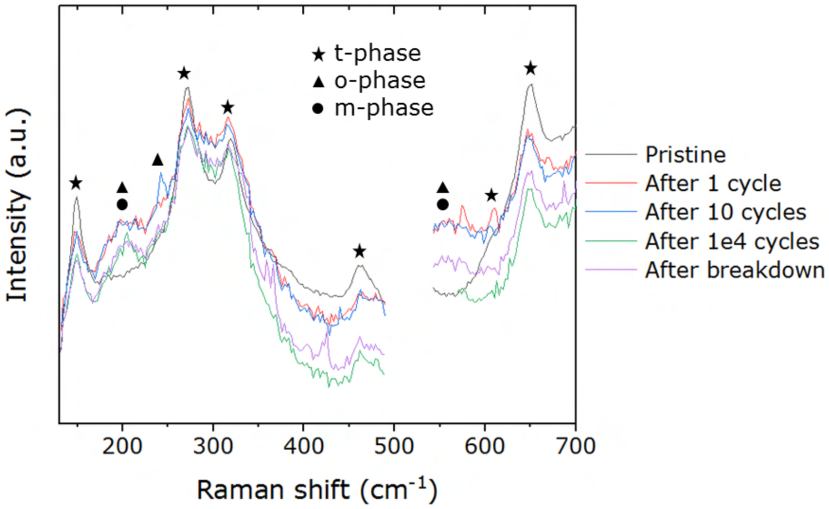

Figure 7.8: Raman spectra of a 30 nm ZrO_2 film with 5 cycles Al_2O_3 interlayer at different device lifetime stages. The main peaks are related to simulated reference spectra for the three main crystalline phases (symbols).

In order to verify the validity of the hypothesis of an irreversible field-induced phase transition, Raman measurements were performed by collaborators on Stack 3 at different stages of its device lifetime with a continuous wave laser of 405 nm wavelength. The capacitor was measured in its pristine state, after 1, 10 and 10000 field cycles and after hard breakdown. Raman spectroscopy presents a twofold advantage in comparison to GIXRD for phase extraction: first, the laser is able to analyze a more confined sample area, allowing single capacitor characterization; second, the main peaks corresponding to the tetragonal and the orthorhombic phase are not overlapping, allowing the two phases to be distinguished.

Figure 7.8 shows the experimentally acquired Raman patterns for Stack 3, as well as the calculated reference main peaks for the t, the polar o- and the m-phase. Reference Raman spectra were simlulated by Alfred Kersch et al. at the Hochschule München, Germany via DFT. The experimentally revealed peaks seem to match well the reference pattern for the t-phase (see star symbols), confirming the result of the GIXRD measurements. Nonetheless, some of these peaks seem to decrease in intensity during device cycling, such as those at ~ 640 cm^{-1} and ~ 270 cm^{-1}. At the same time, new peaks appear which were not present in the first stages of the device lifetime, which can be associated either to the o- or to the m-phase (triangle and circle symbols, respectively), see the peak at ~ 200 and 560 cm^{-1}. These observations would support the hypothesis of a field-induced phase transition happening upon the application of an external field, as speculated above because of switching peak gradual merging.

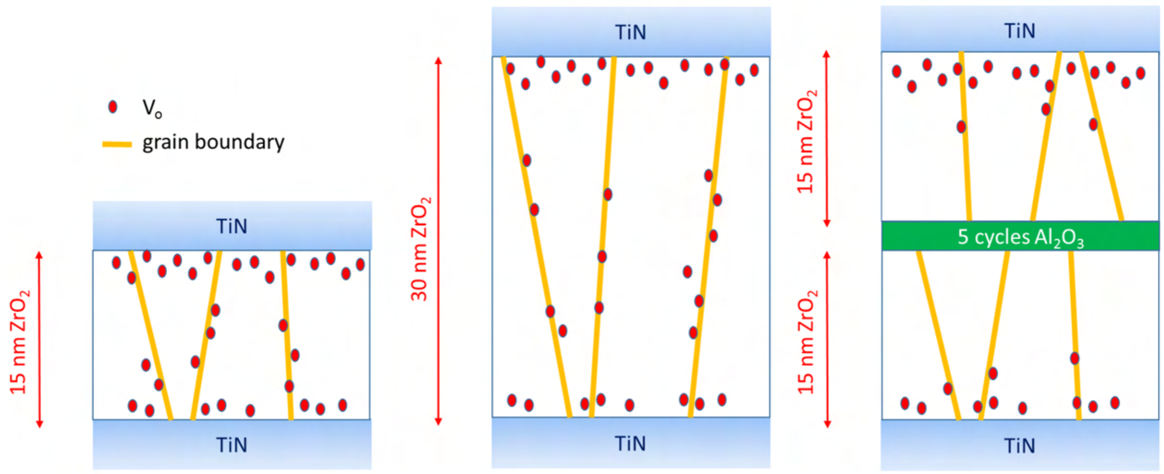

Figure 7.9: Sketch of a 15 nm, a 30 nm and a 30 nm + Al_2O_3 interlayer ZrO_2-based capacitor stack. Grain size and oxygen vacancy distribution are hypothesized based on the measured evidences.

Based on the observations above, the following remarks were drawn and schematically summarized in Figure 7.9:

- in both Stack 1 and Stack 3 the grain growth is limited to an out-of-plane thickness of 15 nm. This avoids excessive grain growth and suppresses the formation of the monoclinic phase, which is instead observed in Stack 2;

- despite grain size being comparable in Stack 1 and Stack 3, the crystallization process ultimately yields two very different phase configurations: the t-phase is detected to be prevalent in Stack 1, resulting in a reversible field-induced phase transition between the t- and the polar o-phase and consequently in the typical antiferroelectric-like behavior with almost zero remanent polarization. Conversely, the o-phase is mostly stabilized in Stack 3, where a wake-up process is observed, probably related to an irreversible phase transition of some of the t-phase present in the layer. Such a statement is confirmed through Raman measurements, showing the disappearance of some of the peaks relative to the t-phase and the emergence of new peaks associated either with the polar o- or the m-phase. Three causes can be inferred for this observation: on one hand, hypothesizing stress and strain in the layer being induced by TiN, the higher total thickness of Stack 3 can mean that lower stress is experienced in the bulk of the film, allowing the transition from the t- to the po-phase; second, given oxygen vacancies are mostly formed at the interface with TiN, a lower total amount of V_o, averaged along film thickness, could be present within Stack 3, shifting the equilibrium from the t- to the po-phase; last but not least, the Al_2O_3 interlayer could also provide additional oxygen, which once again encourages the formation of the po-phase with respect to the t-phase and allows the formation of a relatively low amount of m-phase;

- though the effect of TiN being similar in the case of Stack 2 and Stack 3, given the similar total thickness and surface/bulk ratio, surface energy contributions related to the absence of the interlayer result in a larger m-phase amount. The stronger presence of the m-phase harms device reliability resulting in early device hard-breakdown. Nonetheless, similar po- and t-phase amounts are detected within the two stacks, yielding similar wake-up behavior and remanent polarization values.

Both the electrical and the structural measurements performed on the three layer stacks help to recognize how different effects can concur in the stabilization of the ferroelectric phase and properties in ZrO_2 and possibly in HfO_2-based layers.

7.4 Summary

In this chapter, the effect of oxygen content, strain/stress, dopant introduction and presence of an interlayer were considered both separately and concurrently.

First, a model was introduced supported by DFT calculations, showing that even in undoped HfO_2 thin films ferroelectricity can be obtained by introducing oxygen vacancies, which create a stabilization valley for the t- and subsequently for the polar o-phase. An opposite effect is simulated for an oxygen excess, where oxygen interstitial defects promote the direct transition to the monoclinic phase.

Afterward, the effect of the introduction of dopant atoms was exposed and linked to the appearance of an additional tensile/compressive stress in the layer depending on dopant ionic size. Simulation results were displayed addressing the interplay of doping and different oxygen contents in HfO_2 based layers. It was shown how dopant size can lead to the stabilization of either the t- or the c-phase with increasing dopant concentration and that the dopant elements having a bigger atomic radius as compared to Hf (i.e. Zr) strongly interact with oxygen defects in determining crystallization within the doped HfO_2 layers.

The influence of interface/interlayer stress was also considered through literature reports, showing how lattice and thermal expansion coefficient mismatches can induce additional mechanical solicitations in the films resulting in a more favored polar phase.

Eventually, three ZrO_2 capacitor stacks were fabricated and structural and electrical characterization results were exposed, confirming the strong interplay between surface energy effects, stress and oxygen content in determining the crystallization behavior and the ferroelectric response of the capacitors.

8 Demonstration of a 64 kbit 1T1C FeRAM-based array

Starting from the results and the knowledge acquired within this work, Sony Semiconductor Solutions Corporation was able to develop a 64-kbit 1T1C FeRAM array based on ferroelectric $Hf_{0.5}Zr_{0.5}O_2$. This was reported in [2], [4]. This chapter aims to elucidate the strategy for device integration and to show the outstanding bit functionality and memory reliability demonstrated by the fabricated array.

8.1 Device integration

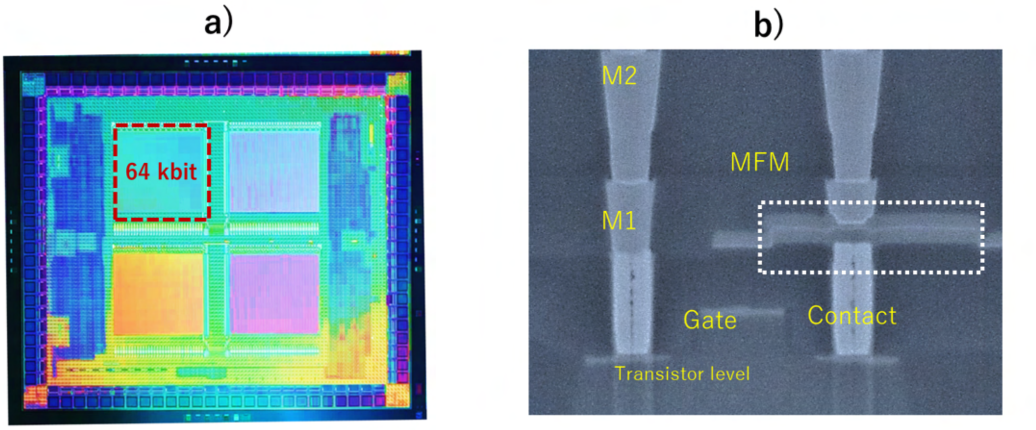

Figure 8.1: a) Optical microscope picture of the 64 kbit 1T1C FeCap array and b) cross-section SEM picture of a FeCap integrated within a back-end of line process. MFM represents the metal-ferroelectric-metal capacitor and M1 and M2 the bit line (BL) contacting metals. Adapted from [2].

Figure 8.1 a) shows a top view optical microscope picture of the fabricated 1T1C FeRAM array. The proposed dedicated circuit included capacitors with a size ranging from 0.06 to 1.0 μm^2. A single capacitor, the dedicated transistor and the back-end of line (BEOL) contacting are shown in the cross section SEM picture in figure 8.1 b). Metal-ferroelectric-metal (MFM) capacitors were annealed at a temperature of 500°C prior to BEOL integration not to interfere with the circuit wiring fabrication. A dedicated sense amplifier was built in order to read the stored data through voltage sensing.

8.2 Data read-out operation

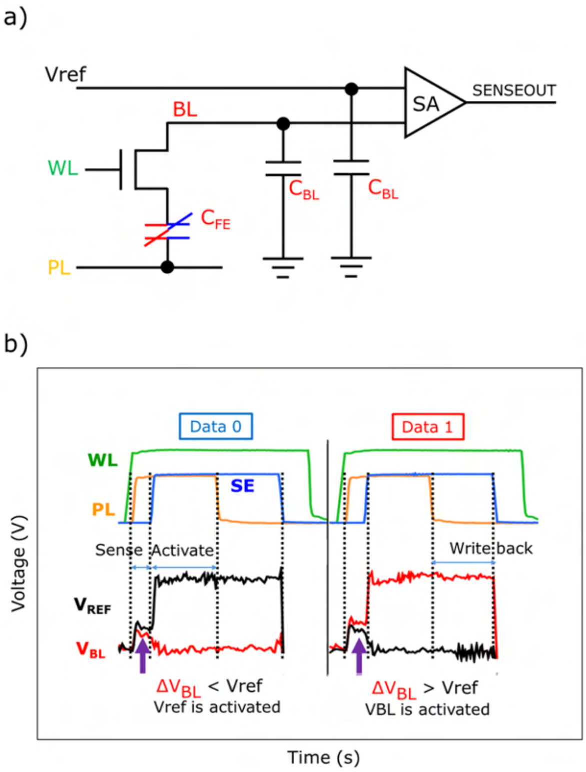

Figure 8.2: a) Schematic representation of the read-out operation. The 1T1C cell is connected to the bit line (BL), word line (WL) and plate line (PL). The sense amplifier (SA) detects the change in the voltage at the BL depending on the capacitance at the BL (C_{BL}) and at the ferroelectric capacitor (C_{FE}); b) time diagram of the read-out operation. First, V_{BL} is sensed and compared with the reference voltage V_{ref} (sense). For Data 0, if V_{BL} is larger than V_{ref}, V_{BL} is discharged to ground. For Data 1, if V_{BL} is smaller than V_{ref}, V_{BL} is activated to V_{DD} by a sense enable pulse (SE) (activate). For destructive read-out, the data has to be written back (write back). Adapted from [2].

Figure 8.2 a) presents a schematic of the reading operation implemented for the 1T1C cell. The read-out operation in a FeRAM was already introduced in chapter 2 and its time diagram is hereby reported in figure 8.2 b). First, the bit line is set to a ground potential. After that, the word line WL (green) is activated and a positive pulse is applied to the plate line PL (yellow). During "Sense", the voltage is measured at the bit line (V_{BL}, red) and compared to a reference voltage (V_{ref}, black). Depending on the polarization state of the ferroelectric, a switching event will or will not take place. In case of no switching, a negative difference between V_{BL} and V_{ref} is detected (Data 0), V_{BL} is set to ground again and the reference voltage is activated to a certain voltage V_{DD} by a sense enable pulse (SE) ("Activate", blue). On the contrary, a switching event in the capacitor will result in a positive difference between the read bit line voltage and the reference voltage (Data 1). In that case, V_{BL} is activated to V_{DD}. The reading operation is destructive and the information has to be refreshed after read-out ("Write back").

The signal should be strong and clean enough to be able to distinguish the two capacitor states. For this reason, the successful data reading presents constraints in terms of the amplitude and width of the applied reading voltage pulse.

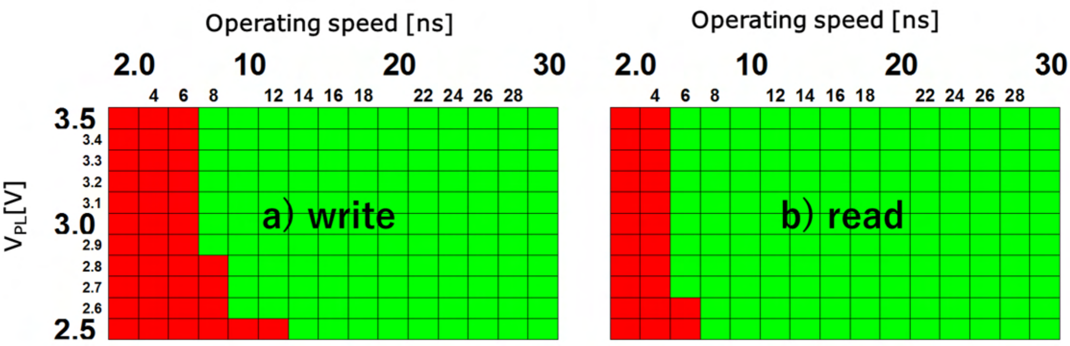

Figure 8.3: Shmoo plot for a) write and b) read operation of 1T1C cells with a capacitor size of 1 μm^2 as a function of write/read pulse amplitude (x-axis) and time (y-axis). Green and red squares represent successful and failed write/read operation, respectively. Adapted from [2].

Figure 8.3 shows a Shmoo plot i.e. a matrix of reading time and voltages, where successful reading is indicated with a green square whereas reading failure with a red one. For a 1 μm^2 capacitor size, no failure was encountered for voltages larger than 2.5 V and write and read times of 14 and 8 ns, respectively.

8.3 Memory window distribution and device scalability

In order to integrate the FeRAM concept in high-density arrays, scalability in terms of capacitor size has to be taken into account. With that purpose, device functionality with respect to device area was analyzed. Figure 8.4 shows the normal probability sigma of bit line voltages V_{BL} differences for a 1T1C FeRAM-based 64 kbit array with 0.06, 0.20, 0.40, and 1.00 μm^2 capacitor size operated with 2 V and 100 ns read voltage amplitude and width. Sigma gives an indication of the width of the probability distribution i.e. the straighter the sigma trend, the more narrow the data distribution. In this case, a small distribution of $\sim$ 10 mV/sigma is observed, meaning almost perfect bit functionality even for the smallest capacitors, as confirmed by the wide read margin between the 1 and the 0 data, related to the memory window. Successful scalability with ferroelectric properties improvement when reducing device thickness from 10 to 8 nm was also demonstrated and reported in [4].

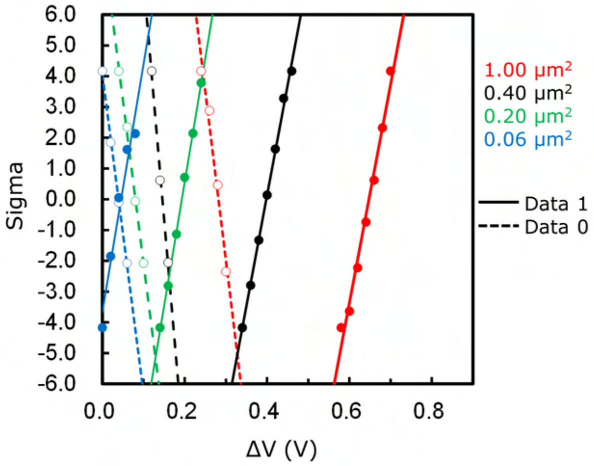

Figure 8.4: Sigma i.e distribution of the memory windows ΔV as calculated from the measured V_{BL} for 1T1C FeRAM-based 64 kbit arrays with 0.06, 0.20, 0.40, and 1.00 μm^2 capacitor size at 2.0 V and 100 ns read voltage amplitude and width. The solid line and the full dots correspond to Data 1, the dashed line and the empty dots to Data 0. Adapted from [4].

8.4 Reliability: time to breakdown and field cycling endurance

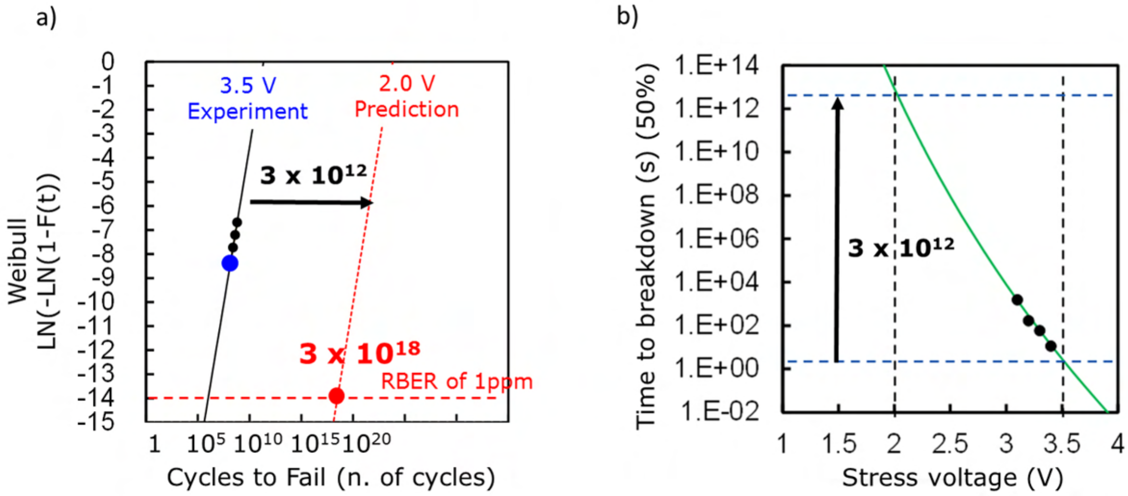

Figure 8.5: a) Weibull distribution fitting plot as a function of number of cycles before device read-out failure. Data points were acquired at 3.5 V and predicted for 2.0 V operating voltages. An increase of $3{\cdot}10^{12}$ cycles before device failure is expected for 2.0 V; b) time to breakdown as a function of stress voltage for 1.00 μm^2 capacitor size devices. A power law fitting (green line) of time dependent dielectric breakdown (TDDB) measurement data points (black dots) was used to estimate the improvement factor of $3{\cdot}10^{12}$ used in panel a). Adapted from [4].

Raw bit error rates (RBERs) were measured on a sample of 4 kbits up to 10^{10} cycles. In figure 8.5 a), the Weibull distribution was plotted as a function of the number of cycles before device hard breakdown. An accelerated measurement at 85°C with 3.5 V and 100 ns operation voltage and time was performed to predict the endurance for a 2.0 V operation voltage. The acceleration factor was calculated through time-dependent dielectric breakdown (TDDB) measurements, as shown in Fig. 8 b). First, the time before hard breakdown when applying a DC stress voltage of 3.1 V, 3.2 V, 3.3 V, and 3.4 V was measured (black dots). The experimental data points were fitted by means of a power law (green curve) in order to extrapolate the time to breakdown at a stress voltage of 2.0 V. An improvement of $3 \cdot 10^{12}$ was calculated, resulting in $3 \cdot 10^{18}$ cycles before device read-out failure for an operation voltage of 2 V at a RBER of 1 ppm. In other words, an endurance larger than 10^{18} cycles can be predicted for a 1 μm^2 large device operated at 2.0 V, 100 ns.

8.5 Summary

In this chapter, the successful functionality of a 64 kbit 1T1C FeRAM array fabricated by Sony Semiconductor Solutions Corporation thanks to the optimization performed within this work was demonstrated. First, the integration process was described. After that, the read-out operation by means of a sense amplifier was elucidated. For 1.00 μm^2 large devices, perfect bit functionality was shown for voltages higher than 2.5 V and write and read times of 14 and 8 ns, respectively. A normal probability distribution demonstrated a narrow memory window distribution confirming device functionality down to a 0.06 μm^2 device size. Accelerated reliability measurements with respect to time to breakdown and cycles to breakdown predicted an endurance larger than 10^{18} cycles for 1 μm^2 large devices operated at 2.0 V and 100 ns.

9 Summary and conclusions

Continuously increasing data production and storage requirements comprise as a drawback the necessity of mastering the down-scaling and the reduction of power consumption of memory devices. Despite the step ahead enabled by the embedding of data memories into microprocessors, traditional memory concepts still require optimization in terms of size, power and cost per bit. For this reason, novel technologies are being explored where bits are stored in an unconventional manner (see magnetic RAM, phase-change RAM, resistive RAM, etc.). Among those, ferroelectric RAM offers a bridge between the scalability and the operational speed of DRAM and the endurance and non-volatility of Flash, being a good candidate for becoming a non-volatile RAM. If in the past the advancement of such a memory concept was stopped because of intrinsic scaling limitation of traditional perovskite materials, the discovery of ferroelectricity in HfO_2-based thin films re-awakened the interest in this class of devices. From that moment onward, along with more conventional memory concepts such as FeRAM and FeFET new solutions were explored such as ferroelectric tunnel junctions, negative capacitance transistors and neuromorphic computing applications.

This work focused on the optimization of the main building block of a 1T1C FeRAM memory array, i.e. the ferroelectric capacitor. The understanding of ferroelectricity establishment and the improvement of the reliability properties were targeted through process optimization of every single layer of the capacitor stack. A $Hf_xZr_{1-x}O_2$ thin film was chosen as active ferroelectric material.

In chapter 4, the fabrication of the ferroelectric oxide itself was addressed. First, different metal precursor combinations were considered and an optimal interval for the deposition temperature was determined to limit the amount of impurities in the targeted film and stabilize a homogeneous growth behavior. It was shown how the ALD window for each source is closely related to the chemistry of its fundamental molecule. In particular, a combination of TEMA-Hf and ZyALD was found to be the most advantageous both in terms of layer growth quality and established ferroelectric properties. Afterward, other deposition parameters were addressed such as chamber temperature and oxygen supply. It was demonstrated how the amount of oxygen introduced during the ALD deposition strongly affects the crystalline phase of the material, with more oxygen leading to the stabilization of the monoclinic phase, the tetragonal phase being favored by low oxygen amounts and the polar, ferroelectric, orthorhombic phase finding an optimum between these conditions. The gradual introduction of ZrO_2 showed an opposite trend compared to oxygen and a scan of the main ferroelectric properties i.e. remanent polarization, wake-up behavior and endurance led to the election of a Zr:Hf 1:1 ratio and of 1 s ozone dose time as optimal deposition parameters. Last but not least, reliability was addressed through retention measurements and results were compared with those obtained for sputtered films, which showed similar trends.

In chapter 5, process optimization moved to the metal electrodes. Nitride, oxide and metal materials such as TiAlN, MoO_x and W were chosen and compared to the more standard TiN electrodes commonly used in ferroelectric capacitors. The influence of the electrode material choice on phase stabilization, ferroelectric properties and reliability of the fabricated devices was elucidated using structural and electrical characterization. Oxygen vacancy migration, depolarization fields and charge injection at the interface between the ferroelectric oxide and the electrode material were recognized as the main causes for retention degradation. The imprint and the effect of different electrode work functions in generating an internal bias field and a more or less pronounced charge injection were addressed. Whilst TiAlN electrodes strongly harmed device reliability, the best properties were shown by TiN and W electrodes. It was shown how materials with a higher WF could result helpful in reducing charge injection and hence improving retention.

Wanting to deploy the optimized ferroelectric material within different technological concepts, ranging from standard memory arrays to newer applications such as neuromorphic computing, a deeper understanding of the polarization reversal mechanism is necessary. Within chapter 6 the existing models describing ferroelectric switching were exposed and their validity for HfO_2-based thin ferroelectric films was evaluated. The nucleation limited switching was chosen as the most fitting model to describe polarization reversal in such thin films, given their high defectivity which results in many nucleation sites and independent switching events taking place within the different grains. It was shown how a multi-grain Landau approach could also macroscopically describe switching and how an inhomogeneous field model gives a statistical perspective on the field required for switching.

By combining the observations from the chapters above, it emerges how many different factors interact in determining the ferroelectric properties of HfO_2-based thin films. Chapter 7 aimed to give an overview of such elements through the help of literature, simulation work and experimental results. First, a model for the crystallization paths in undoped HfO_2 was supplied, showing how oxygen defects alone can favor the stabilization of a certain phase rather than of another. The interaction of such defects with dopant elements was evaluated also through computational analysis, showing how the same doping element and level can result in a different energetic scenario for phase stabilization depending on the oxygen environment. On the other hand, the effects of different dopant elements were also addressed. It was shown how their atomic size as compared to the one of the host material (Hf or Zr) can result in different mechanical stress in the layer and induce the stabilization first of the polar o-phase and later either of the t- or of the c-phase. Different electrode materials as well as interlayers placed within the HfO_2-based thin layer were found to impact the stress/strain, the amount of supplied oxygen and the surface/volume energy contributions as well, also impacting ferroelectricity.

The goal of optimizing a FeCap was successfully reached as demonstrated within chapter 8. A 64 kbit 1T1C array that deployed the ferroelectric HZO layer optimized within this work was demonstrated by Sony Semiconductor Solutions Corporation as hereby reported. Device operation with functional memory window was successful below 2.0 V and 16 ns operation voltage and time. High endurance $> 10^{18}$ applied cycles was extrapolated with the help of an accelerated measurement at high temperature, confirming the competitiveness of FeRAM in the current memory technology landscape.

As an outlook for future advancements, improved behavior with respect to field cycling and retention could be targeted. With the knowledge gained within this study, a trade-off in the amount of oxygen vacancies in the ferroelectric should be pursued, allowing the concurrent stabilization of the orthorhombic polar phase without harming the reliability performance of the device. As a matter of fact, it was shown how oxide electrodes such as MoO_x help suppress wake-up effects in the first cycles of the device lifetime. In turn, tungsten proved to be beneficial for retention performances. In both cases, the presence of an oxidized interface that limits oxygen scavenging resulted in a reduced amount of oxygen vacancies, translating in a decreased defect migration and charge trapping. Nonetheless, the surplus of supplied oxygen favored the stabilization of the monoclinic phase, which resulted detrimental for device endurance. Furthermore, electrodes with a higher work function seemed to improve imprint behavior because of reduced charge injection, thanks to the higher conduction band offset with the ferroelectric oxide.

That said, further optimization is required on the electrode side, in order to target the two reliability aspects concurrently. An optimum amount of oxygen vacancies required for phase stabilization in combination with a high work function electrode could be set as a target for further technology reliability improvement.

Bibliography

[1] S. Hoffmann-Eifert, D. Richter, and S. T.-M. Kinstry, "Dielectric, Ferroelectric, and Optical Properties", in *Polar Oxides: Properties, Characterization, and Imaging*, Weinheim: Wiley- VCH Verlag GmbH \& Co. KGaA, 2006, p. 30.

[2] J. Okuno, T. Kunihiro, K. Konishi, H. Maemura, Y. Shute, F. Sugaya, M. Materano, T. Ali, K. Kuehnel, K. Seide, U. Schroeder, T. Mikolajick, M. Tsukamoto, and T. Umebayashi, "SoC Compatible 1 T1 C FeRAM Memory Array Based on Ferroelectric Hf0.5Zr0.5O2", in *2020 IEEE Symposium on VLSI Technology*, Jun. 2020, pp. 1–2, ISBN: 2158-9682. DOI: `10.1109/VLSITechnology18217.2020.9265063`.

[3] Ava Jiang Tan, Yu-Hung Liao, Li-Chen Wang, Jong-Ho Bae, Chenming Hu, and Sayeef Salahuddin, "Ferroelectric HfO$_2$ Memory Transistors with High-κ Interfacial Layer and Write Endurance Exceeding $10̂{10}$ Cycles}", 2021.

[4] J. Okuno, T. Kunihiro, K. Konishi, H. Maemura, Y. Shuto, F. Sugaya, M. Materano, T. Ali, M. Lederer, K. Kuehnel, K. Seidel, U. Schroeder, T. Mikolajick, M. Tsukamoto, and T. Umebayashi, "High-Endurance and Low-Voltage Operation of 1T1C FeRAM Arrays for Nonvolatile Memory Application", in *2021 IEEE International Memory Workshop (IMW)*, 2021, pp. 1–3. DOI: `10.1109/IMW51353.2021.9439595`.

[5] T Schenk, M Pešić, S Slesazeck, U Schroeder, and T Mikolajick, "Memory technology—a primer for material scientists", *Reports on Progress in Physics*, vol. 83, no. 8, p. 086 501, Aug. 2020, ISSN: 0034-4885, 1361-6633. DOI: `10.1088/1361-6633/ab8f86`.

[6] A. Bhavnagarwala, S. Kosonocky, C. Radens, K. Stawiasz, R. Mann, Q. Ye, and K. Chin, "Fluctuation Limits and Scaling Opportunities for CMOS SRAM Cells", in *IEEE International Electron Devices Meeting, 2005. IEDM Technical Digest.*, 2005, pp. 659–662. DOI: `10.1109/IEDM.2005.1609437`.

[7] J. Valasek, "Piezo-Electric and Allied Phenomena in Rochelle Salt", *Physical Review*, vol. 17, no. 4, pp. 475–481, Apr. 1921. DOI: `10.1103/PhysRev.17.475`.

[8] J. Müller, P. Polakowski, S. Mueller, and T. Mikolajick, "Ferroelectric Hafnium Oxide Based Materials and Devices: Assessment of Current Status and Future Prospects", *ECS Journal of Solid State Science and Technology*, vol. 4, no. 5, N30–N35, 2015. DOI: `10.1149/2.0081505jss`.

[9] T. S. Böscke, J. Müller, D. Bräuhaus, U. Schröder, and U. Böttger, "Ferroelectricity in hafnium oxide thin films", *Applied Physics Letters*, vol. 99, no. 10, p. 102 903, Sep. 2011, ISSN: 0003-6951, 1077-3118. DOI: `10.1063/1.3634052`.

[10] E. T. Breyer, H. Mulaosmanovic, T. Mikolajick, and S. Slesazeck, "Reconfigurable NAND/NOR Logic Gates in 28 Nm HKMG and 22 Nm FD-SOI FeFET Technology", in *2017 IEEE International Electron Devices Meeting (IEDM)*, Dec. 2017, pp. 28.5.1–28.5.4. DOI: `10.1109/IEDM.2017.8268471`.

[11] E. T. Breyer, H. Mulaosmanovic, T. Mikolajick, and S. Slesazeck, “Perspective on Ferroelectric, Hafnium Oxide Based Transistors for Digital beyond von-Neumann Computing”, *Applied Physics Letters*, vol. 118, no. 5, p. 050 501, 2021. DOI: `10.1063/5.0035281`. eprint: `https://doi.org/10.1063/5.0035281`.

[12] H. Mulaosmanovic, E. Chicca, M. Bertele, T. Mikolajick, and S. Slesazeck, “Mimicking biological neurons with a nanoscale ferroelectric transistor”, *Nanoscale*, vol. 10, no. 46, pp. 21 755–21 763, 2018, ISSN: 2040-3364, 2040-3372. DOI: `10.1039/C8NR07135G`.

[13] H. Ryu, H. Wu, F. Rao, and W. Zhu, “Ferroelectric Tunneling Junctions Based on Aluminum Oxide/ Zirconium-Doped Hafnium Oxide for Neuromorphic Computing”, *Scientific Reports*, vol. 9, no. 1, p. 20 383, Dec. 2019, ISSN: 2045-2322. DOI: `10.1038/s41598-019-56816-x`.

[14] B. Max, M. Hoffmann, H. Mulaosmanovic, S. Slesazeck, and T. Mikolajick, “Hafnia-Based Double-Layer Ferroelectric Tunnel Junctions as Artificial Synapses for Neuromorphic Computing”, *ACS Applied Electronic Materials*, vol. 2, no. 12, pp. 4023–4033, Dec. 2020. DOI: `10.1021/acsaelm.0c00832`.

[15] M. Hoffmann, M. Pešić, K. Chatterjee, A. I. Khan, S. Salahuddin, S. Slesazeck, U. Schroeder, and T. Mikolajick, “Direct Observation of Negative Capacitance in Polycrystalline Ferroelectric HfO2”, *Advanced Functional Materials*, vol. 26, no. 47, pp. 8643–8649, Dec. 2016, ISSN: 1616-301X. DOI: `10.1002/adfm.201602869`.

[16] M. Hoffmann, F. P. G. Fengler, M. Herzig, T. Mittmann, B. Max, U. Schroeder, R. Negrea, P. Lucian, S. Slesazeck, and T. Mikolajick, “Unveiling the Double-Well Energy Landscape in a Ferroelectric Layer”, *Nature*, vol. 565, no. 7740, pp. 464–467, Jan. 2019, ISSN: 1476-4687. DOI: `10.1038/s41586-018-0854-z`.

[17] M. Lines and A. Glass, *Principles and Applications of Ferroelectrics and Related Materials*, ser. International Series of Monographs on Physics. OUP Oxford, 2001, ISBN: 978-0-19-850778-9.

[18] N. A. Spaldin, “Analogies and Differences between Ferroelectricsand Ferromagnets”, in *Physics of Ferroelectrics: A Modern Perspective*, Berlin, Heidelberg: Springer Berlin Heidelberg, 2007, pp. 175–218, ISBN: 978-3-540-34591-6. DOI: `10.1007/978-3-540-34591-6âĆĚ`.

[19] R. R. Mehta, B. D. Silverman, and J. T. Jacobs, “Depolarization Fields in Thin Ferroelectric Films”, *Journal of Applied Physics*, vol. 44, no. 8, pp. 3379–3385, 1973. DOI: `10.1063/1.1662770`. eprint: `https://doi.org/10.1063/1.1662770`.

[20] M. Stengel and N. A. Spaldin, “Origin of the Dielectric Dead Layer in Nanoscale Capacitors”, *Nature*, vol. 443, no. 7112, pp. 679–682, Oct. 2006, ISSN: 1476-4687. DOI: `10.1038/nature05148`.

[21] P. D. Lomenzo, C. Richter, T. Mikolajick, and U. Schroeder, “Depolarization as Driving Force in Antiferroelectric Hafnia and Ferroelectric Wake-Up”, *ACS Applied Electronic Materials*, vol. 2, no. 6, pp. 1583–1595, Jun. 2020, ISSN: 2637-6113, 2637-6113. DOI: `10.1021/acsaelm.0c00184`.

[22] P. Wurfel, I. P. Batra, and J. T. Jacobs, "Polarization Instability in Thin Ferroelectric Films", *Physical Review Letters*, vol. 30, no. 24, pp. 1218–1221, Jun. 1973. DOI: `10.1103/PhysRevLett.30.1218`.

[23] B. S. Kwak, A. Erbil, B. J. Wilkens, J. D. Budai, M. F. Chisholm, and L. A. Boatner, "Strain Relaxation by Domain Formation in Epitaxial Ferroelectric Thin Films", *Physical Review Letters*, vol. 68, no. 25, pp. 3733–3736, Jun. 1992. DOI: `10.1103/PhysRevLett.68.3733`.

[24] C. Lichtensteiger, P. Zubko, M. Stengel, P. Aguado-Puente, J. Triscone, P. Ghosez, and J. Junquera, "Ferroelectricity in Ultrathin-FIlm Capacitors", in *Oxide Ultrathin Films*, John Wiley \& Sons, Ltd, 2012, pp. 265–230.

[25] L. D. Landau, "On the Theory of Phase Transitions", *Zhurnal Eksperimental'noi i Teoreticheskoi Fiziki*, vol. 7, pp. 19–32, 1937.

[26] V. L. Ginzburg, "On the Dielectric Properties of Ferroelectric (Segnette-Electric) Crystals and Barium Titanate", *Zhurnal Eksperimental'noi i Teoreticheskoi Fiziki*, vol. 15, pp. 739–749, 1945.

[27] T. Schenk, "Formation of Ferroelectricity in Hafnium Oxide Based Thin Films", Ph.D. dissertation, Technische Universitaet Dresden, Dresden, Germany, 2016.

[28] T. Mikolajick, S. Slesazeck, H. Mulaosmanovic, M. H. Park, S. Fichtner, P. D. Lomenzo, M. Hoffmann, and U. Schroeder, "Next Generation Ferroelectric Materials for Semiconductor Process Integration and Their Applications", *Journal of Applied Physics*, vol. 129, no. 10, p. 100 901, 2021. DOI: `10.1063/5.0037617`. eprint: `https://doi.org/10.1063/5.0037617`.

[29] D. Buck, "Ferroelectrics for Digital Information Storage and Switching", M.S. thesis, MIT Digital Computer Laboratory, 1952.

[30] T. Francois, C. Pellissier, S. Slesazeck, V. Havel, C. Richter, A. Makosiej, B. Giraud, E. T. Breyer, M. Materano, P. Chiquet, M. Bocquet, L. Grenouillet, E. Nowak, U. Schroeder, F. Gaillard, J. Coignus, P. Blaise, C. Carabasse, N. Vaxelaire, T. Magis, F. Aussenac, and V. Loup, "Demonstration of BEOL-compatible ferroelectric Hf $_{0.5}$ Zr $_{0.5}$ O $_{2}$ scaled FeRAM co-integrated with 130nm CMOS for embedded NVM applications", in *2019 IEEE International Electron Devices Meeting (IEDM)*, San Francisco, CA, USA: IEEE, Dec. 2019, pp. 15.7.1–15.7.4, ISBN: 978-1-72814-032-2. DOI: `10.1109/IEDM19573.2019.8993485`.

[31] M. Pešić, U. Schroeder, and T. Mikolajick, "Chapter 10.1 - Ferroelectric One Transistor/One Capacitor Memory Cell", in *Ferroelectricity in Doped Hafnium Oxide: Materials, Properties and Devices*, ser. Woodhead Publishing Series in Electronic and Optical Materials, U. Schroeder, C. S. Hwang, and H. Funakubo, Eds., Woodhead Publishing, 2019, pp. 413–424, ISBN: 978-0-08-102430-0. DOI: `10.1016/B978-0-08-102430-0.00019-X`.

[32] J. Mueller, S. Slesazeck, and T. Mikolajick, "Chapter 10.4 - Ferroelectric Field Effect Transistor", in *Ferroelectricity in Doped Hafnium Oxide: Materials, Properties and Devices*, U. Schroeder, C. S. Hwang, and H. Funakubo, Eds., Woodhead Publishing, Jan. 2019, pp. 451–471, ISBN: 978-0-08-102430-0. DOI: `10.1016/B978-0-08-102430-0.00022-X`.

[33] E. Yurchuk, J. Müller, S. Müller, J. Paul, M. Pešić, R. van Bentum, U. Schroeder, and T. Mikolajick, "Charge-Trapping Phenomena in HfO2-Based FeFET-Type Nonvolatile Memories", *IEEE Transactions on Electron Devices*, vol. 63, no. 9, pp. 3501–3507, Sep. 2016, ISSN: 1557-9646. DOI: `10.1109/TED.2016.2588439`.

[34] T. P. Ma and Jin-Ping Han, "Why Is Nonvolatile Ferroelectric Memory Field-Effect Transistor Still Elusive?", *IEEE Electron Device Letters*, vol. 23, no. 7, pp. 386–388, Jul. 2002, ISSN: 1558-0563. DOI: `10.1109/LED.2002.1015207`.

[35] S. Beyer, S. Dünkel, M. Trentzsch, J. Müller, A. Hellmich, D. Utess, J. Paul, D. Kleimaier, J. Pellerin, S. Müller, J. Ocker, A. Benoist, H. Zhou, M. Mennenga, M. Schuster, F. Tassan, M. Noack, A. Pourkeramati, F. Müller, M. Lederer, T. Ali, R. Hoffmann, T. Kämpfe, K. Seidel, H. Mulaosmanovic, E. T. Breyer, T. Mikolajick, and S. Slesazeck, "FeFET: A Versatile CMOS Compatible Device with Game-Changing Potential", in *2020 IEEE International Memory Workshop (IMW)*, May 2020, pp. 1–4. DOI: `10.1109/IMW48823.2020.9108150`.

[36] M. Trentzsch, S. Flachowsky, R. Richter, J. Paul, B. Reimer, D. Utess, S. Jansen, H. Mulaosmanovic, S. Müller, S. Slesazeck, J. Ocker, M. Noack, J. Müller, P. Polakowski, J. Schreiter, S. Beyer, T. Mikolajick, and B. Rice, "A 28nm HKMG Super Low Power Embedded NVM Technology Based on Ferroelectric FETs", in *2016 IEEE International Electron Devices Meeting (IEDM)*, Dec. 2016, pp. 11.5.1–11.5.4. DOI: `10.1109/IEDM.2016.7838397`.

[37] H. Mulaosmanovic, J. Ocker, S. Müller, U. Schroeder, J. Müller, P. Polakowski, S. Flachowsky, R. van Bentum, T. Mikolajick, and S. Slesazeck, "Switching Kinetics in Nanoscale Hafnium Oxide Based Ferroelectric Field-Effect Transistors", *ACS Applied Materials & Interfaces*, vol. 9, no. 4, pp. 3792–3798, Feb. 2017, ISSN: 1944-8244. DOI: `10.1021/acsami.6b13866`.

[38] E. T. Breyer and S. Slesazeck, "Chapter 10.6 - Ferroelectric Devices for Logic in Memory", in *Ferroelectricity in Doped Hafnium Oxide: Materials, Properties and Devices*, ser. Woodhead Publishing Series in Electronic and Optical Materials, U. Schroeder, C. S. Hwang, and H. Funakubo, Eds., Woodhead Publishing, 2019, pp. 495–513, ISBN: 978-0-08-102430-0. DOI: `10.1016/B978-0-08-102430-0.00024-3`.

[39] M. Hoffmann, S. Slesazeck, T. Mikolajick, and C. S. Hwang, "Chapter 10.5 - Negative Capacitance in HfO2- and ZrO2-Based Ferroelectrics", in *Ferroelectricity in Doped Hafnium Oxide: Materials, Properties and Devices*, ser. Woodhead Publishing Series in Electronic and Optical Materials, U. Schroeder, C. S. Hwang, and H. Funakubo, Eds., Woodhead Publishing, 2019, pp. 473–493, ISBN: 978-0-08-102430-0. DOI: `10.1016/B978-0-08-102430-0.00023-1`.

[40] S. Fujii and M. Saitoh, "Chapter 10.3 - Ferroelectric Tunnel Junction", in *Ferroelectricity in Doped Hafnium Oxide: Materials, Properties and Devices*, ser. Woodhead Publishing Series in Electronic and Optical Materials, U. Schroeder, C. S. Hwang, and H. Funakubo, Eds., Woodhead Publishing, 2019, pp. 437–449, ISBN: 978-0-08-102430-0. DOI: `10.1016/B978-0-08-102430-0.00021-8`.

[41] V. Garcia and M. Bibes, "Ferroelectric Tunnel Junctions for Information Storage and Processing", *Nature Communications*, vol. 5, no. 1, p. 4289, Jul. 2014, ISSN: 2041-1723. DOI: `10.1038/ncomms5289`.

[42] B. Max, M. Hoffmann, S. Slesazeck, and T. Mikolajick, "Ferroelectric Tunnel Junctions Based on Ferroelectric-Dielectric Hf0.5Zr0.5.O2/ A12O3Capacitor Stacks", in *2018 48th European Solid-State Device Research Conference (ESSDERC)*, 3, pp. 142–145, ISBN: 2378-6558. DOI: `10.1109/ESSDERC.2018.8486882`.

[43] S. Fujii, Y. Kamimuta, T. Ino, Y. Nakasaki, R. Takaishi, and M. Saitoh, "First Demonstration and Performance Improvement of Ferroelectric HfO2-based Resistive Switch with Low Operation Current and Intrinsic Diode Property", in *2016 IEEE Symposium on VLSI Technology*, Jun. 2016, pp. 1–2. DOI: `10.1109/VLSIT.2016.7573413`.

[44] B. Max, M. Hoffmann, S. Slesazeck, and T. Mikolajick, "Direct Correlation of Ferroelectric Properties and Memory Characteristics in Ferroelectric Tunnel Junctions", *IEEE Journal of the Electron Devices Society*, vol. 7, pp. 1175–1181, 2019, ISSN: 2168-6734. DOI: `10.1109/JEDS.2019.2932138`.

[45] Sawyer, C. B. and Tower, C. H., "Rochelle Salt as a Dielectric", vol. 35, no. 3, pp. 269–273, 1930, Feb. DOI: `10.1103/PhysRev.35.269`.

[46] A. von Hippel, R. G. Breckenridge, F. G. Chesley, and L. Tisza, "High Dielectric Constant Ceramics", *Industrial & Engineering Chemistry*, vol. 38, no. 11, pp. 1097–1109, Nov. 1946, ISSN: 0019-7866. DOI: `10.1021/ie50443a009`.

[47] G. Shirane and A. Takeda, "Phase Transitions in Solid Solutions of PbZrO3 and PbTiO3 (I) Small Concentrations of PbTiO3", *Journal of the Physical Society of Japan*, vol. 7, no. 1, pp. 5–11, 1952. DOI: `10.1143/JPSJ.7.5`. eprint: `https://doi.org/10.1143/JPSJ.7.5`.

[48] G. Shirane, K. Suzuki, and A. Takeda, "Phase Transitions in Solid Solutions of PbZrO3 and PbTiO3 (II) x-Ray Study", *Journal of the Physical Society of Japan*, vol. 7, no. 1, pp. 12–18, 1952. DOI: `10.1143/JPSJ.7.12`. eprint: `https://doi.org/10.1143/JPSJ.7.12`.

[49] C. A.-P. de Araujo, J. D. Cuchiaro, L. D. McMillan, M. C. Scott, and J. F. Scott, "Fatigue-Free Ferroelectric Capacitors with Platinum Electrodes", *Nature*, vol. 374, no. 6523, pp. 627–629, Apr. 1995, ISSN: 1476-4687. DOI: `10.1038/374627a0`.

[50] T. Furukawa and G. E. Johnson, "Measurements of Ferroelectric Switching Characteristics in Polyvinylidene Fluoride", *Applied Physics Letters*, vol. 38, no. 12, pp. 1027–1029, 1981. DOI: `10.1063/1.92232`. eprint: `https://doi.org/10.1063/1.92232`.

[51] D. Zhao, I. Katsouras, K. Asadi, P. W. M. Blom, and D. M. de Leeuw, "Switching Dynamics in Ferroelectric P(VDF-TrFE) Thin Films", *Physical Review B*, vol. 92, no. 21, p. 214 115, Dec. 2015. DOI: `10.1103/PhysRevB.92.214115`.

[52] S. Fichtner, N. Wolff, F. Lofink, L. Kienle, and B. Wagner, "AlScN: A III-V Semiconductor Based Ferroelectric", *Journal of Applied Physics*, vol. 125, no. 11, p. 114 103, 2019. DOI: `10.1063/1.5084945`. eprint: `https://doi.org/10.1063/1.5084945`.

[53] T. Mikolajick, U. Schroeder, and S. Slesazeck, “The Past, the Present, and the Future of Ferroelectric Memories”, *IEEE Transactions on Electron Devices*, vol. 67, pp. 1434–1443, 2020.

[54] J.-W. Wang, Q.-D. Shen, C.-Z. Yang, and Q.-M. Zhang, “High Dielectric Constant Composite of P(VDF-TrFE) with Grafted Copper Phthalocyanine Oligomer”, *Macromolecules*, vol. 37, no. 6, pp. 2294–2298, Mar. 2004, ISSN: 0024-9297. DOI: `10.1021/ma035685c`.

[55] S. Yang, H. Bao, C. Zhou, Y. Wang, X. Ren, Y. Matsushita, Y. Katsuya, M. Tanaka, K. Kobayashi, X. Song, and J. Gao, “Large Magnetostriction from Morphotropic Phase Boundary in Ferromagnets”, *Physical review letters*, vol. 104, p. 197 201, May 2010. DOI: `10.1103/PhysRevLett.104.197201`.

[56] H. Jaffe, “Piezoelectric Ceramics”, *Journal of the American Ceramic Society*, vol. 41, no. 11, pp. 494–498, 1958. DOI: `10.1111/j.1151-2916.1958.tb12903.x`. eprint: `https://ceramics.onlinelibrary.wiley.com/doi/pdf/10.1111/j.1151-2916.1958.tb12903.x`.

[57] B. Noheda, J. A. Gonzalo, L. E. Cross, R. Guo, S.-E. Park, D. E. Cox, and G. Shirane, “Tetragonal-to-Monoclinic Phase Transition in a Ferroelectric Perovskite: The Structure of $PbZr_{0.52}Ti_{0.48}O_3$”, *Physical Review B*, vol. 61, no. 13, pp. 8687–8695, Apr. 2000. DOI: `10.1103/PhysRevB.61.8687`.

[58] N. Inoue, T. Takeuchi, and Y. Hayashi, “Compositional Design of Pb(Zr, Ti)O/Sub 3/ for Highly Reliable Ferroelectric Memories”, *IEEE Transactions on Electron Devices*, vol. 49, no. 9, pp. 1572–1579, Sep. 2002, ISSN: 1557-9646. DOI: `10.1109/TED.2002.802649`.

[59] T. Sakoda, T. S. Moise, S. R. Summerfelt, L. Colombo, G. Xing, S. R. Gilbert, A. L. S. Loke, S. Ma, R. Kavari, L. A. Wills, and J. Amano, “Hydrogen-Robust Submicron IrOx/Pb(Zr, Ti)O3/Ir Capacitors for Embedded Ferroelectric Memory”, *Japanese Journal of Applied Physics*, vol. 40, no. Part 1, No. 4B, pp. 2911–2916, Apr. 2001. DOI: `10.1143/jjap.40.2911`.

[60] C.-U. Pinnow and T. Mikolajick, “Material Aspects in Emerging Nonvolatile Memories”, *Journal of The Electrochemical Society*, vol. 151, no. 6, K13, 2004. DOI: `10.1149/1.1740785`.

[61] June-Mo Koo, Bum-Seok Seo, Sukpil Kim, Sangmin Shin, Jung-Hyun Lee, Hionsuck Baik, Jang-Ho Lee, Jun Ho Lee, Byoung-Jae Bae, Ji-Eun Lim, Dong-Chul Yoo, Soon-Oh Park, Hee-Suk Kim, Hee Han, Sunggi Baik, Jae-Young Choi, Yong Jun Park, and Youngsoo Park, “Fabrication of 3D Trench PZT Capacitors for 256Mbit FRAM Device Application”, in *IEEE InternationalElectron Devices Meeting, 2005. IEDM Technical Digest.*, Dec. 2005, 4 pp.–343. DOI: `10.1109/IEDM.2005.1609345`.

[62] T. S. Böscke, J. Müller, D. Bräuhaus, U. Schröder, and U. Böttger, *Appl. Phys. Lett.*, vol. 99, p. 102 903, 2011.

[63] J.-C. Dubois, *Ferroelectric Polymers: Chemistry, Physics, and Applications.* H. Singh Nalwa and M. Dekker, Eds. New York, 1996, vol. 8, ISBN: 0-8247-9468-0. eprint: `https://onlinelibrary.wiley.com/doi/pdf/10.1002/adma.19960080622`.

[64] M. Guo, J. Jiang, J. Qian, C. Liu, J. Ma, C.-W. Nan, and Y. Shen, "Flexible Robust and High-Density FeRAM from Array of Organic Ferroelectric Nano-Lamellae by Self-Assembly", *Advanced Science*, vol. 6, no. 6, p. 1 801 931, 2019. DOI: `10.1002/advs.201801931`. eprint: `https://onlinelibrary.wiley.com/doi/pdf/10.1002/advs.201801931`.

[65] P. Muralt, R. G. Polcawich, and S. Trolier-McKinstry, "Piezoelectric Thin Films for Sensors, Actuators, and Energy Harvesting", *MRS Bulletin*, vol. 34, no. 9, pp. 658–664, 2009, ISSN: 1938-1425. DOI: `10.1557/mrs2009.177`.

[66] M. Akiyama, T. Kamohara, K. Kano, A. Teshigahara, Y. Takeuchi, and N. Kawahara, "Enhancement of Piezoelectric Response in Scandium Aluminum Nitride Alloy Thin Films Prepared by Dual Reactive Cosputtering", *Advanced Materials*, vol. 21, no. 5, pp. 593–596, 2009. DOI: `10.1002/adma.200802611`. eprint: `https://onlinelibrary.wiley.com/doi/pdf/10.1002/adma.200802611`.

[67] Fichtner, S., Schoenweger, G., Kreutzer, T.-N., Petraru, A., Kohlstedt, H., Lofink, F., and Wagner, B., "From ISAF (IEEE, 2020) Proceedings", in *ISAF (IEEE, 2020)*, 2020.

[68] H. Harris, K. Choi, N. Mehta, A. Chandolu, N. Biswas, G. Kipshidze, S. Nikishin, S. Gangopadhyay, and H. Temkin, "HfO2 gate dielectric with 0.5 nm equivalent oxide thickness", *Applied Physics Letters*, vol. 81, no. 6, pp. 1065–1067, Aug. 2002, ISSN: 0003-6951, 1077-3118. DOI: `10.1063/1.1495882`.

[69] Y.-S. Lin, R. Puthenkovilakam, and J. P. Chang, "Dielectric property and thermal stability of HfO2 on silicon", *Applied Physics Letters*, vol. 81, no. 11, pp. 2041–2043, Sep. 2002, ISSN: 0003-6951, 1077-3118. DOI: `10.1063/1.1506207`.

[70] M. Bohr, R. Chau, T. Ghani, and K. Mistry, "The High-k Solution", *IEEE Spectrum*, vol. 44, no. 10, pp. 29–35, Oct. 2007, ISSN: 0018-9235. DOI: `10.1109/MSPEC.2007.4337663`.

[71] A. Berthelot, C. Caillat, V. Huard, S. Barnola, B. Boeck, H. Del-Puppo, N. Emonet, and F. Lalanne, "Highly Reliable TiN/ZrO2/TiN 3D Stacked Capacitors for 45 nm Embedded DRAM Technologies", in *2006 European Solid-State Device Research Conference*, Montreux, Switzerland: IEEE, Sep. 2006, pp. 343–346, ISBN: 978-1-4244-0301-1. DOI: `10.1109/ESSDER.2006.307708`.

[72] B Govoreanu and G. S. Kar, "31.6 10x10nm2 Hf/HfOx Crossbar Resistive RAM with Excellent Performance, Reliability and Low-Energy Operation", in *International Electron Devices Meeting 2011*, Washington, DC, USA: IEEE, 2011.

[73] R. Materlik, C. Künneth, and A. Kersch, "The origin of ferroelectricity in Hf $_{1\text{-x}}$ Zr $_{\text{x}}$ O $_{2}$: A computational investigation and a surface energy model", *Journal of Applied Physics*, vol. 117, no. 13, p. 134 109, Apr. 2015, ISSN: 0021-8979, 1089-7550. DOI: `10.1063/1.4916707`.

[74] U. Schroeder, E. Yurchuk, J. Müller, D. Martin, T. Schenk, P. Polakowski, C. Adelmann, M. I. Popovici, S. V. Kalinin, and T. Mikolajick, "Impact of different dopants on the switching properties of ferroelectric hafniumoxide", *Japanese Journal of Applied Physics*, vol. 53, no. 8S1, 08LE02, Aug. 2014, ISSN: 0021-4922, 1347-4065. DOI: `10.7567/JJAP.53.08LE02`.

[75] J. Müller, T. S. Böscke, D. Bräuhaus, U. Schröder, U. Böttger, J. Sundqvist, P. Kücher, T. Mikolajick, and L. Frey, “Ferroelectric Zr0.5Hf0.5O2 Thin Films for Nonvolatile Memory Applications”, *Applied Physics Letters*, vol. 99, no. 11, p. 112 901, Sep. 2011, ISSN: 0003-6951. DOI: `10.1063/1.3636417`.

[76] M. Materano, C. Richter, T. Mikolajick, and U. Schroeder, “Hf $_x$ Zr $_{1-x}$ O $_2$ thin films for semiconductor applications: An Hf- and Zr-ALD precursor comparison”, *Journal of Vacuum Science & Technology A*, vol. 38, no. 2, p. 022 402, Mar. 2020, ISSN: 0734-2101, 1520-8559. DOI: `10.1116/1.5134135`.

[77] A. Pal, V. K. Narasimhan, S. Weeks, K. Littau, D. Pramanik, and T. Chiang, “Enhancing ferroelectricity in dopant-free hafnium oxide”, *Applied Physics Letters*, vol. 110, no. 2, p. 022 903, Jan. 2017, ISSN: 0003-6951, 1077-3118. DOI: `10.1063/1.4973928`.

[78] Y. H. Lee, H. J. Kim, T. Moon, K. D. Kim, S. D. Hyun, H. W. Park, Y. B. Lee, M. H. Park, and C. S. Hwang, “Preparation and characterization of ferroelectric Hf $_{0.5}$ Zr $_{0.5}$ O $_2$ thin films grown by reactive sputtering”, *Nanotechnology*, vol. 28, no. 30, p. 305 703, Jul. 2017, ISSN: 0957-4484, 1361-6528. DOI: `10.1088/1361-6528/aa7624`.

[79] T. Mittmann, M. Michailow, P. D. Lomenzo, J. Gärtner, M. Falkowski, A. Kersch, T. Mikolajick, and U. Schroeder, “Stabilizing the Ferroelectric Phase in HfO2-based Films Sputtered from Ceramic Targets under Ambient Oxygen”, *Nanoscale*, 2021, ISSN: 2040-3364. DOI: `10.1039/D0NR07699F`.

[80] T. Shimizu, K. Katayama, T. Kiguchi, A. Akama, T. J. Konno, and H. Funakubo, “Growth of Epitaxial Orthorhombic YO1.5-Substituted HfO2 Thin Film”, *Applied Physics Letters*, vol. 107, no. 3, p. 032 910, 2015. DOI: `10.1063/1.4927450`. eprint: `https://doi.org/10.1063/1.4927450`.

[81] T. Shimizu, T. Yokouchi, T. Oikawa, T. Shiraishi, T. Kiguchi, A. Akama, T. J. Konno, A. Gruverman, and H. Funakubo, “Contribution of Oxygen Vacancies to the Ferroelectric Behavior of Hf0.5Zr0.5O2 Thin Films”, *Applied Physics Letters*, vol. 106, no. 11, p. 112 904, 2015. DOI: `10.1063/1.4915336`. eprint: `https://doi.org/10.1063/1.4915336`.

[82] U. Böttger, S. Starschich, D. Griesche, and T. Schneller, “Chapter 3.4 - Dopants in Chemical Solution-Deposited HfO2 Films”, in *Ferroelectricity in Doped Hafnium Oxide: Materials, Properties and Devices*, ser. Woodhead Publishing Series in Electronic and Optical Materials, U. Schroeder, C. S. Hwang, and H. Funakubo, Eds., Woodhead Publishing, 2019, pp. 127–143, ISBN: 978-0-08-102430-0. DOI: `10.1016/B978-0-08-102430-0.00010-3`.

[83] X. Sang, E. D. Grimley, T. Schenk, U. Schroeder, and J. M. LeBeau, “On the Structural Origins of Ferroelectricity in HfO2 Thin Films”, *Applied Physics Letters*, vol. 106, no. 16, p. 162 905, 2015. DOI: `10.1063/1.4919135`. eprint: `https://doi.org/10.1063/1.4919135`.

[84] M. H. Park, Y. H. Lee, H. J. Kim, T. Schenk, W. Lee, K. D. Kim, F. P. G. Fengler, T. Mikolajick, U. Schroeder, and C. S. Hwang, “Surface and grain boundary energy as the key enabler to ferroelectricity in nanoscale hafnia-zirconia: Comparison of model and experiment”, vol. 9, no. 28, pp. 9973–9986, 2017.

[85] T. Mittmann, Monica Materano, S. C. Chang, Ilya Karpov, T. Mikolajick, and Uwe Schroeder, "Impact of Oxygen Vacancy Content in Ferroelectric HZO Films on the Device Performance", in *2020 IEEE International Electron Devices Meeting (IEDM)*, San Francisco, CA, USA, 2020.

[86] M. Materano, T. Mittmann, P. D. Lomenzo, C. Zhou, J. L. Jones, M. Falkowski, A. Kersch, T. Mikolajick, and U. Schroeder, "Influence of Oxygen Content on the Structure and Reliability of Ferroelectric Hf $_x$ Zr $_{1-x}$ O $_2$ Layers", *ACS Applied Electronic Materials*, acsaelm.0c00680, Oct. 2020, ISSN: 2637-6113, 2637-6113. DOI: `10.1021/acsaelm.0c00680`.

[87] A. Toriumi, L. Xu, Y. Mori, X. Tian, P. D. Lomenzo, H. Mulaosmanovic, M. Materano, T. Mikolajick, and U. Schroeder, "Material perspectives of HfO $_2$ -based ferroelectric films for device applications", in *2019 IEEE International Electron Devices Meeting (IEDM)*, San Francisco, CA, USA: IEEE, Dec. 2019, pp. 15.1.1–15.1.4, ISBN: 978-1-72814-032-2. DOI: `10.1109/IEDM19573.2019.8993464`.

[88] T. Schenk, C. M. Fancher, M. H. Park, C. Richter, C. Künneth, A. Kersch, J. L. Jones, T. Mikolajick, and U. Schroeder, "On the Origin of the Large Remanent Polarization in La:HfO2", *Advanced Electronic Materials*, vol. 5, no. 12, p. 1 900 303, Dec. 2019, ISSN: 2199-160X. DOI: `10.1002/aelm.201900303`.

[89] R. Athle, A. E. O. Persson, A. Irish, H. Menon, R. Timm, and M. Borg, "Effects of TiN Top Electrode Texturing on Ferroelectricity in Hf1–xZrxO2", *ACS Applied Materials & Interfaces*, Feb. 2021, ISSN: 1944-8244. DOI: `10.1021/acsami.1c01734`.

[90] B. Buyantogtokh, V. Gaddam, and S. Jeon, "Effect of High Pressure Anneal on Switching Dynamics of Ferroelectric Hafnium Zirconium Oxide Capacitors", *Journal of Applied Physics*, vol. 129, no. 24, p. 244 106, 2021. DOI: `10.1063/5.0050535`. eprint: `https://doi.org/10.1063/5.0050535`.

[91] B. Johnson and J. L. Jones, "Chapter 2 - Structures, Phase Equilibria, and Properties of HfO2", in *Ferroelectricity in Doped Hafnium Oxide: Materials, Properties and Devices*, U. Schroeder, C. S. Hwang, and H. Funakubo, Eds., Woodhead Publishing, Jan. 2019, pp. 25–45, ISBN: 978-0-08-102430-0. DOI: `10.1016/B978-0-08-102430-0.00002-4`.

[92] M. Materano, P. D. Lomenzo, A. Kersch, M. H. Park, T. Mikolajick, and U. Schroeder, "Interplay between oxygen defects and dopants: Effect on structure and performance of HfO $_2$ -based ferroelectrics", *Inorganic Chemistry Frontiers*, 10.1039.D1QI00167A, 2021, ISSN: 2052-1553. DOI: `10.1039/D1QI00167A`.

[93] Y. Zhou, Y. Zhang, Q. Yang, J. Jiang, P. Fan, M. Liao, and Y. Zhou, "The Effects of Oxygen Vacancies on Ferroelectric Phase Transition of HfO2-based Thin Film from First-Principle", *Computational Materials Science*, vol. 167, pp. 143–150, Sep. 2019, ISSN: 0927-0256. DOI: `10.1016/j.commatsci.2019.05.041`.

[94] M. H. Park, T. Schenk, and U. Schroeder, "Chapter 3.1 - Dopants in Atomic Layer Deposited HfO2 Thin Films", in *Ferroelectricity in Doped Hafnium Oxide: Materials, Properties and Devices*, ser. Woodhead Publishing Series in Electronic and Optical Materials, U. Schroeder, C. S.

Hwang, and H. Funakubo, Eds., Woodhead Publishing, 2019, pp. 49–74, ISBN: 978-0-08-102430-0. DOI: `10.1016/B978-0-08-102430-0.00005-X`.

[95] E. Yurchuk, J. Müller, S. Knebel, J. Sundqvist, A. P. Graham, T. Melde, U. Schröder, and T. Mikolajick, "Impact of layer thickness on the ferroelectric behaviour of silicon doped hafnium oxide thin films", *Thin Solid Films*, vol. 533, pp. 88–92, Apr. 2013, ISSN: 00406090. DOI: `10.1016/j.tsf.2012.11.125`.

[96] S. Mueller, J. Mueller, A. Singh, S. Riedel, J. Sundqvist, U. Schroeder, and T. Mikolajick, "Incipient Ferroelectricity in Al-Doped HfO2 Thin Films", *Advanced Functional Materials*, vol. 22, no. 11, pp. 2412–2417, 2012. DOI: `10.1002/adfm.201103119`.

[97] F. Mehmood, M. Hoffmann, P. D. Lomenzo, C. Richter, M. Materano, T. Mikolajick, and U. Schroeder, "Bulk Depolarization Fields as a Major Contributor to the Ferroelectric Reliability Performance in Lanthanum Doped Hf $_{0.5}$ Zr $_{0.5}$ O $_2$ Capacitors", *Advanced Materials Interfaces*, vol. 6, no. 21, p. 1 901 180, Nov. 2019, ISSN: 2196-7350, 2196-7350. DOI: `10.1002/admi.201901180`.

[98] A. G. Chernikova, M. G. Kozodaev, D. V. Negrov, E. V. Korostylev, M. H. Park, U. Schroeder, C. S. Hwang, and A. M. Markeev, "Improved Ferroelectric Switching Endurance of La-Doped Hf0.5Zr0.5O2 Thin Films", *ACS Applied Materials & Interfaces*, vol. 10, no. 3, pp. 2701–2708, Jan. 2018, ISSN: 1944-8244. DOI: `10.1021/acsami.7b15110`.

[99] M. Hoffmann, U. Schroeder, T. Schenk, T. Shimizu, H. Funakubo, O. Sakata, D. Pohl, M. Drescher, C. Adelmann, R. Materlik, A. Kersch, and T. Mikolajick, "Stabilizing the ferroelectric phase in doped hafnium oxide", *Journal of Applied Physics*, vol. 118, no. 7, p. 072 006, Aug. 2015, ISSN: 0021-8979, 1089-7550. DOI: `10.1063/1.4927805`.

[100] T. Schenk, S. Mueller, U. Schroeder, R. Materlik, A. Kersch, M. Popovici, C. Adelmann, S. Van Elshocht, and T. Mikolajick, "Strontium Doped Hafnium Oxide Thin Films: Wide Process Window for Ferroelectric Memories", in *2013 Proceedings of the European Solid-State Device Research Conference (ESSDERC)*, Sep. 2013, pp. 260–263. DOI: `10.1109/ESSDERC.2013.6818868`.

[101] L. Xu, T. Nishimura, S. Shibayama, T. Yajima, S. Migita, and A. Toriumi, "Kinetic Pathway of the Ferroelectric Phase Formation in Doped HfO2 Films", *Journal of Applied Physics*, vol. 122, no. 12, p. 124 104, 2017. DOI: `10.1063/1.5003918`. eprint: `https://doi.org/10.1063/1.5003918`.

[102] C. Künneth, R. Materlik, M. Falkowski, and A. Kersch, "Impact of Four-Valent Doping on the Crystallographic Phase Formation for Ferroelectric HfO $_2$ from First-Principles: Implications for Ferroelectric Memory and Energy-Related Applications", *ACS Applied Nano Materials*, vol. 1, no. 1, pp. 254–264, Jan. 2018, ISSN: 2574-0970, 2574-0970. DOI: `10.1021/acsanm.7b00124`.

[103] Xianghan, Xu, Huang, Fei-Ting, Y. Qi, S. Singh, K. M. Rabe, D. Obeysekera, J. Yang, Chu, Ming-Wen, and Cheong, Sang-Wook, "Kinetically-Stabilized Ferroelectricity in Bulk Single-crystalline HfO2:Y",

[104] C. Richter, T. Schenk, M. H. Park, F. A. Tscharntke, E. D. Grimley, J. M. LeBeau, C. Zhou, C. M. Fancher, J. L. Jones, T. Mikolajick, and U. Schroeder, "Si Doped Hafnium Oxide—A "Fragile" Ferroelectric System", *Advanced Electronic Materials*, vol. 3, no. 10, p. 1 700 131, 2017. DOI: `10.1002/aelm.201700131`. eprint: `https://onlinelibrary.wiley.com/doi/pdf/10.1002/aelm.201700131`.

[105] M. H. Park, T. Schenk, C. M. Fancher, E. D. Grimley, C. Zhou, C. Richter, J. M. LeBeau, J. L. Jones, T. Mikolajick, and U. Schroeder, "A Comprehensive Study on the Structural Evolution of HfO2 Thin Films Doped with Various Dopants", *J. Mater. Chem. C*, vol. 5, no. 19, pp. 4677–4690, 2017. DOI: `10.1039/C7TC01200D`.

[106] U. Schroeder, C. Richter, M. H. Park, T. Schenk, M. Pešić, M. Hoffmann, F. P. G. Fengler, D. Pohl, B. Rellinghaus, C. Zhou, C.-C. Chung, J. L. Jones, and T. Mikolajick, "Lanthanum-Doped Hafnium Oxide: A Robust Ferroelectric Material", *Inorganic Chemistry*, vol. 57, no. 5, pp. 2752–2765, Mar. 2018, ISSN: 0020-1669. DOI: `10.1021/acs.inorgchem.7b03149`.

[107] R. Batra, T. D. Huan, G. A. Rossetti, and R. Ramprasad, "Dopants Promoting Ferroelectricity in Hafnia: Insights from a Comprehensive Chemical Space Exploration", *Chemistry of Materials*, vol. 29, no. 21, pp. 9102–9109, Nov. 2017, ISSN: 0897-4756. DOI: `10.1021/acs.chemmater.7b02835`.

[108] T. Schenk, E. Yurchuk, S. Mueller, U. Schroeder, S. Starschich, U. Böttger, and T. Mikolajick, "About the Deformation of Ferroelectric Hystereses", *Applied Physics Reviews*, vol. 1, no. 4, p. 041 103, Nov. 2014. DOI: `10.1063/1.4902396`.

[109] M. H. Park, H. J. Kim, Y. J. Kim, W. Jeon, T. Moon, and C. S. Hwang, "Ferroelectric Properties and Switching Endurance of Hf0.5Zr0.5O2 Films on TiN Bottom and TiN or RuO2 Top Electrodes", *physica status solidi (RRL) – Rapid Research Letters*, vol. 8, no. 6, pp. 532–535, 2014. DOI: `10.1002/pssr.201409017`. eprint: `https://onlinelibrary.wiley.com/doi/pdf/10.1002/pssr.201409017`.

[110] W. Hamouda, A. Pancotti, C. Lubin, L. Tortech, C. Richter, T. Mikolajick, U. Schroeder, and N. Barrett, "Physical Chemistry of the TiN/Hf0.5Zr0.5O2 Interface", *Journal of Applied Physics*, vol. 127, no. 6, p. 064 105, Feb. 2020, ISSN: 0021-8979. DOI: `10.1063/1.5128502`.

[111] M. H. Park, H. J. Kim, K. D. Kim, Y. H. Lee, S. D. Hyun, and C. S. Hwang, "Chapter 3.2 - Impact of Zr Content in Atomic Layer Deposited Hf1-xZrxO2 Thin Films", in *Ferroelectricity in Doped Hafnium Oxide: Materials, Properties and Devices*, ser. Woodhead Publishing Series in Electronic and Optical Materials, U. Schroeder, C. S. Hwang, and H. Funakubo, Eds., Woodhead Publishing, 2019, pp. 75–101, ISBN: 978-0-08-102430-0. DOI: `10.1016/B978-0-08-102430-0.00007-3`.

[112] K. D. Kim, Y. H. Lee, T. Gwon, Y. J. Kim, H. J. Kim, T. Moon, S. D. Hyun, H. W. Park, M. H. Park, and C. S. Hwang, "Scale-up and Optimization of HfO2-ZrO2 Solid Solution Thin Films for the Electrostatic Supercapacitors", *Nano Energy*, vol. 39, pp. 390–399, 2017, ISSN: 2211-2855. DOI: `10.1016/j.nanoen.2017.07.017`.

[113] H. J. Kim, M. H. Park, Y. J. Kim, Y. H. Lee, T. Moon, K. D. Kim, D. Hyun, and C. S. Hwang, "Study on the wake-up effect of ferroelectric Hf0.5Zr0.5O2 films by pulse-switching measurement", p. 10,

[114] Y. Lu, J. Shieh, and F. Tsai, "Induction of Ferroelectricity in Nanoscale ZrO2/HfO2 Bilayer Thin Films on Pt/Ti/SiO2/Si Substrates", *Acta Materialia*, vol. 115, pp. 68–75, 2016, ISSN: 1359-6454. DOI: `10.1016/j.actamat.2016.05.029`.

[115] P. Nukala, M. Ahmadi, Y. Wei, S. de Graaf, S. Matzen, H. W. Zandbergen, B. Kooi, and B. Noheda, "Operando observation of reversible oxygen migration and phase transitions in ferroelectric devices", p. 29,

[116] S. L. Weeks, A. Pal, V. K. Narasimhan, K. A. Littau, and T. Chiang, "Engineering of Ferroelectric HfO2–ZrO2 Nanolaminates", *ACS Applied Materials & Interfaces*, vol. 9, no. 15, pp. 13 440–13 447, Apr. 2017, ISSN: 1944-8244. DOI: `10.1021/acsami.7b00776`.

[117] S. W. Smith, A. R. Kitahara, M. A. Rodriguez, M. D. Henry, M. T. Brumbach, and J. F. Ihlefeld, "Pyroelectric response in crystalline hafnium zirconium oxide (Hf $_{1-x}$ Zr $_{x}$ O $_{2}$) thin films", *Applied Physics Letters*, vol. 110, no. 7, p. 072 901, Feb. 2017, ISSN: 0003-6951, 1077-3118. DOI: `10.1063/1.4976519`.

[118] T. Mittmann, F. P. Fengler, C. Richter, M. H. Park, T. Mikolajick, and U. Schroeder, "Optimizing process conditions for improved Hf 1-x Zr x O 2 ferroelectric capacitor performance", *Microelectronic Engineering*, vol. 178, pp. 48–51, Jun. 2017, ISSN: 01679317. DOI: `10.1016/j.mee.2017.04.031`.

[119] C. S. Hwang, S. K. Kim, and S. W. Lee, "Mass-Production Memories (DRAM and Flash)", in *Atomic Layer Deposition for Semiconductors*, C. S. Hwang, Ed., Boston, MA: Springer US, 2014, pp. 73–122, ISBN: 978-1-4614-8054-9. DOI: `10.1007/978-1-4614-8054-9âĈĎ`.

[120] H. Mulaosmanovic, P. D. Lomenzo, U. Schroeder, S. Slesazeck, T. Mikolajick, and B. Max, "Reliability Aspects of Ferroelectric Hafnium Oxide for Application in Non-Volatile Memories", in *2021 IEEE International Reliability Physics Symposium (IRPS)*, 2021, pp. 1–6. DOI: `10.1109/IRPS46558.2021.9405215`.

[121] S. Deng, Z. Zhao, S. Kurinec, K. Ni, Y. Xiao, T. Yu, and V. Narayanan, "Overview of Ferroelectric Memory Devices and Reliability Aware Design Optimization", in *Proceedings of the 2021 on Great Lakes Symposium on VLSI*, ser. GLSVLSI '21, New York, NY, USA: Association for Computing Machinery, 2021, pp. 473–478, ISBN: 978-1-4503-8393-6. DOI: `10.1145/3453688.3461743`.

[122] J. X. Zheng, G. Ceder, T. Maxisch, W. K. Chim, and W. K. Choi, "First-principles study of native point defects in hafnia and zirconia", *Physical Review B*, vol. 75, no. 10, p. 104 112, Mar. 2007, ISSN: 1098-0121, 1550-235X. DOI: `10.1103/PhysRevB.75.104112`.

[123] X. Zhao and D. Vanderbilt, "First-principles study of structural, vibrational, and lattice dielectric properties of hafnium oxide", *Physical Review B*, vol. 65, no. 23, p. 233 106, Jun. 2002, ISSN: 0163-1829, 1095-3795. DOI: `10.1103/PhysRevB.65.233106`.

[124] J. X. Zheng, G. Ceder, and W. K. Chim, "First-Principles Study on the Concentrations of Native Point Defects in High-Dielectric-Constant Binary Oxide Materials", *physica status solidi (RRL) – Rapid Research Letters*, vol. 2, no. 5, pp. 227–229, Oct. 2008, ISSN: 1862-6254. DOI: `10.1002/pssr.200802152`.

[125] R. Materlik, C. Künneth, M. Falkowski, T. Mikolajick, and A. Kersch, "Al-, Y-, and La-doping effects favoring intrinsic and field induced ferroelectricity in HfO_2 : A first principles study", *Journal of Applied Physics*, vol. 123, no. 16, p. 164 101, Apr. 2018, ISSN: 0021-8979, 1089-7550. DOI: `10.1063/1.5021746`.

[126] D. R. Islamov, V. A. Gritsenko, T. V. Perevalov, V. A. Pustovarov, O. M. Orlov, A. G. Chernikova, A. M. Markeev, S. Slesazeck, U. Schroeder, T. Mikolajick, and G. Y. Krasnikov, "Identification of the nature of traps involved in the field cycling of Hf0.5Zr0.5O2-based ferroelectric thin films", *Acta Materialia*, vol. 166, pp. 47–55, Mar. 2019, ISSN: 13596454. DOI: `10.1016/j.actamat.2018.12.008`.

[127] A. S. Foster, F. Lopez Gejo, A. L. Shluger, and R. M. Nieminen, "Vacancy and interstitial defects in hafnia", *Physical Review B*, vol. 65, no. 17, p. 174 117, May 2002, ISSN: 0163-1829, 1095-3795. DOI: `10.1103/PhysRevB.65.174117`.

[128] P. Buragohain, A. Erickson, P. Kariuki, T. Mittmann, C. Richter, P. D. Lomenzo, H. Lu, T. Schenk, T. Mikolajick, U. Schroeder, and A. Gruverman, "Fluid Imprint and Inertial Switching in Ferroelectric La:HfO2 Capacitors", *ACS Applied Materials & Interfaces*, vol. 11, no. 38, pp. 35 115–35 121, Sep. 2019, ISSN: 1944-8244. DOI: `10.1021/acsami.9b11146`.

[129] S. S. Fields, S. W. Smith, P. J. Ryan, S. T. Jaszewski, I. A. Brummel, A. Salanova, G. Esteves, S. L. Wolfley, M. D. Henry, P. S. Davids, and J. F. Ihlefeld, "Phase-Exchange-Driven Wake-Up and Fatigue in Ferroelectric Hafnium Zirconium Oxide Films", *ACS Applied Materials & Interfaces*, vol. 12, no. 23, pp. 26 577–26 585, Jun. 2020, ISSN: 1944-8244, 1944-8252. DOI: `10.1021/acsami.0c03570`.

[130] W. Hamouda, C. Lubin, S. Ueda, Y. Yamashita, O. Renault, F. Mehmood, T. Mikolajick, U. Schroeder, R. Negrea, and N. Barrett, "Interface Chemistry of Pristine TiN/La: Hf 0.5 Zr 0.5 O 2 Capacitors", *Applied Physics Letters*, vol. 116, no. 25, p. 252 903, Jun. 2020, ISSN: 0003-6951. DOI: `10.1063/5.0012595`.

[131] T. Szyjka, L. Baumgarten, T. Mittmann, Y. Matveyev, C. Schlueter, T. Mikolajick, U. Schroeder, and M. Müller, "Enhanced Ferroelectric Polarization in TiN/HfO2/TiN Capacitors by Interface Design", *ACS Applied Electronic Materials*, Sep. 2020. DOI: `10.1021/acsaelm.0c00503`.

[132] T. Schenk, U. Schroeder, M. Pešić, M. Popovici, Y. V. Pershin, and T. Mikolajick, "Electric Field Cycling Behavior of Ferroelectric Hafnium Oxide", *ACS Applied Materials & Interfaces*, vol. 6, no. 22, pp. 19 744–19 751, Nov. 2014, ISSN: 1944-8244. DOI: `10.1021/am504837r`.

[133] P. D. Lomenzo, M. Materano, T. Mittmann, P. Buragohain, A. Gruverman, T. Kiguchi, T. Mikolajick, and U. Schroeder, "Harnessing Phase Transitions in Antiferroelectric ZrO2 Using the Size Effect", *Advanced Electronic Materials*, vol. 8, no. 1, p. 2 100 556, 2022. DOI:

`10.1002/aelm.202100556`. eprint: `https://onlinelibrary.wiley.com/doi/pdf/10.1002/aelm.202100556`.

[134] T. Shimizu, Y. Tashiro, T. Mimura, T. Kiguchi, T. Shiraishi, T. J. Konnno, O. Sakata, and H. Funakubo, "Electric-Field-Induced Ferroelectricity in 5$\%$ Y-Doped Hf0.5Zr0.5O2: Transformation from the Paraelectric Tetragonal Phase to the Ferroelectric Orthorhombic Phase", *physica status solidi (RRL) – Rapid Research Letters*, vol. n/a, no. n/a, DOI: `10.1002/pssr.202000589`. eprint: `https://onlinelibrary.wiley.com/doi/pdf/10.1002/pssr.202000589`.

[135] E. D. Grimley, T. Schenk, X. Sang, M. Pešić, U. Schroeder, T. Mikolajick, and J. M. LeBeau, "Structural Changes Underlying Field-Cycling Phenomena in Ferroelectric HfO $_2$ Thin Films", *Advanced Electronic Materials*, vol. 2, no. 9, p. 1 600 173, Sep. 2016, ISSN: 2199160X. DOI: `10.1002/aelm.201600173`.

[136] P. D. Lomenzo, S. Slesazeck, M. Hoffmann, T. Mikolajick, U. Schroeder, B. Max, and T. Mikolajick, "Ferroelectric Hf1-xZrxO2 Memories: Device Reliability and Depolarization Fields", in *2019 19th Non-Volatile Memory Technology Symposium (NVMTS)*, 28, pp. 1–8. DOI: `10.1109/NVMTS47818.2019.9043368`.

[137] T. Shimizu, T. Mimura, T. Kiguchi, T. Shiraishi, T. Konno, Y. Katsuya, O. Sakata, and H. Funakubo, "Ferroelectricity Mediated by Ferroelastic Domain Switching in HfO2-based Epitaxial Thin Films", *Applied Physics Letters*, vol. 113, no. 21, p. 212 901, Nov. 2018, ISSN: 0003-6951. DOI: `10.1063/1.5055258`.

[138] M. Lederer, T. Kämpfe, N. Vogel, D. Utess, B. Volkmann, T. Ali, R. Olivo, J. Müller, S. Beyer, M. Trentzsch, K. Seidel, and L. M. Eng, "Structural and Electrical Comparison of Si and Zr Doped Hafnium Oxide Thin Films and Integrated FeFETs Utilizing Transmission Kikuchi Diffraction", p. 11, 2020.

[139] M. Pešić, F. P. G. Fengler, L. Larcher, A. Padovani, T. Schenk, E. D. Grimley, X. Sang, J. M. LeBeau, S. Slesazeck, U. Schroeder, and T. Mikolajick, "Physical Mechanisms behind the Field-Cycling Behavior of HfO $_2$ -Based Ferroelectric Capacitors", *Advanced Functional Materials*, vol. 26, no. 25, pp. 4601–4612, Jul. 2016, ISSN: 1616301X. DOI: `10.1002/adfm.201600590`.

[140] F. P. G. Fengler, M. Pešić, S. Starschich, T. Schneller, C. Künneth, U. Böttger, H. Mulaosmanovic, T. Schenk, M. H. Park, R. Nigon, P. Muralt, T. Mikolajick, and U. Schroeder, "Domain Pinning: Comparison of Hafnia and PZT Based Ferroelectrics", *Advanced Electronic Materials*, vol. 3, no. 4, p. 1 600 505, Apr. 2017, ISSN: 2199-160X. DOI: `10.1002/aelm.201600505`.

[141] A. K. Tagantsev, I. Stolichnov, E. L. Colla, and N. Setter, "Polarization fatigue in ferroelectric films: Basic experimental findings, phenomenological scenarios, and microscopic features", *Journal of Applied Physics*, vol. 90, no. 3, pp. 1387–1402, Aug. 2001, ISSN: 0021-8979, 1089-7550. DOI: `10.1063/1.1381542`.

[142] X. J. Lou, "Polarization Fatigue in Ferroelectric Thin Films and Related Materials", *Journal of Applied Physics*, vol. 105, no. 2, p. 024 101, 2009. DOI: `10.1063/1.3056603`. eprint: `https://doi.org/10.1063/1.3056603`.

[143] W. L. Warren, D. Dimos, B. A. Tuttle, G. E. Pike, R. W. Schwartz, P. J. Clews, and D. C. McIntyre, "Polarization Suppression in Pb(Zr,Ti)O3 Thin Films", *Journal of Applied Physics*, vol. 77, no. 12, pp. 6695–6702, 1995. DOI: `10.1063/1.359083`. eprint: `https://doi.org/10.1063/1.359083`.

[144] E. L. Colla, S. Hong, D. V. Taylor, A. K. Tagantsev, N. Setter, and K. No, "Direct Observation of Region by Region Suppression of the Switchable Polarization (Fatigue) in Pb(Zr,Ti)O3 Thin Film Capacitors with Pt Electrodes", *Applied Physics Letters*, vol. 72, no. 21, pp. 2763–2765, 1998. DOI: `10.1063/1.121083`. eprint: `https://doi.org/10.1063/1.121083`.

[145] A. K. Tagantsev, M. Landivar, E. Colla, and N. Setter, "Identification of Passive Layer in Ferroelectric Thin Films from Their Switching Parameters", *Journal of Applied Physics*, vol. 78, no. 4, pp. 2623–2630, 1995. DOI: `10.1063/1.360122`. eprint: `https://doi.org/10.1063/1.360122`.

[146] J. F. Scott, "Device Physics of Ferroelectric Memories", *Ferroelectrics*, vol. 183, no. 1, pp. 51–63, 1996. DOI: `10.1080/00150199608224091`. eprint: `https://doi.org/10.1080/00150199608224091`.

[147] Y. Park, K. W. Jeong, and J. T. Song, "Effect of Excess Pb on Fatigue Properties of PZT Thin Films Prepared by Rf-Magnetron Sputtering", *Materials Letters*, vol. 56, no. 4, pp. 481–485, 2002, ISSN: 0167-577X. DOI: `10.1016/S0167-577X(02)00536-0`.

[148] I. Shturman, G. E. Shter, A. Etin, and G. S. Grader, "Effect of LaNiO3 Electrodes and Lead Oxide Excess on Chemical Solution Deposition Derived Pb(Zrx,Ti1-x)O3 Films", *Thin Solid Films*, vol. 517, no. 8, pp. 2767–2774, 2009, ISSN: 0040-6090. DOI: `10.1016/j.tsf.2008.10.007`.

[149] D. Zhou, J. Xu, Q. Li, Y. Guan, F. Cao, X. Dong, J. Müller, T. Schenk, and U. Schröder, "Wake-up Effects in Si-doped Hafnium Oxide Ferroelectric Thin Films", *Applied Physics Letters*, vol. 103, no. 19, p. 192 904, 2013. DOI: `10.1063/1.4829064`. eprint: `https://doi.org/10.1063/1.4829064`.

[150] Y. Goh, S. H. Cho, S.-H. K. Park, and S. Jeon, "Oxygen Vacancy Control as a Strategy to Achieve Highly Reliable Hafnia Ferroelectrics Using Oxide Electrode", *Nanoscale*, vol. 12, no. 16, pp. 9024–9031, 2020. DOI: `10.1039/D0NR00933D`.

[151] T. Mittmann, T. Szyjka, H. A. Hsain, M. C. Istrate, P. D. Lomenzo, L. Baumgarten, M. Müller, J. L. Jones, L. Pintilie, T. Mikolajick, and U. Schroeder, "Impact of Iridium Oxide Electrodes on the Ferroelectric Phase of Thin Hf0.5Zr0.5O2 Films", *physica status solidi (RRL) – Rapid Research Letters*, vol. n/a, no. n/a, DOI: `10.1002/pssr.202100012`. eprint: `https://onlinelibrary.wiley.com/doi/pdf/10.1002/pssr.202100012`.

[152] M. Popovici, A. M. Walke, K. Banerjee, N. Ronchi, J. Meersschaut, U. Celano, S. McMitchell, V. Spampinato, A. Franquet, P. Favia, J. Swerts, G. Van den Bosch, and J. Van Houdt, "Ferroelectric La-Doped ZrO2/HfxZr1-xO2 Bilayer Stacks with Enhanced Endurance", *physica status solidi (RRL) – Rapid Research Letters*, vol. n/a, no. n/a, p. 2 100 033, DOI: `10.1002/pssr.202100033`. eprint: `https://onlinelibrary.wiley.com/doi/pdf/10.1002/pssr.202100033`.

[153] A. Chouprik, E. Kondratyuk, V. Mikheev, Y. Matveyev, M. Spiridonov, A. Chernikova, M. G. Kozodaev, A. M. Markeev, A. Zenkevich, and D. Negrov, "Origin of the retention loss in ferroelectric Hf0.5Zr0.5O2-based memory devices", *Acta Materialia*, vol. 204, p. 116 515, Feb. 2021, ISSN: 13596454. DOI: `10.1016/j.actamat.2020.116515`.

[154] S. Mueller, J. Muller, U. Schroeder, and T. Mikolajick, "Reliability Characteristics of Ferroelectric Si:HfO2 Thin Films for Memory Applications", *IEEE Transactions on Device and Materials Reliability*, vol. 13, no. 1, pp. 93–97, Mar. 2013, ISSN: 1558-2574. DOI: `10.1109/TDMR.2012.2216269`.

[155] T. Y. Lee, K. Lee, H. H. Lim, M. S. Song, S. M. Yang, H. K. Yoo, D. I. Suh, Z. Zhu, A. Yoon, M. R. MacDonald, X. Lei, H. Y. Jeong, D. Lee, K. Park, J. Park, and S. C. Chae, "Ferroelectric Polarization-Switching Dynamics and Wake-Up Effect in Si-Doped HfO2", *ACS Applied Materials & Interfaces*, vol. 11, no. 3, pp. 3142–3149, Jan. 2019, ISSN: 1944-8244. DOI: `10.1021/acsami.8b11681`.

[156] J. J. Lee, C. L. Thio, and S. B. Desu, "Retention and Imprint Properties of Ferroelectric Thin Films", *physica status solidi (a)*, vol. 151, no. 1, pp. 171–182, 1995. DOI: `10.1002/pssa.2211510120`. eprint: `https://onlinelibrary.wiley.com/doi/pdf/10.1002/pssa.2211510120`.

[157] J. Rodriguez, K. Remack, J. Gertas, L. Wang, C. Zhou, K. Boku, J. Rodriguez-Latorre, K. R. Udayakumar, S. Summerfelt, T. Moise, D. Kim, J. Groat, J. Eliason, M. Depner, and F. Chu, "Reliability of Ferroelectric Random Access Memory Embedded within 130nm CMOS", *2010 IEEE International Reliability Physics Symposium*, pp. 750–758, 2010.

[158] C. Li, Y. Yao, X. Shen, Y. Wang, J. Li, C. Gu, R. Yu, Q. Liu, and M. Liu, "Dynamic observation of oxygen vacancies in hafnia layer by in situ transmission electron microscopy", *Nano Research*, vol. 8, no. 11, pp. 3571–3579, Nov. 2015, ISSN: 1998-0124, 1998-0000. DOI: `10.1007/s12274-015-0857-0`.

[159] S. Yu, Y. Yin Chen, X. Guan, H.-S. Philip Wong, and J. A. Kittl, "A Monte Carlo study of the low resistance state retention of HfO $_x$ based resistive switching memory", *Applied Physics Letters*, vol. 100, no. 4, p. 043 507, Jan. 2012, ISSN: 0003-6951, 1077-3118. DOI: `10.1063/1.3679610`.

[160] D. J. J. Loy, P. A. Dananjaya, S. Chakrabarti, K. H. Tan, S. C. W. Chow, E. H. Toh, and W. S. Lew, "Oxygen Vacancy Density Dependence with a Hopping Conduction Mechanism in Multilevel Switching Behavior of HfO $_2$ -Based Resistive Random Access Memory Devices",

ACS Applied Electronic Materials, vol. 2, no. 10, pp. 3160–3170, Oct. 2020, ISSN: 2637-6113, 2637-6113. DOI: `10.1021/acsaelm.0c00515`.

[161] G. Arlt and H. Neumann, "Internal Bias in Ferroelectric Ceramics: Origin and Time Dependence", *Ferroelectrics*, vol. 87, no. 1, pp. 109–120, 1988. DOI: `10.1080/00150198808201374`. eprint: `https://doi.org/10.1080/00150198808201374`.

[162] S. Aggarwal and R. Ramesh, "Point Defect Chemistry of Metal Oxide Heterostructures", *Annual Review of Materials Science*, vol. 28, no. 1, pp. 463–499, 1998. DOI: `10.1146/annurev.matsci.28.1.463`. eprint: `https://doi.org/10.1146/annurev.matsci.28.1.463`.

[163] M. Grossmann, O. Lohse, D. Bolten, U. Boettger, and R. Waser, "The Interface Screening Model as Origin of Imprint in PbZrxTi1-xO3 Thin Films. II. Numerical Simulation and Verification", *Journal of Applied Physics*, vol. 92, no. 5, pp. 2688–2696, 2002. DOI: `10.1063/1.1498967`. eprint: `https://doi.org/10.1063/1.1498967`.

[164] S. Kim, J. Koo, S. Shin, and Y. Park, "Improvement of Retention Loss in Pb(Zr,Ti)O3 Capacitors Using Ir/SrRuO3 Top Electrodes", *Applied Physics Letters*, vol. 87, no. 21, p. 212 910, 2005. DOI: `10.1063/1.2135898`. eprint: `https://doi.org/10.1063/1.2135898`.

[165] J. A. Rodriguez, K. Remack, K. Boku, K. R. Udayakumar, S. Aggarwal, S. R. Summerfelt, F. G. Celii, S. Martin, L. Hall, K. Taylor, T. Moise, H. McAdams, J. McPherson, R. Bailey, G. Fox, and M. Depner, "Reliability Properties of Low-Voltage Ferroelectric Capacitors and Memory Arrays", *IEEE Transactions on Device and Materials Reliability*, vol. 4, no. 3, pp. 436–449, Sep. 2004, ISSN: 1558-2574. DOI: `10.1109/TDMR.2004.837210`.

[166] K.-M. Lee, H.-G. An, J.-K. Lee, Y.-T. Lee, S.-W. Lee, S.-H. Joo, S.-D. Nam, K.-S. Park, M.-S. Lee, S.-O. Park, H.-K. Kang, and J.-T. Moon, "Enhanced Retention Characteristics of Pb(Zr, Ti)O3Capacitors by Ozone Treatment", *Japanese Journal of Applied Physics*, vol. 40, no. Part 1, No. 8, pp. 4979–4983, Aug. 2001. DOI: `10.1143/jjap.40.4979`.

[167] K. Takada, S. Takarae, K. Shimamoto, N. Fujimura, and T. Yoshimura, "Time-Dependent Imprint in Hf0.5Zr0.5O2 Ferroelectric Thin Films", *Advanced Electronic Materials*, vol. n/a, no. n/a, p. 2 100 151, DOI: `10.1002/aelm.202100151`. eprint: `https://onlinelibrary.wiley.com/doi/pdf/10.1002/aelm.202100151`.

[168] J. Bouaziz, P. Rojo Romeo, N. Baboux, and B. Vilquin, "Imprint Issue during Retention Tests for HfO2-based FRAM: An Industrial Challenge?", *Applied Physics Letters*, vol. 118, no. 8, p. 082 901, 2021. DOI: `10.1063/5.0035687`. eprint: `https://doi.org/10.1063/5.0035687`.

[169] J. Mohan, H. Hernandez-Arriaga, Y. C. Jung, T. Onaya, C.-Y. Nam, E. H. R. Tsai, S. J. Kim, and J. Kim, "Ferroelectric Polarization Retention with Scaling of Hf0.5Zr0.5O2 on Silicon", *Applied Physics Letters*, vol. 118, no. 10, p. 102 903, 2021. DOI: `10.1063/5.0035579`. eprint: `https://doi.org/10.1063/5.0035579`.

[170] K. Lee, T. Y. Lee, S. M. Yang, D. H. Lee, J. Park, and S. C. Chae, "Ferroelectricity in Epitaxial Y-doped HfO2 Thin Film Integrated on Si Substrate", *Applied Physics Letters*, vol. 112, no. 20, p. 202 901, 2018. DOI: `10.1063/1.5020688`. eprint: `https://doi.org/10.1063/1.5020688`.

[171] A. Morelli, S. Venkatesan, G. Palasantzas, B. J. Kooi, and J. T. M. De Hosson, "Polarization Retention Loss in PbTiO3 Ferroelectric Films Due to Leakage Currents", *Journal of Applied Physics*, vol. 102, no. 8, p. 084 103, 2007. DOI: `10.1063/1.2794859`. eprint: `https://doi.org/10.1063/1.2794859`.

[172] A. Gruverman, H. Tokumoto, A. S. Prakash, S. Aggarwal, B. Yang, M. Wuttig, R. Ramesh, O. Auciello, and T. Venkatesan, "Nanoscale Imaging of Domain Dynamics and Retention in Ferroelectric Thin Films", *Applied Physics Letters*, vol. 71, no. 24, pp. 3492–3494, 1997. DOI: `10.1063/1.120369`. eprint: `https://doi.org/10.1063/1.120369`.

[173] J. Lyu, I. Fina, R. Bachelet, G. Saint-Girons, S. Estandía, J. Gázquez, J. Fontcuberta, and F. Sánchez, "Enhanced Ferroelectricity in Epitaxial Hf0.5Zr0.5O2 Thin Films Integrated with Si(001) Using SrTiO3 Templates", *Applied Physics Letters*, vol. 114, no. 22, p. 222 901, 2019. DOI: `10.1063/1.5096002`. eprint: `https://doi.org/10.1063/1.5096002`.

[174] J. Y. Jo, D. J. Kim, Y. S. Kim, S.-B. Choe, T. K. Song, J.-G. Yoon, and T. W. Noh, "Polarization Switching Dynamics Governed by the Thermodynamic Nucleation Process in Ultrathin Ferroelectric Films", *Physical Review Letters*, vol. 97, no. 24, p. 247 602, Dec. 2006. DOI: `10.1103/PhysRevLett.97.247602`.

[175] C. Mart, N.-D. Kohlenbach, K. Kühnel, S. Eßlinger, M. Czernohorsky, T. Ali, W. Weinreich, and L. M. Eng, "Aging in Ferroelectric Si-Doped Hafnium Oxide Thin Films", *physica status solidi (RRL) – Rapid Research Letters*, vol. n/a, no. n/a, DOI: `10.1002/pssr.202100023`. eprint: `https://onlinelibrary.wiley.com/doi/pdf/10.1002/pssr.202100023`.

[176] R. A. Izmailov, J. W. Strand, L. Larcher, B. J. O'Sullivan, A. L. Shluger, and V. V. Afanas'ev, "Electron Trapping in Ferroelectric HfO2", *Physical Review Materials*, vol. 5, no. 3, p. 034 415, Mar. 2021. DOI: `10.1103/PhysRevMaterials.5.034415`.

[177] W. J. Merz, "Domain Formation and Domain Wall Motions in Ferroelectric $BaTiO_3$ Single Crystals", *Physical Review*, vol. 95, no. 3, pp. 690–698, Aug. 1954. DOI: `10.1103/PhysRev.95.690`.

[178] A. N. Kolmogorov, "Izv Akad Nauk SSSR", *Ser Materm*, vol. 3, pp. 355–359, 1937.

[179] M. Avrami, "Kinetics of Phase Change. I General Theory", *The Journal of Chemical Physics*, vol. 7, no. 12, pp. 1103–1112, Dec. 1939, ISSN: 0021-9606. DOI: `10.1063/1.1750380`.

[180] Y. Ishibashi and Y. Takagi, "Note on Ferroelectric Domain Switching", *Journal of the Physical Society of Japan*, vol. 31, no. 2, pp. 506–510, Aug. 1971, ISSN: 0031-9015. DOI: `10.1143/JPSJ.31.506`.

[181] M. Materano, P. D. Lomenzo, H. Mulaosmanovic, M. Hoffmann, A. Toriumi, T. Mikolajick, and U. Schroeder, "Polarization switching in thin doped HfO2 ferroelectric layers", *Applied Physics Letters*, p. 7, 2020.

[182] A. K. Tagantsev, I. Stolichnov, N. Setter, J. S. Cross, and M. Tsukada, "Non-Kolmogorov-Avrami switching kinetics in ferroelectric thin films", *Physical Review B*, vol. 66, no. 21, p. 214 109, Dec. 2002, ISSN: 0163-1829, 1095-3795. DOI: `10.1103/PhysRevB.66.214109`.

[183] P. Buragohain, C. Richter, T. Schenk, H. Lu, T. Mikolajick, U. Schroeder, and A. Gruverman, "Nanoscopic Studies of Domain Structure Dynamics in Ferroelectric La:HfO2 Capacitors", *Applied Physics Letters*, vol. 112, no. 22, p. 222 901, May 2018, ISSN: 0003-6951. DOI: `10.1063/1.5030562`.

[184] T.-H. Ryu, D.-H. Min, and S.-M. Yoon, "Comparative studies on ferroelectric switching kinetics of sputtered Hf $_{0.5}$ Zr $_{0.5}$ O $_2$ thin films with variations in film thickness and crystallinity", *Journal of Applied Physics*, vol. 128, no. 7, p. 074 102, Aug. 2020, ISSN: 0021-8979, 1089-7550. DOI: `10.1063/5.0013487`.

[185] W. Ding, Y. Zhang, L. Tao, Q. Yang, and Y. Zhou, "The Atomic-Scale Domain Wall Structure and Motion in HfO2-based Ferroelectrics: A First-Principle Study", *Acta Materialia*, vol. 196, pp. 556–564, Sep. 2020, ISSN: 1359-6454. DOI: `10.1016/j.actamat.2020.07.012`.

[186] H.-J. Lee, M. Lee, K. Lee, J. Jo, H. Yang, Y. Kim, S. C. Chae, U. Waghmare, and J. H. Lee, "Scale-free ferroelectricity induced by flat phonon bands in HfO2", p. 5, 2020.

[187] X. Du and I.-W. Chen, "Frequency Spectra of Fatigue of PZT and other Ferroelectric Thin Films", *MRS Proceedings*, vol. 493, p. 311, 1997, ISSN: 0272-9172, 1946-4274. DOI: `10.1557/PROC-493-311`.

[188] Y. Kim, H. Han, W. Lee, S. Baik, D. Hesse, and M. Alexe, "Non-Kolmogorov-Avrami-Ishibashi Switching Dynamics in Nanoscale Ferroelectric Capacitors", *Nano Letters*, vol. 10, no. 4, pp. 1266–1270, Apr. 2010, ISSN: 1530-6984, 1530-6992. DOI: `10.1021/nl9038339`.

[189] S. D. Hyun, H. W. Park, Y. J. Kim, M. H. Park, Y. H. Lee, H. J. Kim, Y. J. Kwon, T. Moon, K. D. Kim, Y. B. Lee, B. S. Kim, and C. S. Hwang, "Dispersion in Ferroelectric Switching Performance of Polycrystalline Hf $_{0.5}$ Zr $_{0.5}$ O $_2$ Thin Films", *ACS Applied Materials & Interfaces*, vol. 10, no. 41, pp. 35 374–35 384, Oct. 2018, ISSN: 1944-8244, 1944-8252. DOI: `10.1021/acsami.8b13173`.

[190] H. F. Kay and J. W. Dunn, "Thickness Dependence of the Nucleation Field of Triglycine Sulphate", *The Philosophical Magazine: A Journal of Theoretical Experimental and Applied Physics*, vol. 7, no. 84, pp. 2027–2034, Dec. 1962, ISSN: 0031-8086. DOI: `10.1080/14786436208214471`.

[191] H. Mulaosmanovic, S. Dünkel, M. Trentzsch, S. Beyer, E. T. Breyer, T. Mikolajick, and S. Slesazeck, "Investigation of Accumulative Switching in Ferroelectric FETs: Enabling Universal Modeling of the Switching Behavior", *IEEE Transactions on Electron Devices*, vol. 67, no. 12, pp. 5804–5809, Dec. 2020, ISSN: 1557-9646. DOI: `10.1109/TED.2020.3031249`.

[192] S. Ducharme, V. M. Fridkin, A. V. Bune, S. P. Palto, L. M. Blinov, N. N. Petukhova, and S. G. Yudin, "Intrinsic Ferroelectric Coercive Field", *Physical Review Letters*, vol. 84, no. 1, pp. 175–178, Jan. 2000, ISSN: 0031-9007, 1079-7114. DOI: `10.1103/PhysRevLett.84.175`.

[193] D. Ricinschi, C. Harnagea, C. Papusoi, L. Mitoseriu, V. Tura, and M. Okuyama, "Analysis of ferroelectric switching in finite media as a Landau-type phase transition", *Journal of Physics: Condensed Matter*, vol. 10, no. 2, pp. 477–492, Jan. 1998, ISSN: 0953-8984, 1361-648X. DOI: `10.1088/0953-8984/10/2/026`.

[194] T. Kwon, “Landau-Khalatnikov Simulations for Ferroelectric Switching in Ferroelectric Random Access Memory Application”, *Journal of the Korean Physical Society*, vol. 46, no. 1, p. 5, 2005.

[195] S. Zhukov, Y. A. Genenko, O. Hirsch, J. Glaum, T. Granzow, and H. von Seggern, “Dynamics of polarization reversal in virgin and fatigued ferroelectric ceramics by inhomogeneous field mechanism”, *Physical Review B*, vol. 82, no. 1, p. 014 109, Jul. 2010, ISSN: 1098-0121, 1550-235X. DOI: `10.1103/PhysRevB.82.014109`.

[196] P. Pandey, C. Alessandri, and A. C. Seabaugh, “Process Dependent Switching Dynamics of Ferroelectric Hafnium Zirconate”, in *2019 Device Research Conference (DRC)*, Ann Arbor, MI, USA: IEEE, Jun. 2019, pp. 49–50, ISBN: 978-1-72812-111-6 978-1-72812-112-3. DOI: `10.1109/DRC46940.2019.9046408`.

[197] S. M. George, “Atomic Layer Deposition: An Overview”, *Chemical Reviews*, vol. 110, no. 1, pp. 111–131, 2010. DOI: `10.1021/cr900056b`. eprint: `https://doi.org/10.1021/cr900056b`.

[198] B. Mamyrin, “Time-of-Flight Mass Spectrometry (Concepts, Achievements, and Prospects)”, *International Journal of Mass Spectrometry*, vol. 206, no. 3, pp. 251–266, 2001, ISSN: 1387-3806. DOI: `10.1016/S1387-3806(00)00392-4`.

[199] B. Fultz and J. Howe, *Transmission Electron Microscopy and Diffractometry of Materials*, ser. Graduate Texts in Physics. Springer Berlin Heidelberg, 2012, ISBN: 978-3-642-29760-1.

[200] C. Fadley, “X-Ray Photoelectron Spectroscopy: Progress and Perspectives”, *Journal of Electron Spectroscopy and Related Phenomena*, vol. 178–179, pp. 2–32, 2010, ISSN: 0368-2048. DOI: `10.1016/j.elspec.2010.01.006`.

[201] N. Colthup, *Introduction to Infrared and Raman Spectroscopy*. Elsevier Science, 2012, ISBN: 978-0-323-16160-2.

[202] D. Bowen and B. Tanner, *High Resolution X-Ray Diffractometry and Topography*. CRC Press, 1998, ISBN: 978-0-203-97919-8.

[203] Daillant, Jean and Gibaud, Alain, *X-Ray and Neutron Reflectivity: Principles and Applications*. Springer-Verlag Berlin Heidelberg, 2008, vol. 58, ISBN: 978-3-540-88588-7.

[204] M. H. Park, Y. H. Lee, H. J. Kim, Y. J. Kim, T. Moon, K. D. Kim, J. Müller, A. Kersch, U. Schroeder, T. Mikolajick, and C. S. Hwang, “Ferroelectricity and Antiferroelectricity of Doped Thin HfO2-Based Films”, *Advanced Materials*, vol. 27, no. 11, pp. 1811–1831, 2015. DOI: `10.1002/adma.201404531`. eprint: `https://onlinelibrary.wiley.com/doi/pdf/10.1002/adma.201404531`.

[205] P. D. Lomenzo, M. Materano, T. Mittmann, P. Buragohain, A. Gruverman, T. Kiguchi, T. Mikolajick, and U. Schroder, “Harnessing Phase Transitions in Multifunctional Antiferroelectric ZrO2”, 2021.

[206] T. Shimizu, Y. Tashiro, T. Mimura, T. Kiguchi, T. Shiraishi, T. J. Konnno, O. Sakata, and H. Funakubo, "Electric-Field-Induced Ferroelectricity in 5%Y-doped Hf0.5Zr0.5O2: Transformation from the Paraelectric Tetragonal Phase to the Ferroelectric Orthorhombic Phase", *physica status solidi (RRL) – Rapid Research Letters*, vol. 15, no. 5, p. 2 000 589, 2021. DOI: `10.1002/pssr.202000589`. eprint: `https://onlinelibrary.wiley.com/doi/pdf/10.1002/pssr.202000589`.

[207] K. McKenna, A. Shluger, V. Iglesias, M. Porti, M. Nafría, M. Lanza, and G. Bersuker, "Grain boundary mediated leakage current in polycrystalline HfO2 films", *Microelectronic Engineering*, vol. 88, no. 7, pp. 1272–1275, Jul. 2011, ISSN: 01679317. DOI: `10.1016/j.mee.2011.03.024`.

[208] X. Zhao and D. Vanderbilt, "Phonons and lattice dielectric properties of zirconia", *Physical Review B*, vol. 65, no. 7, p. 075 105, Jan. 2002, ISSN: 0163-1829, 1095-3795. DOI: `10.1103/PhysRevB.65.075105`.

[209] J Aarik and A Aidla, "Influence of substrate temperature on atomic layer growth and properties of HfO2 thin films", *Thin Solid Films*, p. 7, 1999.

[210] J. Aarik, A. Aidla, A. Kikas, T. Käämbre, R. Rammula, P. Ritslaid, T. Uustare, and V. Sammelselg, "Effects of precursors on nucleation in atomic layer deposition of HfO2", *Applied Surface Science*, vol. 230, no. 1-4, pp. 292–300, May 2004, ISSN: 01694332. DOI: `10.1016/j.apsusc.2004.02.048`.

[211] K. Kukli, M. Ritala, M. Leskelä, T. Sajavaara, J. Keinonen, A. C. Jones, and J. L. Roberts, "Atomic Layer Deposition of Hafnium Dioxide Films from 1-Methoxy-2-methyl-2-propanolate Complex of Hafnium", *Chemistry of Materials*, vol. 15, no. 8, pp. 1722–1727, Apr. 2003, ISSN: 0897-4756, 1520-5002. DOI: `10.1021/cm021328p`.

[212] K. Kukli, T. Pilvi, M. Ritala, T. Sajavaara, J. Lu, and M. Leskelä, "Atomic layer deposition of hafnium dioxide thin films from hafnium tetrakis(dimethylamide) and water", *Thin Solid Films*, vol. 491, no. 1-2, pp. 328–338, Nov. 2005, ISSN: 00406090. DOI: `10.1016/j.tsf.2005.05.050`.

[213] J. Niinistö, "Atomic Layer Deposition of high-k Dielectrics from novel Cyclopentadienyl-type Precursors", *PhD Thesis*, Helsinki University of Technology, Espoo, p. 72, May 2006.

[214] S. Seppälä, M. Vehkamäki, K. Mizohata, W. Noh, J. Räisänen, M. Ritala, and M. Leskelä, "Comparative study on the use of novel heteroleptic cyclopentadienyl-based zirconium precursors with H $_2$ O and O $_3$ for atomic layer deposition of ZrO $_2$", *Journal of Vacuum Science & Technology A*, vol. 37, no. 2, p. 020 912, Mar. 2019, ISSN: 0734-2101, 1520-8559. DOI: `10.1116/1.5079539`.

[215] J. Aarik, A. Aidla, H. Mändar, T. Uustare, and V. Sammelselg, "Growth kinetics and structure formation of ZrO2 thin films in chloride-based atomic layer deposition process", *Thin Solid Films*, vol. 408, no. 1-2, pp. 97–103, Apr. 2002, ISSN: 00406090. DOI: `10.1016/S0040-6090(02)00123-2`.

[216] R. Matero, M. Ritala, M. Leskelä, T. Sajavaara, A. C. Jones, and J. L. Roberts, "Evaluation of New Aminoalkoxide Precursors for Atomic Layer Deposition. Growth of Zirconium Dioxide Thin Films and Reaction Mechanism Studies", *Chemistry of Materials*, vol. 16, no. 26, pp. 5630–5636, Dec. 2004, ISSN: 0897-4756, 1520-5002. DOI: `10.1021/cm030669f`.

[217] J. Liu, J. Li, J. Wu, and J. Sun, "Structure and Dielectric Property of High-k ZrO2 Films Grown by Atomic Layer Deposition Using Tetrakis(Dimethylamido)Zirconium and Ozone", *Nanoscale Research Letters*, vol. 14, no. 1, p. 154, Dec. 2019, ISSN: 1931-7573, 1556-276X. DOI: `10.1186/s11671-019-2989-8`.

[218] H. Machida, T. Kada, M. Ishikawa, A. Ogura, and Y. Ohshita, "Vapor Pressure of Hf and Si Precursors for Hf $_x$ Si $_{1-x}$ O $_2$ Deposition Evaluated by a Saturated Gas Technique", *Japanese Journal of Applied Physics*, vol. 43, no. 3, pp. 966–967, Mar. 2004, ISSN: 0021-4922, 1347-4065. DOI: `10.1143/JJAP.43.966`.

[219] T. Suntola, "Surface chemistry of materials deposition at atomic layer level", *Applied Surface Science*, vol. 100–101, pp. 391–398, Jul. 1996, ISSN: 01694332. DOI: `10.1016/0169-4332(96)00306-6`.

[220] D. M. Hausmann, E. Kim, J. Becker, and R. G. Gordon, "Atomic Layer Deposition of Hafnium and Zirconium Oxides Using Metal Amide Precursors", *Chemistry of Materials*, vol. 14, no. 10, pp. 4350–4358, Oct. 2002, ISSN: 0897-4756, 1520-5002. DOI: `10.1021/cm020357x`.

[221] V. Miikkulainen, M. Leskelä, M. Ritala, and R. L. Puurunen, "Crystallinity of inorganic films grown by atomic layer deposition: Overview and general trends", *Journal of Applied Physics*, vol. 113, no. 2, p. 021 301, Jan. 2013, ISSN: 0021-8979, 1089-7550. DOI: `10.1063/1.4757907`.

[222] J. Aarik, A. Aidla, H. Mändar, V. Sammelselg, and T. Uustare, "Texture Development in Nanocrystalline Hafnium Dioxide Thin Films Grown by Atomic Layer Deposition", *Journal of Crystal Growth*, vol. 220, no. 1, pp. 105–113, 2000, ISSN: 0022-0248. DOI: `10.1016/S0022-0248(00)00831-9`.

[223] J. Sundqvist, A. Hårsta, J. Aarik, K. Kukli, and A. Aidla, "Atomic layer deposition of polycrystalline HfO2 films by the HfI4–O2 precursor combination", *Thin Solid Films*, vol. 427, no. 1-2, pp. 147–151, Mar. 2003, ISSN: 00406090. DOI: `10.1016/S0040-6090(02)01165-3`.

[224] K. Kukli, M. Ritala, J. Lu, and A. Ha, "Properties of HfO2 Thin Films Grown by ALD from Hafnium tetrakis(ethylmethylamide) and Water", *Journal of The Electrochemical Society*, vol. 151, no. 8, F189–F193, 2004.

[225] K. Kukli, M. Ritala, J. Aarik, T. Uustare, and M. Leskelä, "Influence of growth temperature on properties of zirconium dioxide films grown by atomic layer deposition", *Journal of Applied Physics*, vol. 92, no. 4, pp. 1833–1840, Aug. 2002, ISSN: 0021-8979, 1089-7550. DOI: `10.1063/1.1493657`.

[226] K. Kukli, M. Ritala, T. Sajavaara, J. Keinonen, and M. Leskelä, "Atomic Layer Deposition of Hafnium Dioxide Films from Hafnium Tetrakis(ethylmethylamide) and Water", vol. 8, pp. 199–204, 2002.

[227] J. Niinistö, K. Kukli, M. Kariniemi, M. Ritala, M. Leskelä, N. Blasco, A. Pinchart, C. Lachaud, N. Laaroussi, Z. Wang, and C. Dussarrat, “Novel mixed alkylamido-cyclopentadienyl precursors for ALD of ZrO2 thin films”, *Journal of Materials Chemistry*, vol. 18, no. 43, p. 5243, 2008, ISSN: 0959-9428, 1364-5501. DOI: `10.1039/b810922b`.

[228] S. Bang, S. Lee, S. Jeon, S. Kwon, W. Jeong, S. Kim, and H. Jeon, “Physical and Electrical Properties of Hafnium–Zirconium–Oxide Films Grown by Atomic Layer Deposition”, *Journal of The Electrochemical Society*, vol. 155, no. 9, H633, 2008, ISSN: 00134651. DOI: `10.1149/1.2945908`.

[229] D. H. Triyoso, R. Gregory, M. Park, K. Wang, and S. I. Lee, “Physical and Electrical Properties of Atomic-Layer-Deposited $Hf_xZr_{1-x}O_2$ with TEMAHf, TEMAZr, and Ozone”, no. 155 (1), H43–H46, 2008.

[230] R. I. Hegde, D. H. Triyoso, S. B. Samavedam, and B. E. White, “Hafnium zirconate gate dielectric for advanced gate stack applications”, *Journal of Applied Physics*, vol. 101, no. 7, p. 074 113, Apr. 2007, ISSN: 0021-8979, 1089-7550. DOI: `10.1063/1.2716399`.

[231] S. Migita, H. Ota, K. Shibuya, H. Yamada, A. Sawa, T. Matsukawa, and A. Toriumi, “Phase transformation behavior of ultrathin Hf $_{0.5}$ Zr $_{0.5}$ O $_2$ films investigated through wide range annealing experiments”, *Japanese Journal of Applied Physics*, vol. 58, no. SB, SBBA07, Apr. 2019, ISSN: 0021-4922, 1347-4065. DOI: `10.7567/1347-4065/ab00f6`.

[232] R. Suyama, H. Takubo, and S. Kume, “Synthesis of Hf1-x, Zrx02 (O”, *Journal of the American Ceramic Society*, vol. 68, no. 9, pp. C–237–C–237, Sep. 1985, ISSN: 0002-7820, 1551-2916. DOI: `10.1111/j.1151-2916.1985.tb15797.x`.

[233] Z. Chen, N. Prud’homme, B. Wang, and V. Ji, “Residual stress gradient analysis with GIXRD on ZrO2 thin films deposited by MOCVD”, *Surface and Coatings Technology*, vol. 206, no. 2-3, pp. 405–410, Oct. 2011, ISSN: 02578972. DOI: `10.1016/j.surfcoat.2011.07.036`.

[234] R. Alcala, C. Richter, M. Materano, P. D. Lomenzo, C. Zhou, J. L. Jones, T. Mikolajick, and U. Schroeder, “Influence of oxygen source on the ferroelectric properties of ALD grown Hf $_{1-x}$ Zr $_x$ O $_2$ films”, *Journal of Physics D: Applied Physics*, vol. 54, no. 3, p. 035 102, Jan. 2021, ISSN: 0022-3727, 1361-6463. DOI: `10.1088/1361-6463/abbc98`.

[235] S. J. Kim, D. Narayan, J.-G. Lee, J. Mohan, J. S. Lee, J. Lee, H. S. Kim, Y.-C. Byun, A. T. Lucero, C. D. Young, S. R. Summerfelt, T. San, L. Colombo, and J. Kim, “Large Ferroelectric Polarization of TiN/Hf0.5Zr0.5O2/TiN Capacitors Due to Stress-Induced Crystallization at Low Thermal Budget”, *Applied Physics Letters*, vol. 111, no. 24, p. 242 901, 2017. DOI: `10.1063/1.4995619`.

[236] T. Mittmann, M. Materano, P. D. Lomenzo, M. H. Park, I. Stolichnov, M. Cavalieri, C. Zhou, C.-C. Chung, J. L. Jones, T. Szyjka, M. Müller, A. Kersch, T. Mikolajick, and U. Schroeder, “Origin of Ferroelectric Phase in Undoped HfO $_2$ Films Deposited by Sputtering”, *Advanced Materials Interfaces*, p. 1 900 042, Apr. 2019, ISSN: 2196-7350, 2196-7350. DOI: `10.1002/admi.201900042`.

[237] H.-S. Jung, S. H. Jeon, H. K. Kim, I.-H. Yu, S. Y. Lee, J. Lee, Y. J. Chung, D.-Y. Cho, N.-I. Lee, T. J. Park, J.-H. Choi, S. Han, and C. S. Hwang, "The Impact of Carbon Concentration on the Crystalline Phase and Dielectric Constant of Atomic Layer Deposited HfO2Films on Ge Substrate", *ECS Journal of Solid State Science and Technology*, vol. 1, no. 2, N33–N37, 2012. DOI: `10.1149/2.020202jss`.

[238] K. D. Kim, M. H. Park, H. J. Kim, Y. J. Kim, T. Moon, Y. H. Lee, S. D. Hyun, T. Gwon, and C. S. Hwang, "Ferroelectricity in undoped-HfO $_2$ thin films induced by deposition temperature control during atomic layer deposition", *Journal of Materials Chemistry C*, vol. 4, no. 28, pp. 6864–6872, 2016, ISSN: 2050-7526, 2050-7534. DOI: `10.1039/C6TC02003H`.

[239] M. H. Park, D. H. Lee, K. Yang, J.-Y. Park, G. T. Yu, H. W. Park, M. Materano, T. Mittmann, P. D. Lomenzo, T. Mikolajick, U. Schroeder, and C. S. Hwang, "Review of defect chemistry in fluorite-structure ferroelectrics for future electronic devices", *Journal of Materials Chemistry C*, vol. 8, no. 31, pp. 10 526–10 550, 2020, ISSN: 2050-7526, 2050-7534. DOI: `10.1039/D0TC01695K`.

[240] T. S. Böscke, S. Govindarajan, P. D. Kirsch, P. Y. Hung, C. Krug, B. H. Lee, J. Heitmann, U. Schröder, G. Pant, B. E. Gnade, and W. H. Krautschneider, "Stabilization of Higher-κ Tetragonal HfO2 by SiO2 Admixture Enabling Thermally Stable Metal-Insulator-Metal Capacitors", *Applied Physics Letters*, vol. 91, no. 7, p. 072 902, Aug. 2007, ISSN: 0003-6951. DOI: `10.1063/1.2771376`.

[241] M. Hyuk Park, H. Joon Kim, Y. Jin Kim, T. Moon, and C. Seong Hwang, "The Effects of Crystallographic Orientation and Strain of Thin Hf0.5Zr0.5O2 Film on Its Ferroelectricity", *Applied Physics Letters*, vol. 104, no. 7, p. 072 901, 2014. DOI: `10.1063/1.4866008`. eprint: `https://doi.org/10.1063/1.4866008`.

[242] R. Cao, Y. Wang, S. Zhao, Y. Yang, X. Zhao, W. Wang, X. Zhang, H. Lv, Q. Liu, and M. Liu, "Effects of Capping Electrode on Ferroelectric Properties of Hf0.5Zr0.5O2 Thin Films", *IEEE Electron Device Letters*, vol. 39, no. 8, pp. 1207–1210, Aug. 2018, ISSN: 1558-0563. DOI: `10.1109/LED.2018.2846570`.

[243] Y. Lee, Y. Goh, J. Hwang, D. Das, and S. Jeon, "The Influence of Top and Bottom Metal Electrodes on Ferroelectricity of Hafnia", *IEEE Transactions on Electron Devices*, vol. 68, no. 2, pp. 523–528, Feb. 2021, ISSN: 1557-9646. DOI: `10.1109/TED.2020.3046173`.

[244] G. Karbasian, R. dos Reis, A. K. Yadav, A. J. Tan, C. Hu, and S. Salahuddin, "Stabilization of Ferroelectric Phase in Tungsten Capped Hf0.8Zr0.2O2", *Applied Physics Letters*, vol. 111, no. 2, p. 022 907, 2017. DOI: `10.1063/1.4993739`. eprint: `https://doi.org/10.1063/1.4993739`.

[245] P. D. Lomenzo, Q. Takmeel, C. M. Fancher, C. Zhou, N. G. Rudawski, S. Moghaddam, J. L. Jones, and T. Nishida, "Ferroelectric Si-Doped HfO2 Device Properties on Highly Doped Germanium", *IEEE Electron Device Letters*, vol. 36, no. 8, pp. 766–768, Aug. 2015, ISSN: 1558-0563. DOI: `10.1109/LED.2015.2445352`.

[246] H. Fujisawa, S. Hyodo, K. Jitsui, M. Shimizu, H. Niu, H. Okino, and Tadashi Shiosaki, "Electrical Properties of PZT Thin Films Grown on Ir/IrO2 Bottom Electrodes by MOCVD", *Integrated Ferroelectrics*, vol. 21, no. 1-4, pp. 107–114, 1998. DOI: `10.1080/10584589808202055`. eprint: `https://doi.org/10.1080/10584589808202055`.

[247] G. Holzlechner, D. Kastner, C. Slouka, H. Hutter, and J. Fleig, "Oxygen Vacancy Redistribution in PbZrxTi1-xO3 (PZT) under the Influence of an Electric Field", *Solid State Ionics*, vol. 262, pp. 625–629, 2014, ISSN: 0167-2738. DOI: `10.1016/j.ssi.2013.08.027`.

[248] M. H. Park, H. J. Kim, Y. J. Kim, W. Lee, T. Moon, K. D. Kim, and C. S. Hwang, "Study on the Degradation Mechanism of the Ferroelectric Properties of Thin Hf0.5Zr0.5O2 Films on TiN and Ir Electrodes", *Applied Physics Letters*, vol. 105, no. 7, p. 072 902, 2014. DOI: `10.1063/1.4893376`. eprint: `https://doi.org/10.1063/1.4893376`.

[249] Y. Goh, S. H. Cho, S. H. K. Park, and S. Jeon, "Crystalline Phase-Controlled High-Quality Hafnia Ferroelectric with RuO_2 Electrode", *IEEE Transactions on Electron Devices*, vol. 67, no. 8, pp. 3431–3434, Aug. 2020, ISSN: 1557-9646. DOI: `10.1109/TED.2020.2998444`.

[250] R. Cao, B. Song, D. Shang, Y. Yang, Q. Luo, S. Wu, Y. Li, Y. Wang, H. Lv, Q. Liu, and M. Liu, "Improvement of Endurance in HZO-Based Ferroelectric Capacitor Using Ru Electrode", *IEEE Electron Device Letters*, vol. 40, no. 11, pp. 1744–1747, Nov. 2019, ISSN: 1558-0563. DOI: `10.1109/LED.2019.2944960`.

[251] S. Lombardo, C. Kisung, P. D. Lomenzo, C. Richter, U. Schroeder, and A. I. Khan, "Strain-Driven Ferroelectric to Antiferroelectric Transformation in Undoped, Nanocrystalline ZrO2 Thin Films", in elaboration.

[252] R. Alcala, "TiN-Based Electrode Work Function Engineering for Electric Field Biasing of Hf0.5Zr0.5O2 Based Ferroelectric Capacitor Stacks", M.S. thesis, Technische Universitaet Dresden, Dresden, Germany, 2020.

[253] M. Pešić, T. Li, V. Di Lecce, M. Hoffmann, M. Materano, C. Richter, B. Max, S. Slesazeck, U. Schroeder, L. Larcher, and T. Mikolajick, "Built-in Bias Generation in Anti-Ferroelectric Stacks: Methods and Device Applications", *IEEE Journal of the Electron Devices Society*, vol. 6, pp. 1019–1025, 2018. DOI: `10.1109/JEDS.2018.2825360`.

[254] Yeo, Yee-Chia, Tsu-Jae, C. King, and C. hu, "Metal-Dielectric Band Alignment and Its Implications for Metal Gate Complementary Metal-Oxide-Semiconductor Technology", *Journal of Applied Physics*, vol. 92, Dec. 2002. DOI: `10.1063/1.1521517`.

[255] Y. Lee, H. Alex Hsain, S. S. Fields, S. T. Jaszewski, M. D. Horgan, P. G. Edgington, J. F. Ihlefeld, G. N. Parsons, and J. L. Jones, "Unexpectedly Large Remanent Polarization of Hf0.5Zr0.5O2 Metal–Ferroelectric–Metal Capacitor Fabricated without Breaking Vacuum", *Applied Physics Letters*, vol. 118, no. 1, p. 012 903, 2021. DOI: `10.1063/5.0029532`. eprint: `https://doi.org/10.1063/5.0029532`.

[256] L. Alemán-Vázquez, E. Torres-García, R. Villagómez, and J.-L. Cano, “Effect of the Particle Size on the Activity of MoO x C y Catalysts for the Isomerization of Heptane”, *Catalysis Letters - CATALYSIS LETT*, vol. 100, pp. 219–226, Apr. 2005. DOI: `10.1007/s10562-004-3459-0`.

[257] Irfan, H. Ding, Y. Gao, C. Small, D. Y. Kim, J. Subbiah, and F. So, “Energy Level Evolution of Air and Oxygen Exposed Molybdenum Trioxide Films”, *Applied Physics Letters*, vol. 96, no. 24, p. 243 307, 2010. DOI: `10.1063/1.3454779`. eprint: `https://doi.org/10.1063/1.3454779`.

[258] R. Senthilkumar, G. Ravi, C. Sekar, M. Arivanandhan, N. M, and Y. Hayakawa, “Determination of Gas Sensing Properties of Thermally Evaporated WO3 Nanostructures”, *Journal of Materials Science: Materials in Electronics*, vol. 26, Dec. 2014. DOI: `10.1007/s10854-014-2552-4`.

[259] H. Mulaosmanovic, J. Ocker, S. Muller, U. Schroeder, J. Muller, P. Polakowski, S. Flachowsky, R. van Bentum, T. Mikolajick, and S. Slesazeck, “Switching Kinetics in Nanoscale Hafnium Oxide Based Ferroelectric Field-Effect Transistors”, *ACS Appl. Mater. Interfaces*, vol. 9, p. 3792, 2017. DOI: `10.1021/acsami.6b13866`.

[260] M. H. Park, T. Schenk, S. Starschich, C. M. Fancher, H. J. Kim, U. Böttger, C. S. Hwang, A. Toriumi, X. Tian, and U. Schroeder, “Chapter 3.5 - Effect of Surface/Interface Energy and Stress on the Ferroelectric Properties”, in *Ferroelectricity in Doped Hafnium Oxide: Materials, Properties and Devices*, ser. Woodhead Publishing Series in Electronic and Optical Materials, U. Schroeder, C. S. Hwang, and H. Funakubo, Eds., Woodhead Publishing, 2019, pp. 145–172, ISBN: 978-0-08-102430-0. DOI: `10.1016/B978-0-08-102430-0.00011-5`.

[261] P. D. Lomenzo, T. Mikolajick, and Schroeder, Uwe, “Electronic Contributions to Ferroelectricity and Field- Induced Phase Transitions in Doped-HfO2”, in *IEEE International Symposium on Applications of Ferroelectric (ISAF)*, 2021, p. 4.

[262] B. Y. Kim, H. W. Park, S. D. Hyun, Y. B. Lee, S. H. Lee, M. Oh, S. K. Ryoo, I. S. Lee, S. Byun, D. Shim, D.-Y. Cho, M. H. Park, and C. S. Hwang, “Enhanced Ferroelectric Properties in Hf0.5Zr0.5O2 Films Using a HfO0.61N0.72 Interfacial Layer”, *Advanced Electronic Materials*, vol. n/a, no. n/a, p. 2 100 042, DOI: `10.1002/aelm.202100042`. eprint: `https://onlinelibrary.wiley.com/doi/pdf/10.1002/aelm.202100042`.

[263] P. W. Voorhees, “The Theory of Ostwald’s Ripening”, vol. 38, no. 1-2, pp. 231–252, 1985. DOI: `10.1007/BF01017860`.

[264] A. Kruv, S. R. C. McMitchell, S. Clima, O. O. Okudur, N. Ronchi, G. Van den bosch, M. Gonzalez, I. De Wolf, and J. Houdt, “Impact of Mechanical Strain on Wakeup of HfO2 Ferroelectric Memory”, in *2021 IEEE International Reliability Physics Symposium (IRPS)*, 2021, pp. 1–6. DOI: `10.1109/IRPS46558.2021.9405159`.

[265] Y. Cai, Q. Zhang, Z. Zhang, G. Xu, Z. Wu, J. Gu, J. Li, J. Xiang, and H. Yin, “Influence of Applied Stress on the Ferroelectricity of Thin Zr-Doped HfO2 Films”, *Applied Sciences*, vol. 11, no. 9, 2021, ISSN: 2076-3417. DOI: `10.3390/app11094295`.

[266] H. Joh, T. Jung, and S. Jeon, “Stress Engineering as a Strategy to Achieve High Ferroelectricity in Thick Hafnia Using Interlayer”, *IEEE Transactions on Electron Devices*, vol. 68, no. 5, pp. 2538–2542, 2021. DOI: `10.1109/TED.2021.3068246`.

[267] T. Schenk, U. Schroeder, and T. Mikolajick, “Correspondence - Dynamic Leakage Current Compensation Revisited”, *IEEE Transactions on Ultrasonics, Ferroelectrics, and Frequency Control*, vol. 62, no. 3, pp. 596–599, 2015. DOI: `10.1109/TUFFC.2014.006774`.

List of symbols

Symbol	Description	Units
a	retention power law initial polarization fitting parameter	1
A	capacitor area	m^2
α	1st Landau coefficient	$\mathrm{m\,F^{-1}}$
α_0	0th Landau coefficient	$\mathrm{m\,F^{-1}\,K^{-1}}$
b	retention power law polarization decay fitting parameter	1
B	magnetic flux density	T
β	2nd Landau coefficient	$\mathrm{m^5\,F^{-1}\,C^{-2}}$
c	retention power law fitting parameter	1
C	capacitance	F
C_{Curie}	Curie constant	K
C_d	capacitance of the dielectric	F
C_{FE}	capacitance of the ferroelectric	F
C_{BL}	bit line capacitance	F
χ	electric susceptibility	1
χ_e	electron affinity of the ferroelectric material	eV
δ	thermodynamic contribution to domain wall switching	$\mathrm{J\,V^2}$
d	thickness	m
d_{FE}	thickness of the ferroelectric	m
D	electric displacement field	$\mathrm{C\,m^{-2}}$
Δh	crystalline phase energy difference	$\mathrm{eV\,f.u.^{-1}}$
E	electric field	$\mathrm{V\,m^{-1}}$
E_a	activation field	$\mathrm{V\,m^{-1}}$
E_{bias}	internal bias field	$\mathrm{V\,m^{-1}}$
E_C	coercive field	$\mathrm{V\,m^{-1}}$
E_{dep}	depolarization field	$\mathrm{V\,m^{-1}}$
ε_0	vacuum permittivity	$\mathrm{F\,m^{-1}}$
ε_d	relative permittivity of the dielectric	1
ε_{FE}	relative permittivity of the ferroelectric	1
ε_r	relative permittivity	1
f	frequency	Hz
G	Gibb's free energy density	$\mathrm{J\,m^{-3}}$
G^*	defect dependent thermodynamic barrier for phase transition	J
γ	3rd Landau coefficient	$\mathrm{m^9\,F^{-1}\,C^{-4}}$
h	crystalline phase formation energy	$\mathrm{eV\,f.u.^{-1}}$
H	magnetic field	$\mathrm{A\,m^{-1}}$
I	electric current	A
$I_{Hf^{3+}}$	intensity of the Hf^{3+} peak in XPS	counts
I_m	intensity of the monoclinic phase peak in GIXRD	a.u.
I_o	intensity orthorhombic phase peak in GIXRD	a.u.
I_t	intensity tetragonal phase peak in GIXRD	a.u.

Symbol	**Description**	**Units**
k_b	Boltzmann constant	$\mathrm{J\,K^{-1}}$
λ	wavelength of Cu-Kα radiation	m
m	exponent in Merz's law	1
ξ	voltage normalization parameter in the IFM model	1
P	electric polarization	$\mathrm{C\,m^{-2}}$
P_r	remanent polarization	$\mathrm{C\,m^{-2}}$
$P_{r,max}$	maximum remanent polarization	$\mathrm{C\,m^{-2}}$
$P_{r,rel}$	relaxed remanent polarization	$\mathrm{C\,m^{-2}}$
P_s	spontaneous ferroelectric polarization	$\mathrm{C\,m^{-2}}$
q	elementary charge	C
Q	electric charge	C
R	phase transition rate	1
σ	switching homogeneity	1
t	time	s
T	absolute temperature	K
T_0	Curie-Weiss temperature	K
T_C	Curie-temperature	K
T_{dep}	deposition temperature	°C
τ	switching time	s
τ_0	intrinsic switching time constant	s
2θ	detector angle in grazing-incidence X-ray diffraction	°
ϕ	homogeneity related fitting parameter in the IFM	1
ϕ_m	work function of an electrode material	eV
ψ	nucleus interface energy	$\mathrm{J\,m^{-2}}$
V	voltage	V
V_0	switching voltage offset	V
V_{BL}	bit line voltage	V
V_{ref}	reference voltage in FeRAM sensing	V

List of abbreviations

Abbreviation	Description
1C	one capacitor
1T	one transistor
1T1C	one transistor one capacitor
AC	alternating current
AFE	antiferroelectric
ALD	atomic layer deposition
BE	bottom electrode
BEOL	back-end of line
BL	bit line
CBO	conduction band offset
BTO	barium titanate
CMOS	complementary metal-oxide-semiconductor
CSD	chemical solution deposition
CVD	chemical vapor deposition
DC	direct current
DFT	density functional theory
DHM	dynamic hysteresis measurement
DRAM	dynamic random access memory
DUT	device under test
EELS	electron energy loss spectroscopy
ERS	erase
FE	ferroelectric
FeCap	ferroelectric capacitor
FeFET	ferroelectric field-effect transistor
FeRAM	ferroelectric random access memory
FET	field-effect transistor
FHI-aims	Fritz Haber Institute ab initio molecular simulations
FTJ	ferroelectric tunnel junction
GIXRD	grazing incidence X-ray diffraction
GPC	growth per cycle
HAXPES	hard X-ray photo-electronspectroscopy
HZO	hafnium zirconium oxide
IFM	inhomogeneous field mechanism
KAI	Kolmogorov-Avrami-Ishibashi
MEP	minimum energy path
MFIM	metal-ferroelectric-insulator-metal
MFM	metal-ferroelectric-metal
MFMIM	metal-ferroelectric-metal-insulator-metal

Abbreviation	Description
MOSFET	metal-oxide-semiconductor field-effect transistor
MPB	morphotropic phase boundary
NC	negative capacitance
NCFET	negative capacitance field-effect transistor
NLS	nucleation limited switching
NSS	new same state
OS	opposite state
PE	paraelectric
PFM	piezo-force microscopy
PRG	program
PL	plate line
PLD	pulsed laser deposition
PVD	physical vapor deposition
PZT	lead zirconate titanate
RAM	random access memory
RT	room temperature
RTA	rapid thermal annealing
SA	sense amplifier
SBT	strontium barium titanate
SC-1	standard cleaning one
SEM	scanning electron microscopy
SRAM	static random access memory
SS	same state
TDMAHf	Tetrakis(dimethylamido)hafnium
TDMAZr	Tetrakis(dimethylamido)zirconium
TE	top electrode
TEM	transmission electron microscopy
TEMAHf	Tetrakis(ethylmethylamino)hafnium
TEMAZr	Tetrakis(ethylmethylamino)zirconium
TMA	Trimethylaluminum
ToF-SIMS	time of flight secondary ions mass spectroscopy
WF	work function
WL	word line
XPS	X-ray photospectroscopy
XRD	X-ray diffraction
XRR	X-ray reflectivity

Acknowledgments

Here, I would like to thank all the people who supported me, helped me, had to stand me, and took care of me during the last years.

First of all, I would like to express the heartiest thanks to Prof. Thomas Mikolajick, for supervising my Ph.D. thesis, for all the interesting feedback during my doctoral studies and paper writing, and for always leaving me speechless by having an interesting remark independently from the topic. Huge gratitude goes to my supervisor, Dr. Uwe Schroeder, for offering the greatest scientific and personal support, for pushing me to look beyond by constantly being "still a little bit puzzled", for reminding me I can make it and encouraging me to say it out loud. Thanks thanks thanks to the whole Ferro-team here at NaMLab, to Terence, Ruben, Patrick, Furqan, Michael, Halid, Tony, Milan, for the patience, for all the insightful discussions, and the cheerful moments. The sincerest thank you goes to Claudia, for the most efficient collaboration I could hope for and for the incomparable help against the common enemy (particles, particles, and particles). I am very thankful to Jun-san, Tsukamoto-san, and all my "Japanese friends", for more than three years of flourishing collaboration, for making me feel part of the Sony team but also of their families when mine was extremely far away. I would like to extend my thanks to the whole NaMLab team I was lucky to work with for the last five years. I could never imagine a better place where to start a career as a scientist. I will always look back to those first research years with joy and gratitude, and I hope to carry this brilliant mixture of scientific knowledge and mutual help with me to wherever my future will bring me.

I would like to express my gratitude to all the wonderful people I am lucky to call friends. Thanks to Jade, for always being there, no matter if "there" means Milan, Dresden, Hanoi or Tokyo. Thanks to Suse, for taking the time to check in, for the contagious energy and the brightest smiles, for being the best listener and party-buddy at the same time. I want to thank my flatmates Lea and Barbara for the family feeling I could always come back to at the end of the longest days. Thanks to Tommaso, for the countless challenges and the life-changing conversations.

The most special thank you goes to Anthony and Cate. To Anthony, for our common beginning and our common end, and every single day in between. I cannot imagine how these years would have been without you. To Cate, for the spontaneous cakes, for the improvised yoga sessions, and the most genuine love. Thanks to both of you for being my pillars, for accepting me as a whole, for showing me that someone else can know you better than yourself, for bringing out the sun even in the cloudiest days, and for pushing the meaning of the word "friendship" to a whole new level.

Last but not least, the strongest love to my family, because of the trust, the confidence, the support, the affection. You gave me both the freedom to challenge myself and the strength to win these challenges, and if this is a victory, it is yours as much as mine.

Curriculum vitae

Name: Monica Materano
Date of birth: 08.06.1994
Place of birth: Bari, Italy
Nationality: Italian
E-mail address: monicamaterano@gmail.com

Education

2018/01 - now	**Ph.D. candidate in Electrical Engineering** Faculty of Electrical and Computer Engineering, TU Dresden, Germany Thesis: "*Optimization of performance and reliability of HZO-based capacitors for ferroelectric memory applications*"
2015/10 - 2017/09	**Erasmus Mundus M.Sc. in Nanoscience and Nanotechnology** Faculty of Electrical and Computer Engineering, KU Leuven, Belgium and TU Dresden, Germany Thesis: "*Analysis of charge carriers in Al_2O_3-based thin films for silicon solar cells*"
2012/10 - 2015/07	**B.Sc. in Materials and Nanotechnology Engineering** Politecnico di Milano, Italy Thesis: "*Development of a selective contact within organic/inorganic hybrid devices for photoelectrochemical hydrogen synthesis*"

Research experience

2018/01 - now	Scientist at NaMLab gGmbH, Dresden, Germany Optimization of performance and reliability of HZO-based capacitors for memory applications
2019/10 - 2020/01	Visiting Scientist at Sony Semiconductor Solutions Corporation Characterization of 1T1C FeRAM-based arrays
2016/10 - 2017/09	Project Work and Master Thesis at NaMLab gGmbH, Dresden, Germany Al_2O_3-based passivation layer for Si solar cells
2016/02 - 2016/05	Project work at IMEC, Leuven, Belgium Design of a MEMS device for phase and amplitude modulation via Finite Difference Time Domain (FDTD) computational methods

List of publications

A. Journal articles

1. **Monica Materano**, Peter Reinig, Alfred Kersch, Maxim Popov, Marco Deluca, Thomas Mikolajick, Ulrich Boettger, Uwe Schroeder. Raman Spectroscopy as a Key Method to Distinguish the Ferroelectric Orthorhombic Phase in Thin ZrO_2-Based Films. *physica status solidi (RRL) – Rapid Research Letters*, 2100589, 2022.
2. Hanan Alexandra Hsain, Younghwan Lee, **Monica Materano**, Terence Mittmann, Alexis Payne, Thomas Mikolajick, Uwe Schroeder, Gregory N Parsons, Jacob L Jones. Many routes to ferroelectric HfO_2: A review of current deposition methods. *Journal of Vacuum Science & Technology A: Vacuum, Surfaces, and Films*, 40, 1: 010803, 2022.
3. Patrick D Lomenzo, **Monica Materano**, Terence Mittmann, Pratyush Buragohain, Alexei Gruverman, Takanori Kiguchi, Thomas Mikolajick, Uwe Schroeder. Harnessing Phase Transitions in Antiferroelectric ZrO_2 Using the Size Effect. *Advanced Electronic Materials*, 8, 1: 2100556, 2022.
4. Jun Okuno, Takafumi Kunihiro, Kenta Konishi, **Monica Materano**, Tarek Ali, Kati Kuehnel, Konrad Seidel, Thomas Mikolajick, Uwe Schroeder, Masanori Tsukamoto, Taku Umebayashi. 1T1C FeRAM memory array based on ferroelectric HZO with capacitor under bitline. *IEEE Journal of the Electron Devices Society*, 2021.
5. Dong Hyun Lee, Younghwan Lee, Kun Yang, Ju Yong Park, Se Hyun Kim, Pothala Reddi Sekhar Reddy, **Monica Materano**, Halid Mulaosmanovic, Thomas Mikolajick, Jacob L Jones, Uwe Schroeder and Min Hyuk Park. Domains and domain dynamics in fluorite structured ferroelectrics. *Applied Physics Reviews*, 8, 2: 021312, 2021.
6. Lutz Baumgarten, Thomas Szyjka, Terence Mittmann, **Monica Materano**, Yury Matveyev, Christoph Schlueter, Thomas Mikolajick, Uwe Schroeder and Martina Müller. Impact of vacancies and impurities on ferroelectricity in PVD and ALD-grown HfO_2 films. *Applied Physics Letters*, 118, 3: 032903, 2021.
7. **Monica Materano**, Patrick D Lomenzo, Alfred Kersch, Min Hyuk Park, Thomas Mikolajick and Uwe Schroeder. Interplay between oxygen defects and dopants: effect on structure and performance of HfO_2-based ferroelectrics. *Inorganic Chemistry Frontiers*, 8, 10: 2650–2672, 2021.
8. **Monica Materano**, Patrick D Lomenzo, Halid Mulaosmanovic, Michael Hoffmann, Akira Toriumi, Thomas Mikolajick and Uwe Schroeder. Polarization switching in thin doped HfO_2 ferroelectric layers. *Applied Physics Letters*, 117, 26: 262904, 2020.
9. **Monica Materano**, Terence Mittmann, Patrick D Lomenzo, Chuanzhen Zhou, Jacob L Jones, Max Falkowski, Alfred Kersch, Thomas Mikolajick and Uwe Schroeder. Influence of Oxygen Content on the Structure and Reliability of Ferroelectric $Hf_xZr_{1-x}O_2$ layers. *ACS Applied*

Electronic Materials, 2, 11: 3618-3626, 2020.

10. Ruben Alcala, Claudia Richter, **Monica Materano**, Patrick D Lomenzo, Chuanzhen Zhou, Jacob L Jones, Thomas Mikolajick, Uwe Schroeder. Influence of oxygen source on the ferroelectric properties of ALD grown $Hf_{1-x}Zr_xO_2$ films. *Journal of Physics D: Applied Physics*, 54, 3: 035102, 2020.
11. Patrick D. Lomenzo, **Monica Materano**, Claudia Richter, Ruben Alcala, Thomas Mikolajick and Uwe Schroeder. A Gibbs energy view of double hysteresis in ZrO_2 and Si-doped HfO_2. *Applied Physics Letters*, 117, 14: 142904, 2020.
12. **Monica Materano**, Claudia Richter, Thomas Mikolajick and Uwe Schroeder. $Hf_xZr_{1-x}O_2$ thin films for semiconductor applications: An Hf- and Zr- ALD precursors comparison. *Journal of Vacuum Science & Technology A: Vacuum, Surfaces, and Films*, 38, 2: 022402, 2020.
13. Min Hyuk Park, Dong Hyun Lee, Kun Yang, Ju-Yong Park, Geun Taek Yu, Hyeon Woo Park, **Monica Materano**, Terence Mittmann, Patrick D Lomenzo, Thomas Mikolajick, Uwe Schroeder and Cheol Seong Hwang. Review of defect chemistry in fluorite-structure ferroelectrics for future electronic devices. *Journal of Materials Chemistry C*, 8, 31: 10526-10550, 2020.
14. F. Mehmood, M. Hoffmann, P. D. Lomenzo, C. Richter, **M. Materano**, U. Schroeder and T. Mikolajick. Bulk Depolarization Fields as a Major Contributor to the Ferroelectric Reliability Performance in Lanthanum Doped $Hf_{0.5}Zr_{0.5}O_2$ Capacitors. *Advanced Materials Interfaces*, 1901180, 2019.
15. Uwe Schroeder, **Monica Materano**, Terence Mittmann, Patrick D Lomenzo, Thomas Mikolajick, Akira Toriumi. Recent progress for obtaining the ferroelectric phase in hafnium oxide based films: impact of oxygen and zirconium. *Japanese Journal of Applied Physics*, 58: SL0801, 2019.
16. Terence Mittmann, **Monica Materano**, Patrick D Lomenzo, Min Hyuk Park, Igor Stolichnov, Matteo Cavalieri, Chuanzhen Zhou, Ching-Chang Chung, Jacob L Jones, Thomas Szyjka, Martina Müller, Alfred Kersch, Thomas Mikolajick, Uwe Schroeder. Origin of Ferroelectric Phase in undoped HfO_2 Films deposited by Sputtering. *Advanced Materials Interfaces*, 6, 11: 1900042, 2019.
17. M. Pešić, T. Li, V. Di Lecce, M. Hoffmann, **M. Materano**, C. Richter, B. Max, S. Slesazeck, U. Schroeder, L. Larcher and T. Mikolajick. Built-in Bias Generation in Anti-ferroelectric Stacks: Methods and Device Applications. *IEEE Journal of the Electron Devices Society*, 6: 1019–1025, 2018.

B. Conference contributions

1. Jun Okuno, Takafumi Kunihiro, Kenta Konishi, Hideki Maemura, Yusuke Shuto, Fumitaka Sugaya, **Monica Materano**, Tarek Ali, Maximilian Lederer, Kati Kuehnel, Konrad Seidel, Uwe

Schroeder, Thomas Mikolajick, Masanori Tsukamoto and Taku Umebayashi. High-Endurance and Low-Voltage operation of 1T1C FeRAM Arrays For Nonvolatile Memory Application. *IEEE International Memory Workshop (IMW)*, Dresden, Germany, May 2021.

2. T. Mittmann, **M. Materano**, S.-C. Chang, I. Karpov, T. Mikolajick and U. Schroeder. Impact of oxygen vacancy content in ferroelectric HZO on the device performance. *International Electron Device Meeting (IEDM)*, San Francisco, CA, USA, December 2020.
3. P.D. Lomenzo, C. Richter, **M. Materano**, T. Mikolajick, U. Schroeder, T. Schenk, D. Spirito and S. Gorfman. AFE-like Hysteresis Loops from Doped HfO_2: Field Induced Phase Changes and Depolarization Fields. *Joint Conference of the IEEE International Frequency Control Symposium and International Symposium on Applications of Ferroelectrics (IFCS-ISAF)*, Keystone, CO, USA, October 2020.
4. Jun Okuno, Takafumi Kunihiro, Kenta Konishi, Hideki Maemura, Yusuke Shute, Fumitaka Sugaya, **Monica Materano**, Tarek Ali, Kati Kuehnel, Konrad Seide, Uwe Schroeder, Thomas Mikolajick, Masanori Tsukamoto, Taku Umebayashi. SoC compatible 1T1C FeRAM memory array based on ferroelectric $Hf_{0.5}Zr_{0.5}O_2$. *IEEE Symposium on VLSI Technology*, Honolulu, HI, USA, October 2020.
5. Akira Toriumi, Lun Xu, Yuki Mori, Xuan Tian, Patrick D Lomenzo, Halid Mulaosmanovic, **Monica Materano**, Thomas Mikolajick and Uwe Schroeder. Material perspectives of HfO_2-based ferroelectric films for device applications. *International Electron Device Meeting (IEDM)*, San Francisco, CA, USA, December 2019.
6. T. Francois, L. Grenouillet, J. Coignus, P. Blaise, C. Carabasse, N. Vaxelaire, T. Magis, F. Aussenac, V. Loup, C. Pellissier, S. Slesazeck, V. Havel, C. Richter, A. Makosiej, B. Giraud, E.T. Breyer, **M. Materano**, P. Chiquet, M. Bocquet, E. Nowak, U. Schroeder and F. Gaillard. Demonstration of BEOL-compatible ferroelectric $Hf_{0.5}Zr_{0.5}O_2$ scaled FeRAM co-integrated with 130 nm CMOS for embedded NVM applications. *International Electron Device Meeting (IEDM)*, San Francisco, CA, USA, December 2019.
7. **M. Materano**. Effect of ALD oxidant dose time on ferroelectric properties of HfO_2 and $Hf_{0.5}Zr_{0.5}O_2$ thin films. *7th INTERNATIONAL SYMPOSIUM ON INTEGRATED FUNCTIONALITIES (ISIF)*, Dublin, Ireland, August 2019.
8. **M. Materano**, T. Schenk, C. Richter, T. Mittmann, Chuanzhen Zhou, J.L. Jones, T. Mikolajick and U. Schroeder. Comparison of Zr ALD-precursors for dielectric and ferroelectric device applications. *EuroCVD 22 - Baltic ALD 16*, Luxembourg, June 2019.
9. Pratyush Buragohain, Adam Erickson, Claudia Richter, Pamenas Kariuki, **Monica Materano**, Tony Schenk, Haidong Lu, Uwe Schroeder, Alexei Gruverman. Electrode material effect on the switching behavior of ferroelectric HfO_2-based thin films. *APS March Meeting Abstracts*, Boston, Massachusetts, USA, March 2019.

Declaration of Authorship

I, the undersigned .... hereby declare that I am the sole author of this thesis. To the best of my knowledge this thesis contains no material previously published by any other person except where due acknowledgement has been made. This thesis contains no material which has been accepted as part of the requirements of any other academic degree or non-degree program, in English or in any other language.

Place, Date:

Name (printed letters):

Signature